UNIVERSITY OF Southampton

University of Southampton Research Repository

Copyright © and Moral Rights for this thesis and, where applicable, any accompanying data are retained by the author and/or other copyright owners. A copy can be downloaded for personal non-commercial research or study, without prior permission or charge. This thesis and the accompanying data cannot be reproduced or quoted extensively from without first obtaining permission in writing from the copyright holder/s. The content of the thesis and accompanying research data (where applicable) must not be changed in any way or sold commercially in any format or medium without the formal permission of the copyright holder/s.

When referring to this thesis and any accompanying data, full bibliographic details must be given, e.g.

Thesis: Author (Year of Submission) "Full thesis title", University of Southampton, name of the University Faculty or School or Department, PhD Thesis, pagination.

Data: Author (Year) Title. URI [dataset]

in collaboration with

FACULTY OF MEDICINE

Human Development and Health

Volume 1 of 1

Development of an integrated, printed cell-scaffold construct for bone repair

Thesis for the degree of PhD

Daniel Kee Oon Tang

September 2018

Abstract

The rising incidence of bone disorders, exacerbated by an increasing ageing population worldwide, has resulted in an unmet need for more effective therapies. Bone tissue engineering is seen as a means of developing alternatives to conventional bone grafts for the repair or reconstruction of bone defects through the utilisation of biomaterials, cells, and signalling factors. However, skeletal tissue engineering faces several challenges in order to achieve full translation into clinical practice. The use of additive manufacturing techniques to biofabricate bone offers one potential solution, with its inherent capability for reproducibility, accuracy and customisation of scaffolds, as well as the potential capability for cell and signalling factor delivery. This thesis outlines the approach taken to develop such an integrated construct, which could possibly be used for bone repair. Chapter 1 begins by providing an overview of the current understanding of bone biology and the factors involved in bone repair, before proceeding to examine the current state of bone biofabrication and the necessary factors for success, while discussing the key issues limiting its use to date. The chapter concludes by stressing the need for standardisation of methods for bioprinting, *in vitro* and *in vivo* approaches and analyses, and calls for improvements to design and bioprinting software if biofabrication is to achieve its potential for clinical translation. Chapter 2 summarises the core materials and methods used throughout the project. The next three chapters describe the process leading up to the creation of a biofabricated construct through harnessing the osteogenic capacity of STRO-1 enriched bone marrow stromal cells and biocompatible materials. Chapter 3 describes established isolation and culture protocols for STRO-1 enriched bone marrow stromal cells and confirms that STRO-1 enriched bone marrow stromal cells are induced to undergo osteogenic differentiation by 1,25-dihydroxyvitamin D_3 stimulation, and when seeded onto microporous, micro-rough titanium templates, despite an inverted culture approach. The results suggest STRO-1 enriched bone marrow stromal cells are a suitable cell type for use in bone repair. Chapter four details the various combinations, and potential, of multi-material bioinks for cell encapsulation and delivery purposes. Bioinks, composed of chemically cross-linked, 4% w/v low viscosity alginate, and to a lesser extent, gelatin containing 1% w/v hyaluronic acid, were found to be suitable for STRO-1 enriched bone marrow stromal cell delivery, demonstrating cell viability and proliferation post-seeding. Chapter 4 also describes the methods used in the design, generation, and characterisation of novel polycaprolactone-based scaffolds manufactured by a three-dimensional printer. Although polycaprolactone has been utilised in biomedical devices for decades, the inherent hydrophobicity of polycaprolactone has limited its use as a scaffold for cell seeding, usually requiring post-processing steps to resolve this problem. In this project, non-treated, porous, cylindrical polycaprolactone-based scaffolds were not only reproducibly manufactured by melt extrusion printing with high resolution, but were also shown to be biocompatible, with an average total porosity of 52%. Microcomputerised tomography image reconstruction analyses further revealed that 99.5% of the created pores were interconnected. Chapter 5 reports the creation of an integrated construct potentially suitable for bone reparation purposes. A manual aerosol spray was used to coat printed scaffolds with a biomimetic bioink. While the process did not result in an appreciable reduction in porosity, confocal light and scanning electron microscopy showed major alterations to the surface topography of the scaffolds. STRO-1 enriched bone marrow stromal cells deposited by this aerosol method onto non-treated, as well as biomimetic bioink-coated, 3D printed scaffolds demonstrated good viability, increased ALP activity, and underwent osteogenic differentiation over 21 days *in vitro*. Chapter 6 surmises the findings of this project, and concludes with a personal perspective on the future (potential) direction of biofabrication in bone tissue engineering.

Table of contents

List of Figures

List of Tables

List of Videos

Acknowledgements

This thesis is dedicated to my parents, in particular to my terminally ill father, for their unwavering belief in my abilities, and their constant support during my pursuit of this PhD degree at such a late stage of my career. I am forever indebted to them for instilling in me the zeal for learning new skills and expanding horizons of knowledge, whilst always reminding me of the importance of perseverance, practicality, and preparation in times of uncertainty or adversity.

I would like to express my gratitude and appreciation to my supervisor, Professor Richard Oreffo, first for having provided me with the opportunity to be involved in this exciting research project, and secondly, for his guidance, tutelage, and patience during these three years with the Bone and Joint Research Group in Southampton. I would also like to thank our overseas collaborators in this project, Professors Ou Keng-Liang and Yang Liang-Yo, as well as their team at Taipei Medical University, for their generous support and provision of the three-dimensional printing facilities, without whom this project would not have been at all possible.

Last, but by no means least, my gratitude goes out to the following people (in no particular order) for their invaluable assistance and support during the past three years, without whom progress in this project would have been near impossible:

- David Johnston and Patricia Goggin (both Biomedical Imaging Unit, Southampton General Hospital), for their time and expertise in confocal light microscopy and scanning electron microscopy imaging respectively
- Stuart Lanham (Bone and Joint Research group, Institute for Developmental Sciences), for his patient assistance with micro-computerised tomography imaging and analysis.

Declaration of Authorship

I, Daniel Kee Oon Tang, declare that this thesis and the work presented in it are my own and has been generated by me as the result of my own original research.

'Development of an integrated, printed cell-scaffold construct for bone repair.'

I confirm that:

1. This work was done wholly or mainly while in candidature for a research degree at this University;
2. Where any part of this thesis has previously been submitted for a degree or any other qualification at this University or any other institution, this has been clearly stated;
3. Where I have consulted the published work of others, this is always clearly attributed;
4. Where I have quoted from the work of others, the source is always given. With the exception of such quotations, this thesis is entirely my own work;
5. I have acknowledged all main sources of help;
6. Where the thesis is based on work done by myself jointly with others, I have made clear exactly what was done by others and what I have contributed myself;
7. Parts of this work have been published as:

   i) Sections 1.4 to 1.7 are an updated version of the following publication:
   Tang D, Tare RS, Yang L-Y, Williams DF, Ou K-L, Oreffo ROC. Biofabrication of bone tissue: approaches, challenges and translation for bone regeneration. Biomaterials 2016; 83; 363-82.

   ii) Section 3.2 is a version of the publication listed below:
   Tang D, Yang L-Y, Ou K-L, Oreffo ROC. Re-positioning titanium: an in vitro evaluation of laser-generated microporous, micro-rough titanium templates as a potential bridging interface for enhanced osseointegration and durability of implants. Frontiers in Bioengineering and Biotechnology 2017; 5; 77.

Signed: (DANIEL KEE OON TANG)

Date: 25/09/2018

List of Abbreviations

1,25-VitD3	1,25-dihydroxyvitamin D_3
3D	three-dimensional
3DF	three-dimensional fibre deposition
°C	degrees Celsius
x *g*	times the unit of gravity
αMEM	minimum essential medium eagle, alpha modified
ALP	alkaline phosphatase
AM	additive manufacturing
AP1	activator protein 1
ATF4	activating transcription factor 4
B-TCP	beta-tricalcium phosphate
BMP	bone morphogenetic protein
BMSC	bone marrow stromal cells
c-fms	colony-stimulating factor-1 receptor
Ca	calcium
CAD	computer-assisted design
CapG	capping protein (actin filament), gelsolin-like
CCL2/5	C-C motif chemokine ligand 2 or 5
cDNA	complementary deoxyribonucleic acid
CO_3^{2-}	carbonate
cm^3	cubic centimetres
CT	computed tomography
Ct	cycle time
CTG	CellTracker™ green
CYP	cytochrome P450
DAP12	DNAX-activating protein of 12Kda
DAPI	4',6-diamidino-2-phenylindole
DC-STAMP	dendritic cell-specific transmembrane protein
DKK1	Dickkopf-related protein 1
DMEM	Dulbecco's Modified Eagle's Medium
DMP1	dentin matrix acidic phosphoprotein 1
DPBS	Dulbecco's Phosphate Buffered Saline

ECM	extracellular matrix
EDS	Energy-dispersive X-ray spectroscopy
EDTA	ethylenediaminetetraacetic acid
EPC	endothelial progenitor cells
ERK1/2	extracellular signal-related kinases 1 or 2
FcRγ	Fc receptor γ chain
FCS	foetal calf serum
FDM	Fused deposition modelling
FGF	fibroblast growth factor
FITC	fluorescein isothiocyanate
Fra1	fos-receptor antigen 1
FSH	follicle stimulating hormone
fs	femtoseconds
g	grams
GFP	green fluorescent protein
GPa	gigapascals
HA	hydroxyapatite
HS	heparan sulphate
ID	inhibitor of DNA binding
IGF-1	insulin-like growth factor 1
ITAM	immunoreceptor tyrosine-based activation motif
J	joules
kD	kilodalton
kHz	kilohertz
kV	kilovolt
m	metres
M	molar
MCSF	macrophage colony-stimulating factor
MEPE	matrix extracellular phosphoglycoprotein
Mg	magnesium
µCT	micro-computerised tomography
µg	micrograms
µl	microlitres
µM	micromolar

µm	micrometres
µs	microseconds
mg	milligrams
MG63	human osteosarcoma cells
mJ	millijoules
ml	millilitres
mM	millimolar
mm	millimetres
MMP9	matrix metalloprotease 9
MP	mesenchymal progenitors
MPa	megapascals
MPa.s	megapascal-second
MRI	magnetic resonance imaging
Mt1-MMP	membrane-associated type 1 matrix metalloprotease
MPa	megapascals
MSC	mesenchymal stem cells
N.A.	not applicable
NFAT2	nuclear factor of activated T-cells 2
NFATc1	nuclear factor of activated T-cells cytoplasmic 1
NF-κB	nuclear factor kappa-light chain-enhancer of activated B cells
ng	nanograms
nm	nanometres
OCN	osteocalcin
OPG	osteoprotegerin
OPN	osteopontin
ORP150	150-kDa oxygen-regulated protein
P	phosphorus
PBS	phosphate buffered saline
PCL	polycaprolactone
PDGF	platelet-derived endothelial growth factor
PET	positron emission tomography
PFA	paraformaldehyde
PGE_2	prostaglandin E_2
PHEX	phosphate-regulating neutral endopeptidase, X-linked

pl	picolitres
PLLA	poly-L-(lactic acid)
PLGA	poly(lactic-co-glycolic acid)
PS	penicillin-streptomycin
PTH	parathyroid hormone
RANK	receptor activator of nuclear factor kappa-B
RANKL	receptor activator of nuclear factor kappa-B ligand
RNA	ribonucleic acid
ROI	region of interest
rpm	revolutions per minute
RT-qPCR	quantitative reverse transcription polymerase chain reaction
Runx2	runt-related transcription factor 2
SDF-1	stromal cell-derived factor 1
SEM	scanning electron microscopy
SLA	stereolithography
SOST	sclerostin
SPECT	single-photon emission computerised tomography
SSC	skeletal stem cells
STL	standard tessellation language
TEM	transmission electron microscopy
TNFα	tumor necrosis factor alpha
T_g	glass transition temperature
TGF-β1/3	transforming growth factor- β1 or 3
Ti6Al4V	titanium aluminium vanadium alloy
TiO_2	titanium oxide
TRAP	tartrate-resistant acid phosphatase
TRITC	tetramethylrhodamine
TSH	thyroid stimulating hormone
VEGF	vascular endothelial growth factor
Wnt	wingless-related integration site
w/v	working volume
wt%	percent weight
VOI	volume of interest
v/v	volume to volume

Chapter 1: Biofabrication in bone tissue engineering

An increasing ageing population worldwide, coupled with the rising incidence of bone and joint disorders, have resulted in an unmet need for more effective treatments. Although bone grafts remain the gold standard of treatment for repairing bone defects, there are problems associated with such a procedure. The mainstay of current joint and dental replacement strategies involve the surgical implantation of artificial prostheses. However, current artificial implants possess limited functionality and often require replacement following 10 to 15 years of use. Cases where such implants fail at earlier time-points are well documented, and more recently, some alloy-based implants have even been reported to cause corrosion- or wear-related toxicity in patients. Given the limitations of current therapies, there has been an increasing focus in developing alternative biomimetic approaches that are based on the underlying principles of regenerative medicine, with the ultimate goal of creating personalised treatments for patients that are not only effective, but also safe. The approach of utilising biomaterials, cells, and/or signalling factors to repair bone defects or generate skeletal tissue substitutes has been termed as bone tissue engineering. Ongoing progress in the field has already contributed to an improved understanding of bone biology, functionality, and pathophysiology, in addition to enabling advances in associated disciplines such as material sciences, drug discovery, cellular biology, and (bio)mechanical engineering. Despite this, bone tissue engineering has yet to achieve full translation into clinical practice, with bone tissue engineers continuing to face a myriad of complicated challenges.

One approach seen to have the potential of overcoming some of the issues faced involves the use of additive manufacturing techniques, which have a proven capability for reproducibility and accuracy, as well as the potential for customisation. The term, biofabrication, was coined in 2009 to describe the various additive manufacturing processes used to create constructs for tissue regenerative or replacement purposes. This thesis investigates the possibility of utilising existing additive manufacturing techniques to create an integrated biocompatible, osteoinductive construct through combining existing biomaterials with human STRO-1 enriched bone marrow stromal cells. The complex process of developing this integrated construct is detailed over six chapters. In order to demonstrate the rationale underpinning the approaches taken during this study, and to better explain the expanding interest in biofabrication for bone tissue engineering, it is imperative to begin with an overview of normal bone development, biology, and

pathophysiology, followed by a review of current literature regarding the state of play in bone tissue engineering and biofabrication.

1.1 The interplay between composition, structure and functionality of bone

Bone is an innervated, vascularised integrated organ consisting of bone tissue encased within the periosteum, a dense layer of bone-forming cells and vascularised connective tissue. Bone marrow, composed of haematopoietic and skeletal stem cells, is located in the trabecular cavities of flat bones as well as the proximal epiphyses of the humeri and femora, and plays a role in haematopoiesis and bone remodelling (1). Bones enable locomotion, provide structural support and protection to vital organs, in addition to performing homeostatic functions such as the regulation of serum calcium and phosphate levels (2).

The four principal cell types in bone – osteoprogenitor cells, osteoblasts, osteoclasts, and osteocytes – form two types of bone tissue, cortical and trabecular bone (Figure 1-1) (2). Both types of bone tissue contain bone extracellular matrix (ECM), which consists of organic and inorganic components. Inorganic components compose 50 to 65 per cent of the dry mass of bone. This mineralised component is a complex combination of calcium (Ca), phosphorus (P), magnesium (Mg), zinc, silicon, and carbonate (CO_3^{2-}). This is reflected in the Ca:P ratio in natural bone, which ranges from 1.37 to 1.87. Hydroxyapatite (HAP), with the chemical formula $Ca_{10}(PO_4)_6(OH)_2$ and a Ca:P ratio of 1.67, is the most abundant of the inorganic components [2], and is often used in bone tissue engineering for its osteoinductive and mineralising effects (3). Organic components contribute 35 to 50% of the dry mass of bone. Type I collagen constitutes 90 to 95 per cent of this organic component. The remaining constituents consist of: 1) glycosaminoglycans such as fibronectin (FN), 2) proteoglycans such as heparan sulphate (HS), and 3) structural glycoproteins secreted by osteoblasts such as the vitamin K-dependent polypeptide osteocalcin (OCN, which promotes osteoclast precursor recruitment, attachment and differentiation into osteoclasts), osteopontin (OPN, which regulates the growth and size of hydroxyapatite crystals), osteonectin, osteoadherin, and bone sialoprotein (which promotes mineralisation by binding to calcium ions and type 1 collagen, thereby raising the local calcium concentration) (4). Osteoblasts also release membrane-enclosed vesicles containing alkaline phosphatase (ALP) and other enzymes that raise the local phosphate ion concentration. With high local concentrations of both ions, the matrix vesicles become a foci for HAP crystal formation, the first step in the calcification of the matrix [1, 3, 4]. Specific points

along the collagen fibres serve as nucleation sites for HAP (Figure 1-2) (5). This interwoven scaffolding network consisting of organic and inorganic elements contributes to the tensile strength as well as the rigidity of bone, thus imparting its structural and mechanical functionality. However, despite the similarity in their biological and chemical composition, the two types of bone tissue differ in their macroscopic architecture and appearance (Figure 1-1).

Cortical or compact bone is the hard outer layer, making up 10 to 30 per cent of bone. It is 80 to 90 per cent mineralised, and accounts for about 80 per cent of bone tissue mass in the human body (1). Its high density and thickness enables bones to withstand mechanical loading and stress. This is reflected by a Young's modulus of 7 to 30 GPa and a compressive strength of 100 to 230 MPa (6), which is the consequence of a hierarchical structure organised down to the nanoscale level (Figure 1-2). Cortical bone is composed of osteons that are 170 to 250 micrometres (µm) in diameter. Osteons have a central vascular channel (60 to 90 µm in diameter), called the Haversian canal, and a highly mineralised outer boundary, known as the cement line (less than five µm in thickness). In the osteons, each vascular channel is concentrically surrounded by lamellae of two to nine µm in thickness. These lamellae, which are composed of collagen fibril bundles, have a twisted plywood arrangement, where neighbouring lamellae have different fibril orientations. Osteocytes reside in lacunae (five to ten µm in diameter) and interconnect through canaliculi [100 to 400 nanometres (nm) in diameter] in areas where lamellae are less organised.

The fibrils (80 to 100 nm in diameter) are surrounded by polycrystalline extrafibrillar mineral platelets (5 nm thickness, 50 to 80 nm width, and 40 to 200 nm length). Extrafibrillar as well as the intrafibrillar matrix may also contain molecular components, such as non-collagenous proteins or crosslinks, promoting the formation of sacrificial bonds. In the fibrils, type I collagen molecules (1.5 nm diameter, 300 nm length) and hydroxyapatite nanocrystals (50 nm width, 25 nm height, 1.5 to 4 nm thickness) form a composite structure, where arrays of collagen molecules staggered at 67 nm are embedded with nanoplatelets of hydroxyapatite mineral (5). This highly organised orientation of collagen fibrils in cortical bone is in marked contrast to the randomly orientated collagen fibres seen in woven bone that forms during the initial healing phase of bone repair. Volkmann's canals, orientated at right angles to the long axis of the bone, connect the periosteal neurovascular supply to those of the central canals and medullary cavity. Together with the

Haversian canals, Volkmann's canals ensure the adequate vascularisation of bone tissue, allowing for the exchange of sufficient nutrients and the removal of waste metabolites, in addition to enabling bone to perform its homeostatic functions (1).

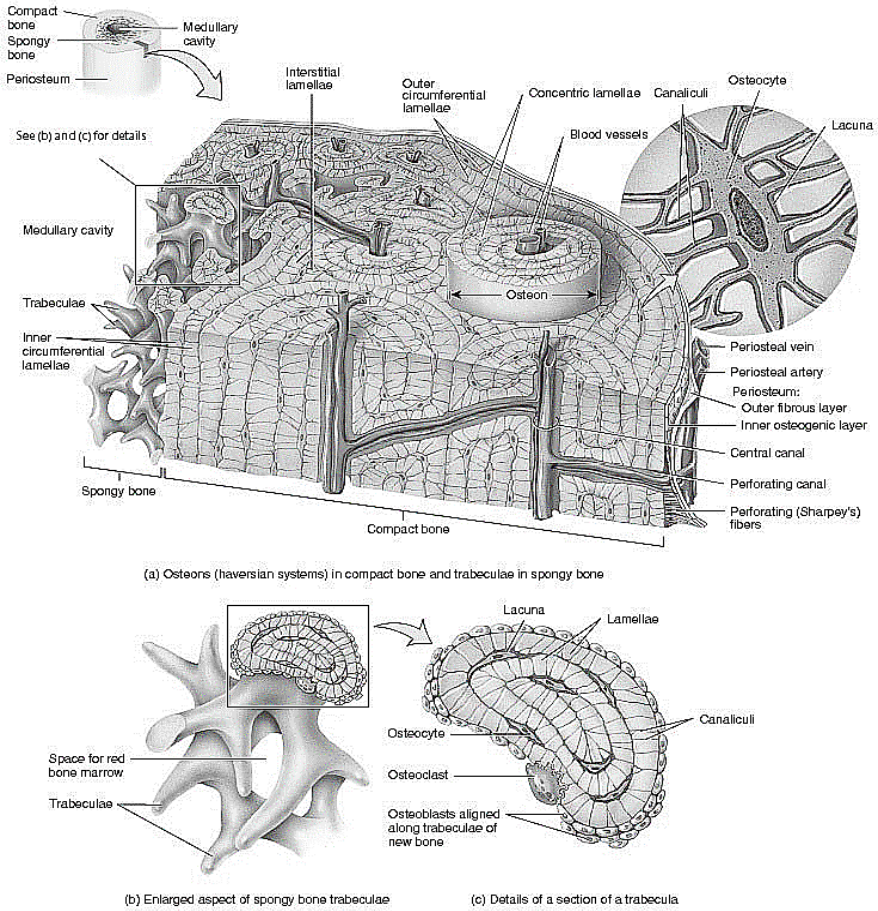

Figure 1-1 Bone microstructure.

(a) Haversian systems in cortical bone (b) Trabeculae forming cancellous bone (c) Cross-section of a trabecula. Modified from (2).

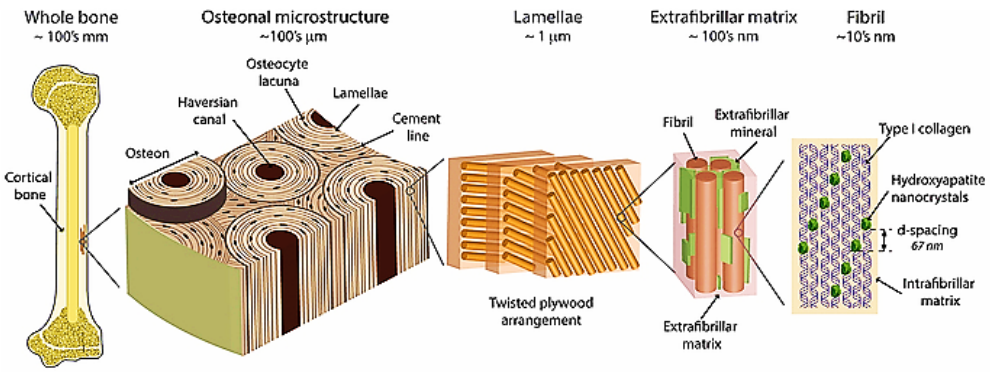

Figure 1-2 Hierarchical structure of cortical bone down to the nanoscale level.

Reproduced from (5).

Trabecular (also known as spongy or cancellous) bone comprises the remaining 30 to 90 per cent of bone, and is located in the interior of bones next to the marrow cavity. It is 50 to 90 per cent porous, forming an open, honeycomb-like structure. This results in a large surface area for cellular interactions, thereby optimising the homeostatic functionality of bone such as calcium and acid-base regulation. Trabecular bone has a lower compressive strength of 2 to 12 MPa and a Young's modulus of 0.05 to 0.5 GPa (6) as a consequence of the porosity as well as the irregularly arranged lamellae which align along stress lines to form trabeculae (Figure 1-1) (1, 2). The difference in structural organisation between the two types of bone confers plasticity and the capacity to withstand microdamage (7). Both types of bone undergo dynamic remodelling throughout the lifespan of the individual, enabling self-repair (to an extent) but also ensuring the maintenance of healthy bone. Complex interactions between mechanical loading, chemical stimuli, osteoprogenitor cells, osteoblasts, osteocytes, and osteoclasts bring about bone formation, remodelling and maintenance.

1.1.1 Osteoprogenitor cells

Osteoprogenitor cells are committed osteogenic cells that undergo mitotic differentiation into osteoblasts, and form bone under default differentiation conditions. It remains unclear as to the exact mechanism whereby stem cells are triggered to differentiate into osteoprogenitor cells. Osteoprogenitor cells play a major role in bone growth and repair, not just through osteoblastogenesis, but also in the regulation of osteoclastogenesis by elaborating the function of Macrophage Colony-Stimulating Factor (MCSF) and Receptor Activator of Nuclear factor kappa-B Ligand (RANKL) (8). Known bone loss with ageing or menopause has been postulated to be a result of a decrease in stem cell or osteoprogenitor cell number, as well as a reduced responsiveness of osteoprogenitor cells to signalling factors or local bone microenvironment changes, resulting in altered differentiation potentials (9). Studies by Lee *et al* using murine pre-osteoblast cell lines (MC3T3-E1) suggest osteoprogenitor cells play a key role in implant osseointegration by initiating the inflammatory response to implanted biomaterials via the extracellular signal-related kinases 1 and 2 (ERK1/2) pathway (8).

Work first carried out by Friedenstein, Owen, and colleagues in the 1960s demonstrated a rapidly adherent fibroblastic cell originating from bone marrow stroma that could establish colonies in a density-dependent manner. When progeny of such cells were transplanted *in vivo* in diffusion chambers (closed systems),

cartilage was noted to form in the relatively anaerobic interior and bone on the relative aerobic exterior of these chambers. In contrast, when these cells were transplanted *in vivo* using a scaffold (open systems), the colonies formed a bone/marrow system comprising bone, osteocytes, osteoblasts, marrow adipocytes of donor origin, haematopoiesis-supportive stroma, and haematopoiesis of recipient origin (10). This population of cells, when plated at low density, were plastic adherent (10). However, in 1995, Long *et al* would report this non-adherent layer of cultured human bone marrow contained a smaller (but more mature) population of colony-forming unit-fibroblastic cells that could also be induced to form bone. These cells were identified by immune-adherence isolation (11). Studies by other groups have since identified osteoprogenitor cells in not only bone marrow stromal populations (confirming the earlier findings of Friedenstein *et al*), but also in cell populations derived from calvaria and other bones through the use of functional assays of proliferation and differentiation capacity *in vitro* (termed as the colony-forming units-osteogenic assay), as well as in peripheral blood (12). The latter cell population appear to be a subset of colony-forming units-fibroblastic, and colony-forming units-ALP (13). The relationship between adherent and non-adherent osteoprogenitor populations has yet to be elucidated. Various studies have shown osteoprogenitor cells to be relatively rare (ranging from less than 1% in foetal rat calvaria to 0.5–1 X 10^{-5} of the nucleated cells of unfractionated rat and mouse bone marrow, to less than 1 X 10^{-8} in human peripheral blood). However, Bianco *et al* utilised functional assays *in vitro* and *in vivo* to show osteoprogenitor cell frequency in adherent human bone marrow cell layers is significantly higher, ranging from 1% to 10% of adherent cells (9).

Bone marrow remains a frequently used source of osteogenic cells. The heterogeneity of bone marrow, coupled with the paucity of developmental stage-specific markers for osteogenic cells, has made the isolation of a homogeneous subpopulation of osteogenic cells a difficult task. Furthermore, osteoprogenitor cells measurable using functional bone nodule assays have demonstrated a limited capacity for self-renewal in both calvaria and stromal populations *in vitro*, which is consistent with being true committed progenitors with a finite lifespan. While some osteoprogenitor cells have been shown to undergo osteogenic differentiation as a default pathway *in vitro*, others require stimuli other than serum alone (9). These issues make utilising osteoprogenitor cells for bone tissue engineering an unrealistic target. As such, the search for the fraction of multipotent, clonogenic, self-renewing cells from human bone marrow stroma continued. This clonogenic fraction, which

could be secondarily isolated from heterotropic grafts, expanded, and serially transplanted, was first shown in humans, and later in the mouse, to coincide with perisinusoidal reticular cells (14). These cells were initially labelled as osteogenic stem cells, and later as bone marrow stromal cells by Friedenstein and co-workers. The term 'skeletal stem cells' (SSCs) has been applied to these cells in recent times (15) to differentiate these multipotent self-renewing stromal progenitors found in the bone marrow sinusoids from multipotent cells originating in other tissues which are capable of osteogenesis. SSCs are further detailed in 3.1.1.

1.1.2 Osteoblasts

Osteoblasts (Gr. *osteon*, bone + Gr. *blastos,* germ) are mononucleate cells of about 15 to 30 µm in diameter, and make up four to six per cent of the total resident cells in bone (1). Osteoblasts have a life span of a few months and are non-mitotic. Osteoblasts differentiate from osteoprogenitor cells in the periosteum and bone marrow under the regulation of Runt-related transcription factor 2 (Runx2) and osterix (16). Osteoblast activity is stimulated by parathyroid hormone (PTH) (17) as well as a raft of other osteotrophic agents (further detailed in 1.2.3).

Under the control of Bone Morphogenetic Protein (BMP) and Wingless-related integration site (Wnt) signalling pathways, SSCs are committed to become osteoprogenitor cells, which then undergo proliferation into pre-osteoblasts. This proliferative phase is maintained by the helix-loop-helix proteins Twist and Inhibitor of DNA binding (ID). Insulin-like Growth Factor 1 (IGF1), Prostaglandin E_2 (PGE_2), and 1,25-VitD3 induce the cessation of pre-osteoblast proliferation, resulting in the loss of their spindle-shaped morphology and the subsequent formation of large cuboidal active osteoblasts. Type 1 collagen, ALP, bone sialoprotein, OPN, and OCN are some of the markers used to demonstrate osteoblast maturation. Runx2, osterix (through its interaction with Nuclear Factor of Activated T-cells 2 or NFAT2) and Wnt/β-catenin are some of the key intrinsic factors that regulate osteoblast maturation and bone formation (as highlighted in Figure 1-3) (9). In addition to intranuclear receptors for 1,25-VitD3, osteoblasts also possess membrane receptors for PTH, oestrogen and progesterone (17).

When inactive, osteoblasts appear as narrow, spindle-shaped cells lying on the bone surface. Active osteoblasts synthesise and line the bone ECM (also known as osteoid). Under light microscopy, these active osteoblasts can be seen to be in direct contact with the bone surface and can be identified by their cuboidal to

columnar appearance, a basal round nucleus, large Golgi apparatus, abundant mitochondria, and a strongly basophilic cytoplasm containing Periodic acid-Schiff-positive granules (which contain precursors of bone ECM glycoproteins) (1). Long branching cytoplasmic processes extending from the cell bodies on the side of bone ECM formation penetrate deep into the osteoid. Some mature mineralising osteoblasts become embedded into the secreted matrix and undergo terminal differentiation into osteocytes. Remaining osteoblasts either undergo apoptosis or become bone lining cells (Figure 1-3) (17).

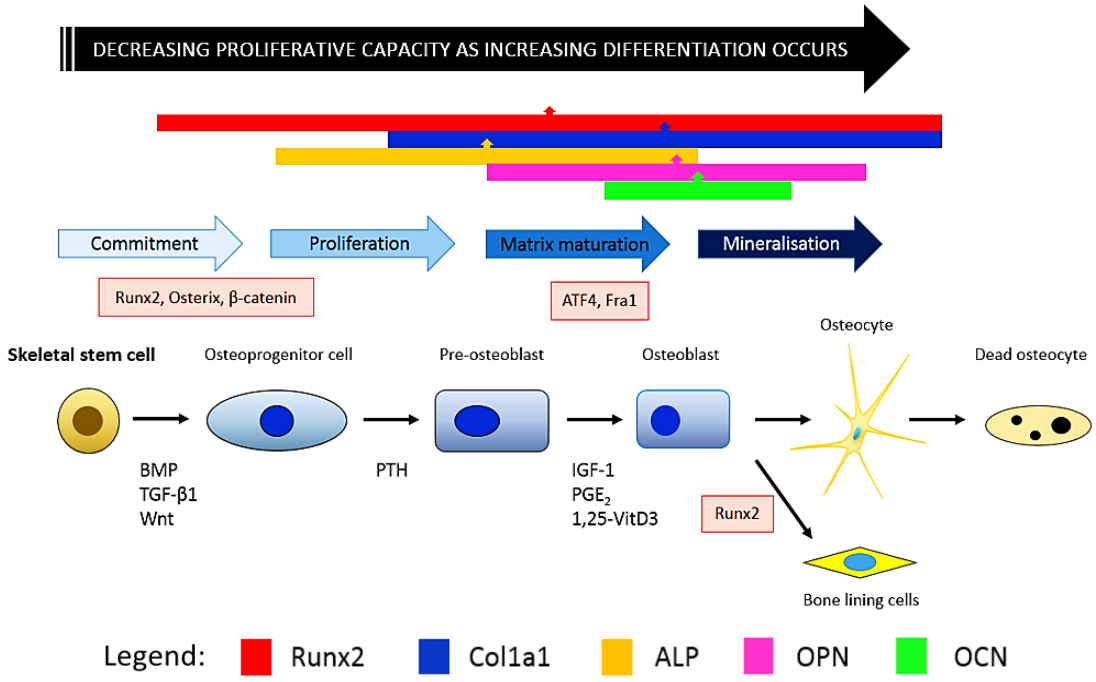

Figure 1-3 Summary of osteoblastogenesis.

Upregulation of osteogenic differentiation markers (marked by coloured bars) occurs at different (and sometimes, overlapping) stages of osteoblastogenesis, and is driven by multiple signalling factors. Abbreviations: ATF4 – activating transcription factor 4, Fra1 - Fos-related antigen 1. Modified from (17).

1.1.3 Osteoclasts

Osteoclasts (Gr. *osteon*, bone + Gr. *klastos*, broken) are motile, exocrine, multi-nucleated cells (of up to fifty nuclei), with a diameter of 40 to more than 100 µm, that originate from haematopoietic cells of the macrophage-monocytic lineage (1). MCSF and RANKL, which bind to colony-stimulating factor-1 receptor (c-fms) and Receptor Activator of Nuclear factor kappa-B (RANK) respectively, trigger the differentiation of macrophage-monocytic cells into osteoclast progenitors which further differentiate into osteoclasts (17). Co-stimulation by Immunoreceptor

Tyrosine-based Activation Motif (ITAM)-containing adaptors DNAX-activating protein of 12Kda (DAP12) and Fc Receptor γ chain (FcRγ) results in the activation of Nuclear Factor Kappa-light chain-enhancer of activated B cells (NF-κB), Activator Protein 1 (AP1) and Nuclear Factor of Activated T-cells cytoplasmic 1 (NFATc1), which in turn, upregulate essential osteoclast genes such as cathepsin K, Matrix Metalloprotease 9 (MMP9), Dendritic Cell-specific Transmembrane Protein (DC-STAMP), Tartrate-Resistant Acid Phosphatase (TRAP) and β3 integrin, allowing for the final differentiation of the osteoclast progenitor into the multinucleated functional osteoclast (Figure 1-4).

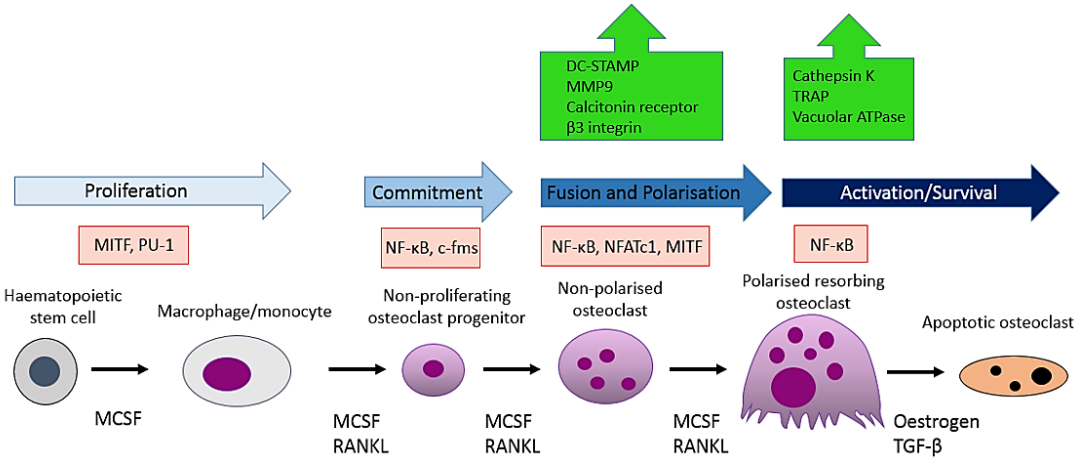

Figure 1-4 Summary of osteoclastogenesis.

Modified from (17).

Osteoclastic resorption is a key contributor to the process of bone remodelling in response to growth or changing mechanical stresses. Osteoclast activity is inhibited by calcitonin and stimulated by RANKL (produced by PTH-activated osteoblasts). Active osteoclasts are found within, or near enzymatically etched crypts in the matrix known as resorption bays (previously called Howship lacunae). The cellular aspect in apposition to bone is characterised by fine irregular microvilli that form a ruffled border; its high surface area facilitates bone resorption through the secretion of several organic acids (that dissolve the mineral component) and lysosomal proteolytic enzymes (including collagenase, which cause ECM degradation), thereby keeping the pH low within the resorption cavity. This primary function of osteoclasts is reflected by the presence of numerous mitochondria, multiple Golgi complexes, lysosomes and membrane-bound vesicles located throughout the cell when visualised by electron microscopy. The release of calcium into the extracellular fluid and subsequently, the circulatory system, underpins the mechanism whereby regulation of osteoclastic activity influences long-term calcium

homeostasis. An area of cytoplasm rich in actin filaments underlies the ruffled border, facilitating its motility during bone resorption (1, 4). The activity of these actin filaments is regulated by Rho/Rab GTPases (18).

1.1.4 Osteocytes

Osteocytes (Gr. *osteon*, bone + Gr. *kytos*, cell) measure 9 by 20 μm in size, and comprise 90 to 95 per cent of all cells in mature bone tissue (1). Osteocytes are the longest-lived bone cell (up to decades), and are descended from matrix-producing osteoblasts that have not undergone apoptosis towards the end of a bone formation cycle, becoming passively incorporated into the osteoid. The mechanism underlying osteocytogenesis remains unclear (Figure 1-5). The osteocyte develops from the matrix-producing osteoblast, which expresses Runx2 and osterix (both necessary for osteoblast differentiation), ALP and collagen (both necessary for osteoid production) in addition to OCN (produced by the late osteoblast). OCN continues to be expressed by osteocytes (19). Some designated osteoblasts become embedded in the osteoid through an unknown mechanism, undergoing a morphological change, from a large cuboidal cell shape into a stellate one, with more than fifty slender dendritic projections (called osteocyte processes) that interconnect with other embedded osteocytes and osteoblasts on the bone surface via gap junctions. Compared to osteoblasts, osteocytes appear flat and almond-shaped, with a markedly reduced endoplasmic reticulum and Golgi apparatus. Osteocyte nuclear chromatin also appears more condensed (1, 20).

As osteoid mineralises around the osteocyte processes, canaliculi are formed, creating the microporosity that characterises mineralised bone. Osteocyte bodies reside in lacunae, with a small amount of surrounding extracellular fluid that permits the diffusion of molecules, oxygen and nutrients through the lacunar-canaliculi network. 150-kDa Oxygen-regulated protein (ORP150) has been suggested to help preserve osteocyte viability in a hypoxic environment. Sclerostin (SOST), which is produced predominantly by osteocytes (and is therefore used as a marker for mature osteocytes), appears to inhibit Wnt signalling in osteoblast lineage cells, promoting osteoblast differentiation and negatively regulates bone formation and remodelling (4). SOST acts as an antagonist against lipoprotein receptor 5, a positive regulator of bone mass. Mutations in the SOST gene (which codes for sclerostin) causes high bone mass in humans. Antibodies against SOST are being considered for treating postmenopausal osteoporosis given their specificity and anabolic effect on bone formation (19). In aged bone, there is

reduced bone remodelling and these lacunae are empty. Molecules such as Membrane-associated type 1 Matrix Metalloprotease (Mt1-MMP) and E11/gp38 glycoprotein are involved in canaliculi and dendrite formation while capping protein (actin filament), gelsolin-like (CapG) and destrin regulate the cytoskeleton. Mechanical loading increases E11/gp38 expression, with maximal expression occurring in regions of potential bone remodelling, thus allowing for dendritic elongation and modification of their surrounding microenvironment. Phosphate-regulating neutral endopeptidase, X-linked [PHEX, for which osteopontin (OPN) is a substrate], dentin matrix acidic phosphoprotein 1 (DMP1) and matrix extracellular phosphoglycoprotein (MEPE) control matrix biomineralisation and mineral metabolism through their regulation of fibroblast growth factor-23 (FGF23) which reduces 1,25-VitD3 levels (4, 19, 21). There are studies that suggest osteocytes are not only involved in phosphate regulation and calcium availability, but that osteocytes are able to remove and replace bone matrix, contributing to mineral homeostasis through osteocytic osteolysis. There is also evidence that osteocytes regulate osteoblast and osteoclast activity, in addition to producing soluble factors that target distant organs, such as the kidney and muscle.

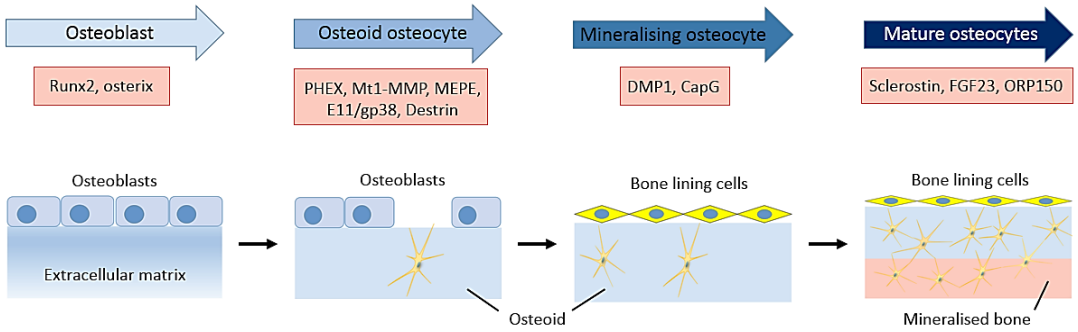

Figure 1-5 Gene marker expression during osteocytogenesis.

Modified from (19).

1.2 Bone development and physiology

1.2.1 Developmental skeletogenesis

Bone develops by two processes. Most flat bones, such as the frontal and parietal bones of the skull, the mandible, and the maxilla, are formed through intramembranous ossification. Intramembranous ossification begins during gestation through aggregation of mesenchymal cells at sites of richly vascularised connective tissue, forming the mesenchymal condensation layer. Within this layer is the ossification centre, whereby these groups of mesenchymal cells differentiate into

osteoblasts, which secrete osteoid. ALP, also secreted by osteoblasts, mineralises the osteoid through precipitation of inorganic calcium phosphate salts, the dominant form of which is HAP. During this ossification process, some osteoblasts become encapsulated within the matrix and become osteocytes. These islands of developing bone form walls delineating cavities containing capillaries, bone marrow and undifferentiated cells. Several such groups simultaneously form at the ossification centre, and the fusion between the developing walls results in the spongy appearance of bone. Osteoblasts arrange themselves on trabecular surfaces and continue producing bony matrix. As these trabeculae thicken, osteoblasts merge to form a three-dimensional latticework of trabecular bone. Intervening connective tissue that remains among the walls is penetrated by developing blood vessels and undifferentiated mesenchymal cells, resulting in the formation of primary bone marrow. The ossification centres grow radially and fuse together, replacing the original connective tissue. Osteoclasts migrate to trabecular surfaces to resorb bony matrix, enabling bone remodelling to occur. In selected regions, trabecular bone is converted to compact bone. The deposition of concentric layers of matrix around trapped blood vessels forms the osteons while a layer of specialised connective tissue invests the developing bone, forming the periosteum (1, 2, 22).

Short and long bones are formed by endochondral ossification (Figure 1-6). Prx1+ progenitor cells nearest the centre of an emerging limb bud undergo mesenchymal condensation. These cells express Col2a1 as chondrogenic differentiation occurs, resulting in the formation of a cartilage template. Innermost differentiating cells upregulate Col10a1 expression as they hypertrophy, triggering the local formation of a thin bony collar that impedes oxygen and nutrient diffusion into the underlying cartilage. Chondrocytes produce ALP and swell, enlarging their lacunae. These changes compress the matrix into narrow trabeculae, leading to calcification of the matrix as well as chondrocyte death. Blood vessels from the periosteum (known as the periosteal bud) perforate through the bone collar, bringing in haematopoietic and osteoprogenitor cells. Osteoblasts adhere to the calcified cartilage matrix, producing continuous layers of primary bone that surround the matrix remnants, resulting in the formation of the primary ossification centre. Vascular invasion also bisects the endochondral structure, forming two inversely stratified and distally opposed growth plates that establish a longitudinal axis of growth. Perpendicular growth is driven by periosteal osteoblasts. Secondary ossification centres, which appear later at the epiphyses of the cartilage template, develop in a similar manner as bones grow in length and width. Erosion of cartilage

by osteoclasts during the expansion and remodelling phases of these primary and secondary ossification centres results in the formation of a porous three-dimensional primitive marrow cavity (1, 4, 16). BMP signalling has recently been found to play a crucial role in Prx1+ progenitor condensation as well as in the formation of normal bone ECM (16).

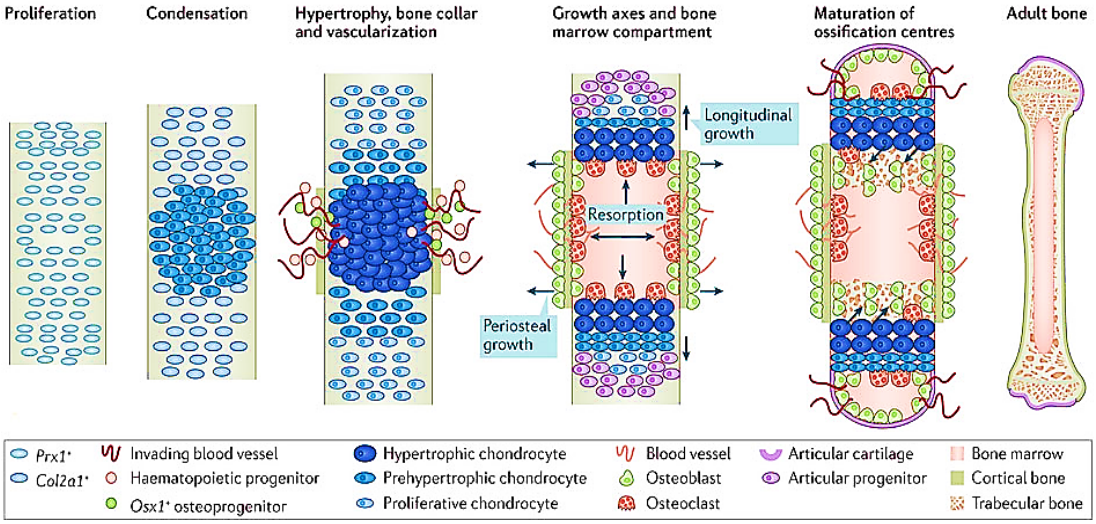

Figure 1-6 Schematic summary of the key stages of developmental skeletogenesis involving endochondral ossification.

Reproduced from (16).

In mature endochondral bone, the interior of the diaphysis remains constant. Chondrocytes, arranged in columns on two fronts on both sides of the central region, eventually form the epiphyseal plates (at the junction between the diaphysis and epiphyses) that determine the longitudinal growth of the diaphysis. Figure 1-7 shows the zones that make up this epiphyseal plate: 1) the resting zone, consisting of hyaline cartilage and chondrocytes, 2) the proliferative zone, where chondrocytes (expressing Col2a1) undergo rapid division, forming columns of stacked cells parallel to the long axis of the bone that cause the longitudinal elongation of the bone, 3) the hypertrophic zone, comprising of swollen chondrocytes (expressing Col10a1) with glycogen-filled cytoplasm, and 4) the calcified zone, where chondrocytes undergo apoptosis and the septa of the matrix becomes calcified through the formation of HAP crystals. The ossification zone is where bone tissue first appears through the deposition of osteoid by osteoblast over spicules of calcified matrix. Longitudinal growth of bone is achieved through repeated cycles of proliferation, hypertrophy and mineralisation of chondrocytes. Towards the end of foetal life through to puberty, ossification centres appear in the two epiphyses of

long bones. Post-adolescence, growth plates close and thus, growth in length ceases. This occurs under the influence of testosterone in men, and oestrogen in women. It should be noted that epiphyseal closure occurs at different times in different bones, and is complete in all bones by the age of twenty. Bone widening, however, may still occur (1, 4). Bone is only able to perform its mechanical role through the process of remodelling and maintenance.

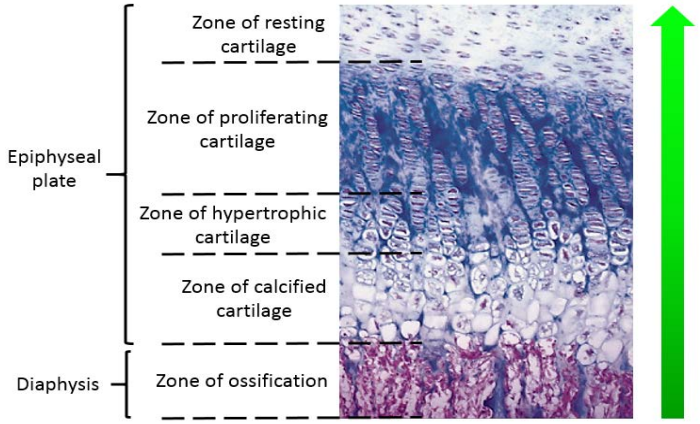

Figure 1-7 Histological appearance of the epiphyseal growth plate in long bones.

Direction of bone growth is indicated by the green arrow. The size of the epiphyseal plate remains constant during the growth phase. Adapted from (1).

1.2.2 The process of fracture healing

Fracture healing is a complex biological process that is intertwined with those of the innate immune system. Following trauma or damage, bone heals either by the direct intramembranous or indirect pathway; the latter is the most common, and comprises of intramembranous and endochondral ossification. Primary fracture healing requires anatomical reduction and rigidly stable conditions, achieved by surgical intervention via open reduction and internal fixation methods which minimises the fracture gap and inter-fragmentary motion. In such conditions, bone is able to heal by direct regeneration of anatomical lamellar bone followed by Haversian systems, without the need for remodelling to occur. When a slightly larger gap exists between bone fragments, gap healing occurs, whereby the voids are filled with direct deposition of intramembranous woven bone and the Haversian systems are re-established through osteoclast-mediated remodelling (23, 24).

Complete rigidity is not possible in most fractures treated by splinting, intramedullary nailing or external fixation methods. In these scenarios, secondary fracture healing, which involves intramembranous and endochondral ossification,

occurs. Figure 1-8 and Figure 1-9 summarise the sometimes simultaneous biological events, starting with the localised formation of a haematoma. The fibrin network provides the initial matrix for inflammatory cell influx triggered by platelet-derived factors, local tissue macrophages, complement fragments, as well as signals released from necrotic tissue. Neutrophils arrive within the first 24 hours and recruit macrophages and monocytes to the fracture site which in turn, work in combination with osteomacs (macrophages resident in the peri- and endosteum) to regulate the inflammatory response, a critical stage of secondary fracture healing (Figure 1-9) (23).

Macrophages phagocytose necrotic cells and the initial fibrin mesh, and secrete chemotactic and inflammatory mediators such as tumor necrosis factor alpha (TNFα), interleukin-1β (IL-1β), interleukin-6 (IL-6), and C-C motif chemokine ligand 2 (CCL2), which trigger the recruitment of MSC, local osteoprogenitor cells, and fibroblasts. Stromal cell-derived factor 1 (SDF-1) mediates the local and systemic recruitment of MSC while platelet and macrophage derived signals guide the proliferation, differentiation and ECM synthesis of recruited MSC and osteoprogenitor cells. This enables the removal of the haematoma and cessation of the acute inflammatory response within a week after the initial damage, allowing for the generation of granulation tissue rich in proliferating mesenchymal cells and neovasculature embedded within a collagen matrix (4, 23, 24).

Disruption to local vasculature with subsequent reactive arteriolar contraction results in the fracture site being hypoxic, particularly in the area close to the fracture gap. This low oxygen tension, together with a degree of micromotion and microenvironmental signals, guide MSC differentiation along the chondrogenic pathway. Chondrocytes produce cartilage, which extends throughout the gap, connecting the ends of the fracture. In conjunction with fibrotic tissues, the soft callus provides initial mechanical stability and becomes the scaffold for endochondral bone formation. While this occurs, in areas with better blood supply and greater stability, new woven bone forms via intramembranous ossification. This begins in the inner layer of periosteum and advances towards the gap. The woven bone covers the external surface of the soft callus. Chondrocytes in the soft callus hypertrophy and undergo apoptosis, secreting calcium and factors that stimulate vascular ingrowth into the cartilage scaffold-stabilised gap. Increased blood flow is accompanied by osteoprogenitor cell differentiation into osteoblasts and deposition of woven bone onto the cartilage scaffold, creating a hard callus. As the cartilage mineralises, the mechanical stability of the fracture site increases until the new bone

formed is able to support physiological loads independently. Osteoclasts remove immature woven bone and cartilage matrix, initiating remodelling which regenerates the Haversian system, but establishment of the normal integrity of bone can take months or even years to complete (1, 23).

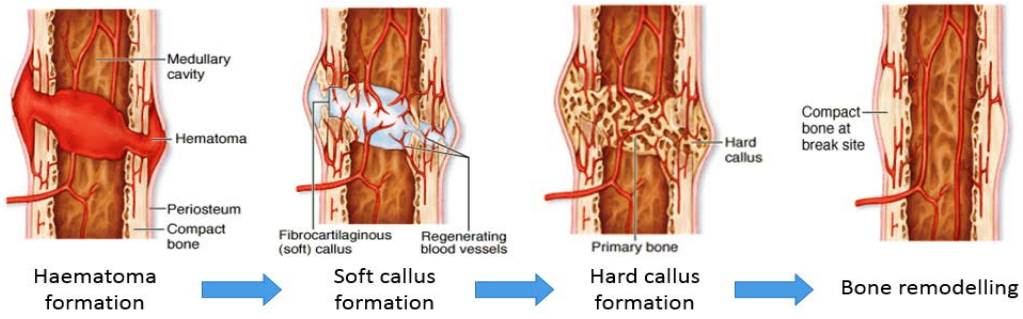

Figure 1-8 Stages of bone fracture healing.

Adapted from (1).

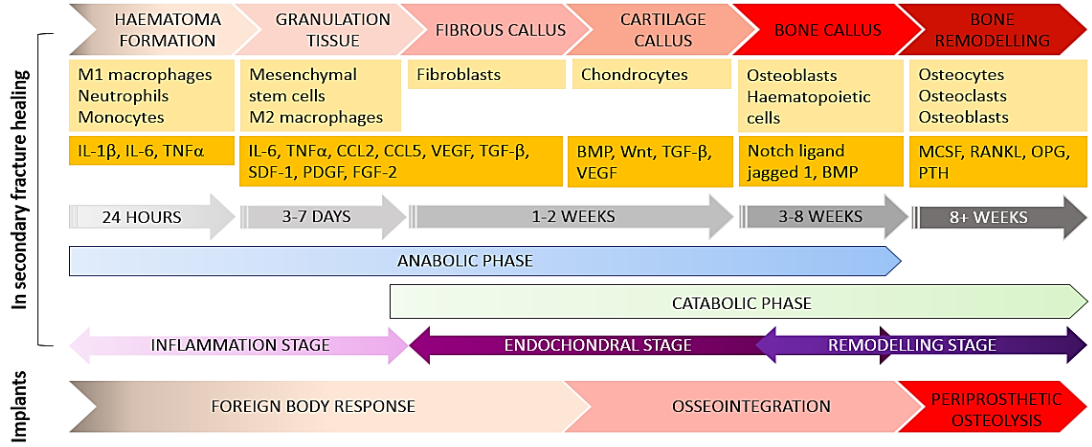

Figure 1-9 Stages of secondary fracture healing, compared to bone healing with implants.

Key cellular components and regulatory factors at each stage of healing are highlighted in beige and yellow respectively. Abbreviations: PDGF – platelet-derived endothelial growth factor, FGF-2 – fibroblast growth factor 2. Adapted from (1, 23, 24).

1.2.3 Bone remodelling and maintenance

Bone remodelling is a result of a complex coupling of osteoblast (bone formation) and osteoclast (bone resorption) activity, under the tight control of several hormones, growth factors and neuro-mechanical stimulation (Table 1-1) (25). Figure 1-10 is a simplified representation of this process (26). Osteoblasts, osteocytes, osteoclasts, and bone lining cells are organised in specialised units

(central to the bone remodelling process) called bone multicellular units. New bone formation occurs at bone resorption sites in each cycle of bone remodelling which maintains the microarchitecture that facilitates the mechanical function of bone. Osteocytes regulate bone formation through the release of Wnt antagonists, SOST and DKK1, which in turn are inhibited by mechano-signals and PTH. Wnt signalling in osteocytes controls the production of osteoprotegerin (OPG), a decoy receptor for the key osteoclast differentiation factor RANKL. In the bone resorption cavity, calcium, transforming growth factor- β1 (TGF-β1) and IGF-1 are released in response to osteoclastic activity. Osteoblasts stimulate osteoclastic differentiation of osteoclast precursors through Wnt5a. The matricellular signalling effected by TGF-β1 and IGF-1 is integrated with the Sema4D-Plexin B1-mediated osteoclast-osteoblast interaction. Sema4D, whose secretion by osteoclasts is stimulated by increased RANKL, inhibits osteoblast differentiation. Osteoblasts are induced to migrate to the resorption sites and differentiate through the secretion of Wnt10b by osteoclasts at the end of the resorption phase. Osteoblasts, in turn, inhibit osteoclastogenesis (and therefore bone resorption) via OPG and RANKL secretion.

Stimulus	General effect on bone
Oestrogen, Testosterone	Mainly anabolic
IGF-1 Growth hormone Mechanical signals	Anabolic
Calcitonin Thyroid stimulating hormone (TSH) Adiponectin	Anti-resorptive
Follicular stimulating hormone (FSH) 1,25-VitD3 Hypothalamic leptinergic signals through adrenergic innervation Prostaglandin E_2	Pro-resorptive
Thyroid hormone	Pro-resorptive in excess Anabolic during growth
Parathyroid hormone	Pro-resorptive in excess Anabolic if intermittent

Table 1-1 Effects of various stimuli on bone remodelling.

Modified from (25).

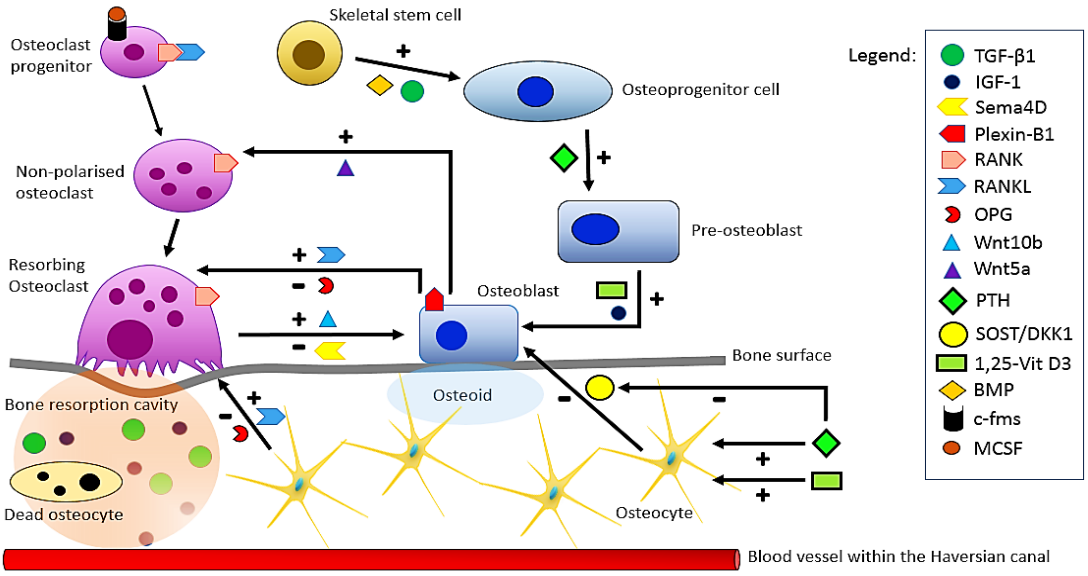

Figure 1-10 Signalling factors influencing new bone formation.

Adapted from (26).

The process of remodelling comprises of six sequential phases: quiescence, activation, resorption, reversal, formation, and termination. Activation involves the detection of an initial remodelling signal, such as increased calcitonin, 1,25-VitD3, or parathyroid hormone secretion. This occurs as part of serum calcium and phosphate homeostasis, a function performed by bone. In response, osteoclast activity is increased at resorption cavity sites. Osteoblasts respond to osteocyte-generated signals or direct endocrine stimulation by recruiting osteoclast precursors to the bone remodelling compartment. Resorption usually occurs over a limited period, depending on the degree of stimulation of osteoclast differentiation and activity. Osteoclasts adhere to bone via the integrin $\alpha v\beta 3$ and secrete hydrochloric acid and acidic proteases such as MMP9 (4, 25, 27). The reversal phase is characterised by the disappearance of most of the osteoclasts. This phase, which occurs over several weeks, begins with the release of osteogenic signals from osteoclasts. Bone lining cells retract to give osteoclasts access to the bone matrix. Reversal cells (mononucleated cells of osteoblast lineage on the eroded surface in the wake of osteoclast activity) cover about eighty per cent of the eroded surface, forming a cellular bridge between the bone-forming osteoblasts and resorbing osteoclasts. A canopy over the whole remodelling site is formed by adjacent bone marrow mesenchymal cells (28). Exposure of these cells along with bone lining cells to the eroded matrix as well as other signals may trigger the recruitment of local osteoprogenitor cells to the bone remodelling compartment, enabling increased

osteoblastogenesis, leading to the formation phase, which is distinguished by the replacement of osteoclasts with osteoblasts. Mineralisation of the new bone matrix occurs during the termination phase, which includes the terminal differentiation of active osteoblasts into bone lining cells. Maintenance of the resting bone surface environment ensues until the next cycle of remodelling is triggered (27).

Bone undergoes constant remodelling to accommodate dynamic mechanical stresses in addition to repairing developing fatigue fractures. Under optimal conditions, bone can heal completely without the formation of a fibrous scar, such that the regenerated tissue cannot be distinguished from its state prior to injury in either function or form (4, 25). Impairment in this remodelling process occurs in osteoporosis, which is in turn, results in an increased fracture risk, particularly amongst the elderly. Bisphosphonates remain the most widely used medication to modulate osteoporosis; however, bisphosphonates do cause some significant side-effects such as jaw osteonecrosis. Newer treatments in the form of monoclonal antibodies to DKK1 and SOST, are currently in phase three trials while anti-RANKL antibody therapy, such as denosumab, and anti-cathepsin K antibody, odanacatib, are already licensed for use in osteoporosis treatment (Figure 1-11) (4, 27, 29).

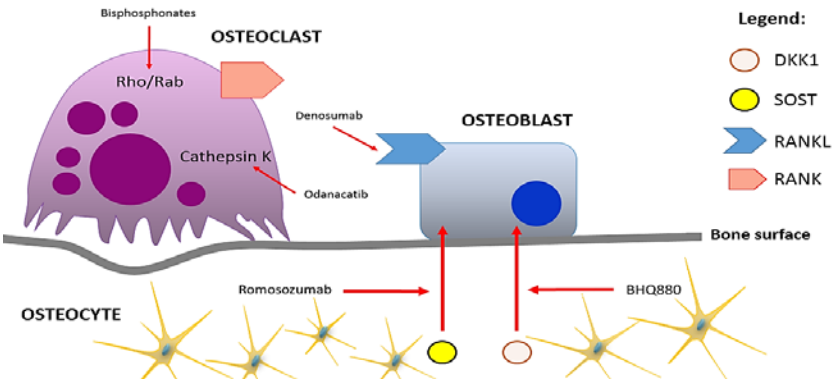

Figure 1-11 Current bone protective agents inhibit specific osteoblast anabolic and osteoclastic catabolic pathways to improve bone quality or slow down disease progression.

BHQ880 inhibits DKK1 while romosozumab inhibits SOST, preventing DKK1 and SOST inhibition of Wnt signalling, thus promoting new bone formation. Denosumab inhibits RANKL-RANK signalling, preventing osteoclast activation. Odanacatib inhibits cathepsin K and lysozyme production, preventing bone resorption. Bisphosphonates inhibit the prenylation of Rho and Rab GTPases, resulting in the loss of the sealing zone and the ruffled border of osteoclasts, thereby inhibiting osteoclast activity and inducing apoptosis. Red arrows indicate an inhibitory effect. Adapted from (29).

1.3 Failure to self-repair

Five to ten percent of all bone fractures are prone to delayed bone union or progress to a non-union or the development of a pseudoarthrosis (30). A delayed union is a failure of bone union within six months of the occurrence of the injury, and includes fractures that take longer than expected to heal. Non-union occurs due to an arrest in the fracture repair process, and typically happens in large segmental defects (functional cause) or when bone repair is affected by pathological causes. The five types of non-union are septic, hypertrophic, atrophic, oligotrophic, and pseudoarthrosis. The pathophysiology behind impaired or failed bone repair is often multifactorial, as listed in Table 1-2. Similar factors can also contribute to implant failure post-operatively in patients undergoing joint or dental surgery.

Causative factor	Mode of action
Mechanical (most common): • Inadequate fracture reduction • Insufficient fracture stabilisation • Inoperability • Fracture location e.g. distal tibial, scaphoid, and base of fifth metatarsal fractures • Type of fracture pattern	Excessive movement within the fracture site destabilises callus formation and can disrupt blood flow. Segmental fractures and fractures with butterfly fragments can compromise blood supply to the intercalary segment. Inadequate blood flow reduces availability of oxygen and the efficiency of waste and nutrient exchange, necessary for new bone formation.
Pathological: • Acute and/or chronic infection (local or systemic) e.g. osteomyelitis, septic arthritis • Autoimmune disorders e.g. rheumatoid arthritis, systemic lupus erythematosus	Infection or inflammation disrupts bone formation and in chronic cases, remodelling. Abnormal immune function predisposes to lowered immune resistance and chronic inflammatory states.
• Malignancy (local or metastatic): - Primary e.g. multiple myeloma, bone - Secondary e.g. prostate, thyroid, kidney, breast	Pathological fractures possess abnormal bone physiology, with an increased risk of fracture occurrence and associated complications. There is also the possibility of inoperability of fractures.
• Haematological disorders - Sickle cell disease - Polycythaemia e.g. thrombocytosis - Coagulopathies e.g. anti-phospholipid syndrome, factor V Leiden	Increased risk of thrombosis in chronic infection, systemic lupus erythematosus, sickle cell disease, malignancy, and coagulopathic disorders can result in poor blood supply.
• Endocrine (if untreated and pre-existing): - Hypogonadism - Hyper/Hypoparathyroidism - Hyper/Hypothyroidism - Hypopituitarism - Osteomalacia in adults, rickets (hereditary or acquired) in children	Excessive/inadequate levels of sex hormones, PTH, thyroid hormone, TSH, FSH, or growth hormone can disrupt osteoblast-osteoclast control of bone formation and in chronic cases, remodelling. Increased unmineralised bone due to low, or resistance to, 1,25-VitD3, resulting in low bone strength.
• Osteoporosis - Age-related (Type I, loss of oestrogen or reduced bioavailable testosterone)	Loss of bone mass occurs due to increased bone resorption and reduced response to anabolic hormone stimulation. Bone porosity,

- Senile (Type II, > 70 years of age) - Secondary - Disuse (loss of mobility)	microdamage and cement line density increases with age. Higher amount of non-enzymatic crosslinks at the collagen fibril level, increased water content, and a higher density of smaller osteons result in lower bone plasticity and a higher fracture risk.
• Renal osteodystrophy	Abnormally low or high bone turnover, and to a lesser extent, mineralisation, occurs amidst a background of chronic kidney disease.
Genetic: • Osteogenesis imperfecta • Ehlers-Danlos syndromes • Marfan syndrome	Mutation of collagen genes and defects in lysyl hydroxylase (Ehlers-Danlos) and fibrillin-1 glycoprotein (Marfan) reduce bone strength.
• Osteopetrosis	Abnormal osteoclast bone resorption.
• Paget's disease	Rapid bone turnover causing a disorganised mosaic pattern of woven and lamellar bone.
Iatrogenic: • Glucocorticoids (excess/chronic use)	Glucocorticoids interfere with native sex hormone regulation of bone formation and remodelling and cause a shift from osteoblastogenesis to adipogenesis.
• Bilateral orchidectomy or oophorectomy • Parathyroidectomy • Thyroidectomy • Chemo- or radiotherapy • Immune modulator agents	Loss of hormone production through surgical removal of, or chemical and/or radiation damage to the ovaries, testes, parathyroid, and/or thyroid disrupts bone formation. Some types of immunosuppressants can cause an imbalance in bone turnover.
• Alcoholism	Chronic alcohol excess increases cortisol levels, disrupts calcium, vitamin D and sex hormone homeostasis, and affects balance and gait.

Table 1-2 Summary of causes for the failure of bone to self-repair.

Adapted from (4, 5).

Successful fracture healing is dependent on interlinking factors, which affect the mechanical stability of the fracture, the influx of osteogenic and inflammatory cells, growth factors and chemotactic mediators, and adequate vasculature. These factors are further influenced by systemic co-morbidities such as smoking, diabetes mellitus, and obesity, which can adversely affect bone healing (23). Moreover, this regenerative ability declines with increasing age (30, 31). Orthopaedic implants only last 10 to 15 years, requiring revision surgery that can be fatal for patients who are less medically fit. Such patients face the prospect of losing their independence, or at best, living with a disability, through loss of function or mobility. These patients might additionally have to endure chronic pain caused by a malfunctioning implant,

which could worsen underlying co-morbidities or cause anxiety and/or depression (32). Taken together with a rising incidence of joint replacement surgeries as well as an increase in the ageing population (and life expectancy) worldwide, there has never been a greater need for new treatments for patients with musculoskeletal diseases as evidenced by bone being the second most transplanted tissue (33).

1.3.1 Current therapeutic options

Most orthopaedic procedures today that aim to restore damaged or failing skeletal tissue involve replacement components. Such conventional methods include partial to total artificial prosthetic implants (for instance, metal-based hip and knee joint replacements), and cadaveric or processed tissue (33). The mainstay of treatment for critical-sized bone defects remains bone grafting (34). A bone graft is an implanted material, used alone or in combination with other materials, that promotes bone healing through osteoinduction, osteoconduction and osteogenesis. Tissue viability, defect size, graft size, shape and volume, biomechanical properties, graft handling, and cost are just some of the factors influencing the selection of an ideal bone graft. This can be in the form of an autograft (harvested from the patient), an allograft or xenograft (obtained from a donor or animal), or a customised synthetic or biomaterial substitute (32). Over two million bone grafts are carried out annually (Table 1-3). However, current approaches remain far from ideal.

	Advantages	**Disadvantages**
Autograft	Osteogenic Osteoconductive Osteoinductive	Increased patient morbidity: pain and infection at donor site, visceral injury during harvesting Lack of vascularisation Limited quantity and availability
Allograft or Xenograft	Osteoconductive Osteoinductive High availability No donor site morbidity	Lacking osteogenicity / vascularisation Relatively higher rejection risk Risk of disease transmission Higher cost
Engineered substitutes using biological or synthetic materials	Ability to incorporate growth factors and stem cells to improve osteogenicity and graft incorporation Can be moulded to match the defect site using 3D printing techniques No donor site morbidity	Osteogenicity is limited by material porosity. Poor neovascularisation Variable biodegradability of different materials Unknown immune response Limited mechanical properties

Table 1-3 Advantages and disadvantages of various types of bone grafts (32, 33).

1.3.2 Tissue engineering as a potential therapeutic approach

The reparative capacity of bone has provided a natural paradigm to aid and inform tissue engineering strategies to generate new treatment options. Tissue engineering, involving the use of relevant scaffolds, appropriate factors, and/or cells, has developed in recent times to meet this demand. The concept of tissue engineering was first defined by Langer and Vacanti in 1993 as an interdisciplinary field that applies the principles of life sciences and engineering towards the development of biological substitutes which restore, maintain, or improve tissue function or a whole organ (35). Such approaches have in some cases improved graft incorporation, osteoconductivity, osteoinductivity and osseointegration (36). Scaffolds typically consist of a solid support structure with an interconnected pore network, while matrices are often hydrogels containing encapsulated cells. Both forms must support cell colonisation, proliferation, differentiation and migration. Additionally, scaffolds should possess appropriate physicochemical properties (such as strength, stiffness, biodegradability, surface chemistry) that are necessary for tissue formation as well as being capable of withstanding and responding to mechanical stresses (Table 1-4) (37).

Biocompatibility	The ability of a scaffold to support normal cellular activity without toxicity to the host tissue, particularly on degradation. The ideal bone scaffold is osteoconductive, osteoinductive and osteogenic, while promoting angiogenesis, allowing the formation of new blood vessels around the implant within a few weeks of implantation. A number of natural and synthetic materials are currently being investigated for use as scaffolds.
Biodegradability (Bioresorbability)	The degradation of a scaffold with time, preferably at a controlled resorption rate, is necessary to create space for new bone tissue to grow into, and eventually replace the synthetic scaffold. The rate of degradation can be varied according to the application required, such as the controlled release of an incorporated biomolecule.
Mechanical similarity	The ideal bone scaffold should match the properties of the host bone in coping with load transfers and withstanding mechanical stress. Given the differences in the geometry and mechanical properties of cortical and trabecular bone, designing a scaffold that can mimic such varied properties has proven to be a difficult challenge.
Pore size and porosity	This is critical for the diffusion of nutrients and oxygen for cell survival and proliferation, for which a minimum pore size of 100 μm is required. It has been shown that 200 to 350 μm pore sizes are optimal for bone tissue in-growth. Recent studies have demonstrated that multi-scale porous scaffolds (combining micro- and macro-porosities) are superior to macro-porous scaffolds in enabling cell attachment and invasion. However, increasing porosity reduces the mechanical strength of the scaffold.

Table 1-4 Factors for scaffold design in bone tissue engineering (37).

Despite the advances in scaffold fabrication brought about by additive manufacturing (AM) techniques, cell-based treatments are not yet available for clinical use. Currently, cell-based therapies rely on manual cell seeding and culturing of pre-fabricated scaffolds (38). This is time-consuming, inefficient and operator dependent, reflecting the fact that current cell-based therapies are typically only applicable on a limited scale. This lack of cost-effectiveness has, to date, curtailed translation from the laboratory to clinical use as a mainstream therapeutic option. Furthermore, cell seeding of pre-fabricated scaffolds does not recreate the cellular organisation of native tissues, nor address the issue of construct vascularisation. Fabricated scaffolds are typically porous in order to facilitate cell incorporation, resulting in constructs lacking sufficient mechanical strength. The methods used to fabricate these scaffolds have (typically) variable abilities in controlling pore size, geometry and interconnectivity (39). Spatial distribution of manually seeded cells is therefore random. To address these issues, cells are being incorporated into the AM process to create living cell-biomaterial-biomolecule constructs. Termed as biofabrication, this approach has been gaining momentum over the past decade (40).

1.4 Additive manufacturing in current tissue engineering

AM (also known as rapid prototyping or solid freeform fabrication) was developed in the 1980s, providing the required ability to deliver a high level of control over the architecture of the construct and the flexibility to scale-up fabrication, while guaranteeing the standardisation of the manufacturing process. This has provided customised scaffolds with precise geometries for use in replacing damaged or diseased tissues and organs. Early scaffolds developed using conventional fabrication techniques have lacked precision and reproducibility.

Cell-free scaffolds have been successfully used in clinical settings for bone and osteochondral tissue repair (32, 41). AM has enabled the manufacture of three-dimensional (3D) artificial implants using a myriad of biomaterials in not just an increasingly precise and reproducible manner, but also capable of meeting stringent performance criteria for clinical use in patients (42). This is reflected by the increasing use of 3D printed artificial implants in place of conventional metallic implants in hip replacement surgery. Growing interest in developing a personalised, cost-effective approach to medical therapy in recent years has not only led to the increasing utilisation of AM technologies in the fabrication of 3D constructs for use

in tissue engineering (43), but has also driven advancements within AM techniques (Figure 1-12).

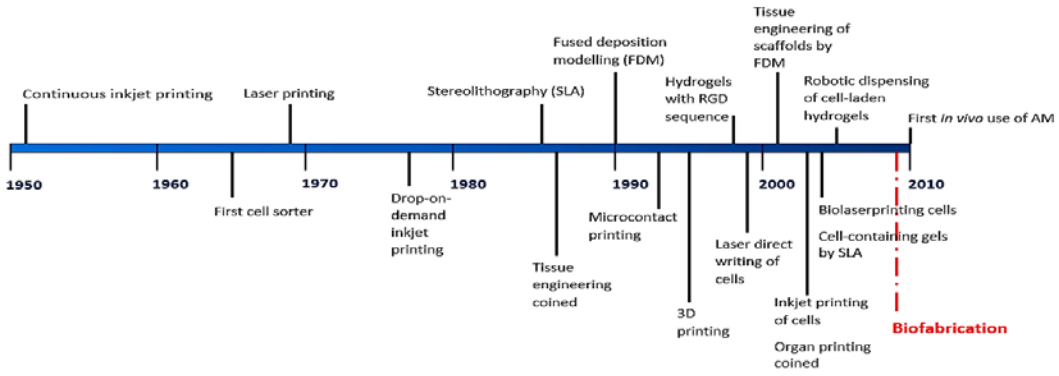

Figure 1-12 Additive Manufacturing and its uses in tissue engineering.

Adapted from (43).

In general, AM techniques allow the creation of a 3D object using data generated by computer-assisted design (CAD) software or imported from 3D scanners such as magnetic resonance imaging (MRI), single-photon gamma rays (SPECT) and X-ray computed tomography (CT). The CAD model is converted to a standard tessellation language (STL) file, which directs the computer system controlling the 3D printer, thereby enabling the operator to designate the orientation and size of the object to be generated layer-by-layer. Coupled with the development of a variety of biomaterials suitable for the different AM techniques, AM has enabled the automated fabrication of scaffolds with tuneable and reproducible properties (43, 44). The American Society for Testing and Materials International Committee F42 on AM Technologies has classified AM technologies into seven different processes in accordance with the method of layer deposition and bonding (Table 1-5).

Process	AM Technique	Advantages	Disadvantages	Printing applications	Living cells
Photopolymer vat	Stereolithography Two-photon polymerisation	High-dimensional accuracy Transparent materials	Single composition Cytotoxic photoinitiator Photopolymer materials only Post-processing required Limited cell printing ability with heterogeneous cell distribution	Clinical implants Surgical guides Tissue engineering scaffolds Cell-incorporated 3D constructs 3D micro-vasculature networks	Yes

Material jetting	Drop on demand inkjet printing Poly-jet technology	Fast Wide range of biomaterials Inexpensive existing technology Fabrication of composite structures Multi-cell printing	Nozzle blockage common Low bioink viscosity limits up-scalability of 3D constructs Poor mechanical strength of 3D constructs	Clinical implants Surgical guides Tissue engineering scaffolds Cell-incorporated 3D constructs Biofabrication	Yes
Material extrusion	Non-melt extrusion: 3D bioplotting, solvent-based extrusion freeforming, Robocasting, direct-write assembly, Electrospinning, pressure-assisted microsyringe Melt extrusion: Fused deposition modelling, 3D fibre deposition, multiphase jet solidification	Cheap mechanism with relatively good throughput No post-processing needed Low material wastage Cytocompatible Rapid Non-toxic materials with good properties	Low accuracy Poor mechanical strength Precise control of ink rheology necessary Use of solvents Low accuracy Weak bonding between dissimilar polymer layers	Tissue engineering scaffolds Cell-incorporated 3D constructs Biofabrication Clinical implants Tissue engineering scaffolds	Yes No
Powder bed fusion	Selective laser sintering Selective laser melting Electron beam melting Selective mask sintering	Wide range of biomaterials High material strength Good material properties	Thermal stress and degradation Accuracy limited by particle size Atmosphere control needed for metal printing	Surgical implants with complex structure Tissue engineered scaffold Medical devices	No
Directed energy deposition	Laser engineering net shape Laser cladding Directed metal deposition	Wide range of biomaterials Good material properties	Low accuracy Thermal stress Atmosphere control needed for machining	Orthopaedic implants	No
Sheet lamination	Laminated object manufacturing Ultrasonic consolidation	Low temperature process	Shrinkage Significant wastage Delamination	Orthopaedic implants	No

Binder jetting	3D printing	Low temperature process Fast Allows fabrication of composite structures	Powder form of material needed Powder entrapment High porosity Low surface quality Accuracy limited by particle size Cell-changing environment	Clinical implants Tissue engineering scaffolds	No

Table 1-5 Classification and applications of AM techniques.

Modified from (32).

1.5 Biofabrication approaches in bone tissue engineering

The aim of bone tissue engineering is to create clinically relevant grafts that can be used therapeutically. At present, fabricated implants typically suffer from poor osseointegration and tissue formation, driving the need for enhanced growth rate, mechanical properties and an improved yield of newly formed bone. Advances in AM technology allow tissue engineers to micro-engineer scaffold nanotopography to aid, and even enhance, cellular attachment, growth, interaction and cell migration (45). Biofabrication techniques take this further by providing a means of controlling the uniformity of cellular distribution or localisation on the surface of a scaffold (46-49). Advances in AM technology have allowed the concomitant spatial printing of different cell types on 3D scaffolds to generate complex tissues (38, 50, 51). Growth factors or other compounds of interest can be incorporated within a cellular matrix or integrated within the scaffold itself during the printing process, providing a method for controlled drug delivery and release (39, 52-57). Timed release of drugs or growth factors could be further manipulated by nanoparticle or liposome encapsulation of these substances to achieve a delayed or temporal release (if desired) on the development of the tissue of interest (56, 58). As bone requires its composite cells to be at different stages of proliferation, differentiation and maturation within a multi-layered organised structure, such an approach is attractive in bioprinting cells onto a suitable scaffold to create bone (59). Central to this remains the ability of bioprinted cells to retain functional capacity as well as permitting bone remodelling brought about by external and internal stimuli (60). This has seen an increase in the number of studies combining biofabrication and biomimetic techniques to recapitulate the *in vivo* ECM microenvironment (61). Some

recent strategies have looked to exploit the paracrine effect of the secretome of MSC or stromal cells (shuttled through extracellular vesicles or embedded within ECM molecules) to not only target osteoinduction, but also the inflammatory and immunity processes involved in regeneration (62).

The ability to seed cells and biomolecules in 3D space, with an increasingly high degree of precision, in a user-controlled, pre-defined manner affords biofabrication an advantage over standard techniques (Table 1-6). Precision printing enables the generation of a customised 3D construct that is a closer fit to the defect (in comparison to traditional bone grafts), reducing the possibility of engraftment or repair failure. Biofabricated bone will, ultimately, eliminate the need for donor bone grafts, allowing patients to have their operations earlier (thereby reducing wait times for surgery while regaining functionality sooner), and with lower physical and psychological morbidity. The risk of rejection of the biofabricated bone tissue is lower with the use of autologous cells. Thus, biofabrication represents a more cost-effective way to treat patients with musculoskeletal defects in addition to providing a new therapy for patients unable to be treated by conventional methods.

	Printing stem cells	**Printing biomolecules**
Applications	Stem cell genomics Patches for wound healing *Ex vivo* tissue generation	Protein and DNA arrays Tissue engineering uses
Advantages (compared to conventional methods)	Programmable, Low cost 3D complexity High throughput	Programmable, Low cost Non-contact, reducing risk of cross-contamination No modification required for proteins or substrates
Disadvantages	Cytocompatibility in both solid and liquid forms Viscosity has to be lower than a threshold as defined by the printing method	Lower resolution compared to state-of-the-art protein array Number of available binding sites on the receiving substrate Cytocompatibility, Viscosity

Table 1-6 Printing stem cells and biomolecules.

Modified from (39).

Several AM techniques have been used for the generation of 3D scaffolds, and more recently, in the printing of tuneable hydrogels for bone tissue engineering. The main three forms of AM techniques (Figure 1-13) that have been used for the biofabrication of bone tissue are discussed in further detail below.

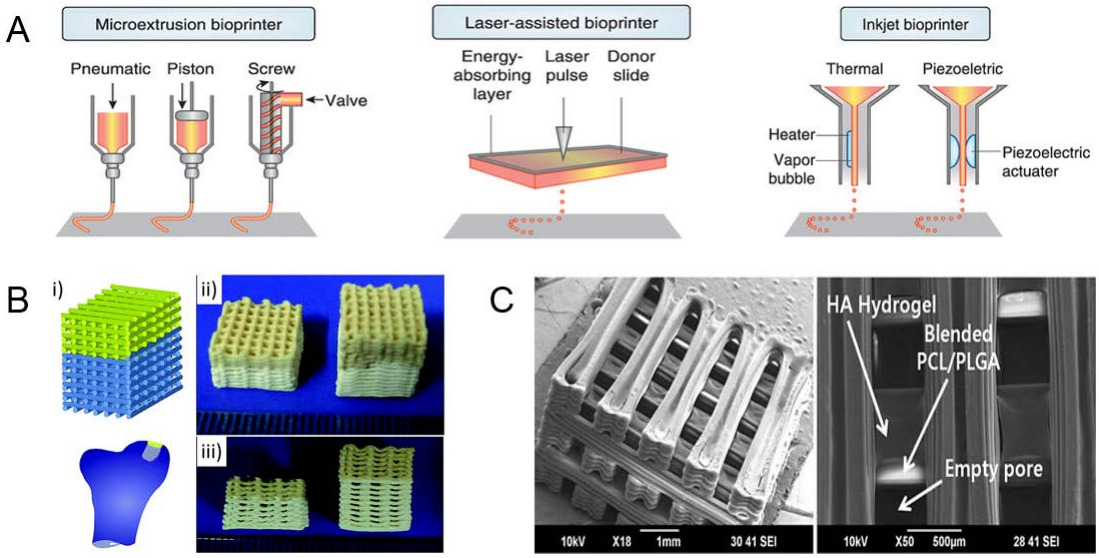

Figure 1-13 Common bioprinting methods.

A) Components of microextrusion, laser-assisted, and inkjet bioprinters: Microextrusion printers use pneumatic or mechanical (screw or piston) dispensing systems to extrude continuous beads of material and/or cells. Laser-assisted printers utilise lasers focused on an absorbing substrate to generate pressures that propel cell-containing materials onto a collector substrate. Thermal inkjet printers electrically heat the printhead to produce air-pressure pulses that force droplets from the nozzle, whereas acoustic printers use pulses formed by piezoelectric or ultrasound pressure. Reproduced from (63). B) CAD model (i) and photographs (ii and iii) of 3D printed bipartite scaffolds for osteochondral defect repair. The bony part (bottom layer, white) is made of alginate/gelatin/hydroxyapatite and the chondral part is composed of alginate/gelatin (top layer, beige). The stability of the two parts was achieved by dual crosslinking of alginate and gelatin using 1 M calcium chloride and 2% w/w N-(3-dimethlyaminopropyl)-N'-ethylcarbodiimide. Reproduced from (64), with permission of The Royal Society of Chemistry. C) Scanning electron micrograph image of a multi-head deposition system fabricated hybrid scaffold consisting of blended polycaprolactone (PCL) and poly(lactic-co-glycolic acid) (PLGA) filled with hydroxyapatite hydrogel. Reproduced from (65).

1.5.1 Microextrusion deposition method

In microextrusion method printing, thin thermoplastic granules or filaments are heated until melted and guided by a controlled robotic device, to form the 3D construct. The liquid material is extruded and hardens immediately. The previously formed layer (as the substrate for the next layer) must be maintained at a temperature just below the solidification point of the material to ensure good

interlayer adhesion (43). This form of dispensing-based bioprinting enables quick and easy dispensing of a clinically relevant-sized construct.

Fedorovich *et al* demonstrated the use of a pneumatic dispensing system-based bioplotter (EnvisionTEC GmbH, Germany) in depositing 3D fibres composed of various hydrogels and goat BMSC that were used to generate bone grafts. The authors showed that cells were not damaged during the printing process and that the cells in alginate constructs retained their ability to undergo osteogenic differentiation two weeks after printing (66). The same group also created heterogeneous hydrogel constructs consisting of endothelial progenitor cells (EPC) derived from peripheral blood and goat multipotent stromal cells to promote neovascularisation during bone regeneration. The separately printed EPCs and multipotent stromal cells, formed blood vessels and bone respectively after *in vivo* implantation (67). Scaffold porosity was shown to affect cell viability of goat and human multipotent stromal cell-laden hydrogels printed using a Bioscaffolder pneumatic dispensing system (3D fibre deposition, or 3DF, machine (68)). Porosity modulation permitted the generation of fully interconnected pores to ensure sufficient nutrient and oxygen supply, which are necessary for the viability of embedded multipotent stromal cells and the fabrication of a clinically relevant-sized 3D construct.

Fedorovich *et al* also fabricated viable centimetre-scaled structured tissues using a 3DF machine (49). Fluorescent-labelled human chondrocyte and osteogenic progenitor cells were encapsulated in alginate hydrogel and printed into 10 mm by 20 mm cell-seeded scaffolds. The cells, which were printed on different areas of each scaffold, remained in their scaffold compartments throughout the culture period. Cell viability was high throughout the printing process. *In vitro* and *in vivo* distinct tissue formation was observed. This is significant as most biofabricated 3D constructs are much smaller and of little clinical relevance, suggesting the possibility of creating 3D constructs that can be used to repair osteochondral defects. The falling cost of extrusion-based bioprinters has led to an increase in the number of studies into its use in the manufacture of scaffolds as well as cell-laden matrices. The most recent notable study was by Kang *et al*, who used a custom-built extrusion printer to bioprint a PCL-based bone graft using human amniotic fluid stem cells incorporated in a gelatin, glycerol, fibrinogen and hyaluronic acid bioink (69). At 5 months post-implantation in rats, new bone formation as well as construct vascularisation was observed. However, the osteogenicity and osseointegrative

capability of the construct cannot be truly ascertained given the construct was initially cultured in BMP-2-containing media prior to implantation.

1.5.2 Laser-assisted cell printing

Laser-assisted bioprinting, amongst the first methods to be investigated for cell printing, is a modified version of laser-induced forward transfer. One of the key reasons for the attractiveness of laser-assisted bioprinting was the ability to perform cell-by-cell deposition (theoretically enabling precise cell micropatterning at a cell-level resolution) which may improve cellular interaction (43, 70). A laser-assisted bioprinter consists of a pulsed laser source, a receiving substrate for patterning and assembling cells and biomaterials, in addition to a target (which is transparent to the laser wavelength and coated with bioink to print). A necessary component is a laser-absorbing interlayer with a high heat transfer coefficient – usually located between the target and the bioink – which allows heat to be transferred to the bioink. Individual cells in suspension are 'guided' (based on differences in refractive indices) by directed laser beams (which function as optical tweezers) and deposited onto solid surfaces.

Barron *et al* were among the first to demonstrate cell viability using this form of bioprinting. Human osteosarcoma cells deposited onto a biopolymer matrix using biological laser processing were 100 per cent viable after six days of incubation (71). Catros *et al* used laser-assisted bioprinting to deposit inorganic nano-hydroxyapatite and human osteoprogenitor cells onto a target consisting of a quartz slide with a titanium interlayer and a bioink layer. The authors were able to create an on-demand pattern of nano-HAP and human osteoprogenitor cells (72) and demonstrated that laser-assisted bioprinting was an effective method in fabricating 3D constructs using luciferase-tagged human osteosarcoma cells (MG63) as the bioink and polycaprolactone (PCL) electrospun scaffold as the substrate. Adopting a layer-by-layer assembly method in creating a 3D construct was superior to seeding a single locus of the scaffold. The majority of cells survived the printing process when a layer-by-layer assembly was used (73). More recently, Keriquel *et al* utilised laser-assisted bioprinting to fabricate an *in situ* construct, consisting of murine bone marrow stromal precursor D1 cells arranged in different patterns within a 1.2% w/v nano-HAP and 2 mg/ml collagen matrix, to treat critical-sized calvarial defects in mice. Bioprinted cells proliferated for 42 days post-implantation. The study also showed the importance of cell seeding patterns at low cell densities, wherein a significant increase in the homogeneity of bone repair at 2

months was observed when the cells (at a density of 700 – 800 cells/mm^2) were deposited in a ‘disk pattern’ as opposed to a ‘ring pattern’. The authors postulated this result was due to the paracrine regulation of bioprinted cells (74).

1.5.3 Inkjet-based cell printing

This AM method is a useful, facile, low cost approach for the presentation of microenvironmental features to cells in order to increase cell survival or manipulate cell behaviour on printed surfaces. Inkjet bioprinting is capable of generating microscale organisation of deposited cells (75) without compromising cell viability or inducing damage to phenotype or genotype (48, 76). Furthermore, this approach offers the possibility of multiple print heads being used to simultaneously print multiple cell types (thereby enabling a high-throughput capability) in addition to bioprinting biomolecules alongside biomaterials, therefore allowing the fabrication of complex multicellular constructs.

Commercial drop-on-demand inkjet printers, such as piezoelectric and thermal printers, have been adapted to print picolitre droplets of biological materials with microscale precision. In general, the process involves depositing a stream of microparticles of a binder material over the surface of a powder bed, which joins the particles together where the object is to be generated (43). Compared to extrusion method printing and laser-assisted bioprinting, the use of inkjet printing in bone tissue engineering remains relatively unexplored as existing inkjet technology lacks the ability to print materials of high viscosity or tensile strength. Constructs created by inkjet methods tend to lack bulk mechanical strength, resulting in small structures of little clinical relevance. This issue continues to restrict the utility of inkjet bioprinting in bone biofabrication. However, Ahmed *et al* demonstrated that surface cellular deposition into a bone defect can be facilitated by fibrin scaffolds fabricated using inkjet bioprinters (77). Inkjet-based printing is one of the main methods that has been used to fabricate cell-laden hydrogels (38, 78). Gao and colleagues have reported the bioprinting of human MSC suspended in poly(ethylene glycol) dimethylacrylate containing either bioactive glass or HAP nanoparticles to evaluate their effect on osteogenesis. Not only were the cells viable post-printing, but superior osteogenesis was demonstrated in the construct containing HAP (79). Table 1-7 summarises the advantages and limitations of these commonly used methods in bone biofabrication.

3D printing method	Advantages	Limitations
Microextrusion deposition	Good precision and microscale resolution Wide variety of biomaterials Capable of printing physical or compositional gradients, cell and bioactive factor bioprinting Potential for upscalable construct fabrication	Cell survival post-bioprinting dependent on bioink properties, printing temperature, and build time Often requires use of support materials to fabricate porous constructs, increasing build time Low to moderate cost
Laser-assisted bioprinting	Nanoscale precision and prints at ambient conditions Capable of printing multiple physical or compositional gradients, and simultaneous cell and bioactive factor bioprinting	Remains extremely cost-prohibitive Limited upscalability
Inkjet-based cell printing	Low cost Capable of printing gradients and simultaneous cell and bioactive factor bioprinting, with high cell viability post-bioprinting High printing speeds	Limited biomaterial choice due to bioink printing requirements Poor resolution Limited upscalability

Table 1-7 Advantages and limitation of common 3D printing methods used in bone biofabrication.

Modified from (80).

1.6 Limitations affecting bone biofabrication

The suggestion that biofabricated bone will be in routine clinical use to treat musculoskeletal disease within the next five years is unrealistic. Biofabrication techniques have yet to generate an engineered substitute that can be scaled up for clinical use. Despite staggering advances in AM technology in the past decade, tissue engineers have not been able to completely resolve the key issues, such as vascularisation and tissue necrosis, which tissue engineering counterparts in the 1970s had faced when work began on growing tissues for organ transplantation.

1.6.1 Cell viability and functionality

A key starting point in the success of any form of transplant therapy (with or without the use of scaffolds) is the viability of the transplanted cells. Transplanted

cells must survive for a sufficient period in order to perform their function post-transplant. In the case of biofabrication, the printed cells must first survive both the processing and printing steps. Bioprinted cells are subject to a wide variation in environmental and culture conditions (extracellular milieu not withstanding) before, during, and following printing. Such extreme changes in conditions can adversely affect cellular processes and homeostatic mechanisms or result in cellular damage and subsequent cell death (76). To successfully bioprint functional tissues or organs for implantation, cell membrane damage and cell death should be limited to ten percent of the total number of printed cells.

Although AM processes can impart a high level of spatial accuracy and definition, bioprinting can result in decreased cell viability, depending on the approach adopted. The application of an aqueous or aqueous-gel environment at temperatures from room temperature to 38°C can prove challenging (41). The use of laser-assisted bioprinting techniques in tissue engineering has been constrained by such an issue (71, 72, 81). Furthermore, mechanical injury (which can be observed immediately) is influenced by bioink viscosity as well as laser energy, and biochemical injury such as DNA damage, is related to thermal, ultraviolet, metallic residue deposition or mechanical injury-induced secondary injury (48).

There is emerging evidence indicating laser-assisted bioprinting does not induce cellular alterations, hinder cell proliferation or affect functionality (47, 70, 82). This evidence for laser-assisted bioprinting safety ranges from analysis of viability of i) laser-assisted bioprinting -printed and non-printed single human MG63 cells that were cultured for nine days in two dimensional (2D) culture (71), ii) viability of laser-assisted bioprinting -printed 10^8 per ml murine MSCs twenty-four hours later (82), and iii) viability and phenotype of human osteoprogenitor cells that had been laser-assisted bioprinting -printed and cultured in 2D (72). However, the majority of such conducted studies were performed *in vitro*. The true extent to which the printed cells remain viable in addition to maintaining their functionality cannot be fully determined by short-term investigations, nor can studies fully demonstrate any *in vivo* differences in cell survival and behaviour when these printed cells are exposed to different environmental conditions or stimuli. The approach taken by Fedorovich *et al* in performing a longer term *in vivo* study of the performance of 3D biofabricated hydrogel implants containing printed goat EPCs (derived from peripheral blood) and multipotent stromal cells (50) is an initial step but there remains a need for longer term, standardised studies using human primary cells to address these issues. The

possibility of carcinogenesis arising from occult damage to bioprinted cells remains a key area to be investigated, highlighting the need for long-term studies *in vivo* and, when in clinical use, in patients, to ascertain the safety of biofabricated bone.

Cell viability can be adversely affected by the cytocompatibility of the biomaterial used or the process(es) required to manufacture the scaffold being used. For example, many hydrogels are attractive given their cytocompatibility. Several types of, and applications for, hydrogels in tissue engineering have been extensively reviewed (78, 83-85). While hydrogels have been designed to provide cells with a fully hydrated 3D environment comparable to the ECM of native tissue, their limited intrinsic mechanical strength restricts the scaling up of biofabricated 3D constructs for use in bone tissue engineering (84). This issue can be remedied by increasing polymer concentration and crosslinkage density (Table 1-8). However, the crosslinking method employed can affect biofabrication, either through disrupting the fabrication process due to crosslinking failure, or by prolonging the fabrication time, due to the need for post-processing steps to be undertaken to improve the mechanical properties of the hydrogel. These issues lead to a reduction in cell viability and functionality (84, 86).

Hybrid 3D constructs, comprised of thermoplastic biomaterials and cell-laden hydrogels, have been suggested as a way to resolve the lack of mechanical strength of hydrogels. Recent composite systems include non-woven scaffolds manufactured via solution-electrospinning techniques and scaffolds fabricated via 3D printing. For example, PCL was melted and extruded using pneumatic pressure. Human chondrocyte cell-laden alginate solution was then dispensed between the PCL lines. The dispensing process was repeated layer by layer to create a reinforced 3D cell-laden structure (87). A small decrease in cell viability was observed after one day, likely attributable to heat shock from the adjacently deposited PCL (which was deposited at 160°C). Similarly, Visser *et al* reinforced soft gelatin methacrylate hydrogels with highly organised, high porosity PCL microfibre networks that were 3D printed by melt-electrospinning. Although the stiffness of the composite construct was 54-fold higher than the hydrogel or microfibre scaffold alone, only 78 per cent of the embedded human chondrocytes remained viable after seven days of culture (Figure 1-14) (88). No AM technique for cell-laden hydrogel bioprinting has proven to be completely cytocompatible.

Crosslinking		Advantages	Disadvantages
Physical	*Ionic*	Reversible interactions Constant viscosity during printing Good biocompatibility	Additional agent(s) and/or post-processing steps may be needed Mechanically weak
	Stereo-complex	Reversible interactions Constant viscosity during printing Good biocompatibility	Relatively slow gelation High viscosity of building blocks reduces cell survival. Additional agent(s) and/or post-processing steps may be needed Mechanically weak
	Thermal	Reversible interactions Constant viscosity during printing Good biocompatibility Rapid reassembly to gels post-printing	Post-processing crosslinking needed
Chemical	*Ultraviolet*	Irradiation-induced polymerisation does not affect viscosity during printing Allows post-processing stabilisation of mechanically weak physically crosslinked hydrogel constructs	High reaction rates necessary May involve exposure of constructs to irradiation – risk of tumorigenesis as yet uncharacterised
	Wet-chemical	No irradiation or other further stabilisation is needed Mechanically stable	Potentially cytotoxic agents Trigger with stringent control of crosslinking kinetics is required to avoid viscosity changes in the nozzle during printing to ensure crosslinking occurs

Table 1-8 Advantages and disadvantages of crosslinked hydrogels for biofabrication.

Adapted from (84).

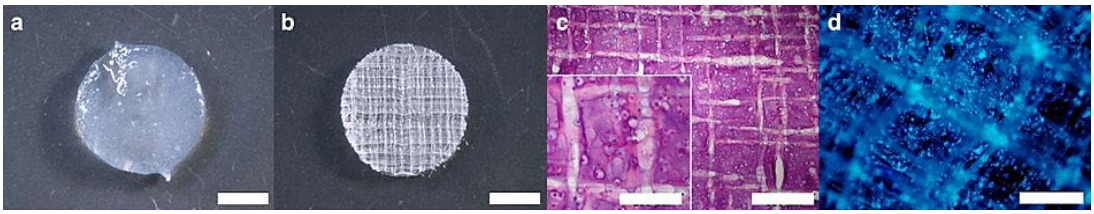

Figure 1-14 Hybrid 3D printed constructs.

a) Stereomicroscopy image of a gelatin methacrylate-HAP gel (scale bar, 2 mm) and b) of a 93 per cent porous PCL scaffold reinforced gelatin methacrylate-HAP gel on day 1 (scale bar, 2 mm). c) Haematoxylin-Eosin staining after seven days culture show chondrocytes remaining within the gelatin methacrylate component and retaining a rounded morphology (scale bar, 500 µm; inlay, 200 µm). d) DAPI staining confirms a homogenous distribution of cells throughout the construct (scale bar, 200 µm). Reproduced from (88).

1.6.2 Vascularisation of biofabricated bone

Bone is a metabolically active tissue supplied by an intraosseus vasculature with osteocytes located no greater than 100 µm from an intact capillary (20, 89). Angiogenesis occurs spontaneously upon implantation of a bone graft. This vascular response is triggered by inflammation. The capillary networks that form are transient and regress within a few weeks. Host-derived neovascularisation of the implant is slow (at a rate of less than 1 mm a day), and thus insufficient for constructs that are of a clinically relevant size due to the limited degree of penetration into the implant to form functional capillaries. As complex engineered 3D constructs of clinically relevant size cannot be sustained by the diffusion of nutrients alone, creating a functional vascular network is necessary for ensuring a nutrient supply and equally critically, waste removal (particularly that of degradation by-products) throughout the tissue construct. This remains a challenging technical hurdle in the field of biofabrication, and has hindered the generation of clinically successful engineered constructs (90, 91). In order to solve this issue, strategies involving the use of co-culture systems, bioreactors to provide perfusion and mechanical stimuli, the microfabrication of microchannels using AM methods, and biomaterials and growth factors to direct cell behaviour, are being studied (91, 92).

Even if upscalability is achieved, the difficulty of vascularising biofabricated bone adds to the problem of ensuring construct viability, as larger constructs require more nutrients and oxygen. *In vitro*, this increased demand could be resolved by using bioreactors (44, 93), which induce fluid flow throughout the construct. For example, dynamically cultured 3D bioprinted HAP/tricalcium phosphate scaffolds

seeded with MC3T3-E1 cells in osteogenic media were subjected to flow perfusion in a bioreactor, resulting in uniform cell distribution and 95 per cent viability throughout the construct at all time-points (two to twenty one days) while 80 per cent of the cells in the core of scaffolds that were statically cultured were non-viable. Spinner flask, rotating wall vessel reactor, and flow perfusion bioreactors have been used to apply mechanical stimulation and fluid flow to bone tissue constructs with resulting increment in bone formation. Initiation and progression of angiogenesis and endothelial cell function are affected by haemodynamic forces as exerted by blood flow (inducing shear stress and cyclic strain) (91). Perfusion bioreactors are capable of mimicking this effect (94). Increasing interest in the design of bioreactors is timely as the development of more complex forms of bioreactors will be needed for larger constructs (93, 95).

Microscale technologies offer flexibility in creating precise 3D architectures with embedded vascularised and capillary networks. Current approaches involve the creation of a trench that is moulded into one layer before a second layer is aligned and deposited, forming laminated channel(s) or grooves in an iterative manner (96). Moroni *et al* created microscale 3D scaffolds consisting of organised hollow fibres with controllable diameter and thickness that could be used as a vascularised network (97). Initial work by Cui *et al* who utilised a bioink comprising of human microvascular endothelial cells and fibrin in a drop-on-demand printing technique to generate a 3D tubular microvascular-like structure (75) has indicated that 3D printing microvasculature is possible given the right set-up.

Although promising, layer-by-layer assembly is a very slow process, which places constraints on the cells and choice of materials used for fabrication. Formation of structural artefacts throughout constructs can occur, compromising the efficacy of such methods. Current bioprinting technology has limitations on the print resolution, cells and materials that can be used. To overcome these limitations, an alternative strategy has been to 3D print sacrificial biomaterials to generate a vascular network, as demonstrated by Miller *et al,* Lee *et al*, and Kolesky *et al* (96, 98, 99). Previous 3D sacrificial moulding of perfusable channels required the use of cytotoxic solvents or processes to remove sacrificial filaments or casting of the supporting material which could not be achieved using living cells or aqueous-based extracellular matrices. Using a customised extrusion method printer, Kolesky *et al* were able to sequentially co-print multiple bioinks comprising of poly(dimethyl siloxane), gelatin methacrylate, cell-based gelatin methacrylate and 40 per cent

Pluronic F127 respectively. The 3D construct underwent ultraviolet processing to induce crosslinking in the gelatin methacrylate layers before being cooled to 4°C to liquefy the sacrificial Pluronic F127 layer, which was extracted using a vacuum process. This left behind interconnected microchannels that were dynamically seeded with human umbilical vein endothelial cells to form endothelialised microvascular networks (99).

Miller *et al* utilised a customised RepRap Mendel 3D printer to print rigid filament networks of carbohydrate glass (containing glucose, sucrose and dextran) as a sacrificial network in engineered tissue containing 10T1/2 cells to create cylindrical networks lined with human umbilical vein endothelial cells (Figure 1-15). The generated network was not only able to support its own weight in an open 3D lattice but could also be dissolved rapidly with good cellular survival.

Construct functionality was demonstrated by the successful perfusion of blood into the construct under high pressure pulsatile flow in addition to being able to sustain the metabolic function of rat hepatocytes in the tissue construct created (96). Such methods could be integrated into the design of bone tissue engineering constructs by the hierarchical incorporation of cell-laden hydrogels and porous osteoconductive scaffolds with synthetic tissue engineered vascular grafts by employing approaches such as that of Miller *et al* and Kolesky *et al*. These approaches could be used to generate microchannels in larger 3D biofabricated bone, which could allow for improved perfusion by bioreactors.

Blood vessel formation is tightly coupled with bone regeneration (100). Vascular endothelial growth factor (VEGF) is known to play a pivotal role in angiogenesis during bone formation. Several studies have been performed investigating the effect on angiogenesis that VEGF, or a combination of growth factors, has in engineered bone constructs. Through covalently immobilising VEGF and angiopoietin-1 onto 3D porous collagen scaffolds, Chiu *et al* showed that co-immobilised scaffolds displayed increased endothelial cell proliferation *in vitro* and in organotypic cultures (101). Shah *et al* created a dual delivery system using polyelectrolyte multi-layer films fabricated through layer-by-layer assembly. Varying ratios of VEGF and BMP-2 were entrapped within different layers of these films. *In vivo*, the mineral density of *de novo* bone was 33 per cent higher in the dual delivery system when compared to films containing BMP-2 only (102).

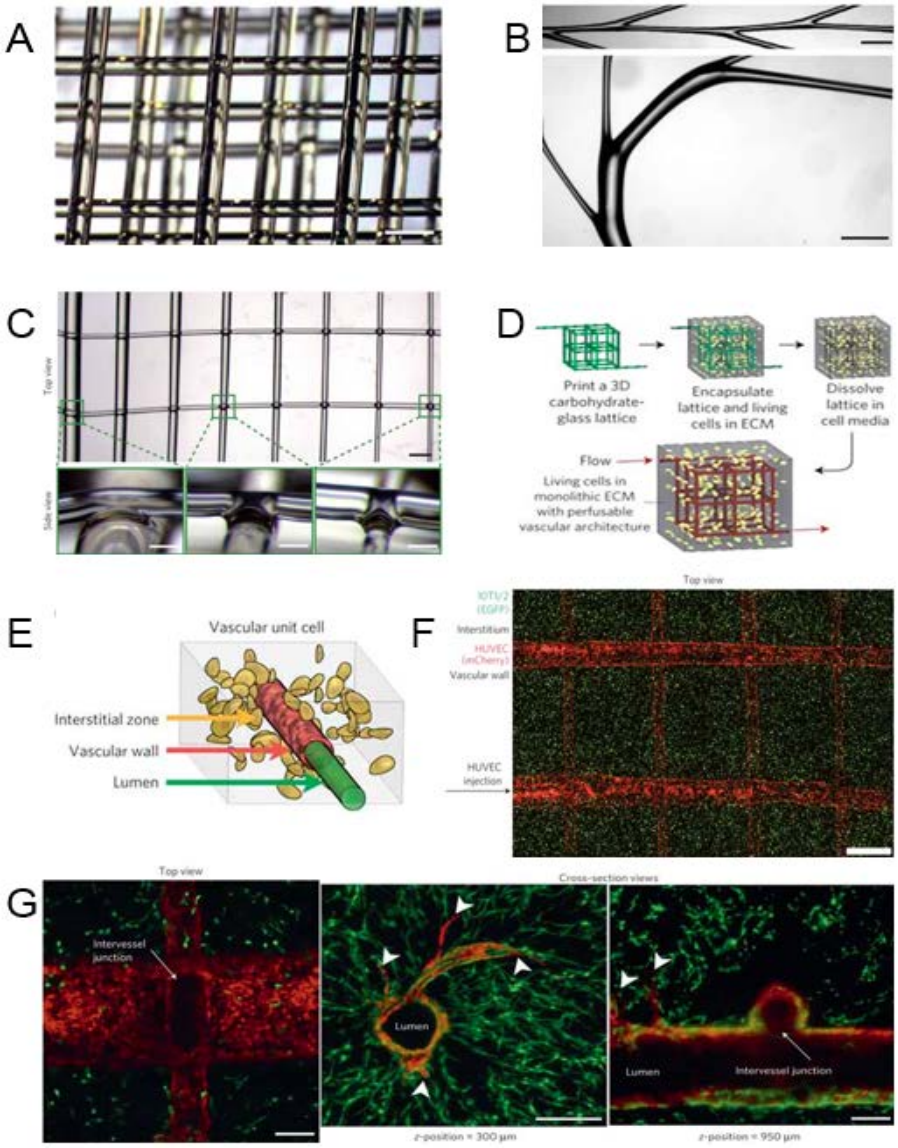

Figure 1-15 Printing vascular networks.

A) Multilayered carbohydrate-glass lattices were fabricated in minutes with precise axial and lateral positioning resolution (scale bar, 1 mm). B) Serial y-junctions and curved filaments (scale bar, 1 mm). C) Top view of the multiscale architectural design (scale bar, 1 mm). Interfilament melt fusions were magnified and shown in side view (insets, scale bar, 200 µm). D) An open, interconnected carbohydrate-glass lattice is printed to serve as a sacrificial element for casting 3D vascular structures. The lattice is encapsulated in ECM along with living cells. This lattice was dissolved in cell media without damage to nearby cells in minutes, yielding a monolithic tissue construct with a vascular architecture matching the original lattice. E) Schematic of three compartments in a 'vascular unit cell' consisting of the vascular lumen, endothelial cells lining the vascular wall, and the interstitial zone comprising of encapsulated cells and matrix. F) Control of the interstitial zone and the lining endothelium of vascularised tissue constructs is demonstrated by encapsulating 10T1/2 cells (1.5 X 10^6 per ml, constitutively expressing eGFP) in the interstitial space of a fibrin gel (10 mg per ml)

followed by seeding of human umbilical vein endothelial cells (constitutively expressing mCherry) throughout the vascular network via a single lumenal injection. Confocal z-stack montage demonstrated human umbilical vein endothelial cells residing in the vascular space with 10T1/2 uniformly distributed throughout the bulk gel after one day in culture (scale bar, 1 mm). G) Partial z-stack of two intersecting channels demonstrated endothelisation of channel walls and across the intervessel junction, while in the surrounding bulk gel 10T1/2 cells are beginning to spread out in 3D. Endothelial cells formed single and multicellular sprouts (white arrowheads) from patterned vasculature, as seen in a z-stack (optical thickness = 200 µm) from deeper within the gel (z-position = 300 µm). Deeper imaging (z-position = 950 µm, optical thickness = 100 µm) confirmed that the vascular lumen remained open throughout vessels and intervessel junctions and that endothelial cells also sprouted from larger vessels (arrowhead). Reproduced from (96).

Scaffold pores are necessary for bone tissue formation, enabling cell migration and in-growth, while allowing nutrient diffusion for cell survival (103). In general, scaffolds with pore sizes greater than 50 µm allow for the latter to occur but at the expense of lower cell adhesion and intracellular signalling whereas scaffolds with pores smaller than 10 µm have the opposite effect. Different cell types require different pore size ranges for effective growth. Osteoblasts were shown to grow better in scaffold areas with larger pores while fibroblasts preferred smaller pores (104). Narayan *et al* reported *in vitro* endothelial cell growth on PLGA scaffolds was enhanced on 5 to 20 µm pore sizes, with lower interpore distance (105). This is in contrast to some *in vivo* studies showing a higher porosity allows for faster bone ingrowth and vascularisation. Higher bone formation occurred in porous HAP scaffolds with 300 to 400 µm pore sizes after implantation in rats. Rapid vascularisation of implanted scaffolds provided an osteogenic microenvironment, explaining the difference in observations. Bai *et al* found that by increasing the pore interconnectivity within the scaffold, the number and size of blood vessels formed increased. In addition, 400 µm pores were noted to be optimal for vascularisation (106) Similar outcomes were obtained by Klenke *et al* who found that vessel formation occurred earlier in ceramic scaffolds with pore sizes larger than 140 µm, with a higher degree of microvascular perfusion and a two-fold increase in new bone formation when pore size increased from 40 to 280 µm (107). Ghanaati *et al* also demonstrated that pore size, porosity and the shape of β-tricalcium phosphate (B-TCP) bone substitutes influenced osseointegration as well as the vascularisation rate *in vivo*. The extent of vascularisation was higher in 40 per cent (rather than 80 per cent) porous scaffolds after ten days post-implantation in rats (108). These studies highlight the limitations of *in vitro* studies in predicting *in vivo* outcomes and

the need to determine the optimum pore sizes for each cell type used for bone tissue engineering.

Porosity has been shown to influence the integrative capability of an implant device or construct. Porous or rough materials integrate in a less fibrotic, better vascularised manner when compared to smooth, solid forms. A key reason for implant failure is the foreign body reaction, where biocompatible biomaterials become encapsulated and undergo phagocytic attack by macrophages. The mechanism by which this occurs remains unknown. Porous biomaterials with a uniform pore size of 30 to 40 µm, regardless of polymer composition or implant site, demonstrated excellent healing with a maximum in vascular density and a high infiltration of macrophages that have been postulated to possess pro-healing, rather than tissue destructive, functionality (109-111). 3D printing techniques can manufacture such scaffolds with uniform, pre-determined porosities, enabling the foreign body reaction to be further studied, and perhaps, even attenuated, thereby allowing for the generation of biofabricated constructs that have superior osseointegrative capability and lower rates of failure than existing implant devices.

1.6.3 Cell-biomaterial interplay for structural and functional integrity

Should the printed cells survive the printing process and retain their functionality, and vascularisation of the construct is achieved, the next key step involves achieving a cellular organisation within the 3D structure capable of enabling locomotion while withstanding mechanical stresses, in addition to performing a wide variety of homeostatic functions. The tissue construct should also be able to integrate with the neighbouring native bone tissue. Given the hierarchical 3D microarchitecture and highly dynamic nature of bone, this complex issue remains unresolved. Furthermore, the rate and efficacy of healing varies with age and health status (31).

1.6.3.1 Cell selection

Given the function of the osteoblast is to make bone, the cell source employed in the cell reparative paradigm is just as crucial as the choice of biomaterial. Thus, the incorporation of MSCs into bone tissue engineering has been a key advancement (Table 1-9). BMSC are the most frequently utilised stem cell source given the wealth of information available on this cell type (112-116). BMSCs are also relatively easy to obtain. Adipose tissue-derived stem cells have been

proposed as a viable alternative given their reported osteogenic ability *in vitro* (117), ease of access and abundance (118) and ability to survive in low oxygen or low glucose environments. Such resilience is an advantage particularly when the blood supply is limited, as in the case of biofabricated bone constructs. More recently, there has been increasing interest in using oral cavity MSCs as well as induced human pluripotent stem cells for biofabrication of bone (118-123).

Cell type	Multipotent or differentiated	Potential for bone tissue engineering	Advantages	Disadvantages
Bone marrow-derived stem cells	Multipotent	Osteogenic Potential for neovascularisation	Relatively easy acquisition Extensively characterised	Donor morbidity Limited proliferative potential Fewer cells compared to other sources. Dependent on age and health of donor
Umbilical vein stem cells	Multipotent	Osteogenic	Proliferative capacity Minimal donor morbidity	Not extensively characterised
Oral cavity mesenchymal stem cells (dental pulp, gingival stem cells)	Multipotent	Osteogenic	Abundant Easy acquisition	Not extensively characterised
Adipose-derived stem cells	Multipotent	Osteogenic Potential for neovascularisation	Easy acquisition Extensively characterised Able to grow in non-ideal conditions	Donor morbidity (due to anaesthesia)
Endothelial progenitor cells (EPC), specifically endothelial colony-forming cells (ECFC)	Lineage-directed	Potential for neovascularisation Supports osteogenic differentiation	Easy acquisition (peripheral blood, umbilical cord blood) Abundant Minimal donor morbidity Can be co-seeded with bone marrow-derived stem cells	Not multipotent Limited proliferating potential of early EPCs Differences in isolation and cultivation procedures make comparison studies on EPC functionality difficult Requires co-seeded cells for stabilisation for neovascularisation

Human umbilical vein endothelial cells	Differentiated	Potential for neovascularisation	Easy acquisition Can be co-seeded with bone marrow-derived stem cells	Not multipotent
Induced pluripotent stem cells	Multipotent Differentiated	Osteogenic Chondrogenic	Easy acquisition Minimal donor morbidity Patient-specific Unlimited self-renewal and higher proliferative capacity than MSCs Relatively established cell reprogramming protocols produce lineage-specific cell types from any cell source	Variable cell reprogramming efficiency. Protocol optimisation still needed Necessary induction into high quality progenitor cells post-transplantation Risk of tumour formation

Table 1-9 Cell types used in bone tissue engineering.

Adapted from (67, 118, 123, 124).

Despite studies being performed in animal models, the reversibility of, or the commitment to, the differentiated state of these various stem cells or whether these cells do retain the capacity to form bone *in vivo*, remains unclear (125). The development of well-defined, proficient protocols to standardise the methods used are necessary (115, 126, 127) in order to meet good manufacturing practice standards (to account for genetic and phenotypic drift). Long-term clinical observation studies *in vivo* will need to be conducted to provide information on the extent of this variability as *in vitro* or even *in vivo* animal model studies cannot accurately replicate the effects of the *in vivo* environment of different individuals on biofabricated bone tissue. As discussed, angiogenesis is crucial in creating a viable biofabricated bone construct. The effect on osteogenesis and angiogenesis of using two, rather than one, cell type has garnered much interest, with increasing evidence for the use of bone marrow stromal cells in generating blood vessels, particularly when seeded onto a scaffold with endothelial cells (67, 90). Human umbilical vein endothelial cells have demonstrated a similar ability to produce blood vessels, particularly when seeded with osteogenic cells (118).

Wang *et al* demonstrated that co-culturing human osteoblasts with human umbilical vein endothelial cells resulted in increased cell numbers and alkaline phosphatase activity. Furthermore, the release of VEGF by human osteoblasts can be increased by 1,25-VitD3 but only in co-cultures of human umbilical vein endothelial cells and human osteoblasts, not in human osteoblasts cultured alone (128). However, the use of co-cultures remains a limited approach in bone tissue engineering as few groups have managed to show improved bone formation using this approach (124, 129). This may be due to a lack of stimulus for the rapid development of new blood vessels that invade the co-culture grafts. By using a biaxial perfusion bioreactor, Liu *et al* were able to show that stimulated co-culture of human foetal bone marrow-derived MSCs and umbilical cord-blood EPCs demonstrated earlier vessel infiltration and increased ectopic bone formation *in vivo* (130). The ability of AM techniques to simultaneously print different cell types with spatial accuracy will aid in this endeavour, as demonstrated by Shim *et al* (51) who utilised a multi-head tissue/organ building system to separately dispense human chondrocytes and MG63 cells which were used to biofabricate osteochondral tissue.

1.6.3.2 Biomaterial selection

Scaffolds generated using AM techniques typically consist of a biomaterial made of ceramic, metal, self-assembly peptides, synthetic or natural polymer (131-133). The use of composite scaffolds is becoming more common due to the specific advantages and disadvantages of each type of biomaterial. Several reviews have comprehensively listed the most common combinations of these biomaterials, with and without cells seeded, that have been investigated using *in vitro* or *in vivo* methods for their potential use in bone tissue engineering (29, 33, 78, 131, 134-137). The ideal scaffold properties for osteogenesis have been highlighted in Table 1-4. Despite this wealth of information, there is no clear consensus as to which biomaterial, or combination of which, is optimal for bone biofabrication. The choice of biomaterial for biofabrication is currently limited by the AM method employed. Some AM methods such as stereolithography require post-processing procedures that are cytotoxic, while laser sintering can cause thermodegradation of the biomaterial, resulting in a loss of precise microstructure, which in turn affects material porosity and cell viability (32, 43, 131). This in turn limits the type of AM technique that can be employed for biofabrication purposes in bone tissue engineering, as reflected by the fact that the most utilised methods over the past decade remain extrusion method, laser-assisted, and inkjet printing.

1.6.3.3 Improving mechanical functionality and osseointegration

In vivo, cells are exposed to a combination of biochemical and physical cues which regulate their function and behaviour (138). Osteogenic cells are known to respond to mechanical stimuli (Figure 1-16). Several microfabricated devices have been created to induce and monitor cellular responses to biochemical gradients and biomechanical forces *in vitro*. These devices can be used to investigate the effect of perfusion on human MSCs in a controlled manner as the devices allow the cells to be stimulated at time-specific intervals (139). The construct properties can be regulated using bioreactor strategies to maximise its functionality. The effect of cell seeding density and biomolecules on osteogenesis and angiogenesis can be categorically evaluated (140), providing information regarding the spatiotemporal characteristics of bone regeneration, which in turn will improve the fabrication of new biomimetic scaffolds while furthering our understanding of stem cell biology.

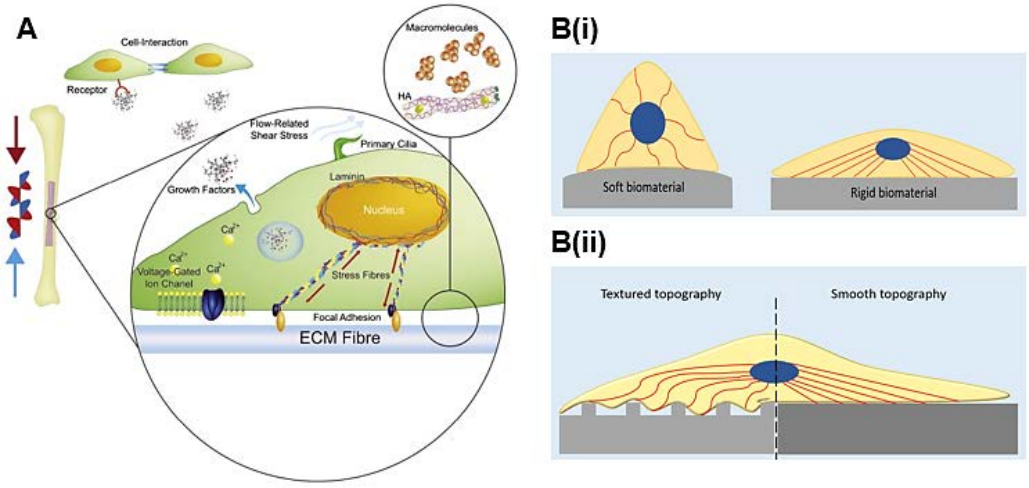

Figure 1-16 Mechanotransduction and osteogenesis.

A) The role of mechanical cues on osteogenic differentiation – in native bone, physiological loading induces fluid flow in the canaliculi, resulting in shear stress on osteocytes which transmit these signals to osteoclasts and osteoblasts to remodel bone. Stretching of the cell membrane permits the influx of calcium ions through stretch-activated ion channels. Fluid flow deflects the primary cilia extending from the surface of osteoblasts and osteocytes, altering signal transduction through tensing microtubules. Gap junction intercellular communication further mediates osteoblast differentiation and bone formation through the propagation of calcium signalling cascades. Additionally, the stiffness and topography of bone matrix affects new bone deposition by osteoblasts. B(i) Substrate stiffness affects cell adhesion, migration and differentiation – soft surfaces provide low resistance, reducing focal adhesion strength and cytoskeletal organisation (shown in red). Changes in nuclear shape induce changes in gene expression. B(ii) Similarly, surface roughness, spacing and

randomness in the nanotopography of scaffolds can influence cell adhesion and formation of localised stresses along the cell membrane. Such differences are transmitted via actin filaments (shown in red) to the nucleus, leading to changes in gene expression and cell fate. (A) Reproduced from (138) (B) Adapted from (141).

Different surface modification techniques, such as electrochemical deposition, oxidisation, or anodisation via cathodic pre-treatment, can be employed to further enhance the biocompatibility and osteoinductive capability of biomaterials (138). Electrochemical anodisation was used by Huang *et al* to generate a sandblasted, acid-etched titanium surface, to roughen the material surface. This improved MG63 cell proliferation and osseointegration of the biomaterial (142). Tsai *et al* utilised laser scanning speeds between 10 and 500 mm per sec to modify biomedical grade IV titanium surfaces, creating volcano-like surface layers accompanied by a micro- to nanoporous structure at low scanning speeds, or a wave-like surface layer accompanied by a nanoporous structure at higher scanning speeds (Figure 1-17). A laser scanning speed of 50 mm per sec was found to optimally facilitate MG63 cell adhesion and confluency on the material surface through the generation of a rougher surface layer of titanium oxide (143).

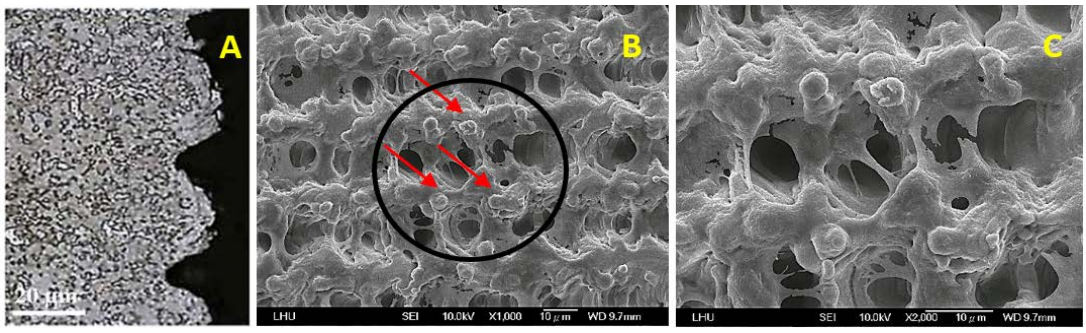

Figure 1-17 Biomedical grade IV titanium surfaces modified using a 1 watt neodymium-doped yttrium orthovanadate laser (wavelength 335 nm) at a scanning speed of 50 mm per sec.

A) Optical micrograph of the cross-section of the modified titanium surface (scale bar represents 20 µm) B) Scanning electron micrograph image of the modified titanium surface with seeded MG63 cells after a one day culture (scale bar represents 10 µm) C) Higher magnification scanning electron micrograph image of the circled area in (B), demonstrating the morphology of seeded MG63 cells (highlighted by red arrows) after a one day culture (scale bar represents 10 µm). Figure 1-14A reproduced from (143); Figures 1-14B and 1-14C from unpublished data, Taipei Medical University.

AM techniques can be used to accurately produce monotonic or graded topographical features on a biomaterial. Micropatterning has been shown to improve

cellular adhesion through focal adhesion formation via forced integrin clustering (133, 144). These topological modifications can take the form of micro- and nano-scale protrusions, pits or grooves, which are able to direct or manipulate stem cell differentiation. Nanopit arrays have been shown to disrupt adhesion formation and cellular migration in human osteoblast cells in addition to impairing osteogenic differentiation of STRO-1 positive SSCs (145). Oh *et al* found that by altering the dimensions of nanotubular-shaped titanium oxide surface structures, the adhesion as well as osteogenic differentiation of human MSCs (without the use of osteogenic media) could be enhanced (146). In these studies, such changes were achieved by making micro- or nanoscale alterations to dimensions of the grooves or the structures respectively. This degree of alteration is dependent on the cell type and biomaterial employed (144, 145, 147).

Surface roughness at the resorption sealing zone can be sensed by osteoclasts through forces applied at different heights and surface angles. 0.1 to 1 μm cracks can stimulate local osteoclast activity. Providing biomaterials with such surface modifications can enhance osseointegration of the implant (133). This was demonstrated by the use of AM to produce Grade 5 titanium (Ti6Al4V) constructs with varying porosity and micro- to nano-scale roughness using human trabecular bone as a template. MG63 cells that were manually seeded onto scaffolds with the highest porosity and surface modifications were shown to undergo greater differentiation and local growth factor production (148). Altering the surface chemistry of the biomaterial or the geometry of the scaffold also affects cell adhesion, migration and differentiation (144, 149). Given that cellular behaviour in microenvironments varies with cell type and cellular interaction, optimisation of micropatterning approaches in biofabricating bone may have to adopt a customised, rather than a ‘one size fits all’, approach (144, 150). 3D printing offers concomitant flexibility and accuracy in generating customised biomaterial constructs, which will also aid in the elucidation of the mechanisms involved in cell-biomaterial interaction.

1.6.3.4 Biochemical signalling for bone biofabrication

In vivo, biochemical signals in the form of growth factors, hormones or cytokines are secreted at local injury sites or in areas undergoing bone remodelling, triggering the migration of progenitors and inflammatory cells (as in the case of bony injury) or the activation of osteoblasts and osteoclasts (as with bone remodelling) (100). This allows for the generation of new bone tissue as part of the healing or remodelling process respectively. Bone tissue engineering has attempted to

harness the regenerative properties of these physiological processes (Table 1-10). Clinical studies typically employ growth factors at supraphysiological doses (mg per ml rather than ng per ml), resulting in adverse effects that include ectopic bone formation, antibody development and possibly, carcinogenesis (133). As such, only a few synthetic grafts containing bioactive molecules are commercially available for surgical use in certain countries (151). Data collated by Gothard *et al* and Santo *et al* indicates there is no consensus as to the appropriate doses of growth factors used for bone tissue engineering, with a wide range of concentrations in use (152). The actual dose of growth factors delivered by constructs *in vivo* when used in defects remains uncertain (153). Conflicting evidence exists for co-utilisation of multiple growth factors (154, 155). A need remains for more studies to ascertain the effects of combining multiple growth factors for use in bone tissue engineering, which will provide valuable information on the synergistic or cumulative effects between growth factor combinations, optimal doses to be used, in addition to a more accurate predictive capability of the *in vivo* effects (including any complications) of multiple growth factor use.

Growth factor	Tissues studied	Observed function
BMP (-2, -7)	Bone, cartilage	Differentiation and migration of osteoblasts, with accelerated bone healing observed
FGF (-1, -2, -18)	Bone, muscle, blood vessel	Migration, proliferation and survival of endothelial cells Increased osteogenic differentiation of MSCs
IGF-1	Bone, cartilage, muscle	Proliferation and differentiation of osteoprogenitor cells
PDGF (-AA, -BB)	Bone, cartilage, blood vessel, muscle	Proliferation, migration, growth of endothelial cells Osteoblast replication in vitro Type 1 collagen synthesis
PTH	Bone	Increased bone formation through osteoblast stimulation with intermittent dosage. Bone resorption if administered continuously
TGF-β3	Bone, cartilage	Proliferation and differentiation of bone-forming cells Enhances hyaline cartilage formation *in vivo* Anti-proliferative to epithelial cells

VEGF	Bone, blood vessel	Enhanced vasculogenesis and angiogenesis but functionality of vasculature dependent on concentration used Reduction or increment in bone formation dependent on concentration when used in combinational delivery with BMP-2

Table 1-10 Growth factors being investigated for bone tissue engineering.

Adapted from (36, 152).

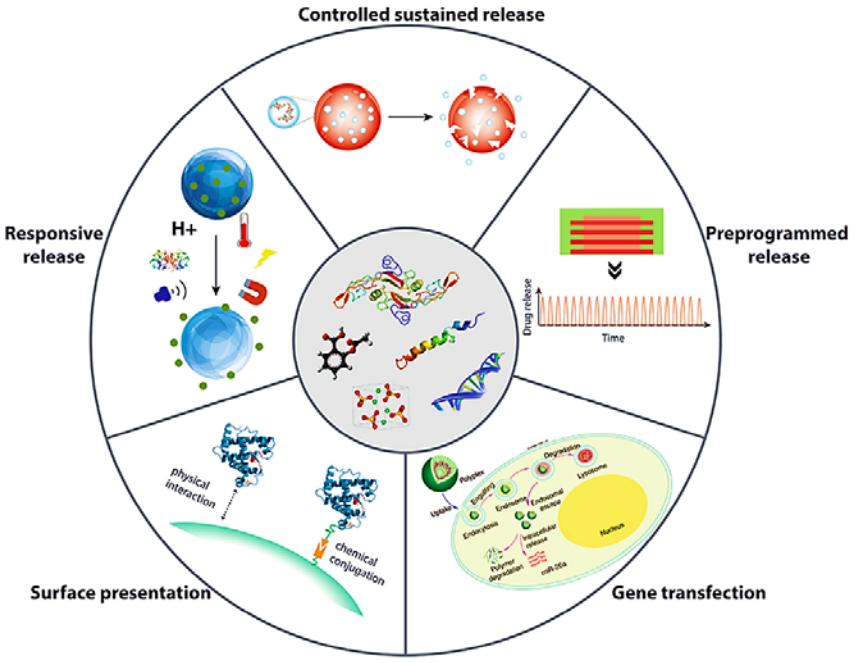

Figure 1-18 Delivery strategies for biochemical signals in bone tissue engineering.

Different biochemical signals require different delivery systems to achieve optimal therapeutic effects. Reproduced from (156).

Figure 1-18 highlights the various delivery strategies for biochemical signals such as unbound, bound within the implant for controlled delivery, coated on the implant surface, or coded within the cells via gene delivery mechanisms (138, 153, 157, 158). Unbound growth factors will allow a bulk release of growth factors, resulting in a steep concentration gradient and rapid clearance from the microenvironment. Although such an approach may be ideal for initial short-term stimulation (as it is dependent on the rate of biodegradation of the biomaterial), it is unpredictable. If prolonged growth factor stimulation is required, physical entrapment (utilising micro- or nanospheres, or liposomes) or covalent binding (via enzymatically cleavable linkers or by chemical conjugation) is a preferable approach

to ensure a more controlled or on-demand release of the growth factor or drug (159, 160). Over a fifteen day period, Sawkins *et al* were able to demonstrate the sustained release of active lysozyme contained within thermoresponsive PLGA microspheres that had been incorporated into extrusion printed poly(ethylglycol)-PLGA constructs (161). The aim of such approaches is to stimulate, and possibly, accelerate angiogenesis as well as osteogenesis in order to enhance the osseointegration of the biofabricated construct while attempting to mimic the physicochemical properties of bone.

Bioactive hydrogels containing protease sensitive sites, cell adhesion molecules such as RGD-containing peptides, and/or biological cues in the form of growth factors, inorganic minerals or drugs, have been developed to respond to their environments and present stimuli on demand (78, 162), thereby mimicking a function performed by ECM. Hydrogels are currently the most investigated method for cellular encapsulation and biochemical delivery *in situ* in tissue engineering. Simmons *et al* incorporated BMP-2 and TGF-β3 into alginate hydrogels that were designed to degrade at different rates by gamma-irradiation. These were used to encapsulate rat bone marrow stromal cells and the effect of single and dual growth factor delivery on these cells was investigated. The authors showed the degree of osteogenesis could be manipulated by controlling the rate of scaffold degradation for the delivery of multiple growth factors (163). Since then, several studies have investigated the efficacy of growth factors (either in isolation or in combination) delivered by a variety of biomaterials for bone regeneration purposes, with varying degrees of success (56, 62, 164). Lu *et al* embedded gelatin microparticles containing BMP-2 and IGF-1 into bilayered oligo(poly(ethylene glycol) fumarate hydrogels in a spatially controlled manner to investigate their effect on the repair of a femoral condyle osteochondral defect in rabbits. Dual delivery of BMP-2 and IGF-1 resulted in greater subchondral bone repair, increased bone growth at defect margins, and lower bone specific surface than hydrogels containing single growth factors, demonstrating a synergistic relationship between the growth factors in enhancing bone repair (165). Radhakrishnan and colleagues recently developed an injectable osteochondral scaffold to treat an osteochondral defect in rabbits (166). The scaffold consisted of a chondral layer (comprising 2% alginate-poly(vinyl alcohol) hydrogel with chondroitin sulfate nanoparticles) overlaid with a similar subchondral hydrogel layer, which consisted of 1% nano-HAP. The subchondral layer exhibited higher osteoblast proliferation and ALP activity, with complete closure of the defect at 8 weeks in the bilayered gradient scaffold cohort.

There has been increasing interest in utilising existing 3D printing methods to incorporate growth factors or drugs into scaffolds (creating bioactive scaffolds) in a spatiotemporal distribution (creating bioinstructive scaffolds) (57, 167). Spatial patterns of BMP-2 were created on a fibrin surface using an inkjet bioprinter. 10 µg per ml BMP-2 was loaded onto a sterilised print head and printed onto a fibrin-coated glass surface in a spatial pattern. Murine muscle-derived stem cells seeded onto the BMP-2 pattern exhibited ALP activity, indicating osteogenic differentiation. Those seeded outside the BMP-2 pattern were undifferentiated (168). An observed reduction in biological activity of bioprinted recombinant human BMP-2 was due to drug degradation during spraying through the nozzles (169). As the majority of growth factors have a short half-life *in vivo*, researchers also need to consider the biochemical properties of scaffolds as well as the agents being used. Progress in 3D printing growth factors and the current limitations of the approaches used are extensively covered in a recent review by Koons *et al* (57).

1.7 The possibility for clinical translation

A major challenge for the successful translation of any cell therapy to be used for regenerative medicine purposes remains their robust production on a large scale. Thus, bioprocessing steps involved in the manufacturing process must be scalable and reproducible, in keeping with good clinical and good manufacturing practice standards safe for patient application and affordable (170). Despite high resolution and reproducibility, laser-assisted bioprinting techniques offer low throughput (print speeds typically 5 kHz), small scale manufacture of constructs as the characteristic droplet volume is 1 pl (70). Inkjet bioprinting suffers from similar limitations (Table 1-5). While the microscale organisational ability allows generation of superior 3D constructs compared to some AM methods, inkjet printing technology typically struggle to generate large scaled structures (a single instrument printing single cells at 10 kHz takes twenty-seven hours to generate a 1 cm^3 structure (48). Thus, scalability currently limits efficacy and use of biofabrication in clinical regenerative therapies.

Extrusion method printing provides a higher resolution than inkjet-based printing in generating large constructs for clinical therapeutic use. However, larger constructs will require the incorporation of a controlled microenvironment around the printing stage (52). With the falling cost of AM technology, biofabricating methods can advance at a faster rate and improve accuracy, efficiency and scalability. These additional requirements increase the complexity of the bioprinting process, and until

these problems can be resolved, may preclude the ability to upscale biofabricated bone constructs and the widespread use of AM methods in biofabrication.

Computed tomography and magnetic resonance imaging are currently used to generate a 3D imprint. More recently, 3D laser scanning approaches have been used to obtain 3D digital images of body contours. AM technology has steadily advanced to allow for the simultaneous printing of multiple biomaterials. This technology has slowly extended to the bioprinting of multiple cell types, albeit to a limited extent at present. The standard file format used to control AM bioprinters is STL. This makes use of meshes of triangles that simulate the watertight outer surfaces of objects. While this works for solid objects with limited complexity, STL is an impractical format if internal pore architecture is an integral part of the computer-aided design. An STL mesh of a few millimetre-sized scaffold with well-defined porosity exceeds one million triangles, taking up hundreds of megabytes of storage space as well as requiring significant (and expensive) computational power to design and manipulate (43). A new method to create porous models from medical imaging-derived data was developed whereby CT-derived anatomical data was converted into a volumetric mesh (comprising of interconnected wireframes) using existing methods to generate a breast prosthesis (171). Another approach using a volume-based, non-continuum formulation to account for the variations in bone density and strain energy densities current finite element methods do not take into account these changes (172). Such an approach will enable the study of the effects of biomechanical forces on bone remodelling and improve the accuracy of *in silico* predictive models that would reduce the numbers of animals used in *in vivo* studies. Thus, new methods of computer-aided design are needed to improve the precision of construct design, reduce the storage space and processing power required to operate the software, as well as improve *in silico* modelling methods (60).

1.7.1 Automation and controlled production

Compared to traditional static cultures, bioreactors enhance fluid diffusion within the scaffold, permitting a means for controlled culture conditions. Costa *et al* demonstrated the application of automated AM technology to design and fabricate different anatomically shaped bioreactors and highly porous sheep tibia scaffolds in one manufacturing step; without incurring increased costs or the need for additional engineering steps (93). Human osteoblasts that were seeded using a bi-directional perfusion approach were homogenously distributed throughout the scaffold, remaining viable after six weeks of culture. The experiment also highlighted the

importance of both the shape and inner structure of the device in determining the perfusion of fluid within the scaffold architecture, and therefore, the nutrient flow pattern. Through developing novel methods that assimilate existing technologies into bioreactor setups to allow online or real-time readouts of biological parameters such as gene expression, metabolic activity and protein production, the biofabrication process can be directed to enable real-time adjustment of bioprocess parameters, which would maximise the quality of the construct. Bioreactors are not only useful for perfusing 3D constructs or providing stimuli to facilitate osteogenesis. At present, stem cell isolation, expansion and differentiation consists of conventional manual techniques dependent on operator expertise. This carries a risk of processing inconsistencies, contamination, and variation in cell number and phenotype. Bioreactors provide a more robust approach to automating this process in order to meet good manufacturing practice standards. Cells can be reliably isolated from biopsies, enabling their expansion to achieve sufficient numbers in a highly reproducible fashion through the use of microcarrier-based bioreactor systems such as wave bags and stirred tanks. Aggregate expansion using shake flasks and hollow fibre systems (some of which are commercially available) have also been developed to expand progenitor cell populations.

1.7.2 Evaluating a biofabricated construct: clinical efficacy and safety

Strategies to enhance bone repair and regeneration have been hindered by limitations in research models currently available to evaluate bone repair processes. Typical *in vitro* cell culture models use single or dual cell populations and are incapable of recreating *in vivo* spatial arrangements. *In vivo* animal models can generate vast amounts of relevant data on bone repair processes as well as assessing (to an extent) the efficacy of bioprinted or biofabricated bone constructs, but these studies usually involve large numbers of animals which raise ethical concerns, are expensive and labour-intensive. The *in vivo* data obtained can often be complicated by systemic influences. Development of *ex vivo* organ cultures (173) to study bone repair processes, and the increasing utilisation of chick chorio-allantoic membranes for studying vascularisation (174) and the cytocompatibility of biomaterials and growth factors (175), have both helped to reduce the numbers of animals used, tackling the ethical issues surrounding the use of animals in experiments while partially resolving other study limitations.

The development of an *ex vivo* organotypic culture model of embryonic chick femurs has provided a reproducible, cost-effective, robust model that is

responsive to external stimuli, allowing for the evaluation of bone repair and tissue responses over a defined period (176). This model has been further refined to assess the effect of biomaterial scaffolds on bone formation in critical size defects (173). Despite these advances, there remains a paucity of comparable data in the literature regarding long-term *in vitro* and *in vivo* characterisation of bioprinted and biofabricated bone constructs. Experiments conducted to assess the mechanical strength and functionality of the bone construct should be performed at fixed time intervals over a pre-defined period using standardised techniques. Measurements should also be carried out when the biomaterial used has completely degraded to ascertain the true functionality of the new bone formed. Such experiments require a long-term approach, are expensive to run, and reduce the cost-effectiveness of the product, but are necessary to establish clinical efficacy.

The ideal biofabricated bone contains a scaffold that degrades, allowing replacement by new bone (Table 1-11). The rate of biodegradation and release kinetics of 3D scaffolds (with or without incorporated biomolecules or inorganic minerals) remains under-investigated, despite several *in vitro* and *in vivo* studies (Table 1-12). Only more recently have similar *in vitro* studies been performed on composite scaffolds as well as biofabricated constructs (177).

Polymer characteristics	Polymer composition, Molecular weight Chemical structure and functionality Chain motility and orientation, Morphology Hydrophilicity, Charge density Polydispersity index Additives or impurities Crystallinity
Scaffold architecture	Pore size and porosity Surface area-to-volume ratio Surface roughness Mass/Density, Size and shape Sterilisation (irradiation) Processing effects – specific to AM method used
***In vitro* factors**	Medium composition and refreshment frequency pH/ionic strength Enzyme concentrations (for example, matrix metalloproteases) Cell type and density Mechanical loads Incubation temperature

***In vivo* factors**	Nutrient diffusion, Vascular access Dynamic pH Tissue modelling and remodelling Mechanical loads Metabolism of degraded products Enzyme concentrations Site of implantation

Table 1-11 Factors affecting scaffold biodegradation.

Adapted from (136).

Biomaterial	Biodegradation time	Compressive, tensile or flexural strength (MPa)	Modulus (GPa)
Bulk degradable polymers:			
Poly(lactic-co-glycolic acid)	1 – 12 months	41.4 to 55.2	1.4 to 2.8
Polylactic acid	5 to 60 months	Pellet: 40 to 120 Film or disk: 28 to 50 Fibre: 870 to 2300	Film or disk: 1.2 to 3 Fibre: 10 to 16
Polycaprolactone	> 36 months	--	--
Polyglycolic acid	1 – 12 months	Fibre: 340 to 920	Fibre: 7 to 14 5 to 7
Surface erodative polymers:			
Poly(anhydrides)	1 month	Compressive: 30 to 40 Tensile: 25 to 27	0.14 to 1.4
Poly(ortho-esters)	1 week to 16 months	Compressive: 4 to 16	2.5 to 4.4
Dense composites:			
Polylactic acid/10-70% Hydroxyapatite fibre	--	Flexural: 50 to 60	6.4 to 12.8 X 10^3
Poly(lactic-co-glycolic acid)/40-85% Hydroxyapatite	--	Flexural: 22	1.1 X 10^3
Porous composites:			
Polylactic acid/50% Hydroxyapatite	--	Compressive: 0.39	10 to 14
Poly(lactic-co-glycolic acid)/60-75% Hydroxyapatite	--	Compressive: 0.07 to 0.22	2 to 7.5
Poly(lactic-co-glycolic acid)/75% bioglass	--	Compressive: 0.42	51
Tricalcium phosphate scaffold with 5% polycaprolactone coating	--	Compressive: 2.41	--
(40% Hydroxyapatite + 60% β-tricalcium phosphate) coated with hydroxyapatite/polycaprolactone	--	Compressive: 2.1	--

Titanium (17 to 58% porosity)	Never	Compressive: 24 to 463	--
Hydroxyapatite (41% porosity)	Years	Compressive: 34.4 ± 2.2	--
B-tricalcium phosphate (50% porosity)	> 36 months	Compressive: 10.95 ± 1.28	--

Table 1-12 Physical properties of some biomaterials used as scaffolds for bone tissue engineering.

Adapted from (37, 177, 178).

Currently used permanent implant materials, such as metals, oxide ceramics, and thermoplastic polymers and elastomers may be associated with corrosion or unintended degradation, infection, and ultimate failure, sometimes necessitating implant removal and replacement. Non-degradable materials may impede stimuli for bone growth (stress shielding), resulting in bone resorption around the implant. Matching the degradation kinetics of a scaffold (179) with cell migration and proliferation (and subsequently tissue formation) enables a stepwise load transfer from the degrading scaffold to the newly deposited ECM. The biomaterial must be safely broken down and excreted (180). As the rate of tissue formation and remodelling occurs at different rates for different tissues and is affected by *in vivo* factors, these *in vitro* and *in vivo* mimetics must be further elucidated. As Table 1-12 shows, the assessment of biodegradability of the biomaterials used in bone tissue engineering is variable and arbitrary. In the development of a novel degradable polymer, most degradation experiments are performed *in vitro* by incubating the polymer in phosphate buffered saline (PBS) at 37°C to study the degradation mechanism. However, *in vitro* degradation behaviour can considerably differ from *in vivo* degradation, where a critical factor can be the ability of degradation products to stimulate late inflammation, possibly compromising tissue regeneration. The site of implantation, and the size and shape of the implant can affect *in vivo* degradation. Assessment of the biodegradability of engineered constructs *in vivo* remains in its infancy, with the focus being the local effect of dissolution products from scaffold degradation on osseointegration and bone formation. Part of the problem is the lack of long-term follow-up studies of these materials when used *in vivo* in patients. Most of these biomaterials are not in widespread clinical usage, reducing the power of any follow-up study to determine the rate of degradation in humans.

Assessing the extent of biodegradation that has occurred involves imaging techniques, which provide an estimated, rather than a precise, measure. Modern microscopy techniques have helped in the evolution of biomaterials, from their composition to their interactions. However, the increasing complexity of these engineered constructs has highlighted the need for more versatile, non-invasive, and non-destructive methods of analyses that would allow for the long-term spatiotemporal monitoring and assessment of morphological, functional and molecular performance of these bioconstructs (181-183). Current studies continue to utilise histological techniques and visualisation by conventional methods (Table 1-13), as a gold standard of analysis (181). Such methods do provide valuable information but these approaches usually require sample destruction at pre-determined experiment end-points, which restricts the opportunity to obtain significant and relevant real-time information from *in vitro* experiments (before implantation of the construct), thereby slowing the development efficiency of successful constructs for *in vivo* testing. Additionally, they provide limited information due to the need to compensate for experimental inconsistencies and sample variations (particularly in *in vivo* experiments). In order to do so, statistical analysis is required which further increases the numbers of animal models used in such studies, and the cost of these experiments, thus limiting its practicality in *in vivo* pre-clinical and clinical settings.

Furthermore, the limited penetration depths for most microscopy techniques is a major constraint when it comes to imaging scaffolds and the cells seeded within (184). To address this key issue, researchers have been exploring several advanced imaging modalities. An ideal imaging tool must be able to resolve signals at a subcellular level whilst being minimally invasive in penetrating the whole body. Critically, it should have sufficient contrast to distinguish the morphological, molecular and physicochemical changes that occur (183, 185). Current medical imaging systems are based on detecting the physical interaction (usually an energy change) between the imaged object (cells, particles, organs, etc.) and an external or internal energy source (electromagnetic waves, ultrasonic waves, etc.) in order to generate an ‘image’. To date, no single imaging modality is suitable for all tissue engineered constructs. Therefore, understanding the capabilities and limitations of each form of imaging is crucial in deciding which imaging modalities to use for assessing different bioconstructs.

Method	Imaging depth	Resolution	Real time acquisition	Endogenous contrast		Molecular imaging with contrast agents	Cost
				Bone	Blood		
Microcomputerised tomography	Full body	0.02 – 0.05 mm	Yes	Very good	Poor unless phase contrast	Yes	Low
Confocal light microscopy	< 100 µm	200 – 1000 nm	Yes	Poor	Poor	Yes	High
Light microscopy	N.A.	200 – 350 nm	No	Poor unless stained	Poor unless stained	Yes	Low
Scanning electron microscopy	N.A.	1 – 5 nm	No	Good	Poor	No	Medium
Magnetic resonance imaging (MRI)	Full body	5 – 200 µm	Yes	Very good	Very good	Very good	High
Positron Emission Tomography (PET)	Full body	1 – 2 mm	No	Good	Poor	Excellent	High
Ultrasound	10mm	20 – 100 µm	Yes	Poor	Good	Good	Low
Optical microscopy	0.3 – 1 mm	0.2 – 1 µm	Yes	Very good	Very good	Excellent	Low
Photoacoustic microscopy	20 mm	50 – 150 µm	Yes	Poor	Excellent	Excellent	Medium

Table 1-13 Imaging techniques used in bone tissue engineering, and their properties.

Abbreviation: N.A. = not applicable. Modified from (184, 185)

Several recently published reviews have detailed how each imaging modality works and the areas in this field, which require further development (181, 183, 185). Imaging modalities that have, and can possibly be, used in bone tissue engineering are highlighted below. Ultrasound, µCT, and MRI have been used to provide anatomical imaging, whereas metabolic imaging has been performed by PET, single photon emission computed tomography (SPECT), and optical imaging (OI, both bioluminescence and fluorescence). Table 1-13 summarises the characteristics of imaging methods available. Each method has its own range of applications, providing specific information based on the properties of each technique (Figure 1-19).

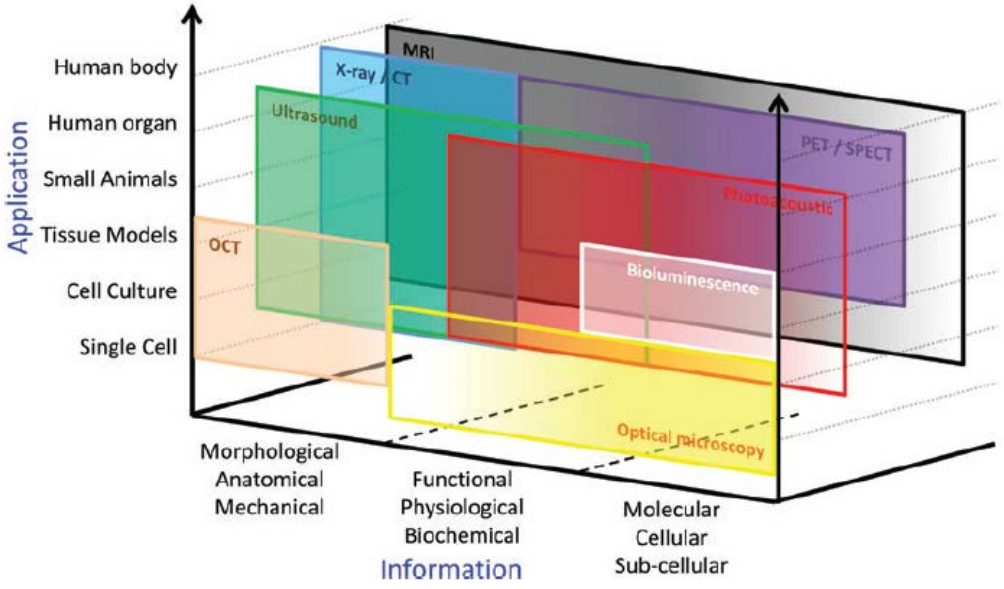

Figure 1-19 Potential applications of advanced imaging modalities.

Abbreviations: CT = computerised tomography, OCT = optical coherence tomography. Modified from (185).

µCT remains the gold standard for bone imaging. Both phase contrast and absorption µCT have been applied to evaluate biomaterials and tissue engineered constructs *in vitro* and *in vivo* (Figure 1-20) (186, 187), demonstrating high contrast and resolution, in addition to generating three-dimensional volume renderings of structures deep within the body. Given that ionising radiation is used, the scan time and energy settings must be optimised for every experiment to minimise tissue or specimen damage – this remains one of the major limitations of µCT imaging *in vivo* especially if acquisition times are long (181, 182).

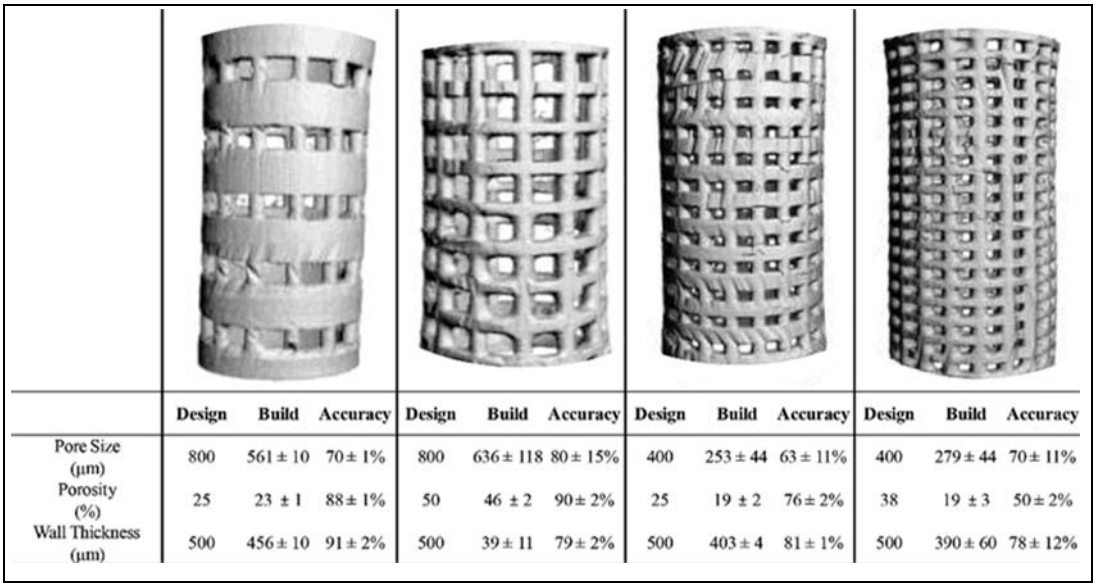

	Design	Build	Accuracy	Design	Build	Accuracy	Design	Build	Accuracy	Design	Build	Accuracy
Pore Size (μm)	800	561 ± 10	70 ± 1%	800	636 ± 118	80 ± 15%	400	253 ± 44	63 ± 11%	400	279 ± 44	70 ± 11%
Porosity (%)	25	23 ± 1	88 ± 1%	50	46 ± 2	90 ± 2%	25	19 ± 2	76 ± 2%	38	19 ± 3	50 ± 2%
Wall Thickness (μm)	500	456 ± 10	91 ± 2%	500	39 ± 11	79 ± 2%	500	403 ± 4	81 ± 1%	500	390 ± 60	78 ± 12%

Figure 1-20 Non-destructive analysis of 3D printed scaffolds by μCT.

μCT analysis of the scaffold pore size, porosity, and wall thickness can be performed to determine printing accuracy in accordance with design parameters. Reproduced from (186).

As such, other forms of imaging could be utilised as an alternative, or as an adjunct, to μCT for bone tissue engineering applications. For example, ^{31}P is abundantly present in bone mineral and cell membranes; the density of this in bone samples can be detected by combining Ultrashort echo time MRI and nuclear magnetic resonance (NMR) spectroscopy. Several *in vitro* and *in vivo* studies utilising this form of imaging have been able to detect the early signs of new mineralisation. Weber *et al* evaluated the formation of ECM in porous PLGA matrices that were implanted into rat tibiae and analysed by ^{31}P-NMR spectroscopy after two, four, or eight weeks. Detection of the inorganic component of the matrix, bioapatite, by ^{31}P-NMR spectroscopy was possible, in addition to the differential quantification of newly deposited bone matrix within the artificial bone graft and that of native bone (Figure 1-21A) (188).

Increased uptake of ^{18}F-fluoride in skeletal areas is known to indicate sites of increased blood flow and bone remodelling, through enhanced osteoblast activity and osteoid production. ^{18}F-NaF PET was used by Lin *et al* to show that bone marrow-derived mesenchymal stem cells expressing BMP-2 and vascular endothelial growth factor contributed to the repair of critical-sized calvarial defects in rabbits through increased angiogenesis and osteogenesis in comparison to controls (189). Similarly, using ^{99m}Tc-MDP SPECT, pre-vascularised tissue engineered constructs, comprising of a co-culture of MSC and MSC-derived endothelial cells in

a porous β-TCP ceramic scaffold, demonstrated greater osteogenesis and vascularisation when implanted to repair large segmental ulnar defects in rabbits (Figure 1-21B) (190). SPECT has been used to monitor the release of labelled bioactive molecules from implanted scaffold materials and its effect on bone formation, allowing the optimisation of growth factor delivery carriers (191).

Different OI techniques are available to perform post-implantation follow-up and *in vivo* characterisation of material performance. One such method is Raman spectroscopy, which can differentiate between the organic and mineral states of the material, without the addition of external fluorescent markers. Bone structure-derived Raman bands reflect the concentration of carbonate, collagen, and phosphate components, which can be used to determine the bone matrix composition, disease state or degree of bone maturation (192). Another approach is to directly label the scaffold with fluorescent probes, which allow for the monitoring of biodegradation and replacement with newly formed bone over time (193).

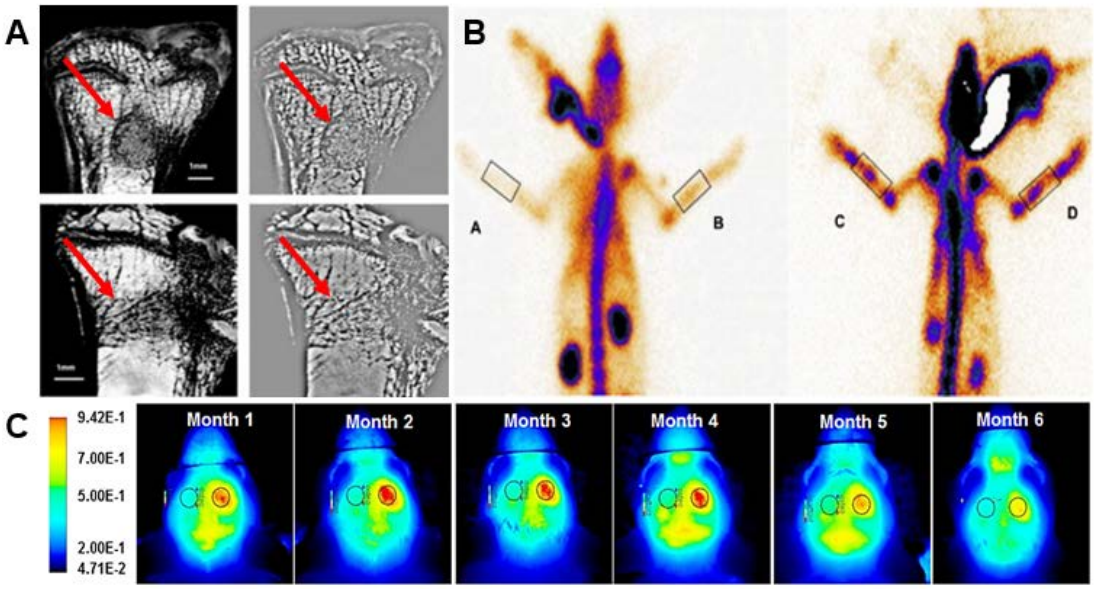

Figure 1-21 Imaging modalities used in analysing bone constructs in vivo.

A) Coronal and sagittal MRI images of a rat tibia, post-28 days implantation of PLGA scaffolds (red arrows) showing non-degradation of the scaffold. High-band filtered images emphasize the perpendicular orientation of the implant bone structure to that of the native trabecular bone. Reproduced from (188). B) SPECT at post-operative week 12: greater osteogenesis occurred in the co-culture seeded scaffold, as illustrated by the highest uptake of ^{99m}Tc-MDP seen in group D, where A = control, B = β-TCP only, C = β-TCP + MSC, D = β-TCP + MSC + MSC-derived endothelial cells. Reproduced from (190). C) Near-infrared optical images of study mouse 2 at one month intervals. The left circle outlines the control,

containing only the silk scaffold, whilst the right circle in each image represents the seeded scaffolds. There is clearly greater osteogenic activity in the seeded group. It can also be determined that osteogenesis appears to peak at four months but persists for longer. Reproduced from (194).

Wartella *et al* adopted a multi-modal imaging approach to monitor *in vivo* osteogenesis of a silk protein scaffold seeded with differentiated mesenchymal stem cells in a critical-sized calvarial defect mouse model over a six month period (194). Whilst MRI indicated mineralisation of the seeded constructs (compared to scaffold-only controls), near-infrared OI with IRDye® 800CW BoneTag™ showed increased osteogenesis in the seeded group (Figure 1-21C) (194). *In vivo* molecular imaging was performed with PET/CT to observe matrix metalloproteinase increase (PET) and corresponding bone formation changes (CT) at different time points after BMP induction (195). Such a method could be employed in monitoring the success of tissue engineered constructs that utilise ECM biology to improve engraftment.

However, there are some caveats: computing power and storage space required to collate and analyse the data obtained using these emerging methods is immense, even by today's standards in information technology. The cumulative cost of equipment is considerable. These issues need to be addressed as it limits researchers' access to these methods. Despite these problems, it can be seen that by combining complementary imaging techniques with improving chemical tools for biomolecular imaging such as nanoparticle agents and labelled antibodies or antibody fragments (196), information regarding chemical and morphological changes caused by biodegradation, the extent of osseointegration of the implant, amongst others, can be gathered whilst allowing for information obtained from *in vitro* experiments to be used to optimise (and shorten) future experiment methods, in addition to aiding with the interpretation and correlation of data obtained during *in vivo* experiments. Furthermore, the ability to obtain *in vivo* real-time data will better inform our understanding of the physiological and biochemical processes involved in healing, inflammation, angiogenesis, and construct integration. These evolving techniques are already in research and clinical use (182, 197, 198), thus providing a consistent and standardised method for analysing and monitoring the long-term outcome of implanted tissue engineered constructs, which would in turn, reduce the numbers of animals used in *in vivo* studies.

1.8 Conclusions

Bone plays many key physiological and functional roles. Over the past 60 years, an improved understanding of bone biology, physiology, and pathology has contributed to the development of current treatments for bone disorders. The rising need for more effective therapeutic approaches has sparked research into the development of tissue regenerative strategies that could be potentially adapted to each patient's requirements. Bone tissue engineering involves a multi-disciplinary approach, by combining (stem) cell biology, drug design, material sciences, and engineering to (ideally) generate functional constructs for use in bone repair. However, bone tissue engineering has yet to achieve full clinical translation as a consequence of several reasons. Current knowledge of bone development and repair, as well as within these allied fields, remain limited. Furthermore, there is often a discrepancy between *in vitro*, *in vivo*, and cross-species experimental outcomes. Conflicting reported results, which stem from a lack of standardisation of methods and analysis approaches, add to the complication. Resolving these issues would certainly help to improve the odds for success.

Advances in bone tissue engineering is clearly dependent on advances within each allied field. For such advances to occur, improvements to existing technology for culturing, real-time monitoring, analysing, and manufacturing are necessary. Recent advancements in imaging and information technology have enabled more frequent and accurate data collection, analysis and simulation, thus aiding better correlation between *in vitro* and *in vivo* studies. Improvements in manufacturing could be achieved by AM techniques. AM is seen as a potential means for manufacturing clinically relevant-sized constructs with high resolution, reproducibility, and functionality. AM techniques are already capable of producing three-dimensional models of reconstructed three-dimensional objects generated from two-dimensional scans (obtained by imaging techniques such as µCT). This function has been instrumental in improving implant generation, and has been recently used by surgeons in pre-operative practice for, and during, reconstructive surgeries to achieve better apposition of implants. Over the past ten years, researchers have begun preliminary investigations into the most suitable AM techniques for integrating biomaterials, cells, and/or osteoinductive factors, in order to create an integrated construct for bone repair that could be studied *in vitro* and *in vivo*. There is increasing interest in this approach, which has been termed as 'bone biofabrication'. Such constructs could provide higher quality, dynamic information

regarding cytocompatibility, osteoinductivity, biodegradability, and mechanical functionality at a macroscopic as well as microscopic level. Additionally, AM techniques can be used to build bioreactors, which can simulate *in vivo* conditions and provide valuable real-time data that can facilitate better construct design as well as reduce the need for animal testing at an early stage of the design process. However, limitations that have plagued tissue engineers for the past fifty years still apply to bone biofabrication. Achieving vascularisation of a large construct remains the primary stumbling block at present. The ideal design of the construct, the choice of the most appropriate cell type for bone tissue regeneration, and the optimal combination of stimulatory factors not only influence the type of AM used, but also remain some of the crucial steps to resolve if successful clinical translation of bone biofabrication is to become a reality in the near future.

1.9 Hypothesis

Given the potential of bone biofabrication, the hypotheses of this thesis are:

1) Human STRO-1 enriched BMSCs possess, and retain, the capacity for osteogenesis when seeded onto scaffolds, and are therefore a suitable cell type for use in bone reparation.

2) Biomaterials can be combined to generate tuneable bioinks, which can be used to deliver STRO-1 enriched BMSCs with high viability and functionality.

3) 3D printing methods are capable of manufacturing porous scaffolds of clinically relevant size with high resolution and reproducibility.

4) STRO-1 enriched BMSCs, biomimetic bioinks, and 3D printed polycaprolactone-based scaffolds can be combined to create an integrated bioconstruct for use in bone repair.

1.10 Aims and Objectives

In conjunction with the above hypotheses, the aims of this research project are:

1) To confirm the osteogenic potential of STRO-1 enriched BMSCs.

2) To elucidate the osteoinductive capabilities of established biomaterials, such as titanium and polycaprolactone (amongst others), in order to identify potential combinations for the generation of composite scaffolds and/or bioinks for use in bone tissue engineering.

3) To design novel porous scaffolds that mimic natural bone architecture.

4) To investigate the feasibility of utilising 3D printing techniques to accurately and reproducibly manufacture scaffolds according to their design.

5) To determine the possibility of 3D printing cell-laden bioinks.

6) To develop methods for integrating 3D printed scaffolds, biomimetic bioinks, and STRO-1 enriched BMSCs, with the objective of creating functional bioconstructs for use in bone reparation.

Chapter 2: General Materials and Methods

2.1 General reagents

Non-sterile 10% Phosphate Buffered Saline (PBS) was made by adding ten PBS tablets (Oxoid, UK) to 1 l of water. 100 ml of this stock solution was diluted with 900 ml of water to obtain 1x PBS.

Basal media for STRO-1 enriched BMSC culture comprised of serum-free Minimum Essential Medium Eagle, alpha modified, with deoxyribonucleotides, ribonucleotides and UltraGlutamine 1 (αMEM) (Lonza, Switzerland) containing 10% foetal calf serum (FCS) (Thermo Fisher Scientific, USA) and 1% penicillin (10000 units), streptomycin (10 mg/ml) (PS) (Lonza, Switzerland).

Osteogenic media used for all experiments involving STRO-1 enriched BMSC culture consisted of basal media with 100 µM ascorbic acid-2-phosphate and 25 nM 1,25-VitD3 (all Sigma Aldrich, UK).

Culture media used for culturing the human osteosarcoma cell line, MG63 (including GFP-transfected human MG63 cell lines) consisted of Dulbecco's Modified Eagle's Medium with 4.5 g/l glucose and L-Glutamine (DMEM) (Lonza, Switzerland) with added 10% FCS and 1% PS. All media were kept at 4°C and warmed up to 37°C in a water bath prior to use.

Unless stated otherwise, cell fixation was performed using 4% paraformaldehyde (PFA), which was made by adding 200 ml of 10% PBS to 8 g of PFA powder (ACROS Organics, USA) in a fume hood. The mixture is magnetically stirred at 50 to 60°C for 30 to 60 minutes until the turbidity is reduced. The pH of the solution is adjusted to 7.4 by the drop-wise addition of 10 M sodium hydroxide solution, at which point the solution becomes clear.

Simulated body fluid (SBF) was made following the protocol published by Bayraktar and Tas (199). The following reagents were added stepwise, and under continuous stirring at 37°C, to deionised water in a clean glass bottle: 6.82 mg/ml sodium chloride (Sigma Aldrich, UK), 2.36 mg sodium hydrogen carbonate, 0.389 mg/ml potassium chloride, 0.148 mg/ml sodium hydrogen phosphate dihydrate, 0.318 mg/ml magnesium chloride hexahydrate, 9.4 µl of 1 M hydrochloric acid (Sigma Aldrich, UK), 0.383 mg/ml calcium chloride dihydrate, 0.074 mg/ml sodium sulphate, and 6.309 mg/ml Trizma® base (both Sigma Aldrich, UK). The pH of the turbid solution was adjusted by adding hydrochloric acid until the pH reached 7.39 ±

0.02 at 37°C (upon which the solution becomes clear). The volume of the solution was measured and topped up with deionised water to make a final volume, which was kept at 4°C for a maximum of one month. All reagents used were from BDH Laboratory Supplies, UK, unless stated otherwise. This method was chosen instead of the protocol by Kokubo and Takadama (200) as it more closely mimics the composition of human blood plasma, with a higher bicarbonate ion concentration of 27 mM (compared to 4.2 mM), and a lower chloride ion concentration of 125 mM (compared to 148 mM).

2.2 MG63 cell culture and passage

The human osteosarcoma cell line, MG63, was used in cell viability experiments, as a comparator cell source (and therefore, control) to STRO-1 positive BMSCs. MG63 cells were selected for their osteogenic behaviour and their strong STRO-1 expression (201), in addition to the defined, consistent characteristics that a cell line imbues. Cultures were derived from in-house stocks stored in liquid nitrogen. The thawed mixture was centrifuged at 11000x *g* for 5 minutes at 18°C and the resulting pellet was re-suspended in DMEM containing 10% FCS and 1% PS. Cell count was performed using the Fast-Read 102® disposable counting slide (Dutscher Scientific, UK). Briefly, each counting chamber consists of ten 4 x 4 grids, with each chamber volume being 37 µl. 25 µl of re-suspended cells was transferred into a counting chamber. Cell count per ml is given by:

$$\frac{\text{Total count}}{\text{Number of complete 4x4 grids counted}} \times 10^4 \times \text{sample dilution (if any)}$$

The cell suspension was transferred into a 75cm^2 Corning® flask for culture at 37°C, 5% CO_2 in a humidified incubator. Media was changed every three to four days. Cells were passaged at 70 to 80% confluency through a 10 minute long incubation with trypsin (0.5 g/l) (Lonza, Switzerland) and ethylenediamine tetraacetic acid (EDTA) (0.2 g/l) solution (Sigma Aldrich, UK) followed by neutralisation with an equivalent volume of DMEM containing 10% FCS and 1% PS. The mixture was centrifuged at 11000x *g* for 5 minutes at 18°C and the resulting pellet was re-suspended in an appropriate volume for further cell culture or experiment. Green fluorescent protein (GFP)-labelled MG63 were cultured and passaged in the manner described above. Unless stated otherwise, all procedures requiring sterile conditions were performed in a Class II Biological Safety Cabinet

(NuAire, UK). Organic materials were disposed of in 1% Rely+On™ Virkon® solution (DuPont, USA) at the end of experiments.

2.3 Biofabrication using the 3DDiscovery bioprinter

The 3DDiscovery bioprinter (regenHU Ltd, Switzerland) is a commercial 3D bioprinting platform built for research use, particularly for the purposes of tissue engineering. A customised version was purchased by Taipei Medical University in September 2015.

2.3.1 The 3DDiscovery bioprinter

The 3DDiscovery is a robotic dispensing system that consists of a three-axis positioning system with a tool changer, comprising of three different printheads, and a building platform (Figure 2-1). The first printhead is the DD-135N printhead, a contact needle dispensing system that allows time-pressure dispensing of a high viscosity bioink from a cartridge. The second is the CF-300H printhead which is microvalve-based and is used to dispense low to medium viscosity media. It can function either as an electromagnetic inkjet or as a contact needle dispensing system that is capable of precision cell printing. This is also particularly useful in controlling the printing of low viscosity materials, allowing for the accurate printing of microscale structures. Attached bioink cartridges can be kept at a fixed temperature during the printing process. Adjusting the valve opening time (minimum 100 µs) also regulates the volume of material printed. The third is the HM-300H printhead that is based on the precision extrusion deposition technique. It enables thermopolymer melt extrusion printing under pressure and temperature control. The biomaterial melts in the liquefier tank and is pressed to the extruder barrier screw by air pressure. Homogeneous melting of the biomaterial is achieved by heating the added material in the liquefier tank for one hour for every 100°C required. A threaded barrier screw within the HM-300H printhead enables controlled dispensing of the melted thermoplastic material under a specific pressure setting. Increasing the turning speed (revolutions) of this screw increases the volume of material extruded. In all cases, changing the feed rate (mm/s) of the material to be dispensed within the accompanying BioCAD software allows the operator to adjust the volume of bioink being dispensed and thus, enables size adjustment of the deposited material. Further manipulations can be achieved by changing the needle diameter of each printhead. The most frequently used needle size for the HM-300H and the CF-300H printheads were the 0.3 mm and 0.18 mm needles respectively.

No needle was attached to the CF-300H printhead when utilising the jetting mode of that printhead. Switching between the printheads allows different materials to be used in the printing of a composite bioconstruct. The bioprinter also possesses an ultraviolet unit that operates at 365 nm wavelength to allow for photopolymerisation of hydrogels. The instrument requires compressed air (between 5 and 10 bars) to power the tool changer in addition to enabling material flow from the cartridges to the printheads. Adjusting the pressure regulators at the top of the instrument results in changes to the pressure applied to the material cartridges or the tank of the extruder. Changing the pressure applied is therefore another way of controlling the volume of material dispensed by each printhead. Accessory stirrer components were purchased in August 2017 which could be attached to the standard syringes to enable constant stirring of bioinks, thereby ensuring bioink homogeneity in addition to minimising the occurrence of cell sedimentation during prolonged printing times. Stirrer speeds could be adjusted manually via a separate control device. A customised cooling device was built for use with the bioprinter, which would allow the temperature of the printing platform to be regulated between -7 and 10°C. Technical specifications of the bioprinter and its printheads are listed in Table 2-1.

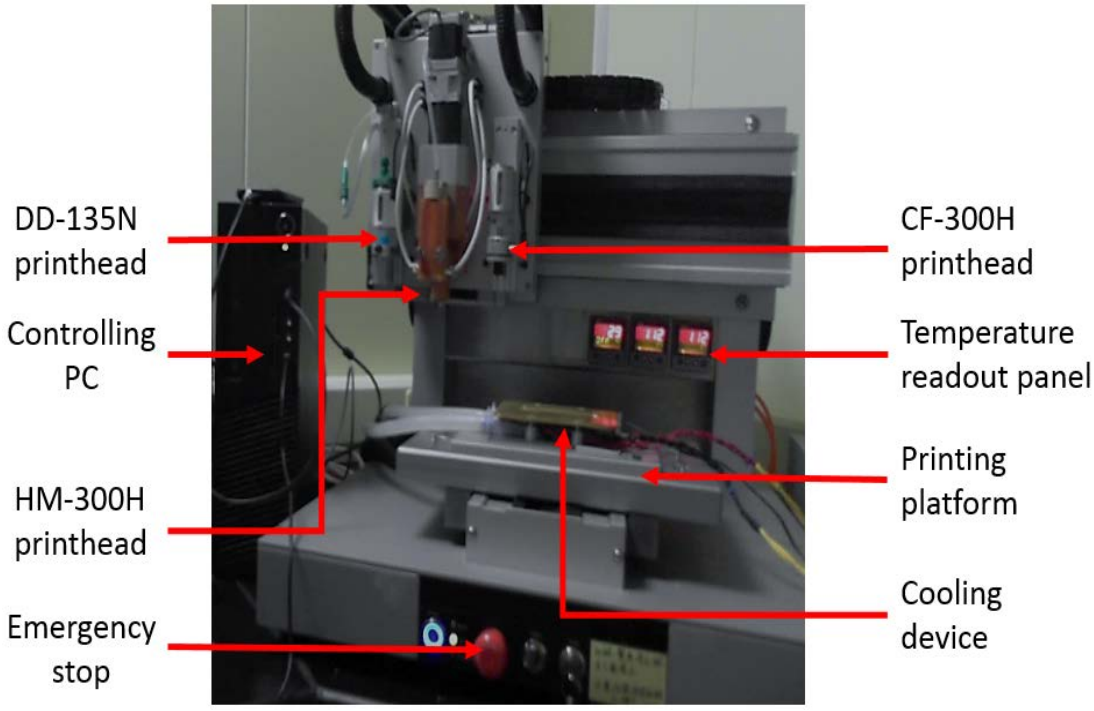

Figure 2-1 3DDiscovery bioprinter with its constituent parts in-situ.

Bioprinter	
• Printable area (Width x Length x Height) • Axis motor resolution • Accuracy per axis • Maximum printing speed • Required input pressure	130 x 90 x 60 mm 2.5 µm < 50 µm 40 mm/sec Minimum 0.5 MPa
DD-135N printhead (Printhead 1)	
• Viscosity range • Fluid storage • Nozzle / Needle diameter • Dispensing mode	50 – 200000 megapascal-second (MPa.s) 3 to 10 cm^3 150 µm to 2 mm Contact needle dispensing
CF-300H printhead (Printhead 2)	
• Viscosity range • Fluid storage • Nozzle / Needle diameter • Heater • Dispensing mode	110 – 1000 MPa.s 3 to 10 cm^3 150 µm, 300 µm Maximum 80°C Electromagnetic jetting / Contact needle dispensing
HM-300H printhead (Printhead 3)	
• Viscosity range • Fluid storage • Nozzle / Needle diameter • Heater • Dispensing mode	Screw design dependent 10 cm^3 tank 180 µm, 330 µm, 410 µm, 510 µm Maximum 250°C. Tank and barrier screw with separate temperature control Contact needle dispensing

Table 2-1 Technical specifications of the bioprinter and associated printheads.

2.3.2 BioCAD

BioCAD is the accompanying customised CAD design software that creates an .iso file (from its generic .bcd format) for printing by the 3DDiscovery bioprinter. This software is unable to import drawing files from other CAD software such as Solidworks or AutoCAD, therefore limiting its cross-compatibility severely. Additionally, its operating licence is specific to the technical specifications of the computer on which the software is installed and each installation of the software requires a separate licence. A second software licence was purchased in June 2016 for use in Southampton.

In brief, to create a new drawing, simply click on the ‘create new’ icon on the drawing toolbar, and then select ‘build new layer’ (Figure 2-2). This defaults to layer 1 and any shape of any size can be built around the centre axis. To print this layer, drag the layer to an assigned level of the design (Figure 2-3). If this layer is not to be printed, then simply fill in the shape with horizontal, vertical or custom

angle lines as layer 2. Assigning the line spacing, choosing whether to strip out the edges of the fill, or to offset the fill lines can be done by clicking on the filling step under the layer 2 tab. Closer inspection of any design can be done by clicking on the 'zoom area' icon, and the drawing will be re-sized. Changing shapes or size is also possible by drawing a new layer and adding it to a level or group. Different materials can be assigned for each layer, along with adjustment of their feed rate (mm/s), layer thickness (mm) and the choice of printhead to print the material. Assigning these properties to a material is done under the 'Tools' tab → 'Materials'.

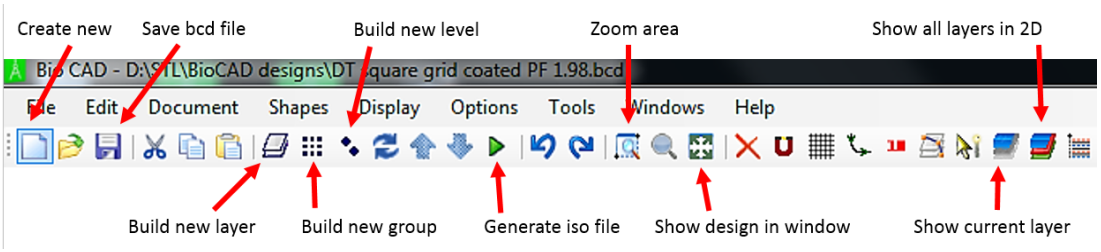

Figure 2-2 Outlined functions of the drawing toolbar of the BioCAD software.

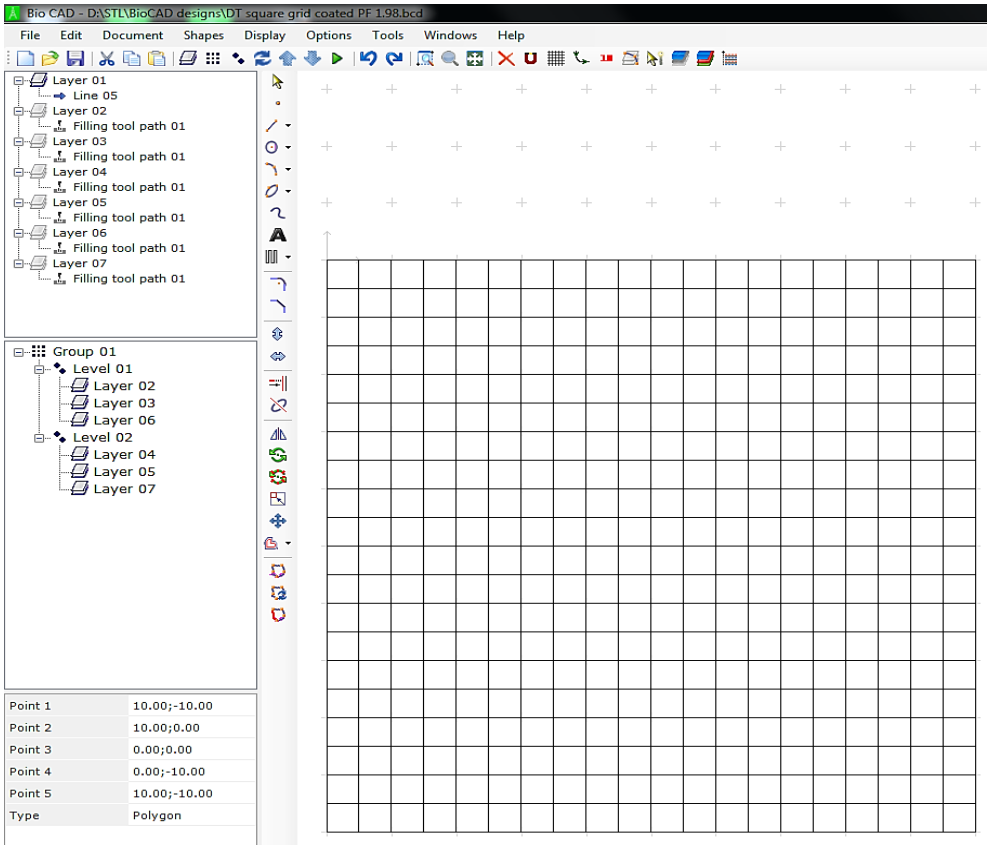

Figure 2-3 Designing a bioconstruct.

A completed square 10 x 10 x 0.96 mm design in BioCAD, showing the assigned layers, levels, and groups in the building of a bioconstruct.

Groups are essentially a combination of levels (and therefore layers) that can be printed repeatedly until a build height is reached. So, if a layer is 0.16 mm high, and each level is made up of 4 different design layers, then group 1 is 0.64 mm tall. If the building height is then adjusted to 1.92 mm, then the printer will repeat the group design three times to finish printing the final construct. As such, adjusting the groups will enable the printing of different layouts or designs into one final bioconstruct. Checking the design of the bioconstruct is only possible in two dimensions by clicking on the 'show all layers' icon on the drawing toolbar. Checking the current layer design can be done by clicking on 'show current layer' icon, which will remove all the other layers from view. Once the design is completed, the drawing can be saved in the .bcd format by clicking on the 'save file' icon and the corresponding .iso file can be created by clicking on the 'generate' icon. A major limitation of the generic .bcd format is that the file type can only be opened in BioCAD. Any changes to the file (and therefore, the .iso file) can only be saved if the BioCAD software is a licenced (and most current) version.

2.3.3 3DDiscovery HMI software

The HMI software can only be operated when the 3DDiscovery printer is switched on and 'ready'. The generated .iso file for printing is loaded onto the software and appears in G-code (far left window, Figure 2-4). The printer will only function if there is sufficient pneumatic pressure to the printer, which is provided by a connected pressure pump.

Figure 2-4 3DDiscovery HMI interface.

The software allows for the adjustment of printing parameters and printhead settings for bioprinting different materials and designs.

Needle length calibration for each printhead is performed prior to adjustment of the individual settings for printing. This is an automated process using a laser calibration method. The needle tip for each printhead can be adjusted for the appropriate printing distance (z-axis). Individual cartridge pressures can be switched on and off, in addition to adjusting the individual printheads feed rate of the material in use, the temperature of the material (only for printheads 2 and 3). Other specific parameters for each printhead (Figure 2-4) can also be adjusted within the software prior to printing to optimise bioink output and reduce the thickness of the fibre printed. There is no capability for volume measurement or calculation, which is a limitation of the software. The software is also unable to provide an estimated time for completion of printing of a sample, which makes it difficult to estimate the time required to complete printing enough bioconstruct replicas for an experiment.

2.3.4 MM Converter

The MM Converter software comes as a separate licenced software for use with the 3DDiscovery printer (Figure 2-5) and can be used to convert a saved 3D image from a 3D laser scanner or 3D-CT scan into an STL format, from which the 3DDiscovery can print out a replica (which can be re-sized by adjusting the ratio of the loaded object), but only using a single material to do so, and in a pre-set printing pattern (which is based on efficiency), thereby limiting its usefulness. MM Converter can import .pdf and .dwxf file formats, but only if these files contain ‘sufficient’ information saved into the meta-data. This results in larger file sizes for either file format, negating the original function of such file formats, which was to allow easy data portability, and without crucial data loss from compression.

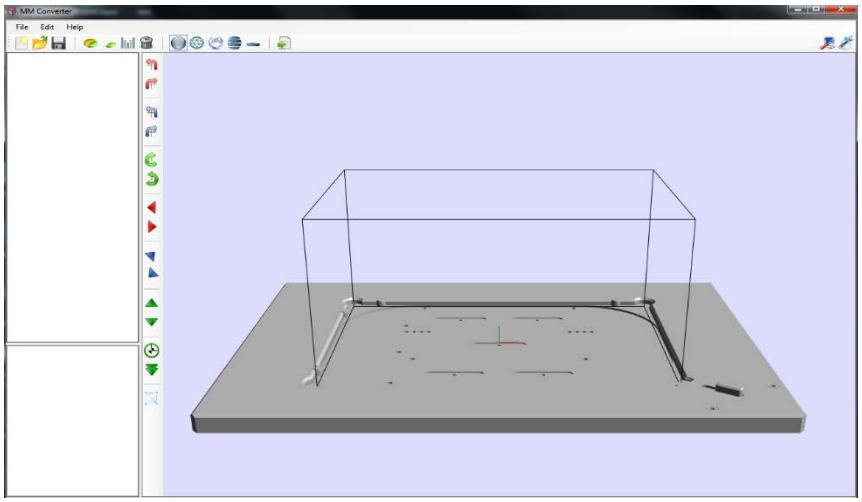

Figure 2-5 MM Converter interface for printing 3D replicas of scanned objects.

2.4 3D printed devices

2.4.1 Suspension/fixation well insert device

To simultaneously seed the 90 µm pore and 9 µm pore surfaces of titanium templates, the template had to be suspended within a well while remaining submerged beneath a sufficient volume of culture medium per well. No vendor could be found selling such a device. The closest matching device is the Alvetex Scaffold well insert made by ReproCELL Europe Ltd. However, the central filter membrane competes with the under-surface of the titanium template for cell adhesion. To resolve this problem, a suspension/fixation well insert device was designed using Solidworks 2015 (Dassault Systemes, France). A hollow cylinder 20 by 4 by 8 mm (width, thickness, height) was initially created, from which four supporting extrusions 2.5 mm thick and 3.5 mm long (and equidistant from each other) were added to the interior of the hollow cylinder. The centre-point of these extrusions was designed to be 4.5 mm from the base of the device. These circular extrusions were chamfered to create flat upper surfaces, which serve as a levelled support for the suspension of appropriate sized scaffolds. Four rectangular spaces (again equidistant from each other), each 4 by 4 by 5 mm in size, were cut from the areas between these extrusions with the aim of enabling culture media changes to be performed easily with minimal disruption to, and without manipulation of, the suspended or fixed 3D scaffold (Figure 2-6). The CAD design was converted to an STL format and 3D printing of the well insert device was performed using a Stratasys Objet Evo260V 3D-printer (Stratasys Ltd., USA). Adjusting the ratio of the dimensions within the accompanying printer software allows for re-sizing of the well insert device to engineer a good fit of the device for the well size of any tissue culture plate.

The bioprinter utilises a biocompatible PolyJet photopolymer (MED610) which is a colourless, odourless bioacrylic compound to produce the device. The support material (SUP705) is a gel-like photopolymer that encases, as well as fills in any spaces, during the printing of the device. The printed device was soaked in a 1 M sodium hydroxide solution overnight to completely remove the support material. The devices were thoroughly washed in running water and sterilised under UV light overnight in a microbiological safety cabinet. The MED610 material used to manufacture the device withstands autoclave temperatures of 123°C, allowing the device to be cleaned and re-used in future experiments. Furthermore, the design also allows for the fixation, and 3D culture, of a scaffold that floats within a well (Figure 2-7).

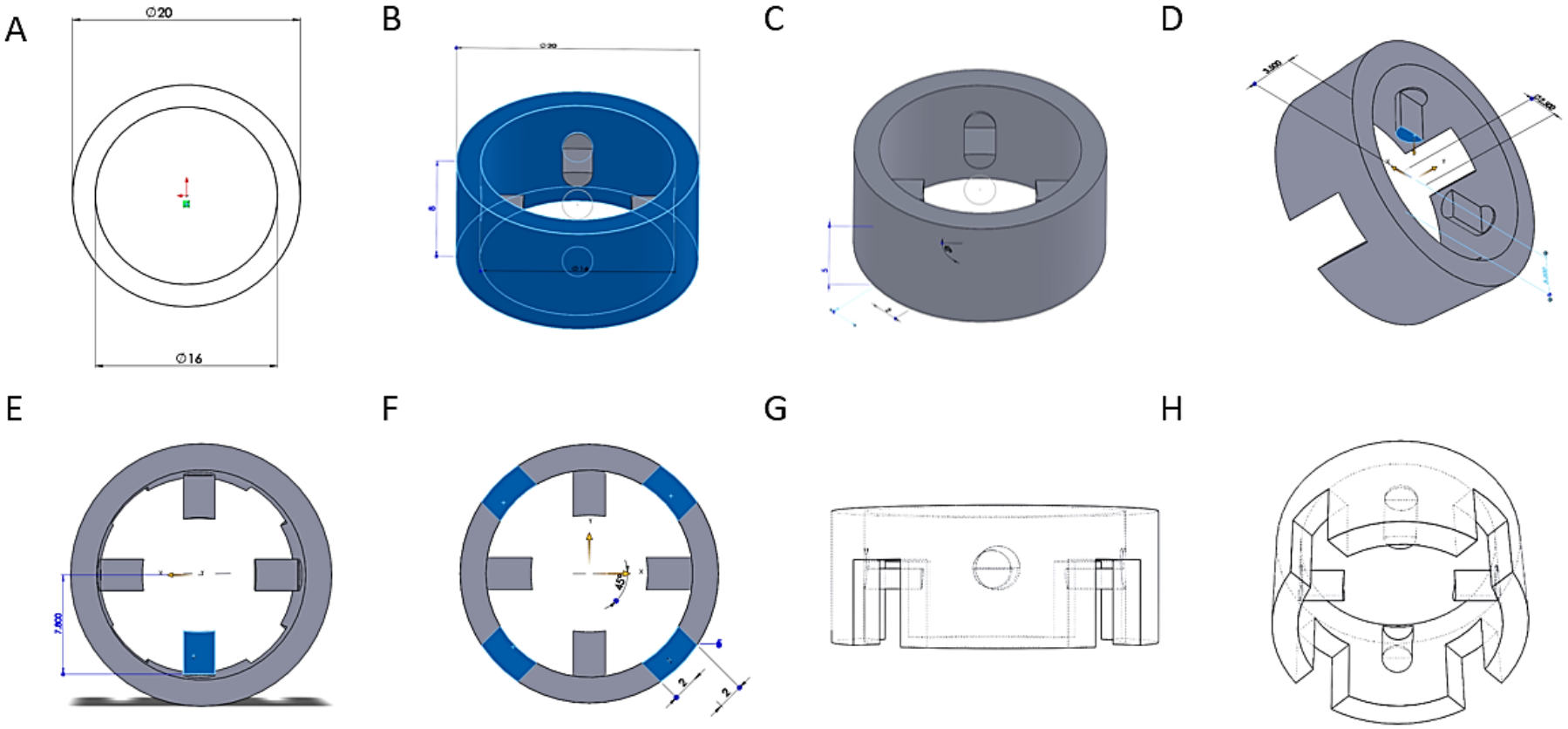

Figure 2-6 Design process of the well insert device.

A to D: Dimensions (in mm) ascribed during the design process using Solidworks 2015 for the creation of a well insert device that fits into a well of a 12-well plate. E to H: Superior, inferior, sagittal, and oblique views of the finished design as drawn in Solidworks 2015. (Copyright © Daniel Kee Oon Tang, March 2015)

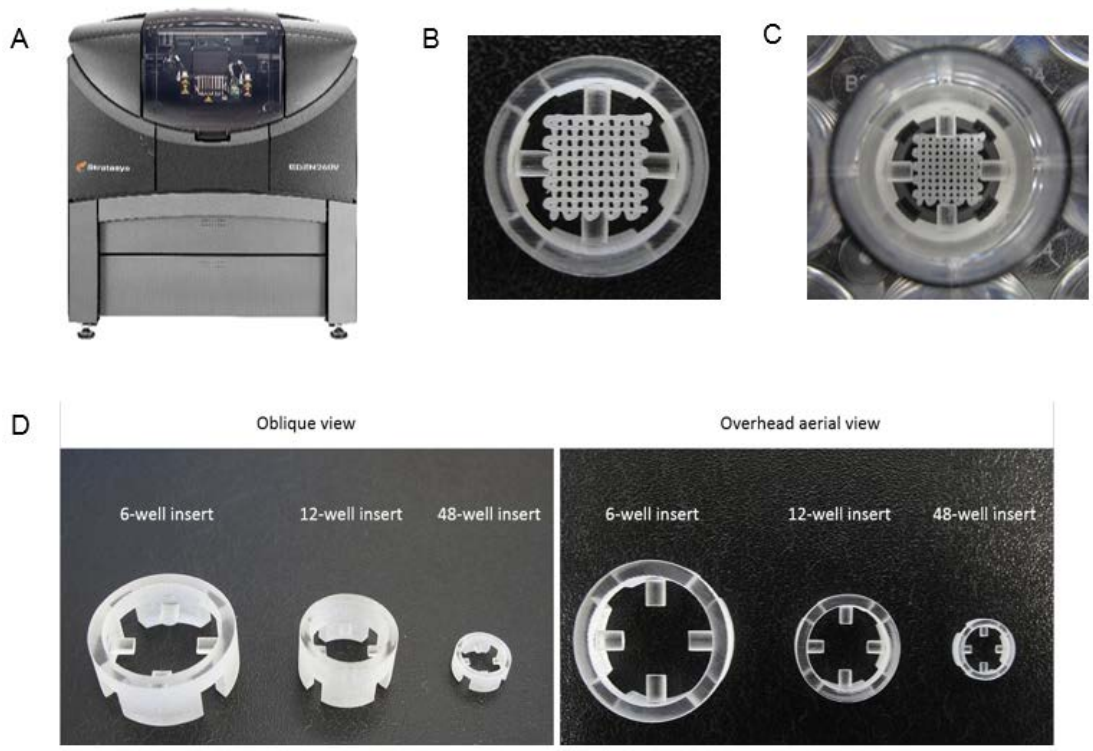

Figure 2-7 3D printed well insert devices.

A) The Stratasys Objet Evo260V bioprinter is capable of 20 µm accuracy and prints photopolymerisable biomaterials. B) Overhead view of a well insert device used to suspend a 10 x 10 x 1 mm 3D printed PCL scaffold. C) Overhead view photograph of a well insert device used to keep the same scaffold submerged within the well of a 12-well plate. D) Oblique (left) and overhead (right) views of different sized 3D printed well insert devices. (Copyright © Daniel Kee Oon Tang, 2015)

2.4.2 Customised hydrogel mould device

In order to reproducibly generate hydrogels of a particular size without the use of 3D printing techniques, moulds are usually required. Most customised moulds are made from silicon-based materials for their non-stick quality, enabling easy retrieval of the solidified hydrogels. However, such moulds are not normally sold by scientific equipment suppliers. As such, Solidworks 2015 was used to design a 3D printed hydrogel mould device for use in experiments conducted in 4.1.

The 3D printed hydrogel mould comprises of three interlocking components, which when combined in a set order, can be used to generate the hydrogels (Figure 2-8, Figure 2-9, Figure 2-10). The formed hydrogels are removed from the mould component (Figure 2-9) by utilising an extruder device (see Figure 2-11). The base component measured 35 by 35 by 6 mm in size. A raised edge for interlocking

with the cover component was generated from the inner face of the base component by extruding a 2 mm thick square that was 30.5 by 30.5 mm in size. A 2.5 mm wide by 3 mm deep square gap was cut within the inner face for interlocking the mould component to the base, thereby providing a directly apposed surface, which prevents gel leakage from the mould columns (Figure 2-8). The upper surface of the mould component measured 24 by 24 by 2 mm in size. A 23 mm square 1 mm thick and 3 mm in height was extruded from the upper surface to form the undersurface of the mould component. Nine cylindrical spaces, each measuring 5 mm in diameter and 2 mm deep and set 3 mm apart from each other, were cut from the upper surface. Two 12 by 6 by 1 mm rectangular structures were extruded from the upper surface to create two handles for removing the mould component from the base component easily. These extruded structures fit into spaces designed in the cover component, while helping with unlocking the cover from the base (Figure 2-9).

The cover component measured 35 by 35 by 6 mm in size. A 31 mm-sized square 3 mm thick and 4 mm deep was cut into the inner surface of the cover component. A 25 mm-sized square 3 mm thick and 3.5 mm deep was also cut from the centre of the inner surface to generate an apposing surface for the mould component. Two gaps measuring 12 by 2 by 5.5 mm were then cut from this central square on the inner surface of the cover component for the extruded handles of the mould component to fit (Figure 2-10). The extruder device measured 25 by 25 by 6 mm in size. A 23.5 mm-sized square gap 2.5 mm thick and 3.5 mm deep was cut from the upper surface of the device. Nine corresponding cylindrical columns measuring 4.5 mm in diameter and 3 mm in height were extruded from the upper surface of the device. These columns were designed to be of greater height than the cylindrical spaces in the mould component so as to enable the retrieval of the formed hydrogels (Figure 2-11). These CAD designs were converted to an STL format and 3D printing of the components for the hydrogel mould and the extruder devices were performed using a Stratasys Objet Evo260V 3D-printer (Stratasys Ltd., USA). Adjusting the ratio of the dimensions within the accompanying printer software allowed for re-sizing of the devices, thereby enabling the creation of different sized hydrogels as required. The printed device was soaked in 1 M sodium hydroxide solution overnight to completely remove the support material. The devices were thoroughly cleaned with a brush under running water and sterilised under UV light overnight in a microbiological safety cabinet prior to use in experiments. The printed devices are shown in Figure 2-12.

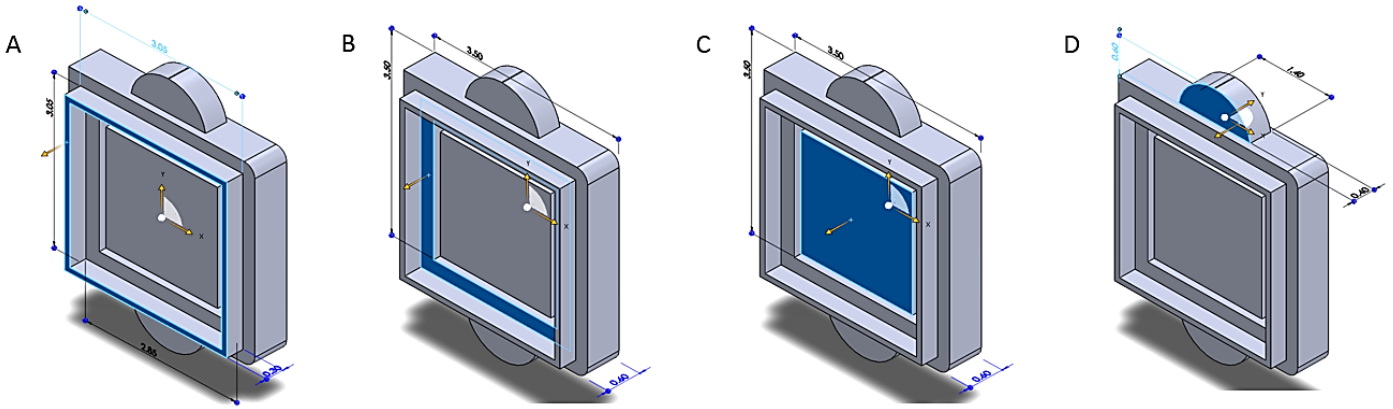

Figure 2-8 Annotated schematic of the design for the base component of the customised hydrogel mould device.

(Copyright © Daniel Kee Oon Tang, 2015)

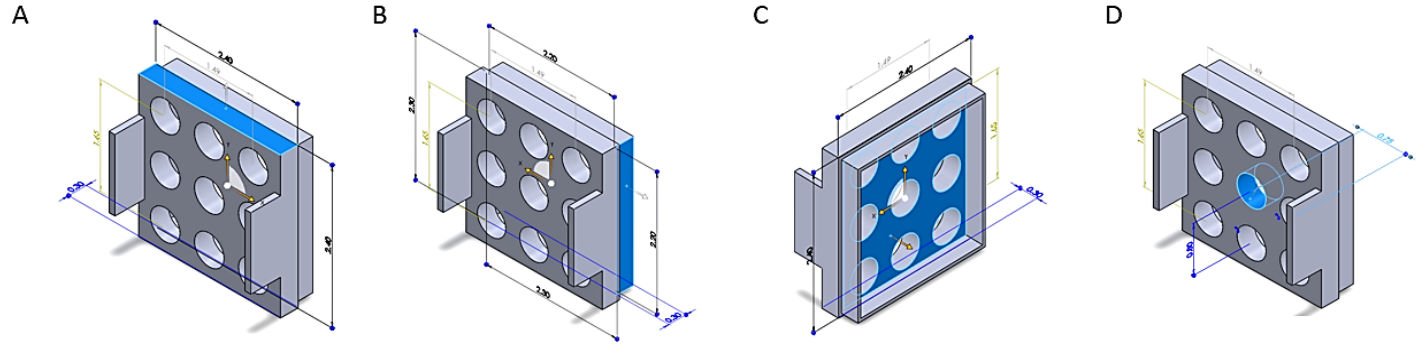

Figure 2-9 Annotated schematic of the design for the mould component of the customised hydrogel mould device.

(Copyright © Daniel Kee Oon Tang, 2015)

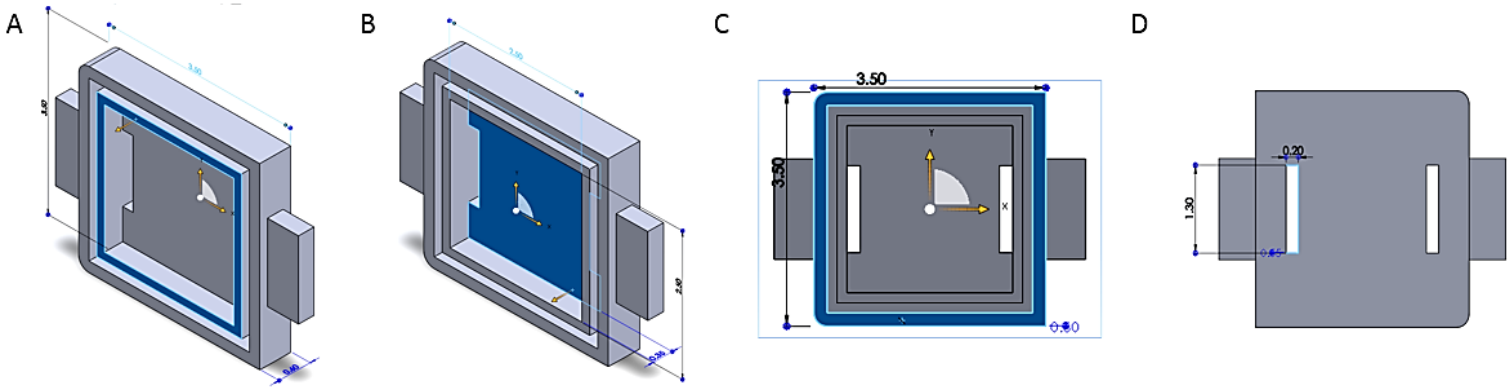

Figure 2-10 Annotated schematic of the design for the cover component of the customised hydrogel mould device.

(Copyright © Daniel Kee Oon Tang, 2015)

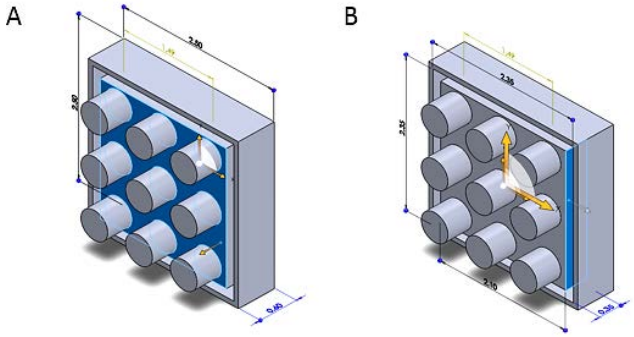

Figure 2-11 Annotated schematic of the design for the extruder device.

(Copyright © Daniel Kee Oon Tang, 2015)

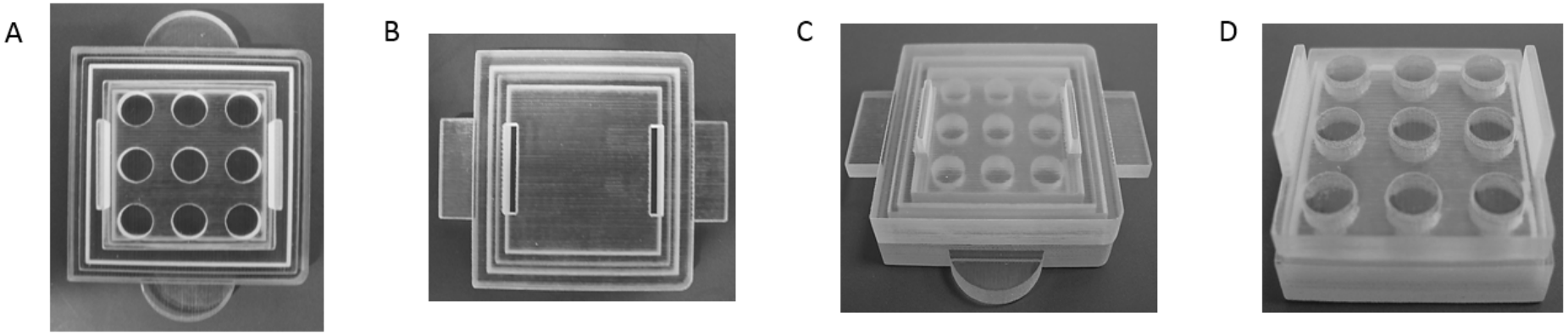

Figure 2-12 Photographs of the interlocking components of the customised hydrogel mould device.

The individual components were designed to interlock to form the device. A) Overview image of the 3D printed mould component combined onto the 3D printed base component. B) Overview image of the 3D printed cover component. C) The 3D printed base, mould, and cover components were combined to form a customised hydrogel mould device. D) The 3D printed mould component was applied to the 3D printed extruder device to enable the formed hydrogel discs to be retrieved from the mould component, generating up to nine 5 mm by 2 mm hydrogel discs per device. The wing elements on each component allow for easy orientation and handling during the combination as well as separation of the various components (Copyright © Daniel Kee Oon Tang, 2015).

2.5 Molecular assessment methods

2.5.1 Ribonucleic acid (RNA) isolation

Prior to quantitative reverse transcription polymerase chain reaction or RT-qPCR, RNA must first be isolated from cell culture or tissue lysates and reverse transcribed into complementary deoxyribonucleic acid (cDNA). The method used was derived from a published protocol by Lee *et al* (202).Cell lysis was performed by incubation with TRIzol® (Thermo Fisher Scientific, USA) for 20 minutes at room temperature, with intermittent trituration using an RNase/DNase-free pipette. To maximise the lysis process, an additional step involving two freeze-thaw cycles was necessary for seeded scaffolds that were larger than 1 cm^3. Cell lysates were stored in -80°C if RNA extraction was not to be performed immediately.

RNA was extracted from cell lysates by adding 200 µl of chloroform (Sigma Aldrich, UK) to every 1 ml of TRIzol® per sample in a fume hood. The mixtures were vortexed for 1 minute to ensure adequate mixing before incubating them for 3 minutes at room temperature. The mixtures were then centrifuged at 11000x *g* for 15 minutes at 4°C in a Heraeus Biofuge fresco centrifuge (Thermo Fisher Scientific, USA). The clear aqueous phase obtained per mixture was then transferred to an ISOLATE II filter column, a part of the ISOLATE II RNA Mini Kit (Bioline, UK), unless stated otherwise. RNA extraction was then performed as per the manufacturers' recommendations. $A_{260/280}$, $A_{260/230}$, and RNA concentrations, in ng per µl, were quantified using a NanoDrop spectrophotometer (Thermo Fisher Scientific, USA) and its accompanying ND-1000 software. 1.2 µl of each sample was used for each reading performed.

2.5.2 Reverse Transcription

SuperScript VILO™ cDNA synthesis kit (Thermo Fisher Scientific, USA) was used to prepare cDNA in 10 µl reaction volumes containing 100 ng of RNA, as per the manufacturers' guidelines. All reagents and RNA samples were kept on ice prior to reactions being run on a ABI Veriti 96-well Thermal Cycler (Thermo Fisher Scientific, USA), at 25°C for 10 minutes, followed by 42°C for 120 minutes, and then 85°C for 5 minutes, with the program terminating at 4°C. cDNA samples were diluted with 20 µl of ultrapure water prior to storage at -20°C.

2.5.3 Quantitative Reverse Transcription Polymerase Chain Reaction

To generate a triplicate for each gene-sample of interest, 15 µl of Power SYBR® Green PCR Master Mix (Thermo Fisher Scientific, USA) was added to an Eppendorf tube containing a mixture of 3 µl of forward primer at 5 µM concentration, 3 µl of reverse primer at 5 µM concentration, 6 µl of ultrapure water, and 3.3 µl of cDNA. Similar triplicates were made for each gene marker expression to be tested, including the housekeeping gene. 10 µl per triplicate volume was pipetted into an assigned well of a 96-well PCR plate (StarLab, UK). This step was repeated until all samples were added. Negative controls for each gene (consisting of the above mixture minus the addition of cDNA) were also plated to determine if self-dimerisation of primers occurred during the process. Prior to sealing the PCR plate with a StarSeal SealingTape Polyoletin Film 100 (StarLab, UK), bubbles within each well were removed using separate needles.

The sealed plate was placed in a MPS1000 plate spinner (Labnet International, Inc., USA) for 30 seconds prior to transfer to the 7500 Real Time PCR system (Thermo Fisher Scientific, USA) for RT-qPCR. Reactions were set up within the accompanying 7500 software (version 2.05), with the holding stage set at 50°C for 120 seconds, followed by the initial denaturation step at 95°C for 10 minutes. The cycling stage was set for 40 cycles at 95°C for 15 seconds and then at 60°C for 60 seconds. Melt curve analysis was conducted after completion of the cycling stage, set at 95°C for 15 seconds, followed by 60°C for 60 seconds, 95°C for 30 seconds and finally 60°C for 15 seconds, to detect the presence of single nucleotide polymorphisms, and if present, whether the dissociation patterns produced indicated the presence of homozygous wildtype, homozygous or heterozygous mutant alleles.

On completion, the threshold value for each gene was adjusted to 0.2 to enable the calculation of ΔCt, ΔΔCt and the relative gene expression ($2^{-\Delta\Delta Ct}$) values, as per Livak and Schmittgen (203). Unless otherwise stated, expression of osteogenic gene markers Runx2, Col1a1, ALP, OPN, and OCN were compared to that of β–actin, which acted as the housekeeping gene. Forward and reverse primers used were purchased from Sigma Aldrich, UK, and are listed in Table 2-2. All materials prior to use were thawed and kept on ice.

Gene marker	Gene-specific primer sequence		T_m (°C)	NCBI Reference Sequence
	Forward	*Reverse*		
β-actin	*GGCATCCTCACCCTGAAGTA*	*AGGTGTGGTGCCAGATTTTC*	58	NM_001101.3
TBP	*TGCACAGGAGCCAAGAGTGAA*	*CACATCACAGCTCCCCACCA*	62	NM_003194.4
Runx2	*GTAGATGGACCTCGGGAACC*	*GAGGCGGTCAGAGAACAAAC*	59	XM_011514966.2
Col1a1	*GAGTGCTGTCCCGTCTGC*	*TTTCTTGGTCGGTGGGTG*	59	XM_005257059.4
ALP	*GGAACTCCTGACCCTTGACC*	*TCCTGTTCAGCTCGTACTGC*	60	NM_000478.5
OCN	*AAGAGACCCAGGCGCTACCT*	*AACTCGTCACAGTCCGGATTG*	62	NM_199173.5
OPN	*GTTTCGCAGACCTGACATCC*	*CATTCAACTCCTCGCTTTCC*	58	NM_001251830.1

Table 2-2 Primers used for RT-qPCR (designed by May De Andres Gonzalez).

Sequences were confirmed using Primer-BLAST (http://www.ncbi.nlm.nih.gov/tools/primer-blast).

2.6 Immunofluorescence staining

2.6.1 CellTracker™ Green and Ethidium homodimer-1

CellTracker™ Green (5-chloromethylfluorescein diacetate, excitation wavelength 492nm, emission wavelength 517nm) is used to identify metabolically active cells. The 50 µg aliquots were stored at -20°C. Ethidium homodimer-1 (excitation wavelength 568nm, emission wavelength 580-620nm) labels membrane damaged cells, and aliquots of a stock concentration of 1 mg/ml were kept at -20°C. Both were obtained from Thermo Fisher Scientific, USA. 10 µl of dimethyl sulfoxide (DMSO) was added to a 50 µg aliquot of CellTracker™ Green. This mixture, along with 25 µl of the stock solution of ethidium homodimer-1, were added to 4.965 ml of basal (or osteogenic) medium. Medium per well was completely removed prior to adding an appropriate volume of the mixture to each well, ensuring that each sample was submerged. After incubation at 37°C, 5% CO_2 for 60 minutes, this mixture was removed and replaced with basal (or osteogenic) medium and returned to the humidified incubator for a further 45 minutes. Samples were then washed in 1x PBS and fixed in a sufficient volume of cold 95% ethanol for 5 minutes. The samples were washed twice in 1x PBS prior to immediate visualisation using a Zeiss Axiovert 200 microscope with FITC (fluorescein isothiocyanate) and TRITC (tetramethylrhodamine) filters.

2.6.2 PKH-26 (Red) Fluorescent Cell Linker dye

PKH-26 (Red) Fluorescent Cell Linker kit for general cell membrane labelling (excitation wavelength 551nm, emission wavelength 567nm) was obtained from Sigma Aldrich, UK, as part of a mini-kit, and stored at 4°C. This approach incorporates ref fluorescent reporter molecules into the cell membrane, and as labelled cells retain biological and proliferative activity, it enables long-term *in vitro* and *in vivo* tracking (the half-life for the latter is greater than 100 days). Following cell passage as described in 2.2, the cell pellet obtained was re-suspended in serum-free αMEM before undergoing centrifugation at 11000x *g* for 5 minutes at 18°C. The supernatant was removed before adding 1 ml of Diluent C to the cell pellet and gently mixing with a pipette to create a 2x cell suspension. Immediately prior to staining, a 2x dye solution was made by combining 4 µl of PKH26 ethanolic dye solution to 1 ml of Diluent C. 1 ml of 2x cell suspension was rapidly mixed with 1 ml of 2x dye solution (in that particular order) and the mixture was incubated for 2 minutes at room temperature. 10 ml of basal medium was added to stop the staining and bind any excess dye remaining. The cells were centrifuged at 11000x *g* for 5 minutes at 18°C. The resultant cell pellet was re-suspended in 10 ml of basal medium and transferred in a new tube before being washed in 10 ml of basal medium twice to ensure removal of any unbound dye. After the final wash, cells were re-suspended in basal medium and a cell count was performed as described in 2.2 prior to use in experiments. Imaging was performed using a Nikon Eclipse T*i* microscope, with a TRITC filter.

2.6.3 Immunocytochemistry: F-actin, vinculin, and nuclear staining

At experiment endpoints, scaffolds seeded with STRO-1 positive BMSCs were fixed in cold 4% PFA for 20 minutes at room temperature. The fixed samples were rinsed twice in wash buffer comprising of 1x PBS and 0.5% Tween-20 (Sigma Aldrich, UK) prior to undergoing a permeabilisation step in which the samples were incubated in 1x PBS containing 0.5% Triton X-100 (Sigma Aldrich, UK) for 20 minutes at room temperature. The samples were then rinsed in wash buffer twice before a blocking buffer consisting of 0.5% Triton X-100 and 5% goat serum (Autogen-Bioclear, UK) in 1x PBS was added to the samples for 60 minutes at room temperature. The blocking buffer was removed and the primary anti-vinculin IgG antibody (part of the FAK100 kit from Merck Millipore, USA) diluted in 1% BSA and 0.5% Triton X-100 in 1x PBS (antibody dilution buffer), 1 in 100 dilution, was added to each sample and left sealed overnight at 4°C in the dark. Samples were rinsed

thrice with wash buffer the next morning before a 1 in 100 dilution of a secondary IgG goat anti-mouse (H+L) antibody (Merck Millipore, USA), in addition to a 1 in 40 dilution of TRITC-conjugated phalloidin (part of the FAK100 kit that stains for F-actin) in antibody dilution buffer, were added to each sample and incubated for 90 minutes at room temperature. Following a triple wash buffer rinse, nuclear counterstaining was performed by incubating samples in a 1 in 200 dilution of DAPI (part of the FAK100 kit) in 1x PBS, or a 1 in 100 dilution of 0.1 mg/ml stock solution of Hoechst 33342 (Sigma Aldrich, UK) in 1x PBS, for 10 minutes at room temperature. Samples were rinsed with wash buffer thrice prior to being stored in 1x PBS for visualisation using a fluorescence microscope or confocal light microscope.

2.7 Scanning electron microscopy (SEM)

Specimens to be scanned were fixed in 3% glutaraldehyde and 4% formaldehyde in 0.1 M PIPES buffer (pH 7.2) for 60 minutes and rinsed twice in 0.1 M PIPES buffer (pH 7.2) over 10 minute intervals. Specimens were then placed into holders and underwent dehydration in increasing concentrations of ethanol (30, 50, 70, and 95%) at 10 minute intervals, culminating with a 20 minute incubation in 100% ethanol. All these steps were performed at room temperature.

Specimens were ensured to be completely immersed in fresh 100% ethanol prior to undergoing critical point drying in a Balzers Critical Point Dryer CPD030 (BalTec Maschinenbau AG, Switzerland). These specimens were transferred into an appropriate-sized specimen holder (with sufficient 100% ethanol for immersion), which was placed into a pressure chamber that was cooled to 10°C. Liquid carbon dioxide was allowed into the chamber until liquid carbon dioxide eventually replaced the ethanol immersing the specimens. Specimens remained in the liquid carbon dioxide for one hour to allow infiltration. At a critical temperature of 31°C, and pressure of 73.8 bars, the liquid carbon dioxide converts to its gaseous form. The chamber was gently vented. Once atmospheric pressure was reached, the specimens were removed from the specimen holders.

At this stage, the specimens were mounted onto appropriate stubs (with the surface to be imaged facing upwards) and a 7 µm-thick gold-palladium sputter coating layer was applied to each specimen. Specimens were placed into a vacuum chamber of an FEI Quanta 200 SEM for imaging, unless stated otherwise. All samples imaged remain stored in a closed container kept at room temperature.

2.8 Statistical analysis

Triplicates were performed for each group in an experiment, with all experiments carried out at least twice, unless otherwise stated. All data was presented as mean ± standard deviation, unless otherwise stated. GraphPad Prism 7.0.3 (GraphPad software, La Jolla California USA, www.graphpad.com) and OriginPro 9.0 (OriginLab, Northampton, MA) were used for all statistical analyses. Paired t-test or two-way ANOVA analyses were performed, where appropriate, to determine the statistical significance of the results obtained, with a *p* value less than 0.05 used to indicate a significant result, and a *p* value less than 0.001 used to indicate an extremely significant result. Statistically significant results were indicated by symbols, where possible, within each graph. Summary tables or 95% confidence interval graphs highlighting significant comparisons were used in situations where this was not appropriate. Sample variance, where possible, was also calculated to determine if the variation within a sample group was significant. A *p* value less than 0.05 was used to indicate a significant variation compared to the test variance (which was set at 1).

Chapter 3: The potential of STRO-1 enriched BMSCs for bone repair

In order to successfully treat critically sized bone defects, cell therapy (with an appropriate carrier) is usually required. There has been some preclinical and clinical data supporting the delivery of stem cells (from different sources) to defect sites in order to enhance bone repair [183]. As discussed in 1.6.3.1, selecting the optimum cell source for bone regeneration remains a challenge. Stem cells, in general, are a diverse group of cells that have the capacity for unlimited self-renewal under controlled conditions, and have the potential to differentiate into a variety of specialised cell types.

In the late 1960s, Friedenstein, Owen, and co-workers utilised *in vitro* culture in diffusion chambers, and transplantation into laboratory animals (either subcutaneously or under the renal capsule) of bone marrow derived cells to characterise cells that composed the physical stroma of bone marrow (10). Due to the minute amount of ECM present in bone marrow, stromal and haematopoietic cells could readily be dissociated into single cell suspensions by gentle mechanical disruption. When these cells were plated at low densities, bone marrow stromal cells (BMSCs) rapidly adhered, were easily separated from non-adherent haematopoietic cells through repeated washing, and formed distinct colonies, each of which was derived from a single precursor cell (10). These colonies were shown to have a high capacity for extended proliferation. Multi-colony derived cells when transplanted into a host animal formed ectopic ossicles complete with a reticular stroma supportive of myelopoiesis and adipocytes. Single colony derived cells however had the ability to completely regenerate bone cells, myelosupportive stroma, and adipocytes of clonal and donor origin, as well as haematopoiesis and vasculature of recipient origin (204). These results defined the ‘stem’ cell nature of the original colony-forming units-fibroblastic from which the clonal strain was derived. These bone marrow derived stromal cells were labelled as osteogenic stem cells, and more recently, skeletal stem cells (15).

These cells are the ‘mesenchymal stem cell’ described by Pittenger and colleagues in 1999 (205). The term ‘mesenchymal stem cell’ (MSC) was coined by Caplan in 1991 to refer to a hypothetical common progenitor of a range of non-hematopoietic, non-epithelial, mesodermal tissue (206). Based on *in vitro* assays and surface phenotyping, it became widely accepted that MSCs exist in a broad range of postnatal tissues, with a broad spectrum of lineage possibilities such as neural tissue, muscle, and adipose tissue. However, the existence of such a

ubiquitous MSC has been subject to criticism in the absence of necessary *in vivo* experimental support (14). Several sources of cells used for bone tissue engineering have been discussed previously (Table 1-8). Not only have bone marrow-derived stem cells been studied the most [104], the reported biological properties and inherent osteogenicity of bone marrow-derived stem cells makes bone marrow a prime source of stem cells for bone tissue engineering (114).

For the purposes of clarity and consistency, the definitions provided by Bianco for SSCs and BMSCs are used to define the cells utilised in all experiments conducted in this thesis (14). SSCs are defined as multipotent, self-renewing stromal progenitors which can be secondarily passaged or transplanted, and *in vivo*, give rise to multiple skeletal tissues and are capable of re-establishing clonogenic, multipotent progenitors residing over bone marrow sinusoids (14). BMSCs refer to non-haematopoietic, non-endothelial cells that provide the stromal scaffold *in situ*. *In vitro*, these cells can be generated by explanted stromal cells, including those generated by total cell suspensions, by progenitors selected by plastic adherence at clonal density, or by phenotype-purified explanted cells (14).

3.1 The capacity of STRO-1 enriched BMSCs for osteogenesis

3.1.1 Introduction

Although mature osteogenic cells could be used to generate new bone, in order for bone turnover to occur, SSCs must be present (114). Identifying SSCs remains an ongoing challenge, despite recent progress by Chan *et al.* Initial data regarding the existence of a self-renewing mouse SSC giving rise to bone, cartilage and stroma *in vivo* (207) has led to the identification of a potential source of human SSC with similar characteristics. Single-cell RNA sequencing of foetal human growth plate cells revealed a population of cells possessing a transcriptome analogous to that of mouse SSCs, with these cells having a podoplanin^{+}CD146^{-} CD73^{+}CD164^{+} signature (208). Interestingly, similar cells were found in adult femoral head tissue (bone and articular cartilage) as well as BMP-2-treated induced pluripotent stem cells and human adipose stroma. The authors however did not demonstrate that the human SSCs isolated from adult tissues or human cell populations gave rise to all downstream populations after serial transplantation, nor did they show self-renewal in an orthoptic environment. Furthermore, as with cells isolated from the bone marrow (113), these cells are few in number. The rarity of SSCs enforces the need for *ex vivo* expansion to create sufficient numbers for use

in regenerative therapy (209). No ECM protein capable of maintaining SSCs in an undifferentiated state has yet been identified. Work by Agata *et al* demonstrated the gradual loss of the *in vivo* osteogenic ability of human SSCs during cell culture and passage (210). Furthermore, although SSCs demonstrate low immunogenicity, SSCs do express histocompatibility antigens upon differentiation. As such, cells used for persistent bone regeneration must be autologous. These issues, in conjunction with variability in cell isolation and expansion protocols, and cell seeding methods (which themselves could affect experimental outcomes), are just some of the issues that help explain why the clinical translation of promising *in vivo* work has so far been limited (211). Attempts to standardise protocols for isolating and expanding human SSCs are underway (115, 209).

SSC enrichment protocols remain based on their cell surface expression profile. Various studies have indicated that adult human SSCs express CD29, CD44, CD54, CD73, CD90, CD105, CD106, CD146, CD166, CD271, and STRO-1 antigens, but do not express haematopoietic markers (CD11, CD14, CD34, CD45, CD235a), adhesion molecules (CD18, CD31, CD56) or co-stimulatory molecules (CD40, CD80, CD86) (113). However, as yet, no single surface marker or panel of markers clearly defines stem cells that differentiate towards the osteogenic lineage (212, 213). The complexity of antigen expression has hampered the isolation of a homogeneous population of SSCs, in spite of the myriad of antibodies that have been developed (214).

One of the current enrichment methods utilises a murine IgM monoclonal antibody, STRO-1, which binds to a trypsin-resistant cell surface antigen in humans (113, 214). STRO-1 positive BMSCs were first identified by Simmons and Torok-Storb in 1991, who showed that the STRO-1 antibody could be used to isolate stromal precursors in freshly aspirated bone marrow suspensions. Simmons and Torok-Storb also showed that STRO-1 positive BMSCs generated adherent cell layers containing adipocytes, smooth muscle cells, and fibroblastic elements in long term bone marrow cultures (215). Subsequent studies have since confirmed STRO-1 positive cells are found in approximately 10 per cent of the bone marrow stromal mononuclear population of healthy donors (113). The STRO-1 antigen was reported as a 75 kilodalton (kD) cell membrane single pass type 1 protein that translocates from the endoplasmic reticulum to the cell membrane in response to intracellular calcium depletion (216). However, other groups have failed to take this observation forward or indeed confirm the finding. In 2016, Gronthos *et al* demonstrated that the

STRO-1 antibody binds to heat shock cognate 70, a cytoplasmic chaperone protein (217). STRO-1 expression has been detected in the endothelium of some blood vessels, dental tissue, and synovial membranes, in addition to cell lines such MG63, and in primary cells such as BMSCs, and *in vitro* passaged ADSCs (201, 216). There is a suggestion that STRO-1 may play a role in clonogenicity, homing and angiogenesis of BMSCs (218). STRO-1 enriched BMSCs remain heterogeneous (215), as reflected by their *in vivo* localisation and *in vitro* multi-potency (demonstrated by MacArthur *et al*) (219). A highly enriched population can be obtained when the STRO-1 antibody is combined with an antibody directed against vascular cell adhesion molecule 1 (CD106) (220). Work done by Gronthos *et al* demonstrated STRO-1 positive BMSCs had high growth potential, and were adherent, colony-forming units-fibroblastic, that could give rise to fibroblasts, smooth muscle, adipocytes, and osteoblasts (221). Shi and Gronthos showed that transplanted STRO-1 positive BMSCs co-expressing CD146 encased in HAP/tricalcium phosphate formed ectopic bone in immunocompromised mice after 3 months (222). These findings form the basis for the hypothesis of this thesis, which is that STRO-1 enriched BMSCs possess an inherent capacity for osteogenesis, and would be a suitable cell type for use in bone tissue engineering.

Gronthos *et al* had previously demonstrated that under 1,25-VitD3 stimulation, STRO-1 positive BMSCs become alkaline phosphatase-positive, and formed mineralised tissue *in vitro* and *in vivo* (221, 223). Vitamin D can be naturally synthesised in the skin through sun exposure. 1,25-VitD3, the highly active form of Vitamin D *in vivo*, is synthesised through the hydroxylation of vitamin D_3 by cytochrome P450 oxidase (CYP) 25-hydroxylases, CYP27A1 (mitochondrial) and CYP2R1 (microsomal) (224). 1,25-VitD3 plays a crucial role in bone mineralisation, through its indirect control of calcium absorption in the intestine and the kidneys, or by its direct action on osteoblasts. Vitamin D deficiency leads to rickets in children, and osteomalacia in adults, both of which are associated with bone pain and a higher risk of fractures. This is due to a higher amount of unmineralised bone matrix (osteoid) covering bone surfaces, thereby preventing tissue resorption and causes the age of the remaining mineralised bone tissue to rise (5). Studies performed by Beresford *et al* to investigate the effect of 1,25-VitD3 on human bone cells demonstrated a dose-dependent (1×10^{-10} to 1×10^{-7} M) stimulatory effect on ALP and type I collagen production within as early as 24 hours of exposure (225). A dose-dependent (5×10^{-11} to 5×10^{-8} M) inhibition of *in vitro* bone cell proliferation was also observed. Further work by Franceschi *et al* showed a four-fold increase in

ALP activity in MG63 cells exposed to 10 nM of 1,25-VitD3 (226). It was also noted that maximal ALP activity occurred when MG63 cells were cultured in media containing 50 µg/ml of ascorbic acid and 10 nM 1,25-VitD3.

It has since been shown that 1,25-VitD3 exerts its osteoinductive effects by binding to, and regulating, the intranuclear vitamin D receptor, a ligand-dependent transcription factor present in osteoblasts. Vitamin D receptor heterodimerises with the retinoid X receptor, controlling the expression of vitamin D associated target genes regulating calcium homeostasis, cell proliferation and differentiation, and apoptosis (224, 227). Vitamin D receptor expression is regulated by 1,25-VitD3, PTH, and glucocorticoids, which themselves influence bone formation *in vivo* (as discussed in 1.6.3.4) (227). 1,25-VitD3 has been shown to stimulate osteopontin and osteocalcin synthesis as well as increase the activity of osteoclasts (through RANKL production) and osteocyte synthesis of fibroblast growth factor-23 (which is involved in phosphate homeostasis) (19, 224, 227, 228). Taken together, these findings confirm the osteoinductive effect of 1,25-VitD3, and form the basis for utilising 1,25-VitD3 and ascorbic acid in osteogenic cultures in the experiments conducted during this project.

As stated in 1.9, the hypotheses of this thesis are:

1) Human STRO-1 enriched BMSCs possess, and retain, the capacity for osteogenesis when seeded onto scaffolds, and are therefore a suitable cell type for use in bone reparation.

2) Biomaterials can be combined to generate tuneable bioinks, which can be used to deliver STRO-1 enriched BMSCs with high viability and functionality.

3) 3D printing methods are capable of manufacturing porous scaffolds of clinically relevant size with high resolution and reproducibility.

4) STRO-1 enriched BMSCs, biomimetic bioinks, and 3D printed polycaprolactone-based scaffolds can be combined to create an integrated bioconstruct for use in bone repair.

In conjunction with the above hypotheses, the aims of this research project are:

1) To confirm the osteogenic potential of STRO-1 enriched BMSCs.

2) To elucidate the osteoinductive capabilities of established biomaterials, such as titanium and polycaprolactone (amongst others), in order to identify potential combinations for the generation of composite scaffolds and/or bioinks for use in bone tissue engineering.

3) To design novel porous scaffolds that mimic natural bone architecture.

4) To investigate the feasibility of utilising 3D printing techniques to accurately and reproducibly manufacture scaffolds according to their design.

5) To determine the possibility of 3D printing cell-laden bioinks.

6) To develop methods for integrating 3D printed scaffolds, biomimetic bioinks, and STRO-1 enriched BMSCs, with the objective of creating functional bioconstructs for use in bone reparation.

3.1.2 Materials and Methods

3.1.2.1 Isolation of STRO-1 enriched Bone Marrow Stromal Cell (BMSC)

Human bone marrow was obtained from patients undergoing hip surgery at Southampton General Hospital and Spire Southampton Hospital, with full ethical consent (LREC 194/99). Bone marrow samples from male or female donors were processed within 48 hours of surgery, for the isolation of STRO-1 enriched BMSCs, as described by Tare *et al* (115). Bone fragments within each sample were crushed using a sterile instrument before 5 ml of serum-free αMEM was added to the marrow sample and shaken vigorously by hand for 5 minutes. The blood-coloured, cloudy supernatant was transferred into a clean 50 ml universal tube. This process was repeated until the serum-free medium appears unchanged in its appearance. The collected volume underwent centrifugation at 11000x *g* for 5 minutes at 18°C in a Heraeus Megafuge 1.0R centrifuge (Thermo Fisher Scientific, USA). The loose pellet obtained (after the supernatant was carefully discarded) was re-suspended in 10 ml of basal medium and re-centrifuged as above. The supernatant was removed and 25 ml of basal medium (as described in 2.1) was added to the pellet before being transferred to a new 50 ml universal tube by passing through a 70 µm cell strainer (Thermo Fisher Scientific, USA) to remove any debris. 20 ml of Lymphoprep (STEMCELL Technologies, France) was added to a 50 ml universal tube followed by the slow addition of 25 ml of cell suspension onto the Lymphoprep surface at a 45° angle.

The sample was then centrifuged at 15000x *g* for 40 minutes at 18°C; this is the only part of the process when the centrifuge brakes are off. A distinct buffy coat (mononuclear cell) layer formed between the pink medium layer above and the clear Lymphoprep-containing layer below. This interface layer was carefully removed using a 3 ml pastette and placed into a new 50 ml universal tube. An appropriate volume of medium was added to the extracted volume to make a total volume of 50 ml, prior to being centrifuged at 11000x *g* for 4 minutes at 18°C. The supernatant was discarded before 2 ml of MACS blocking buffer (Table 3-1) was added. The re-suspended pellet was incubated on a rotator for 30 minutes at 4°C, after which 8 ml of chilled MACS buffer (Table 3-1) was added.

MACS blocking buffer • Mix and filter just before use	17 ml αMEM + 2 ml human AB serum (Sigma Aldrich, UK) + 0.2 g bovine serum albumin (BSA) (Thermo Fisher Scientific, USA) + 1 ml FCS
MACS buffer • De-gas using a vacuum	1 l 1x PBS (sterile) + 5 g BSA + 0.74448 g EDTA

Table 3-1 Composition of MACS blocking buffer and MACS buffer solutions.

The sample was centrifuged at 11000x *g* for 5 minutes at 18°C, with the resulting pellet re-suspended in 0.5 ml of STRO-1 hybridoma supernatant (made in-house) and incubated for 30 minutes on a rotator at 4°C. 10 ml of chilled MACS buffer was added to the mixture, which was then centrifuged at 11000x *g* for 5 minutes at 18°C. This washing step was repeated thrice. The pellet was re-suspended in 800 µl of chilled MACS buffer before 200 µl of MACS rat anti-mouse IgM microbeads (Miltenyi Biotec, Germany) was mixed in and incubated for 15 minutes on a rotator at 4°C. 9 ml of chilled MACS buffer was added to the mixture and centrifuged at 11000x *g* for 5 minutes at 18°C. This was repeated three times before re-suspending the pellet in 2 ml of chilled MACS buffer. At this stage, the cells could be stained with a STRO-1-FITC antibody (Thermo Fisher Scientific, USA) to identify STRO-1 positive cells via flow-assisted cytometry (FACS). 5 µl of a 1 in 200 dilution FITC antibody per 1 ml of MACS buffer can be added to the cell suspension and incubated for 15 minutes prior to the next stage.

A MACS column was inserted into a magnetic holder slot on a magnet stand, and a 30 ml collection tube was placed below the column. The column was then filled with 3 ml of chilled MACS buffer. Just before the fluid level reached the base of the column, 2 ml of the cell suspension was added to the side of the column slowly to avoid bubble formation, followed by 9 ml of chilled MACS buffer. This step

extracts the majority of cells that were not bound to the MACS IgM microbeads. The drained column was removed from the magnetic bracket and filled with 5 ml of chilled MACS buffer. A supplied sterile plunger was used to rapidly expel the STRO-1 enriched cells from the column into a sterile collecting tube. The collected cells were centrifuged at 11000x *g* for 5 minutes at 18°C and were washed twice in 10 ml basal medium using the same centrifugation step. The pellet was re-suspended in 10 ml basal medium and a cell count, using a Fast-Read 102® disposable counting slide, was performed prior to culture. 5 X 10^5 cells in 20 ml of basal medium were added to 175 cm^2 Corning® cell culture flasks (Sigma Aldrich, UK) and incubated in a humidified, 37°C, 5% CO_2 incubator (NuAire, UK) for 14 days prior to passage.

3.1.2.2 STRO-1 enriched BMSC population expansion and storage

Adherent STRO-1 enriched BMSCs were passaged as follows. Basal medium was changed once weekly until cultures were approximately 80% confluent, at which point the STRO-1 enriched BMSCs underwent their first passage. BMSCs were washed with sterile Dulbecco's Phosphate Buffered Saline without calcium and magnesium (DPBS) (Lonza, Switzerland) before being incubated at 37°C, 5% CO_2 with 0.02% w/v collagenase IV solution (Sigma-Aldrich, UK) for 30 minutes, followed by trypsin- EDTA diluted with DPBS for 10 minutes. Complete cellular detachment was encouraged by gentle agitation of the cell culture flask and confirmed by light microscopy. Trypsin-EDTA was neutralised with an equivalent volume of basal medium, and the cell suspension was centrifuged at 11000x *g* for 5 minutes at 18°C. The pellet obtained was re-suspended in basal medium and a cell count was performed using a Fast-Read 102® disposable counting slide (2.2).

Each 175 cm^2 Corning® cell culture flask could then be split into two to three 175 cm^2 cell culture flasks. Cell cryopreservation was performed by adding approximately 1 X 10^6 cells suspended in 0.9 ml of basal medium to 0.1 ml of sterile DMSO per cryovial. Cryovials were transferred into a cryopreservation container and stored at -80°C before transfer to liquid nitrogen storage. STRO-1 enriched BMSCs were not passaged greater than three times for experiments, and no greater than two times prior to cryopreservation.

3.1.2.3 Determination of cell viability and functionality

STRO-1 enriched BMSCs were isolated from human bone marrow from a male patient, aged 63, following the protocol described above in 3.1.2.1 and 3.1.2.2. 1 X 10^4 M63 P1 STRO-1 enriched BMSCs were seeded per well of a 6-well plate.

Triplicates were performed to investigate the differences between seeded cells that were cultured in basal and osteogenic media. Cell viability at days 7, 14, and 21 was assessed using CellTracker™ Green and ethidium homodimer (2.6.1).

STRO-1 enriched BMSCs were isolated from human bone marrow from a female patient, aged 70, following the protocol described in 3.1.2.1 and 3.1.2.2. 1 X 10^4 F70 P1 STRO-1 enriched BMSCs were seeded per well of a 6-well plate. Triplicates were performed, with 1 group of cells cultured in basal medium, while the other group were cultured in osteogenic medium. Cytoskeletal staining for F-actin, vinculin, and nuclear counterstaining was performed at days 7, and 21 (2.6.3).

ALP staining was also performed at day 7, 14, and 21 end-points to determine the functionality of the cultured F70 P1 STRO-1 enriched BMSCs. At each end-point, cells were washed in 1x PBS twice prior to being fixed in 95% ethanol for 10 minutes. The cells were rinsed in 1x PBS before being left to dry over a 30 minute period. Just before use, 0.0024 g of Fast Violet B (Sigma Aldrich, UK) was added to a solution containing 9.6 ml of deionised water and 400 µl of Naphtol AS-MX Phosphate Alkaline (Sigma Aldrich, UK). 600 µl of the light yellow solution was added to each sample well. The plates were wrapped in aluminium foil and incubated at 37°C for 30 to 60 minutes. Plates were checked for any colour changes at the 30 minute interval. The reaction was stopped by adding an equivalent volume of deionised water and images were immediately taken using a Canon digital camera. Microscopy images were taken using a Zeiss Axiovert 200 microscope.

3.1.2.4 The potential of STRO-1 positive BMSCs for osteogenesis

STRO-1 enriched BMSCs were isolated from human bone marrow samples from eight patients (six males aged 56, 63, 64, 66, 67, and 76, and two females aged 70 and 71) following the protocol described in 3.1.2.1 and 3.1.2.2. 1 X 10^4 cells were seeded per well of a 6-well plate in a triplicate manner, whereby one group of cells was cultured in basal medium while the other group was cultured in osteogenic medium (containing 1,25-VitD3) for 7, 14, and 21 days. Plates were set-up in the same manner for each patient. At each end-point, the cells were lysed in TRIzol® and RNA extraction was performed as described in 2.5.1. Reverse transcription and RT-qPCR was performed using the RNA extracted, as described in 2.5.2 and 2.5.3. To determine the osteogenic potential of the STRO-1 enriched BMSCs, the relative expressions of Runx2, Col1a1, OPN, and OCN were calculated following the method described in 2.5.3, using β-actin as the housekeeping gene.

Relative gene expressions for each marker in the osteogenic group were then normalised against the $2^{-\Delta\Delta Ct}$ values obtained for the day 7 basal group for each patient. Calculated values were plotted as means ± standard error of mean.

3.1.2.5 Statistical analysis

Statistical significance was determined by two-way ANOVA analysis, with a *p* value less than 0.05 deemed to be statistically significant. Tukey *post-hoc* multi-comparison testing was performed to determine the statistical significance of differences observed between culture groups, culture time, or interaction thereof.

3.1.3 Results

STRO-1 enriched BMSCs were viable at 7, 14, and 21 days of culture on tissue culture plastic, as demonstrated by the uniform distribution of green fluorescence of the CellTracker™ Green and the absence of red fluorescence of the ethidium homodimer stain at each time-point (Figure 3-1). Seeded STRO-1 enriched BMSCs actively proliferated, as reflected by increasing cell numbers and reducing intercellular space over the 21 day period. Despite cell seeding density being similar in both groups at the start of the experiment, cellular proliferation was slightly higher in the osteogenic cohort at day 7, but this observed difference became less apparent by day 21 of culture. Morphological differences between the basal and osteogenic cohort were noticeable by day 14, and became more evident by day 21, with the development of a mixed population of elongated, spindle-shaped cells and larger, stellate-shaped cells (Figure 3-1 and Figure 3-2). Cytoskeletal staining of STRO-1 enriched BMSCs cultured in osteogenic medium not only demonstrated higher F-actin and vinculin activity in the osteogenic group as culture time progressed, but also when compared to cells cultured in basal medium (Figure 3-2).

Cell functionality differences were qualitatively shown by staining of STRO-1 enriched BMSCs that were cultured in basal and osteogenic conditions for 21 days with naphthol AS-MX phosphate and fast violet B salt. Although the intensity of the red coloration increased as culture time progressed for both groups, slightly greater ALP activity (at all time-points) was seen in wells containing cells cultured in osteogenic medium compared to basal medium, as indicated by the greater intensity of the red coloration (Figure 3-3).

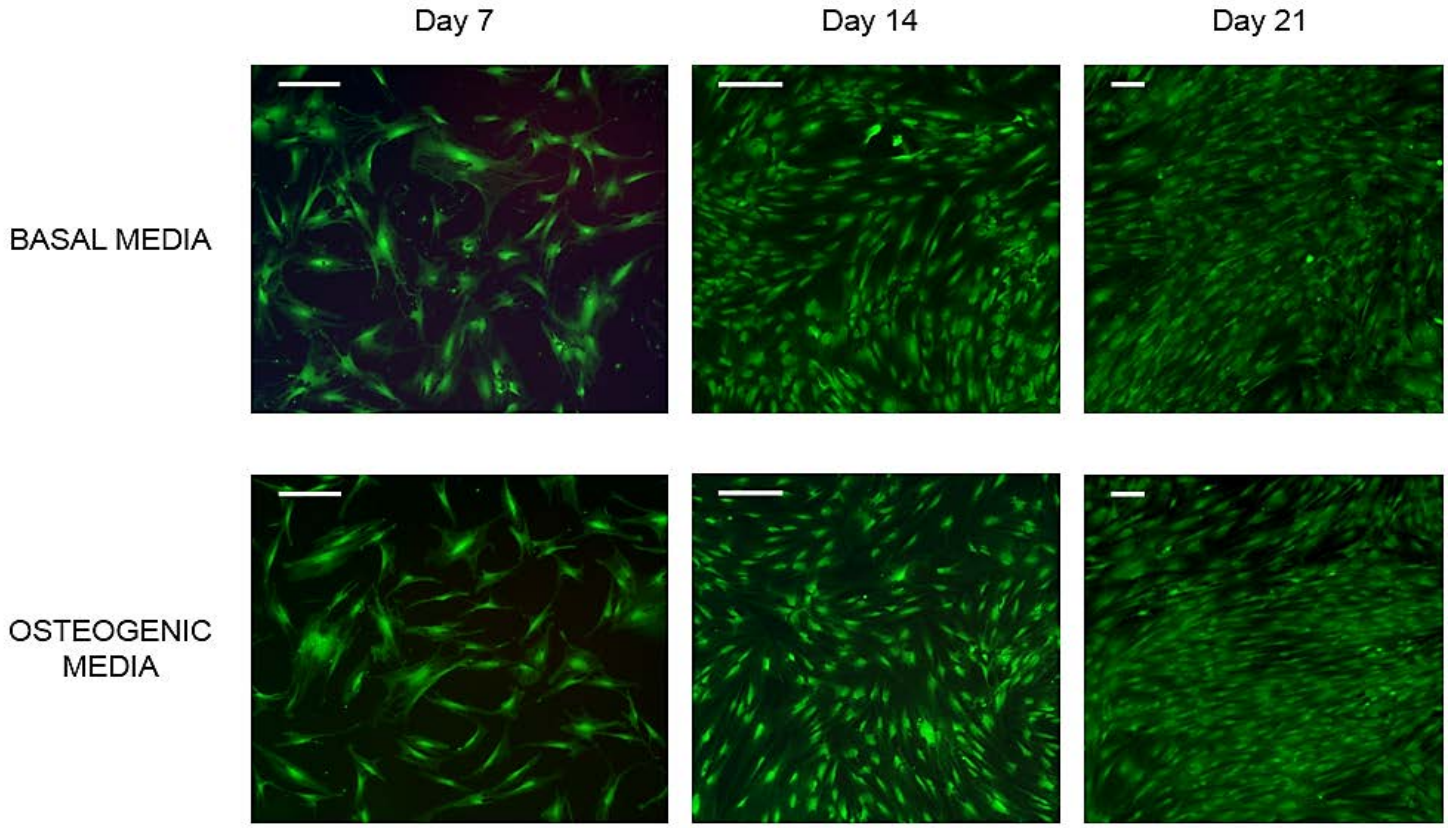

Figure 3-1 Cell proliferation of STRO-1 over time in basal and osteogenic (containing 25 nM 1,25-VitD3) culture conditions.

CellTracker™ Green and ethidium homodimer-1 labelled STRO-1 enriched BMSCs at days 7, 14, (scale bars represent 200 µm) and 21 (scale bar represents 100 µm) in basal (top row) and osteogenic (bottom row) media showing seeded cells were viable and proliferated over time. These merged images were taken on a Zeiss Axiovert 200 microscope, using FITC and TRITC filters.

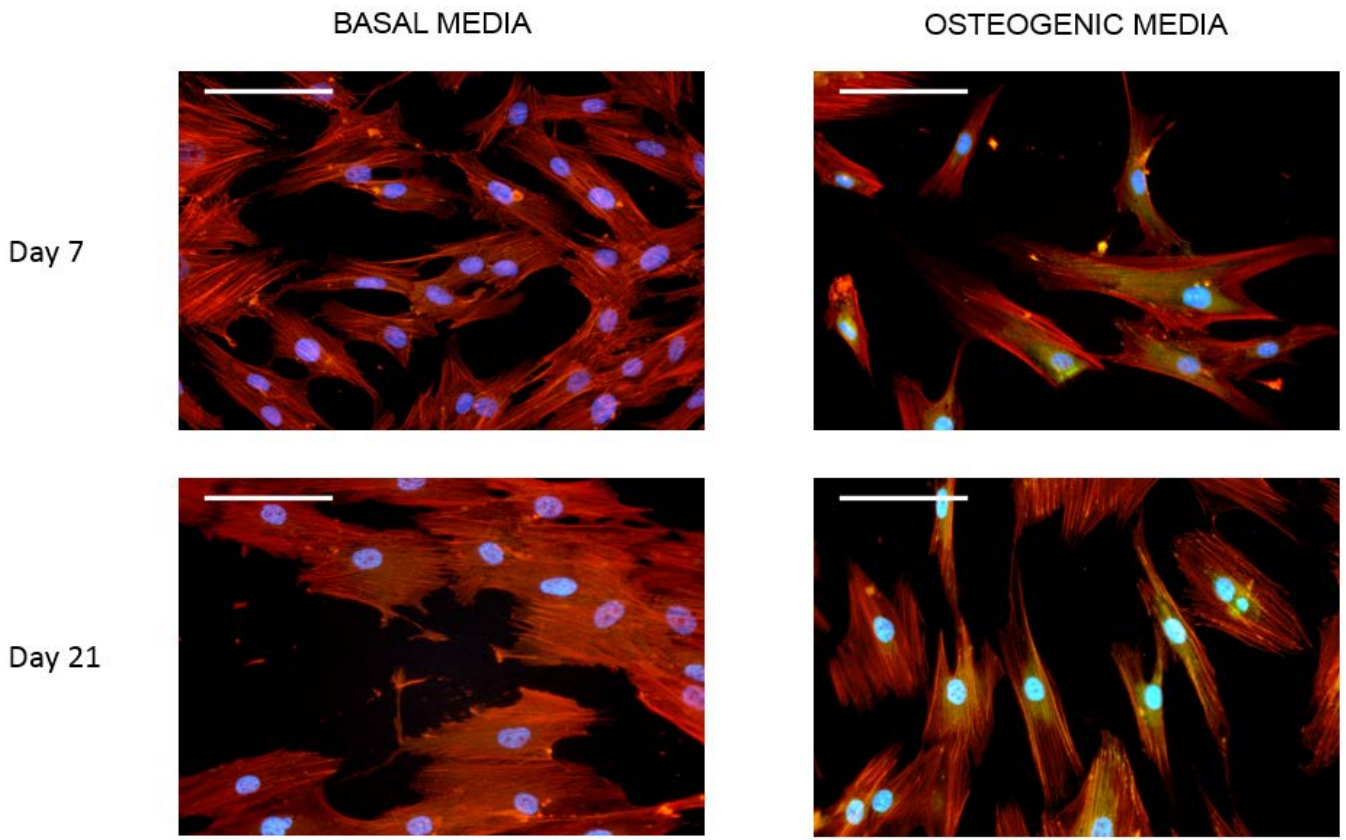

Figure 3-2 Cytoskeletal staining of STRO-1 enriched BMSCs over time in basal and osteogenic culture conditions.

Nuclei counterstaining with DAPI (blue), vinculin staining (green) and F-actin staining with phalloidin (red) of STRO-1 enriched BMSCs cultured in basal and osteogenic media at days 7 and 21. Scale bars represent 100 µm.

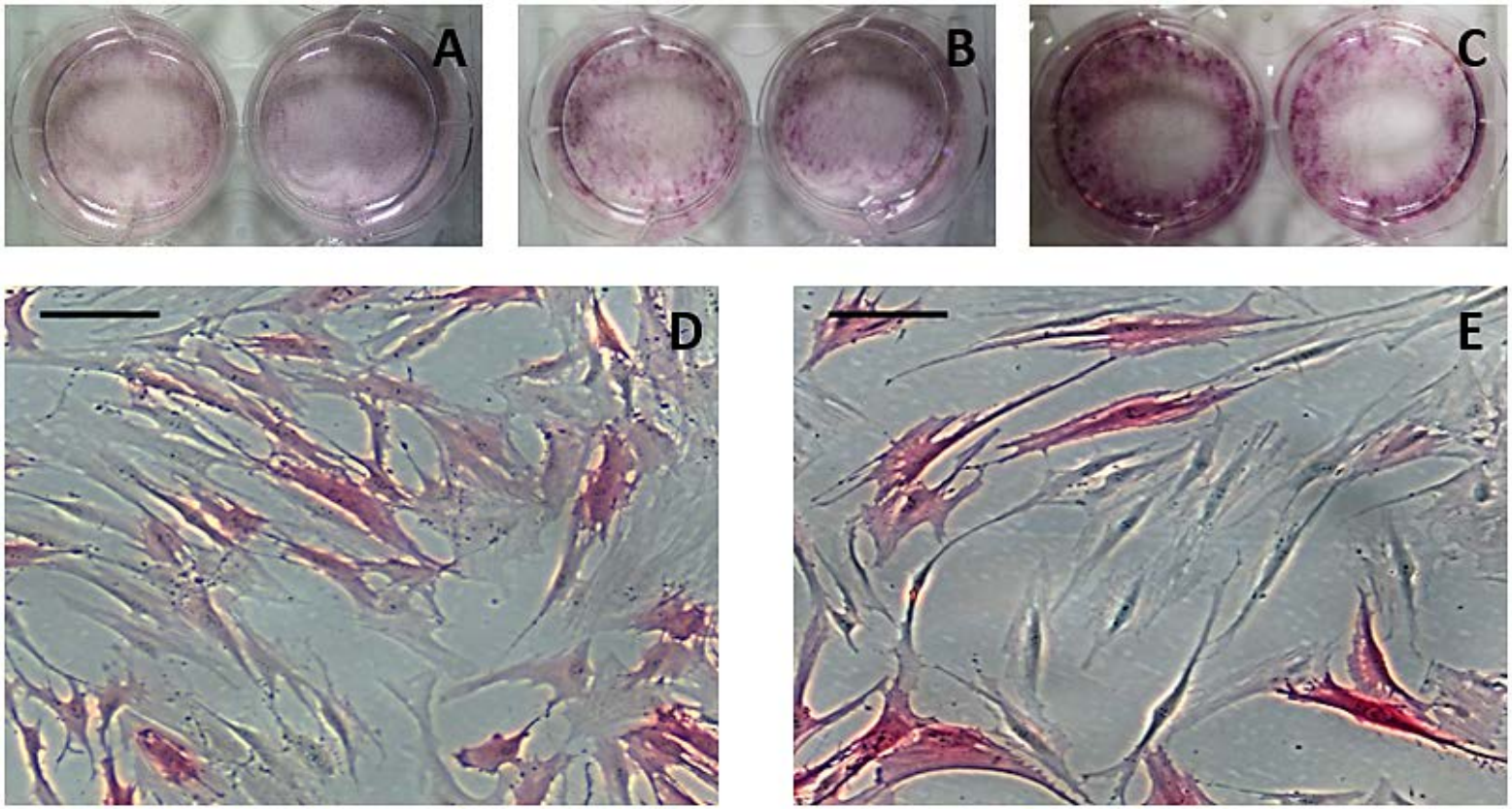

Figure 3-3 ALP staining of STRO-1 enriched BMSCs cultured in basal and osteogenic conditions.

ALP staining at day: A) 7, B) 14, and C) 21. Cells in wells on the left were cultured in basal medium while those on the right were grown in osteogenic medium, and demonstrated higher ALP expression. Positive ALP staining of F70 P1 STRO-1 enriched BMSCs grown in D) basal medium and E) osteogenic medium, at day 7, demonstrating a slightly greater ALP activity in the osteogenic group (both scale bars represent 100 µm).

STRO-1 enriched BMSCs from eight patients were cultured in basal and osteogenic media under similar experimental conditions. Early and late osteogenic differentiation markers for both cohorts were charted at days 7, 14, and 21 (see Figure 3-4 and Figure 3-5). The four gene markers appeared to demonstrate an overall tendency towards increased expression as time progressed, irrespective of culture condition. The overall degree of increment for all gene markers was higher in the osteogenic cohort across all time-points (Figure 3-4 and Figure 3-5). In keeping with the observed cellular proliferation (Figure 3-1), Runx2 and Col1a1 gene expression increased with time in both basal and osteogenic conditions (Figure 3-4). In contrast, upregulation of OPN, and OCN in particular, although maintained throughout the culture period in the osteogenic cohort (Figure 3-5), showed that cellular differentiation peaked at day 7, as indicated by an average 4.6-fold increase in OPN, and a 66-fold increase in OCN expression. In spite of the absence of an osteoinductive agent, there was an observed transient increase in OPN and OCN gene expression in the basal cohort, which peaked at day 14.

Figure 3-6 and Figure 3-7 illustrate the inherent variability of the eight patients in response to the osteoinductive effects of 1,25-Vit D3. Seven patients appeared to respond as expected to 1,25-VitD3 stimulation over the 21 day culture period, with increased relative expression of OPN and OCN being evident within the osteogenic group by day 7 of culture. In contrast, F70 P1 STRO-1 enriched BMSCs cultured under osteogenic conditions demonstrated a consistently lower expression level of OPN and OCN at all time-points. This qPCR result corresponded with the lower than expected increase in ALP activity between the basal and osteogenic groups for the cultured F70 P1 STRO-1 enriched BMSCs (Figure 3-3).

Despite the trends observed, two-way ANOVA analysis with Tukey post-hoc testing between the two cohorts at different time-points revealed no statistically significant differences between the relative expressions of each gene marker, except for Col1a1 gene expression (Table 3-2). Although there were clearly variable responses between patients to the osteoinductive effect of 1,25-VitD3, two-way ANOVA analyses by Tukey multiple comparison test revealed a statistically significant effect of culture method ($F(1, 7) = 7.94$, $p < 0.026$, $h^2 = 0.042$) and the interaction between time and culture approach on OCN gene expression levels ($F(2, 14) = 4.77$, $p < 0.026$, $h^2 = 0.222$) (Table 3-3).

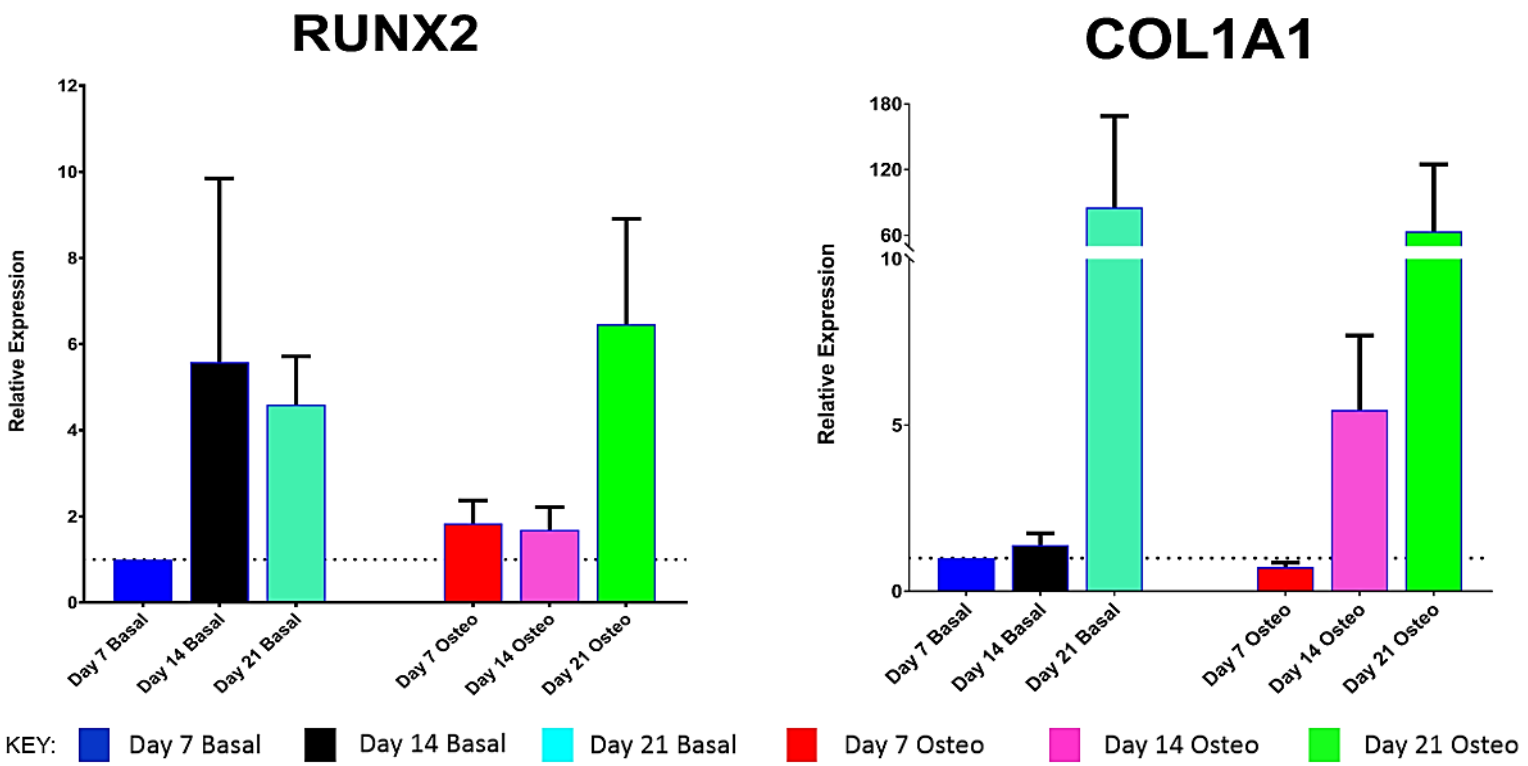

Figure 3-4 Relative gene expression over time of early stage osteogenic differentiation markers of STRO-1 enriched BMSCs cultured in basal and osteogenic conditions compared to day 7 basal medium.

STRO-1 enriched BMSCs isolated from eight different patients cultured in both basal and osteogenic media over a 21 day period demonstrated a general trend of increased mean relative expressions of Runx2 and Col1a1 over time. Although there were no significant differences between the culture groups over time with Runx2 expression, there were some significant differences in Col1a1 expression between culture groups over time, as listed in Table 3-2.

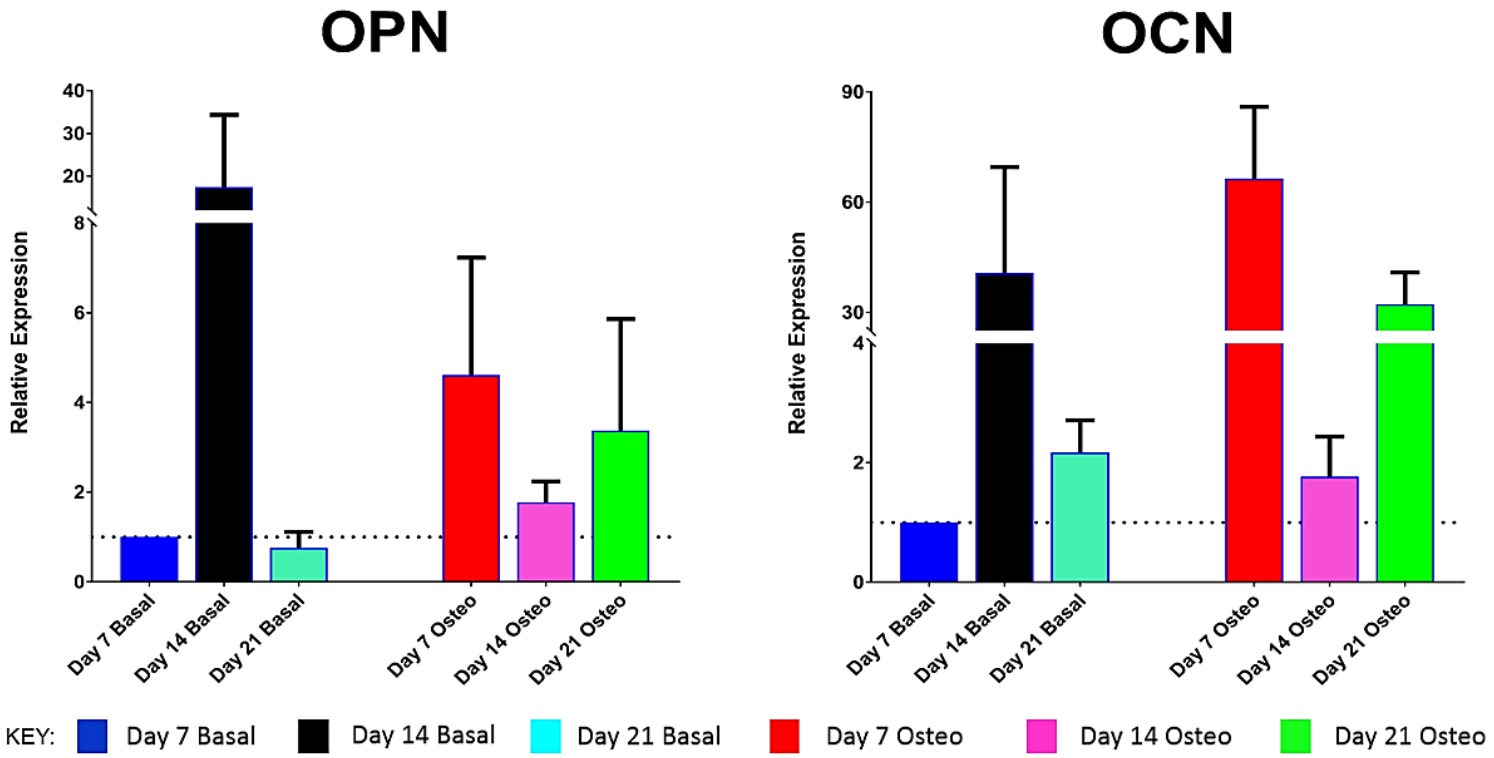

Figure 3-5 Relative gene expression of late stage osteogenic differentiation markers over time of STRO-1 enriched BMSCs cultured in basal and osteogenic conditions compared to day 7 basal medium.

Although STRO-1 enriched BMSCs isolated from eight different patients cultured in basal and osteogenic media over a 21 day period showed a general increase in the relative expressions of OPN and to a greater extent, OCN, the differences in culture approach over time were not statistically significant. This non-significance could be attributed to the inherent variability in the individual responses to 1,25-VitD3 stimulation, which is highlighted by the scatter plot charts below (Figure 3-6 and Figure 3-7).

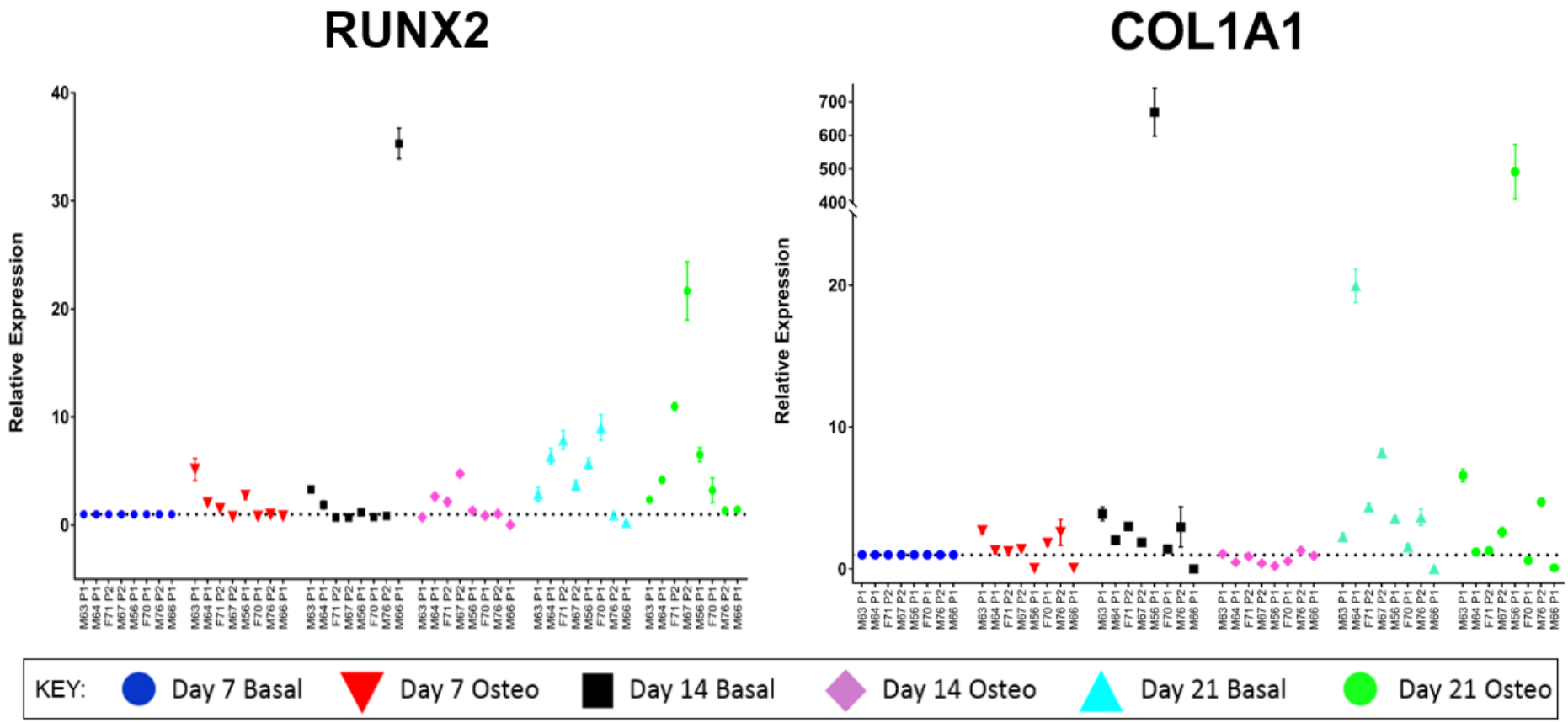

Figure 3-6 Scatter plot charts of Runx2 and Col1a1 gene expression per patient at each time point over a 21 day culture period.

The scatter plots demonstrate the variability in gene expression for each patient, which appeared to become increasingly pronounced as time passed, irrespective of culture conditions, and the sex and age of the patient. (Abbreviations: M = male, F = female, P = passage number).

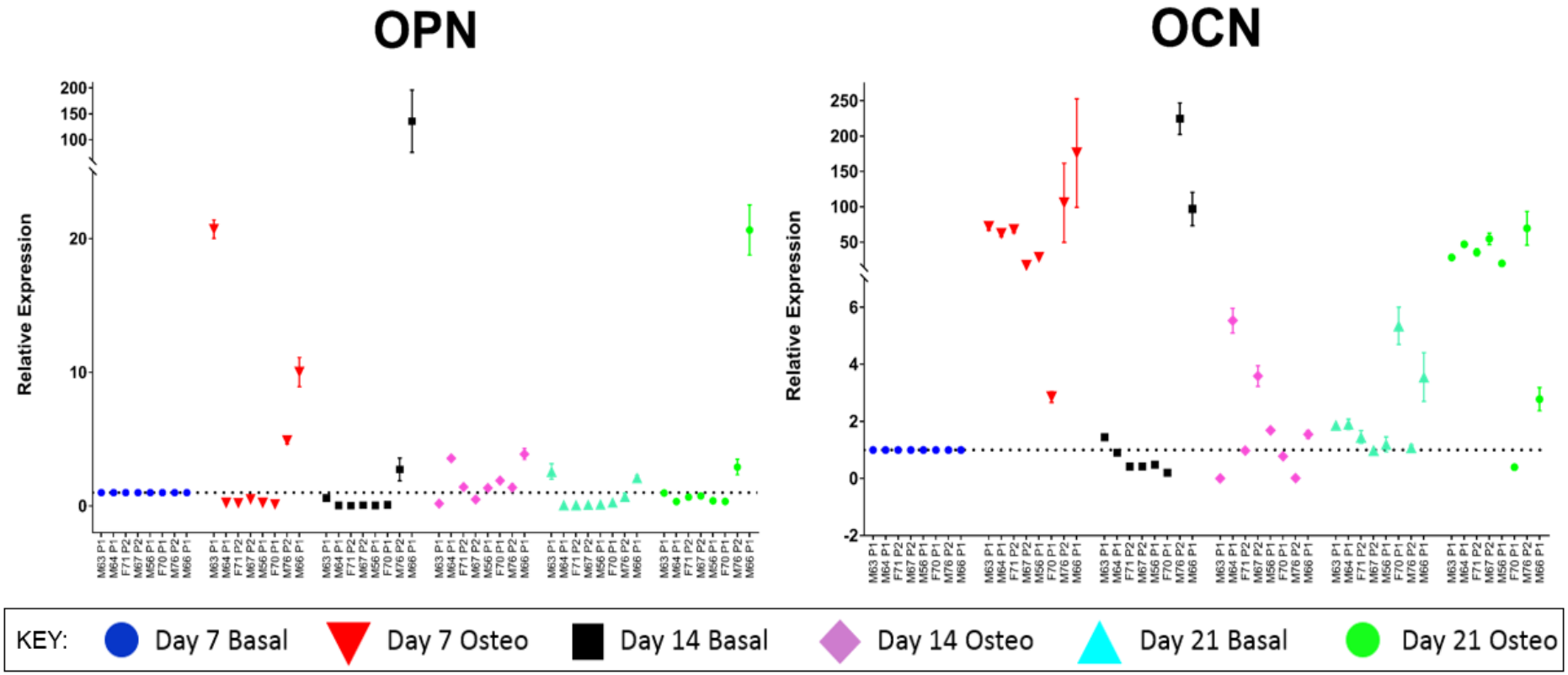

Figure 3-7 Scatter plot charts of OPN and OCN gene expression per patient at each time point over a 21 day culture period.

Although the scatter plots indicate a more consistent, overall increase in osteogenic differentiation markers in the osteogenic cohort over time, the plots also demonstrate a significant variation in the individual responses to 1,25-VitD3 exposure, particularly at earlier time points. (Abbreviations: M = male, F = female, P = passage number).

Tukey comparison test	Mean Difference	p value
Day 7 Basal Media vs Day 21 Basal Media	-84.51	0.001
Day 7 Basal Media vs Day 21 Osteogenic Media	-62.63	0.0027
Day 7 Osteogenic Media vs Day 21 Basal Media	-84.78	0.001
Day 7 Osteogenic Media vs Day 21 Osteogenic Media	-62.9	0.0026
Day 14 Basal Media vs Day 21 Basal Media	-84.12	0.0002
Day 14 Basal Media vs Day 21 Osteogenic Media	-62.24	0.0028
Day 14 Osteogenic Media vs Day 21 Basal Media	-80.05	0.0003
Day 14 Osteogenic Media vs Day 21 Osteogenic Media	-58.17	0.005

Table 3-2 Significant mean differences in gene expression of STRO-1 enriched BMSCs cultured over a 21 day period in basal and osteogenic media.

Tukey post-hoc testing only showed significant differences in Col1a1 gene expression changes.

Gene marker	*Variable*	*F (DFn, DFd)*	*p value*	*h^2*
Runx2	Time	F (2, 14) = 1.655	0.226	0.081
	Approach	F (1, 7) = 0.047	0.835	0.0011
	Interaction	F (2, 14) = 1.123	0.353	0.045
Col1a1	Time	F (2 ,14) = 1	0.392	0.085
	Approach	F (1 ,7) = 0.65	0.446	0.0007
	Interaction	F (2, 14) = 1.18	0.338	0.0024
OPN	Time	F (2, 14) = 0.83	0.456	0.27
	Approach	F (1, 7) = 0.47	0.514	0.30
	Interaction	F (2, 14) = 1.04	0.378	0.43
OCN	Time	F (2, 14) = 1.06	0.373	0.023
	Approach	F (1, 7) = 7.94	0.026	0.042
	Interaction	F (2, 14) = 4.77	0.026	0.22

Table 3-3 Two-way ANOVA analyses of the effect of culture time and approach.

Neither culture time nor approach were statistically significant factors in affecting the changes in gene expression observed, except for OCN gene expression wherein culture approach was a significant factor.

3.1.4 Discussion

To summarise, the results of the above experiments indicate:

- *STRO-1 enriched BMSCs appear to develop a stellate morphology when cultured over time in 1,25-VitD3-containing media*
- *ALP staining indicated that ALP activity increased when STRO-1 enriched BMSCs were cultured in osteogenic media containing 1,25-VitD3*
- *Greater upregulation of osteogenic differentiation markers, Runx2, Col1a1, OPN, and OCN, occurred in STRO-1 enriched BMSCs cultured under osteogenic conditions, albeit with patient variability in the response to 1,25-VitD3 stimulation.*

STRO-1 enriched BMSCs were viable, migrated, and steadily proliferated on standard tissue culture plastic, demonstrating morphological changes in both culture conditions, as shown by CellTracker™ Green and ethidium homodimer-1 staining performed at various time-points (Figure 3-1). Cell numbers were noted to initially increase at a slightly faster rate in the osteogenic cohort, as reflected by a greater upregulation of Runx2 among the osteogenic cohort at day 7 (Figure 3-4). Populations of mixed morphology (spindle-like and stellate-like) were seen particularly in the STRO-1 enriched BMSC population cultured under osteogenic conditions by day 14, indicating one group of cells were proliferating alongside a subpopulation of cells that were undergoing differentiation induced by 1,25-VitD3. The stellate morphology observed in both populations (Figure 3-1 and Figure 3-2) is known to indicate osteogenic differentiation (229, 230). Hong *et al* had shown that despite mouse osteoprogenitor MC3T3-E1 cells possessing a cell spreading morphology when cultured under osteogenic conditions (containing 0.1 μM dexamethasone and 10 mM β-glycerophosphate), F-actin filament density increased, indicating early osteoblast differentiation (230). This increase in F-actin activity as differentiation occurred (albeit under the influence of a known, but different osteoinductive agent, 1,25-VitD3) was observed in this study, as illustrated by the increased (and more condensed) phalloidin staining, in addition to, increased vinculin (an intermediate cytoskeletal component) activity within the osteogenic cohort, further corroborating increased cytoskeletal activation (Figure 3-2).

Concomitant ALP staining indicated an almost simultaneous increase in ALP occurred during the phase of growth and differentiation of STRO-1 enriched BMSCs. ALP is a metalloenzyme that is attached by a glycophosphatidylinositol

anchor to the exterior of cell plasma membranes, and to the membrane of matrix vesicles (231). ALP exists as four isoforms in humans – placental, placental-like, intestinal, and liver/bone/kidney (otherwise known as tissue non-specific). Siffert histochemically demonstrated the role of ALP in osteogenesis in 1950 (232). Since then, ALP expression has been shown to be principally regulated by BMP, Runx2, 1,25-VitD3, PTH, and retinoic acid, further indicating the involvement of ALP in the early stages of osteogenesis (225, 226, 231). ALP has often been used as a marker of osteogenic activity and neotissue mineralisation in tissue engineering studies. However, the mechanism through which ALP initiates early bone mineralisation has only more recently been investigated. Patients with hypophosphatasia, which results from mutations in the gene that codes for tissue non-specific ALP, have under-mineralised bone tissue (231). As STRO-1 enriched BMSCs proliferated (and also matured), ALP activity was observed to be higher in the osteogenic group (Figure 3-3), as demonstrated by the increased formation of the red complex of naphthol AS-MX and fast violet B salt (233). Greater increased ALP activity in the osteogenic cohort over time indicated a larger subpopulation of STRO-1 enriched BMSCs had differentiated into intermediate pre-osteoblasts, and potentially, osteoblasts, under 1,25-VitD3 osteoinduction. This result is in keeping with work by Gronthos and colleagues, who demonstrated that normal human bone cells expressing STRO-1^-/ALP^+ phenotypes represented fully differentiated osteoblasts while STRO-1^+/ALP^+ phenotypes were intermediate pre-osteoblasts (221).

Although the relative expression of the four osteogenic differentiation markers appeared to increase at all three time-points in both culture conditions, the increment in gene marker expression was generally higher in the osteogenic cohort (Figure 3-4 and Figure 3-5). *In vitro*, human osteoblasts decrease proliferation and increase mRNA expression of osteogenic markers such as OPN and OCN when exposed to exogenous 1,25-VitD3 (224, 225). Runx2 is the master gene of osteoblast differentiation (234), and is expressed in mesenchymal condensations starting at E10.5. Runx2 is a key transcription factor involved in the osteoblastic differentiation of mesenchymal progenitors, and remains the earliest cell-specific transcriptional determinant known in osteoblasts. Runx2 haploinsufficiency results in a skeletal dysplasia called cleidocranial dysplasia (234). Figure 3-4 indicated Runx2 upregulation was observed as early as day 7, which translated to the proliferative and differentiation phase of culture, and as the cultured cells matured, increasing Col1a1 gene expression over time suggested the onset of deposition of ECM by the differentiating STRO-1 enriched BMSCs. Upregulation of Col1a1 gene expression in

the osteogenic cohort was initially greater than in the basal cohort. However, the mean difference in Col1a1 gene expression increment appeared to equilibrate by day 21, whereby there was no longer a statistically significant difference between the two cohorts in Col1a1 gene expression levels (Figure 3-4, Table 3-2). This observation appeared to indicate that as more STRO-1 enriched BMSCs differentiated into mature osteoblasts over time, Col1a1 gene expression in the osteogenic cohort was possibly suppressed by prolonged exposure to 1,25-VitD3. These results are similar to findings by Bellows *et al*, who had shown that 1,25-VitD3 treatment upregulated OPN and OCN but slightly downregulated Col1a1 in mature rat osteoblasts (228). Increased Col1a1 expression is indicative of the formation and deposition of ECM by proliferating and maturing osteoblasts. There is evidence to suggest that 1,25-VitD3 does not enhance, and in some studies, inhibits Runx2 and Col1a1 expression in murine osteoblasts at doses of 10 nM (235). However, 1,25-VitD3 has been shown to have the reverse effect in human and rat osteoblasts (227), highlighting the importance of choosing the right animal model for an *in vivo* study involving the effect of 1,25-VitD3 on bone development and mineralisation. In this study, regular exposure to 1,25-VitD3 had an overall stimulatory, rather than inhibitory, effect on human STRO-1 enriched BMSCs, as demonstrated by the early upregulation of the late osteoblast markers, OPN and OCN, by day 7 (Figure 3-5, Table 3-3), which indicated early osteogenic differentiation and rapid progression towards mature osteoblast phenotypes. The observed greater and more persistent upregulation of OCN (where culture condition was statistically significant in the outcome, as summarised in Table 3-3), in the osteogenic cohort over time was a further indication of osteogenic differentiation of STRO-1 enriched BMSCs into mature osteoblasts under the potent stimulation of 1,25-VitD3 (Figure 3-5, Table 3-3) (236). Although there is also evidence to support the role of 1,25-VitD3 in promoting angiogenesis, and its role in optimising bone mineralisation *in vivo* (227), the supraphysiological doses used in the above *in vitro* experiments (and others) may not accurately reflect the *in vivo* effect on seeded STRO-1 enriched BMSCs of serum levels of 1,25-VitD3 (where normal levels are 500 times less).

Figure 3-4 and Figure 3-5 appear to suggest osteogenic differentiation also occurred in the basal cohort, albeit to a lesser extent. Figure 3-6 and Figure 3-7 (which show the individual gene marker changes over time, and in response to 1,25-VitD3 stimulation) clarify this observed increase in OPN and OCN in the basal cohort, identifying M66 P1, and to a lesser extent, F70 P1, cultures as the causes

for the skewness of the overall results. In such a context, these findings indicate that osteogenic differentiation of STRO-1 enriched BMSCs in basal culture might occur, but perhaps to a lesser extent than indicated in Figure 3-4 and Figure 3-5, when compared to STRO-1 enriched BMSCs cultured in osteogenic media. Such an extrapolation would be in keeping with the inherent osteogenic potential of STRO-1 enriched BMSCs as SSCs, given that a proportion of proliferating STRO-1 enriched BMSCs intrinsically undergo cellular maturation over time in basal culture, which could result in increments in osteoblastic gene expression as well as ALP activity.

Figure 3-6 and Figure 3-7 also highlight the inherent variation of patient responses to 1,25-VitD3 stimulation. An unexpected finding was that 1,25-VitD3 had a much weaker osteoinductive effect on F70 P1 STRO-1 enriched BMSCs, when compared to the other seven patients studied. This observed effect could be a result of 1,25-VitD3 resistance through a rare hereditary mutation in the Vitamin D receptor gene or an environmental factor (237). The ethics restrictions of this research project do not allow for additional medical history (personal or familial) or medication information to be disclosed, making it impossible to accurately identify or conclude the cause(s) for these observed variations. Furthermore, calculated variance for time and culture approach (and their interaction) did not show either factor had a statistically significant effect on gene expression levels between the two cohorts studied (with the exception of OCN as listed in Table 3-3). Despite these issues and the relatively few subjects tested, the overall results obtained in this study still suggested that donor age, sex differences, and cell passage number, did not significantly affect the osteogenic potential of STRO-1 enriched BMSCs, which is in keeping with work performed by Brusnahan *et al* (238).

3.1.5 Conclusions

STRO-1 enriched BMSCs were shown to undergo osteogenic differentiation when induced by 1,25-VitD3, developing a stellate morphology and demonstrating increased ALP activity as well as increased Runx2, Col1a1, OPN, and OCN gene expression levels over time, despite the inherent biological variation among patient responses to 1,25-VitD3 stimulation. The above findings suggest that STRO-1 enriched BMSCs could potentially be a suitable cell source for use in bone tissue regeneration. To further confirm the feasibility of utilising these cells for bone repair purposes, the next phase of this research project involved the evaluation of the biocompatibility, and effect, if any, of seeding STRO-1 enriched BMSCs onto a commonly used biomaterial in medical devices and implants, titanium.

3.2 The osteoinductive effect of titanium on STRO-1 enriched BMSCs

3.2.1 Introduction

Metals, such as stainless steel, cobalt-based alloys, as well as titanium and its alloys, have served as mainstream materials for creating biomedical implants with superior mechanical strength and resilience for use in long-term load-bearing applications, for many years in comparison to biomaterial alternatives such as polymers and bioceramics. Titanium, an allotropic element discovered in 1791, was only able to be isolated in sufficient amounts in 1946 when the Kroll process was invented. To date, titanium and titanium alloys are preferred for biomedical applications, given their high elastic modulus, proven biocompatibility, and established resistance to corrosion and fatigue deformation (239, 240). The crystallographic structure of medical grade pure titanium is alpha phase (hexagonal closed-packed), while alloys such as Ti6Al4V are alpha-beta phase (both hexagonal closed-packed and body-centred cubic). The spontaneous formation of a 1.5 to 10 nm thick native oxide film (TiO_2), on the surface of titanium (and titanium alloys) upon exposure to air at room temperature has been identified as primarily responsible for the physical and biological properties of titanium (241). However, significant numbers of titanium-based load-bearing implants still fail within 15 years of implantation because of infection, aseptic loosening and interfacial instability due to poor bonding between the bone and the implant surface (242). Stress shielding caused by a mismatch in modulus between bone and implant (10 to 30 GPa for cortical bone compared to 120 GPa for titanium alloys) and wear-induced osteolysis due to excessive metal ion release in the implant area (particularly with alloy-based implants) are additional factors that can lead to implant failure in patients (240, 241).

Given an increasingly ageing population worldwide, there has been a rapid expansion of research in the field of biomaterials and scaffold fabrication methods for tissue engineering and regenerative medicine purposes (243), with an increasing trend towards utilising polymeric, ceramic, and/or organic materials (or a combination thereof) to generate biocompatible scaffolds with varying geometry, porosity, and topography (244). In the past decade, there has been growing interest in the use of various AM techniques for the generation of these scaffolds, with tissue biofabrication becoming a major focus of tissue engineering research (245, 246). A concurrent development in bone tissue engineering has seen an increased use of porous-surfaced and highly porous metallic implants. Their popularity is due to increased clinical success in their use in hip and knee arthroplasties. Ongoing optimisations to fabrication methods to further improve

the success of these implants are currently being investigated (247). One approach has been to utilise surface modification techniques to generate topographical adjustments at a micro- and nano-structural level in the creation of new orthopaedic and dental implants. Surface characteristics of biomaterials have previously been shown to exert a critical influence over the speed of osseointegration (248, 249). Implants that can rapidly osseointegrate enhance implant stability and allow for earlier implant loading and patient mobility (250). Such surface modification approaches have been demonstrated *in vitro* and *in vivo* to facilitate earlier osseointegration between the implant surface and native bone (251-255), crucial for healing and successful bone regeneration in-situ. Approaches to enhance osseointegration include i) anodic oxidation to enhance the thickness of the naturally occurring oxide layer, ii) sandblasting, or acid etching to create surface roughness for enhanced cellular adhesion and survival, and wear resistance of titanium implants (256). However, elements within titanium alloys can form other oxides on the alloy surface, reducing the efficacy of treatments (241). A simple, alternative approach is scaffold surface coating. Studies utilising biochemical or biomimetic modification techniques to add collagen type 1 (257), alginate hydrogels containing simvastatin (258), polytetrafluoroethylene (259), and amorphous calcium and phosphorus (260) to titanium implants have shown increased osteogenesis of seeded human MSCs, human osteoblasts, MG63 cells, and osteoprogenitor cells respectively.

Increasing surface micro-roughness, with feature sizes similar to osteoclast resorption pits (up to 100 µm in diameter) and cell dimensions, can enhance osteoblast differentiation and local factor production *in vitro*, increase bone-to-implant contact *in vivo*, and improve wound healing (254). There remains, however, conflicting evidence regarding the effect of nano-scale surface roughness on osteoblast differentiation, particularly in the concomitant absence of micro-scale surface roughness. Indeed some studies have attempted to combine both micro- and nano-scale roughness to promote osseointegration (253, 261). Although initial results appeared to show increased osteoblast proliferation and differentiation, the creation of such tailored surfaces without alteration or modification of other surface characteristics, has proved challenging and separation of nano-scale effects from other surface features, for example, surface chemistry, surface energy and micro-scale roughness (254), has proved difficult.

A different approach has been the development of porous materials for coating load-bearing implants to enhance bone ingrowth and thus improve implant fixation (240, 262-264). However, the optimal pore size in facilitating cell infiltration and colonisation remains debatable (240, 262, 265, 266). Nevertheless, there is a general consensus that increasing the porosity of any device results in decreased mechanical integrity and

modulus (267). Traditional methods for fabricating porous titanium alloy implants include freeze casting, solid state processing (powder or fibre sintering, metallurgy), electro-deposition, space holder method, and liquid state processing (direct or spray foaming, metal injection moulding) (241). Typically, the final product is brittle due to localised stress concentrations at pore walls, and the shape and size of porosity achieved with such techniques is somewhat random. These limitations can be partially overcome with the use of AM technologies such as selective laser melting (268, 269), selective electron beam melting, and laser engineered net shaping (264). It must be noted that the quality of the generated constructs can vary considerably depending on design and fabrication parameters, which in turn, are closely related to the type of AM process being used. Post-processing steps (such as heat treatment or surface modification techniques) are usually required to reduce thermal stresses within the structures generated and to minimise microstructural changes that occur as part of the layer-by-layer building process (270).

Titanium has long been investigated for its biocompatibility and its effect on different cell types such as MG63 cells (271), osteoblasts (272), and human MSCs (255). However, no previous study has investigated the effect of titanium on STRO-1 enriched BMSCs, despite their osteogenic potential as shown in 3.1. Given the challenges faced in improving current implant technology for bone replacement therapy and the potential systemic toxicity of alloys in use in current implants, laser-modified microporous, micro-rough medical grade IV titanium templates were utilised to determine how i) surface topography, ii) composition, iii) wettability, and iv) pore geometry and size, could influence the cellular behaviour of STRO-1 enriched BMSCs, in addition to whether such properties could induce the osteogenic differentiation of STRO-1 enriched BMSCs even under basal conditions. STRO-1 enriched BMSCs cultured on standard tissue culture polystyrene (TCP) in basal and osteogenic conditions (the latter containing 25 nM 1,25-VitD3) were chosen as comparative controls to ascertain any differences in the viability, proliferative capacity, and extent of osteoinduction of these seeded STRO-1 enriched BMSCs. This approach was designed to differentiate the impact of culture conditions and biomaterials on the osteogenic differentiation of the seeded cells. Seeded surfaces of these templates were also inverted and suspended within a culture well to better simulate a three-dimensional culture environment to further determine if such conditions could affect cellular adhesion and migration (and indirectly, osseointegration). Lastly, as titanium- and alloy-based surfaces are known to react with their microenvironment (potentially reducing the efficacy and osseointegrative capacity of implants) this study investigated whether different methods of sterilisation and storage could alter the surface properties of titanium templates.

As stated in 1.9, the hypotheses of this thesis are:

1) Human STRO-1 enriched BMSCs possess, and retain, the capacity for osteogenesis when seeded onto scaffolds, and are therefore a suitable cell type for use in bone reparation.

2) Biomaterials can be combined to generate tuneable bioinks, which can be used to deliver STRO-1 enriched BMSCs with high viability and functionality.

3) 3D printing methods are capable of manufacturing porous scaffolds of clinically relevant size with high resolution and reproducibility.

4) STRO-1 enriched BMSCs, biomimetic bioinks, and 3D printed polycaprolactone-based scaffolds can be combined to create an integrated bioconstruct for use in bone repair.

In conjunction with the above hypotheses, the aims of this research project are:

1) To confirm the osteogenic potential of STRO-1 enriched BMSCs.

2) To elucidate the osteoinductive capabilities of established biomaterials, such as titanium and polycaprolactone (amongst others), in order to identify potential combinations for the generation of composite scaffolds and/or bioinks for use in bone tissue engineering.

3) To design novel porous scaffolds that mimic natural bone architecture.

4) To investigate the feasibility of utilising 3D printing techniques to accurately and reproducibly manufacture scaffolds according to their design.

5) To determine the possibility of 3D printing cell-laden bioinks.

6) To develop methods for integrating 3D printed scaffolds, biomimetic bioinks, and STRO-1 enriched BMSCs, with the objective of creating functional bioconstructs for use in bone reparation.

3.2.2 Materials and Methods

3.2.2.1 Production of laser processed porous titanium templates

Titanium templates (10 x 10 x 0.1 mm) were manufactured under commercial license by Industrial Technology Research Institute, Taiwan, and provided by Taipei

Medical University, Taiwan (Figure 3-8). Each titanium template was machined in air using an 800 nm wavelength regenerative amplified titanium:sapphire laser (SPITFIRE, Spectra-Physics), operated at a repetition rate of 1 kHz, with a pulse duration of 120 fs. Maximal pulse energy was 3.5 mJ. The laser power was monitored by a detector and adjusted using a half-wave plate and a polarisation beam splitter. A mechanical shutter controlled irradiation timing. The machining lens comprised a long working distance 10x objective lens, with 0.26 numerical aperture (M Plan Apo NIR, Mitutoyo). The position of the objective lens could be adjusted in the z-axis, and the focused spot diameter used was approximately 5 µm. Micropores were produced by moving the sample on an x–y mobile stage. The fabrication process was monitored continuously via a coaxial machine vision system. 90 µm pores were created on one surface of a medical grade IV titanium sheet using the focused laser beam which bored through the thickness of the material (in a conical fashion), generating 9 µm pores on the under-surface of the 0.1 mm-thick titanium sheet. The pore sizes were chosen to mimic the size of osteoclast resorption pits, which can measure up to 100 µm in diameter. The edges of each template were generated by laser cutting.

Fifty templates underwent post-processing ethylene oxide sterilisation (EOS) at Taipei Medical University Hospital, Taiwan. Once sterilised, each template was individually vacuum-sealed in sterile packaging. Twenty templates were rinsed in an antibacterial, anti-mycotic solution before being exposed to ultraviolet light (UV) for two hours and air-dried, prior to storage at room temperature in a sealed petri dish. Four non-patterned medical grade IV titanium squares were also provided for surface characterisation comparison testing.

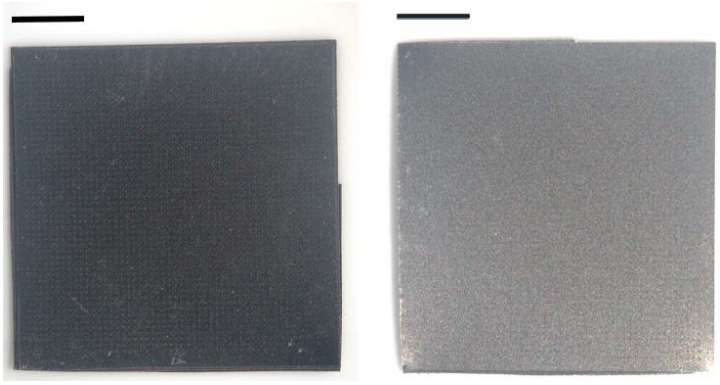

Figure 3-8 Titanium template surfaces.

Left: Photograph of the 90 µm pore surface, showing the regular pore pattern imprint on the template surface. Right: Photograph of the under-surface. Scale bars represent 200 µm.

3.2.2.2 Surface characterisation

3.2.2.2.1 Surface appearance and roughness

Qualitative assessments of the macro-and microstructure of each surface were acquired by scanning electron microscopy (SEM, FEI Quanta 200, Thermo Fisher Scientific, USA). Cell-free templates were analysed without the addition of a conductive coat. The working distance for visualisation was between 9.53 and 9.62 mm, with a spot size of 3 nm, and an accelerating voltage of 10 kV under high vacuum conditions.

Colleagues at Taipei Medical University measured the surface roughness of each surface of a cell-free EOS template using a microfigure measuring instrument (ET4000A, Kosaka Laboratory Ltd., Japan). Each sample was fixed onto a sample platform and scanned using a 1 µm needle tip, under a 10 µN force and a speed of 5 mms^{-1}, for 1 mm in length. Roughness values (arithmetic average roughness: R_a, and geometric average roughness: R_q) were calculated from measurements performed at three different points per sample. In order to determine whether the manufacturing process resulted in changes to the surface roughness, similar measurements were carried out on non-patterned medical grade IV titanium (cut to the same dimensions).

3.2.2.2.2 Surface chemical composition and wettability

Colleagues at Taipei Medical University used a JEOL JSM-6500F SEM (JEOL Japan, Inc., Japan) with a Si(Li) detector to perform energy-dispersive X-ray spectroscopy (EDS) to determine the surface composition of non-patterned medical grade IV titanium, EOS, and UV titanium templates. As the tested templates contained no biological material, no fixation or drying steps were required. Each template was fixed onto a copper stub and electrically grounded by carbon coating, before each surface was sputter-coated with an ultra-thin platinum film. Imaging was then performed in a high vacuum using a 10 kV electron beam and working distance of 15 mm. Single-point measurements and mapping analyses were performed using INCAEnergy software (Oxford Instruments, UK). Each surface characterisation procedure was performed on six regions of two areas of each template per sterilisation method, and the average reading from two templates was calculated.

Surface wettability is the ability of a liquid to maintain contact with a solid surface, and is the net result of intermolecular adhesive and cohesive forces. The

angle made by the intersection of the liquid/air and liquid/liquid interfaces is known as the contact angle. As the spreading tendency of a liquid drop over a flat, solid surface increases, the contact angle decreases, indicating a high wettability. The size of the contact angle is inversely proportional to surface wettability (Table 3-4).

Contact angle	Degree of wettability	Strength of solid-liquid interaction
Θ = 0	Perfect (Superhydrophilic)	Strong
0 < θ < 90°	High (Hydrophilic)	Strong to weak
90° < θ < 150°	Low (Hydrophobic)	Weak
Θ > 150°	Superhydrophobic	Weak

Table 3-4 Relationship between contact angle and surface wettability.

Adapted from (273).

As surface wettability is important in determining cell adhesion (254), it was measured by performing contact angle testing using a GBX Digidrop-DI goniometer (which utilises the sessile drop technique) and its accompanying Visiodrop software (GBX, Ireland) by colleagues at Taipei Medical University. The flat titanium scaffold was positioned on a stage, directly under a 1 ml syringe containing 0.2 ml of deionised water, with a needle attached (internal diameter of 0.61 mm). This syringe was held in place by an aluminium block syringe holder, allowing the software to focus onto the needle tip (focus value of 170 to 180 was used), and the capture window was adjusted to include the tested scaffold surface within its limits. Turning the ratchet pushed down the syringe plunger to create a hanging droplet, the volume of which was estimated by the software. A water droplet volume of 1.5 µl was used for every measurement. A video recording, using a Pixelink camera, captured the images from the time the droplet detached from the needle onto the scaffold surface (by bringing up the stage containing the scaffold to upwards at a steady speed) to the last point where the droplet completed spreading over the scaffold surface. The first image still of the droplet whereby there was no change in its base line on the surface was used to obtain the contact angle measurements. A point was selected on the left bubble edge, followed by the right, and then the apex of the bubble. This automatically gave the left, right, and average angle reading, θ. Point selection was repeated five times per position to improve accuracy. Contact angle measurements per scaffold were performed at three positions on the 90 µm pore surface, with five scaffolds tested per sterilisation method.

3.2.2.3 Isolation, culture, and seeding of human STRO-1 enriched BMSCs

As previously detailed in 3.1.2.1 and 3.1.2.2, STRO-1 enriched BMSCs were isolated from human bone marrow samples from two male patients (aged 66 and 67) and a female patient (aged 70) following hip arthroplasty, with full written, informed patient consent and ethical approval (NHS England Local Research Ethics Committee, number 194/99). Culture media was changed every three to four days. Cells were passaged at 70 to 80% confluency. All experiments undertaken used cells at passage 1 or 2. Cell counts were performed as described in 2.2.

Titanium templates were seeded by manually pipetting 100 µl of basal media containing 1.5 X 10^4 STRO-1 enriched BMSCs directly onto the centre of each template surface. Placing the cell droplet centrally allowed for the observation of cell migration across the template surface during the culture period. This was followed by a 30 minute incubation of the seeded templates in a petri dish placed in a humidified, 37°C, 5% CO_2 incubator. The seeded template surface was inverted prior to being suspended within the well of a Corning® 12-well plate by a custom-made well insert device (see 2.4.1). EOS and UV titanium templates were cultured for 1, 3, 7, 14 and 21 days in basal media (*n* = 3 per time-point). Controls consisted of a similar number of STRO-1 enriched BMSCs seeded onto TCP wells (*n* = 3 per time-point) were cultured in basal and osteogenic media (containing 25 nM 1,25-VitD3).

3.2.2.4 STRO-1 enriched BMSC response and functionality

3.2.2.4.1 Immunocytochemical staining

Seeded EOS titanium templates and TCP controls from days 7 and 14 were fixed in 4% paraformaldehyde for 15 minutes prior to immunocytochemical staining with TRITC-conjugated phalloidin and DAPI as described in 2.6.3. Mouse IgG1 anti-alpha tubulin antibody was used in place of anti-vinculin antibody with no changes to the protocol steps. The final step involved incubation of the templates with HCS CellMask™ Deep Red stain (2 µl per 10 ml PBS; 30 minutes; Thermo Fisher Scientific, USA) which stained the cytoplasm of the seeded cells, allowing for the visualisation of their morphology. Stained titanium templates were kept in PBS prior to imaging using a Leica SP8 Confocal Microscope. Three-dimensional image reconstructions were done using the Leica Application Suite X software.

3.2.2.4.2 Quantitative reverse transcription polymerase chain reaction

Seeded EOS and UV titanium templates (*n* = 3) and TCP controls (*n* = 3) were lysed with TRIzol® reagent (Thermo Fisher Scientific, USA) at day 7, 14, and 21 end-points. RNA extraction, cDNA synthesis and RT-qPCR was performed as described in 2.5 with the exception of TATA-box binding protein (TBP) being used in place of β-actin as the housekeeping gene reference. All primers used are listed in Table 2-2. Relative mRNA levels were calculated using the comparative CT method, and normalised to TBP. Derived relative expression of each gene marker at all time-points was normalised against the relative expression of the same marker from basal day 7 TCP controls.

3.2.2.4.3 Cell viability, proliferation, and functionality

To determine cell viability, triplicate seeded EOS titanium templates and TCP controls in basal and osteogenic conditions were exposed to 0.4 mM Calcein AM and 2 mM ethidium homodimer-1 (Thermo Fisher Scientific, USA) for 1.5 hours in a 37°C incubator at days 1, 3, 7, 14, and 21.

STRO-1 enriched BMSC proliferation on EOS titanium templates and TCP controls in basal and osteogenic conditions at days 3, 7, 10, 14, and 21 were determined using a WST-1 cell proliferation assay (Roche, Switzerland), as per the manufacturer's protocol. Water-soluble tetrazolium is transformed into formazan by mitochondrial succinate dehydrogenase in metabolically active cells. A 1:10 dilution of the reagent to media was used to incubate the samples over a 3 hour period. 100 µl of the resultant mixture was plated in triplicate for each sample in addition to a control consisting of basal media and the WST-1 reagent (incubated under the same conditions). A Varioskan® Flash microplate reader (Thermo Fisher Scientific, USA) was used to read the corresponding optical densities at 420 nm, with a reference reading at 610 nm.

The interaction between the seeded STRO-1 enriched BMSCs and EOS titanium template surface topography was qualitatively examined using a FEI Quanta 200 SEM at days 7, 14, and 21 as per the protocol described in 2.7. The samples were coated with a 7 µm gold-palladium film. The working distance for visualisation was between 10.66 and 11.83 mm, with a spot size of 4 to 4.5 nm, and an accelerating voltage of 10 kV under high vacuum conditions.

Triplicate culture supernatants from seeded EOS titanium templates and TCP controls were collected at days 3, 7, 10, 14, and 21 for ALP activity analysis

using a colorimetric assay (Abcam, UK), according to the manufacturer's instructions. Culture media was changed 24 hours prior to each assay to ensure that the ALP activity measured was over a 24-hour period. This assay kit utilises p-nitrophenyl phosphate as a phosphatase substrate, which turns yellow when dephosphorylated by ALP. Following a 1 hour incubation in the dark in a 25°C incubator, the optical density of the samples and standards was read using a Varioskan® Flash microplate reader at an absorbance wavelength of 405 nm. The results presented are calculated activity values based on the absolute absorbance readings obtained, with no normalisations performed.

3.2.2.5 Statistical analysis

Values are presented as means ± standard deviation. Two-way ANOVA analyses with *post-hoc* testing, was conducted on the influence of culture time and culture approach on cellular proliferation, ALP activity and gene expression. Culture time groups consisted of day 7, 14, and 21 end-points. Culture approach comprised of basal media, osteogenic media, and EOS and UV titanium groups.

3.2.3 Results

3.2.3.1 Surface appearance and roughness

SEM images revealed that the laser process created templates with dual surfaces consisting of a uniformly porous pattern (Figure 3-9). These regularly aligned pores were conical in shape (Figure 3-9). On the upper surface of a template, the pore diameter measured 90.9 ± 2 µm, with an interpore distance of 203.3 ± 1.9 µm while pore diameter on the under-surface measured 9.4 ± 1.1 µm. High magnification SEM images showed the 90 µm pores had a coarser appearance when compared to the interpore areas (Figure 3-9). This difference in surface roughness was confirmed by surface roughness measurements, which demonstrated the 90 µm pore area had a R_a of 2.21 ± 0.27 µm, and a R_q of 3.21 ± 0.34 µm, with the interpore areas (indicated by black arrows) demonstrating R_q values within a 1 µm range (Figure 3-10). The under-surface displayed a R_a of 0.26 ± 0.04 µm, and a R_q of 0.4 ± 0.03 µm (Figure 3-10). The laser process increased the surface roughness of non-patterned medical grade IV titanium, as evidenced by surface roughness measurements of the upper-surface that revealed a R_a of 0.16 ± 0.02 µm, and an R_q of 0.21 ± 0.02 µm (Figure 3-10), The under-surface displayed a R_a of 0.09 ± 0.01 µm, and an R_q of 0.12 ± 0.01 µm (Figure 3-10).

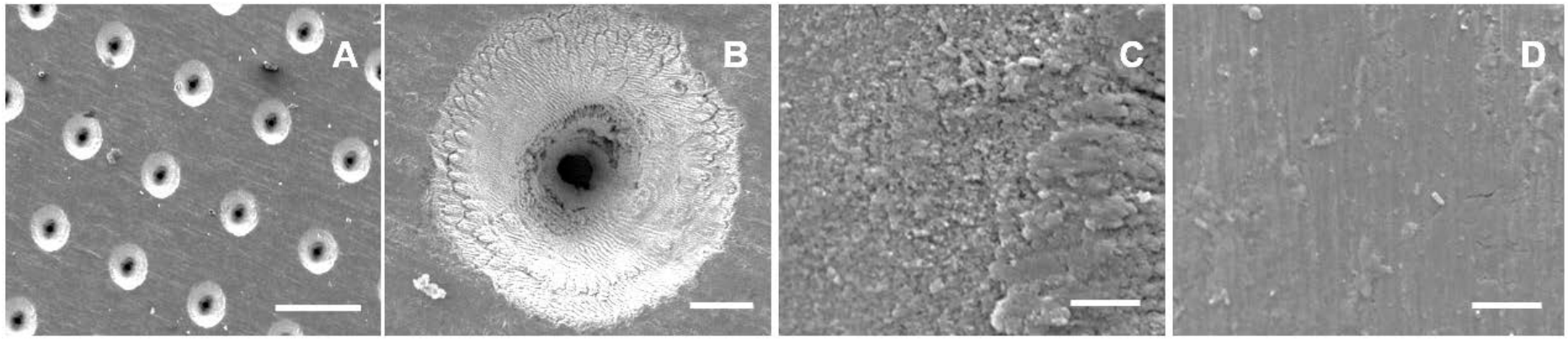

Figure 3-9 Surface appearance of cell-free titanium templates using SEM.

The images demonstrate the different surface topographies across the template surface. A) An overview of the 90 µm pore surface (scale bar represents 200 µm). B) A higher magnification view of a 90 µm pore (scale bar represents 20 µm). C) Surface roughness is evident at a microscale level within the vicinity of the 90 µm pore (scale bar represents 5 µm). D) The interpore area demonstrates a much smoother appearance (scale bar represents 5 µm).

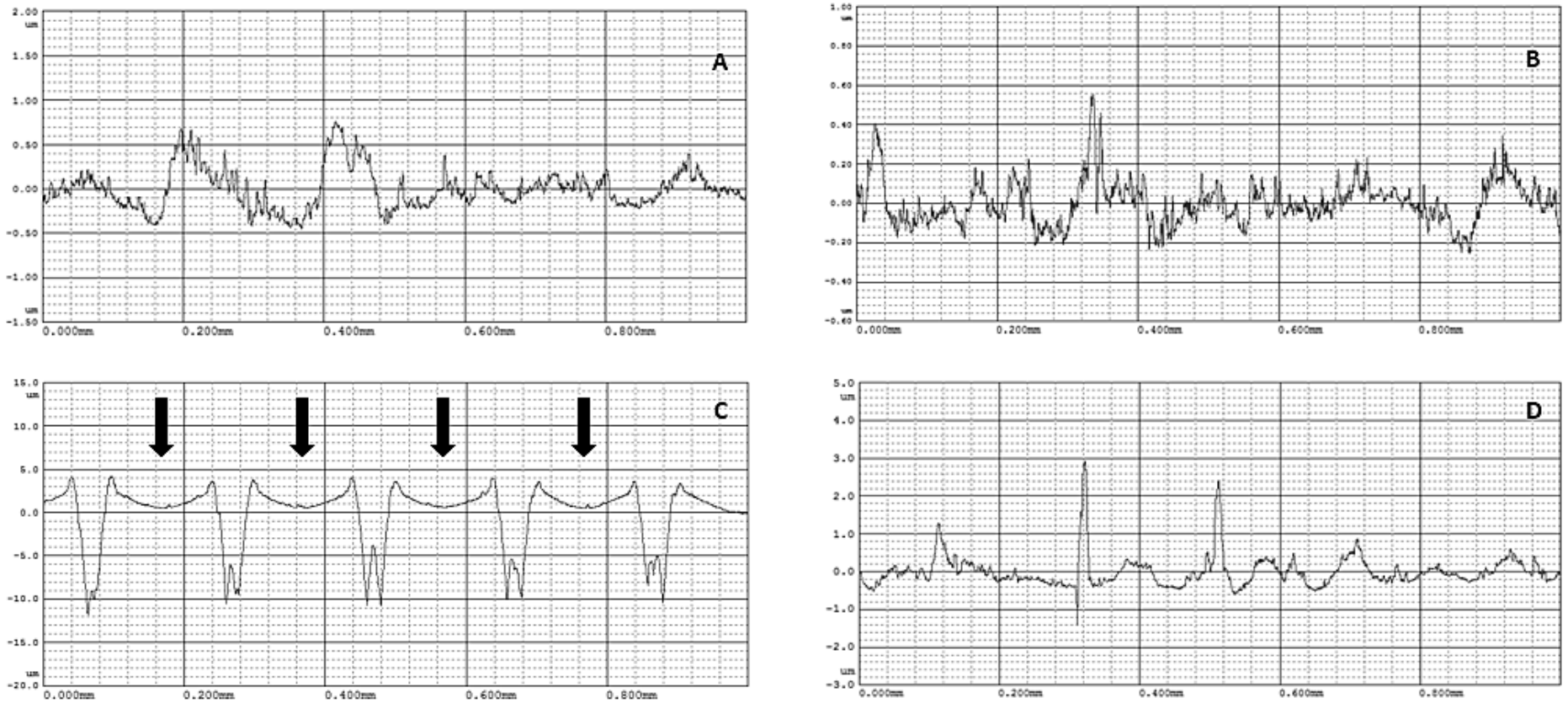

Figure 3-10 Surface roughness measurements.

Surface roughness was determined over a 1 mm length over 3 separate areas of A) the surface of a medical grade IV titanium sheet prior to generation of 90 µm-sized pores, B) the surface of a medical grade IV titanium sheet prior to the generation of 9 µm-sized pores, C) the 90 µm pore surface of an EOS titanium template (black arrows indicate the interpore areas), and D) the 9 µm pore under-surface of an EOS titanium template.

3.2.3.2 Surface chemical composition and wettability

EDS surface mapping revealed that non-patterned medical grade IV titanium controls comprised of 90.2 wt% titanium, 2.7 wt% carbon, and 7.1 wt% platinum. No measurable level of oxygen was detected. EDS surface mapping revealed that EOS titanium templates comprised of 65.8 wt% titanium, 21.6 wt% oxygen, 5.7 wt% carbon, and 6.9 wt% platinum, with the highest concentration of oxygen localised to the immediate vicinity within the 90 µm pores (Figure 3-11Figure 3-11). Focal chemical composition measurements of the 90 µm pore area indicated an average oxygen content of 44.2 ± 3.6 wt% and an average titanium content of 54.1 ± 5.8 wt%. The interpore areas of both surfaces demonstrated no measureable levels of oxygen. EDS surface mapping of the 90 µm pore surface of UV titanium templates revealed the surface was composed of 70 wt% titanium, 18.1 wt% oxygen, 6.4 wt% carbon, and 5.5 wt% platinum, demonstrating a 3.5 wt% reduction in oxygen content in comparison to the 90 µm pore surface of EOS templates (Figure 3-11).

The 90 µm pore surface of EOS titanium templates displayed a contact angle of 87.6 ± 8°, indicating the 90 µm pore surfaces were poorly hydrophilic. Remarkably, the 90 µm pore surface of UV titanium templates had a statistically significant larger contact angle of 112.6 ± 0.9°, which worsened to 118.2 ± 1.5° after two months of storage in air at 25°C, indicating the hydrophobicity of the UV titanium surface increased as the exposed titanium surface interacted with atmospheric particles during storage.

3.2.3.3 Cell adhesion and immunocytochemical staining

SEM image analysis showed STRO-1 enriched BMSCs were adherent on the seeded 90 µm pore surface (Figure 3-13 and Figure 3-13), despite the short incubation time for cell attachment, and the seeded surface being inverted.

HCS CellMask™ Deep Red staining (shown in magenta) confirmed that seeded STRO-1 enriched BMSCs developed an increasingly stellate-shaped morphology over time, as well as a compact and organised aligned orientation of STRO-1 enriched BMSCs within high cell density areas on the template surface (Figure 3-14). Phalloidin staining demonstrated a well-defined localisation of F-actin (shown in red, Figure 3-14) to the apical sides of the cytoplasm in STRO-1 enriched BMSCs while α-tubulin (shown in green, Figure 3-14) extended uniformly from the nucleus throughout the cytoplasm of STRO-1 enriched BMSCs. F-actin and α-tubulin fluorescence signal intensity were noted to increase with culture time, and were

highest in STRO-1 enriched BMSCs seeded on EOS titanium templates (irrespective of cell density). Similarly, organised F-actin and α-tubulin filament orientation was observed within cells within the topmost layer (Figure 3-14 and Video 3-1). However, confocal microscopy revealed that F-actin filament orientation of STRO-1 enriched BMSCs in direct contact with the template surface was not as organised or uniform. Furthermore, F-actin filaments of STRO-1 enriched BMSCs growing within the 90 µm pores were noted to be contracted and condensed (Figure 3-14 and Video 3-1). α-tubulin fluorescence signal intensity of these cells increased over time in culture (Figure 3-15 and Video 3-1). STRO-1 enriched BMSCs cultured on TCP showed fewer F-actin and α-tubulin filament aggregates while filament orientation was markedly less uniform (Figure 3-14). Increased F-actin and α-tubulin fluorescence signal intensities in STRO-1 enriched BMSCs seeded on EOS titanium templates indicated greater cytoskeletal activity in response to stimulation by the EOS titanium template surface topography and surface chemistry, resulting in maintained cellular adhesion despite the culture conditions. Cell confluency severely impeded nuclear and cytoskeletal shape analysis quantification as a function of days in culture at the time points performed.

Leica Application Suite X software was utilised to build a three-dimensional reconstruction of the template, enabling a virtual cross-section analysis of the template (up to a 70 µm depth). Depth image analysis of high cell density areas revealed a two to three cell thick layer on the seeded surface of the template, measuring up to 35 µm (Figure 3-16). Less confluent cell areas showed only an adherent monolayer of cells, up to 10 µm thick. Virtual cross-section reconstruction revealed pore bridging in areas of high cell density. However, STRO-1 enriched BMSCs were only able to grow 25 µm into the 100 µm deep conical pores, and these cells failed to fill the pore space (Figure 3-16, and Video 3-1).

Titanium.mov

Video 3-1 Confocal imaging of adherent STRO-1 enriched BMSCs on the 90 µm pore surface of the titanium templates.

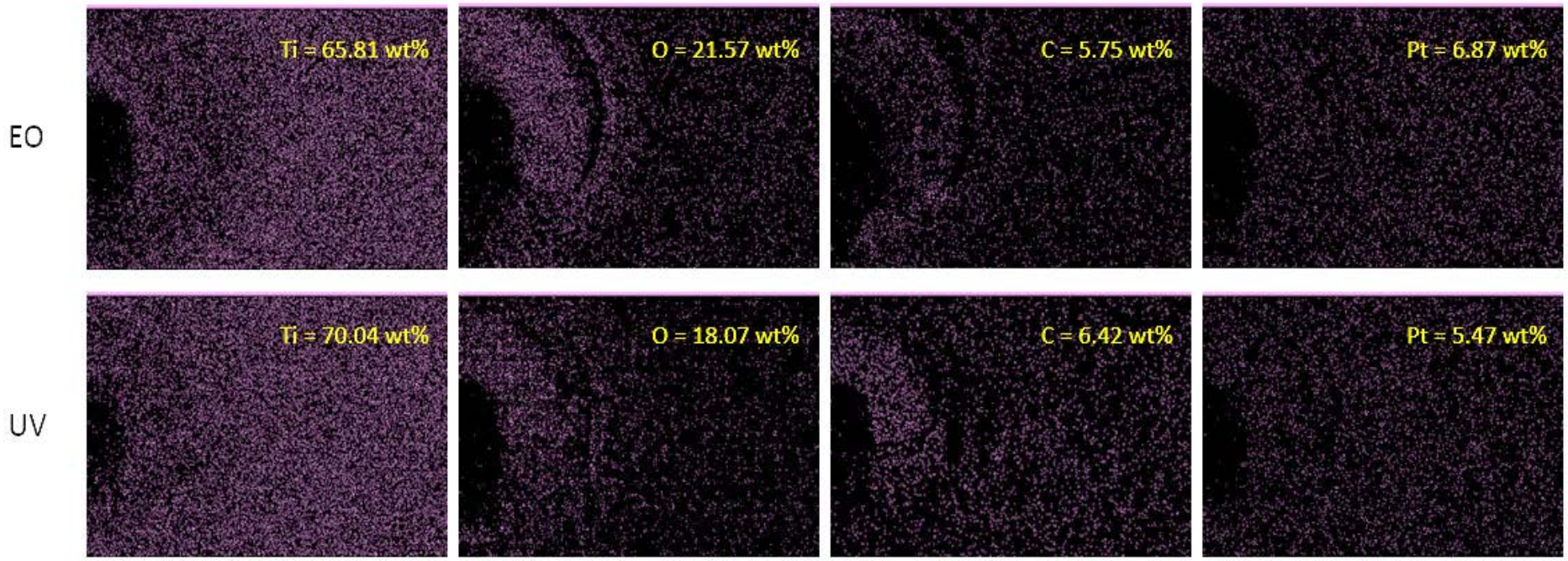

Figure 3-11 Surface mapping by EDS of EOS and UV titanium templates.

EOS templates demonstrated a higher overall weight percent oxygen content when compared to UV templates. Surface mapping (false-coloured magenta) revealed that oxygen distribution was primarily localised to the pore area of the 90 µm pore surface, with a brighter signal intensity in EOS pore areas rather than UV pore areas. This observed difference in oxygen content could be related to the oxidising effect of ethylene oxide gas.

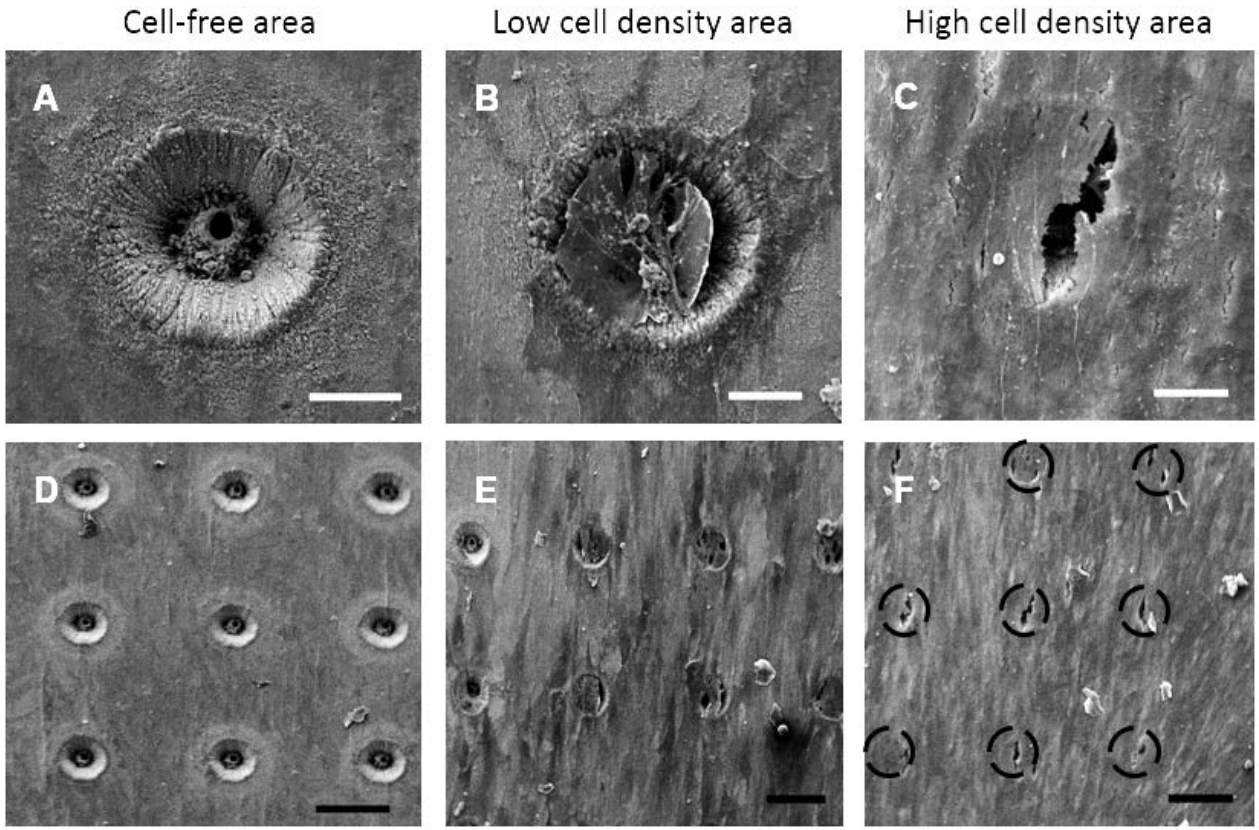

Figure 3-12 SEM images of STRO-1 enriched BMSC-seeded EOS titanium templates at day 7.

A) 90 µm pore without cells (scale bar represents 35 µm). B to C) 90 µm pore appearance as cell density increases (scale bar represents 30 µm). D) 90 µm pore surface without cells (scale bar represents 110 µm). E to F) 90 µm pore surface appearance as cell density increases (scale bar represents 110 µm). Black dashed circles demarcate the 90 µm pores.

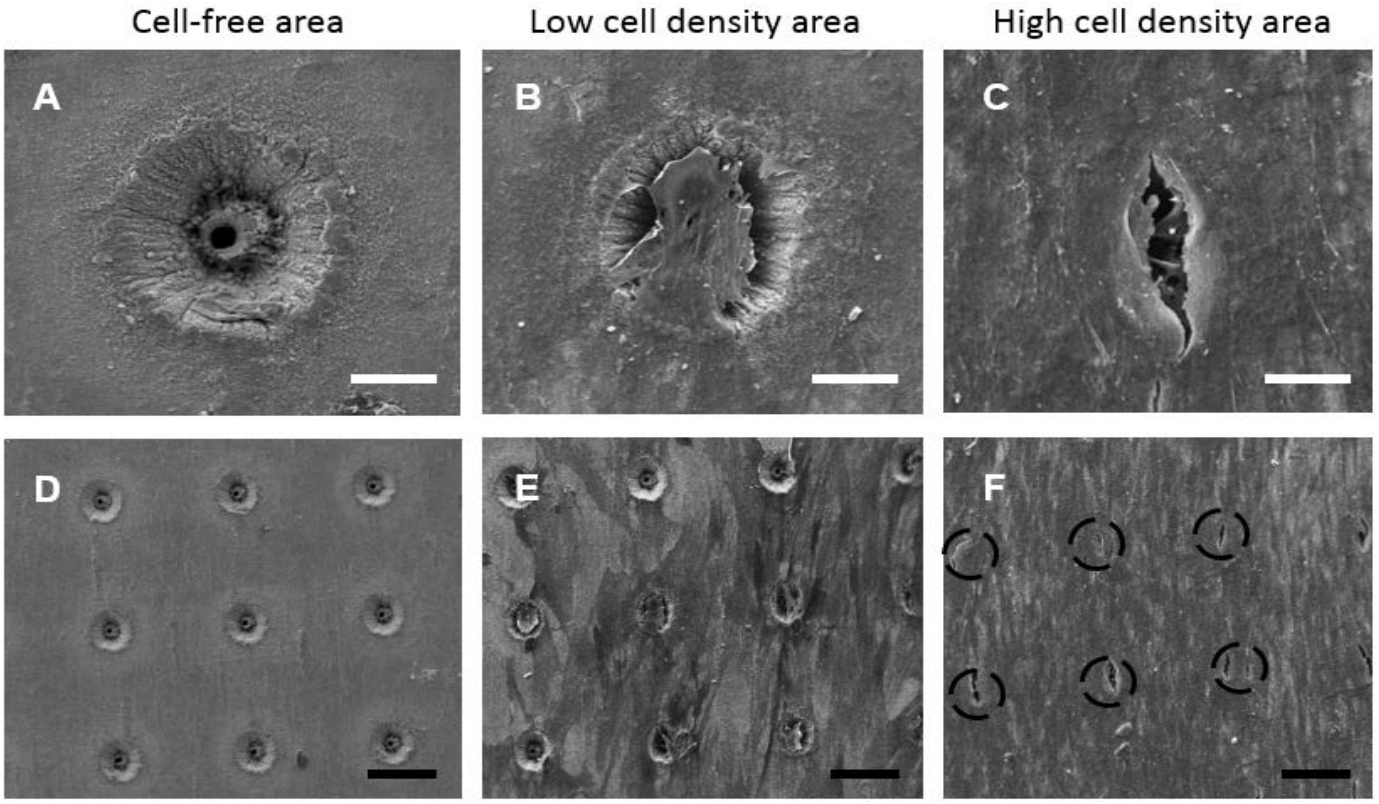

Figure 3-13 SEM images of STRO-1 enriched BMSC-seeded EOS titanium scaffolds at day 14.

The images show the variation in cell density in different areas of a template, in addition to the effect of cell density on cell behaviour on the template surface and pore areas: A) 90 µm pore, no cells (scale bar represents 35 µm). B to C) 90 µm pore appearance as cell density increases (scale bar represents 40 µm), demonstrating cells bridging the pores. D) 90 µm pore surface without cells (scale bar represents 130 µm). E to F) 90 µm pore surface appearance as cell density increases (scale bar represents 150 µm). Black dashed circles mark the position of 90 µm pores.

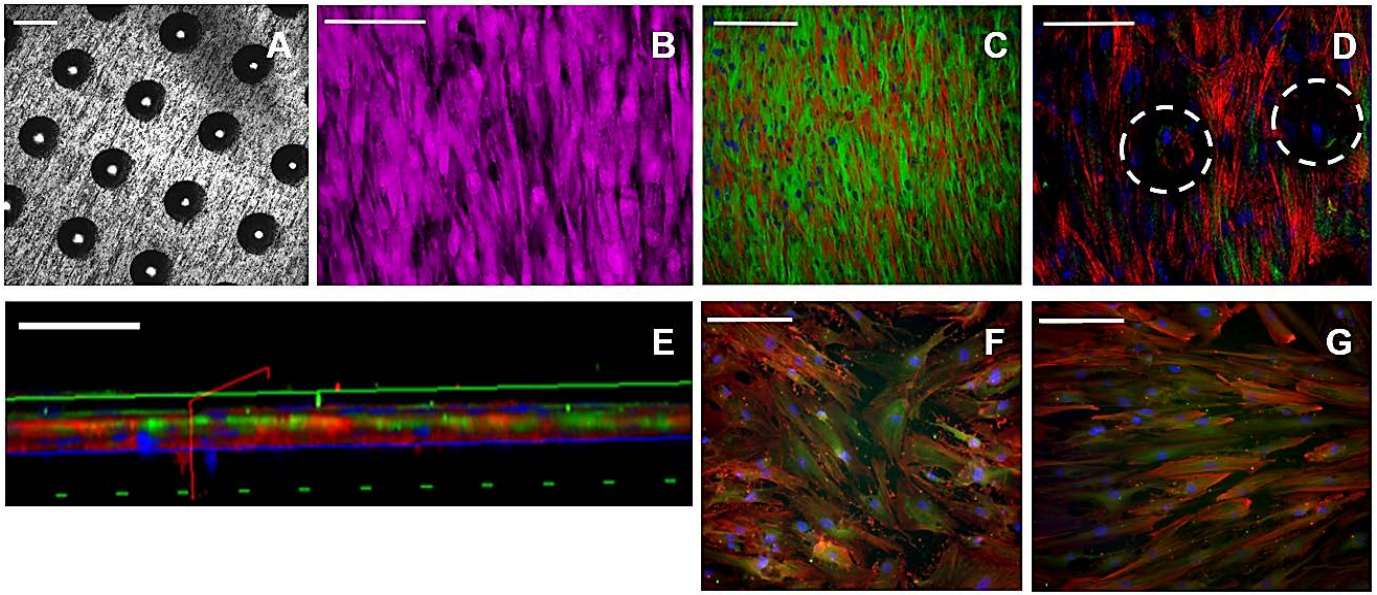

Figure 3-14 Immunocytochemical staining of STRO-1 enriched BMSCs seeded on EOS titanium templates and TCP at day 14.

Confocal microscopy images of the 90 µm pore surface of the titanium template using A) reflectance mode (scale bar represents 100 µm), B) normal mode, showing HCS CellMask™ Deep Red stained STRO-1 enriched BMSCs (magenta) seeded on the 90 µm pore surface of the titanium template (scale bar represents 100 µm). C) Cytoskeletal filament orientation and cell distribution as demonstrated by F-actin (TRITC – red), α-tubulin (AlexaFluor-488 – green), and nuclei (DAPI – blue) stains, scale bar represents 200 µm. D) F-actin, α-tubulin, and nuclei appearance of STRO-1 enriched BMSCs directly in contact with the titanium surface, and STRO-1 enriche BMSCs growing within the 90 µm pores (white dotted circles). Scale bar represents 100 µm. E) Virtual cross-sectional view of (D). The solid blue axis delineates the template surface. Scale bar represents 50 µm. F and G) Cytoskeletal filament orientation of STRO-1 enriched BMSCs cultured on TCP in basal media and osteogenic media respectively. Scale bar represents 200 µm.

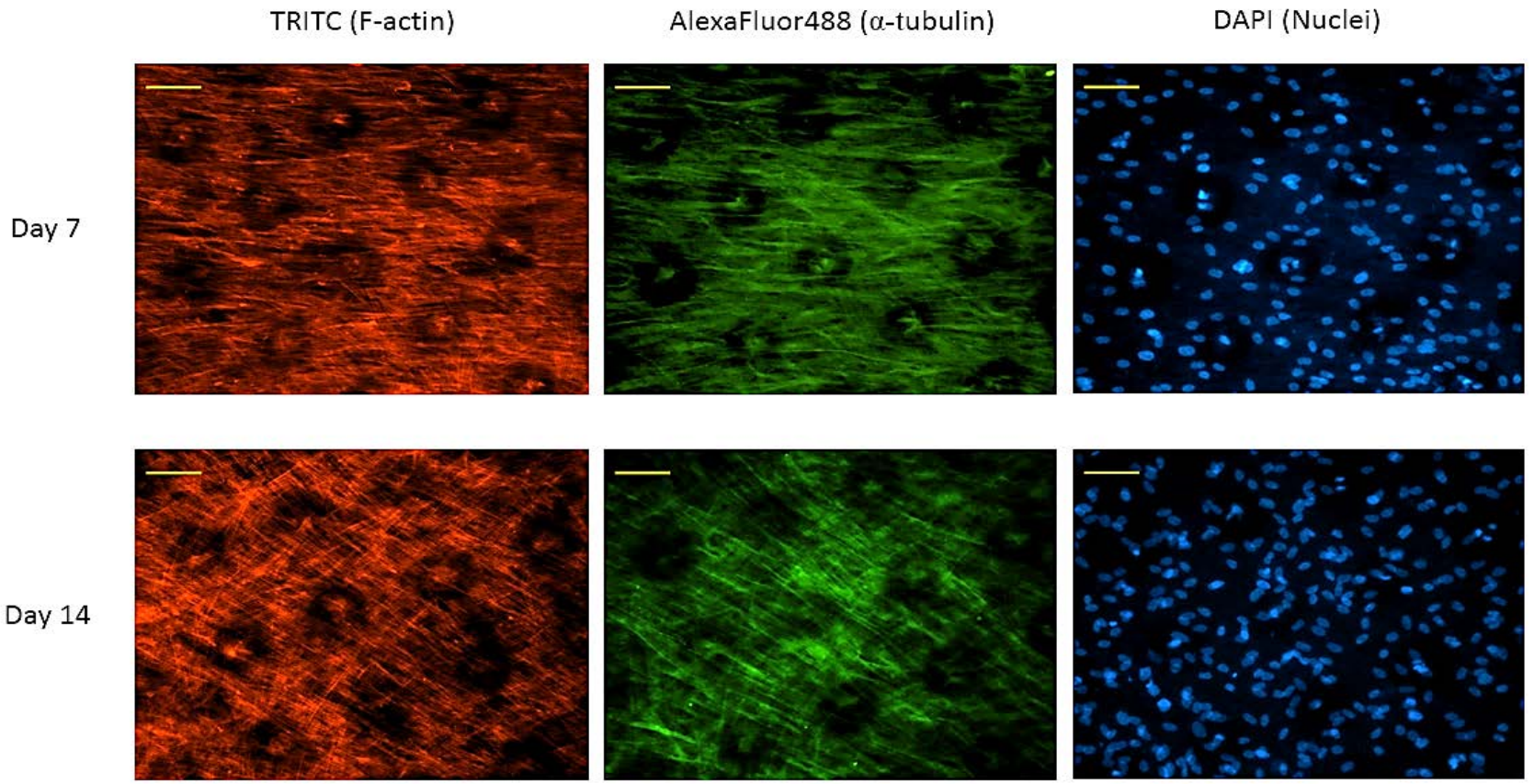

Figure 3-15 STRO-1 enriched BMSC cytoskeletal and nuclei changes over time on EOS titanium templates.

F-actin (red) and α-tubulin (green) filament orientation appears organised by day 7, with a concomitant increase in signal intensity by day 14 as cell density increased due to STRO-1 enriched BMSC proliferation over time, as demonstrated by the increase in nuclei numbers (blue). Scale bars represent 100 µm.

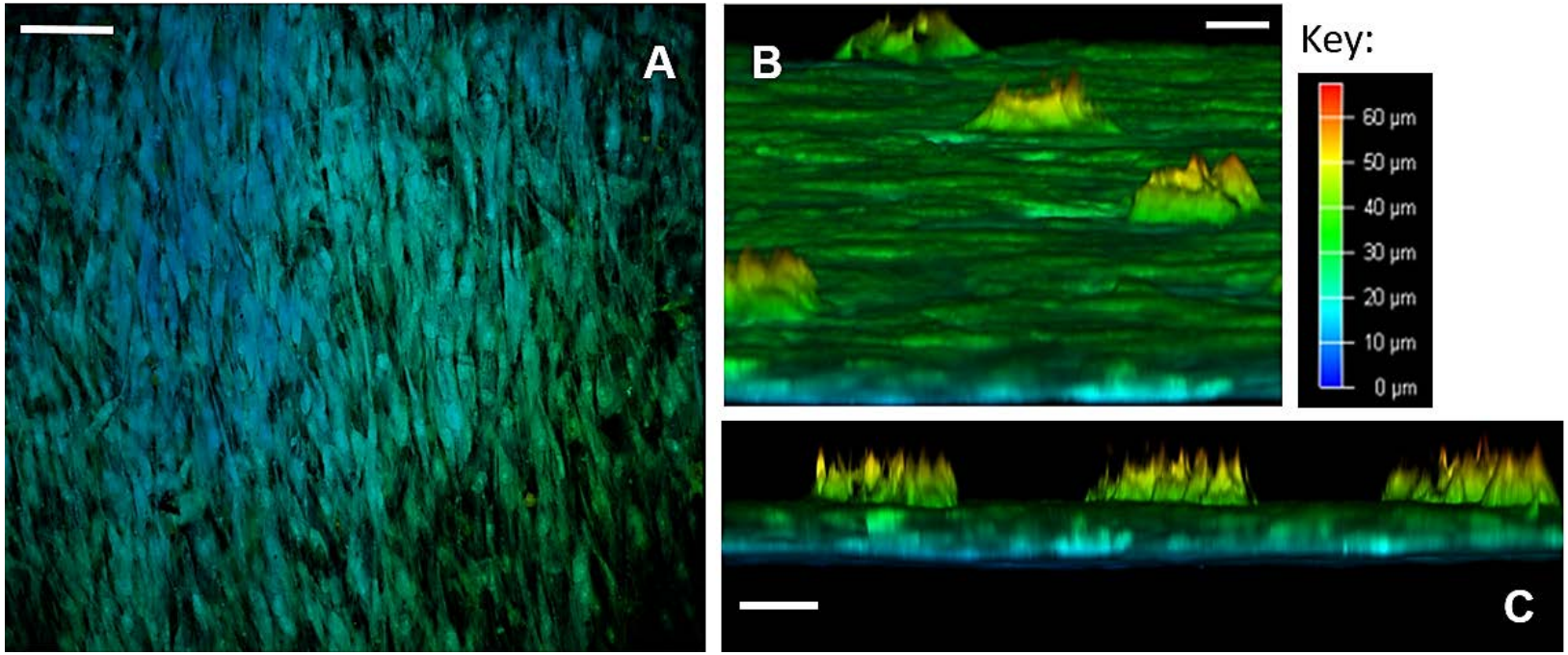

Figure 3-16 Confocal microscopy depth imaging of STRO-1 enriched BMSCs seeded on EOS titanium templates at day 14.

A) Depth imaging revealed the presence of different cell layers covering the template surface. The presence of blue-labelled cells in areas of higher cell density and green-labelled cells in areas of lower cell density indicates cell layer thickness varied by 35 µm on the template surface, depending on cell density (scale bar represents 100 µm). B) Virtual cross-sectional view of the 90 µm pore surface of the template as cultured: STRO-1 enriched BMSCs can be seen growing within the pores up to a depth of 25 µm (scale bar represents 20 µm). C) Virtual cross-sectional view of the titanium template demonstrating the thickness of the cell layer on the template surface, in addition to the uniformity of STRO-1 enriched BMSC growth within the 90 µm pores. Note that STRO-1 enriched BMSCs growing within the pores fail to completely fill the pore space (scale bar represents 50 µm).

3.2.3.4 Quantitative reverse transcription polymerase chain reaction

The derived relative expression of each tested gene marker at all time-points was normalised against the relative expression of the same marker from basal control day 7 samples. TBP was chosen as the housekeeping reference gene as previous studies have shown that β–actin expression changes significantly in three-dimensional culture (274). Two-way ANOVA analyses with Dunnett's multiple comparison test, was performed to determine the effect of culture time and culture approach on gene expression of Runx2, Col1a1, ALP, OPN, OCN, and β–actin. The results are summarised in Table 3-5. The relative gene expression data are summarised in Figure 3-17. Although culture time and culture approach were shown to have a significant effect on gene expression in general, the extent of interaction between these two variables was extremely significant for all gene markers tested. Runx2, the earliest marker of osteogenic differentiation, was significantly downregulated by day 14 in STRO-1 enriched BMSCs seeded on EOS titanium templates. Col1a1 expression was significantly upregulated at day 7, while ALP expression was very significantly elevated in the titanium group at day 21. This elevated ALP expression indicated that seeded STRO-1 enriched BMSCs on EOS titanium were depositing ECM and initiating matrix mineralisation. OPN gene upregulation in the titanium group was initially enhanced at day 7, and remained significantly elevated at days 14 and 21. The degree of increased expression was comparable to STRO-1 enriched BMSCs on TCP maintained in osteogenic media. OCN expression was increased in the titanium group, but to a lesser, non-significant extent. Increased OPN (and OCN expression) indicated that STRO-1 enriched BMSCs seeded on EOS titanium were induced by the template to undergo osteogenic differentiation, albeit to a lesser extent than STRO-1 enriched BMSCs cultured in osteogenic media. A highly significant increase in β–actin expression by day 21 in all three groups was observed, indicating that β–actin expression increased as culture time progressed. Although similar levels of upregulation of Runx2 and Col1a1 expression in STRO-1 enriched BMSCs seeded on UV titanium templates were observed, there was reduced (and less persistent) upregulation of OPN and OCN expression, indicating STRO-1 enriched BMSCs were less induced to differentiate by UV-irradiated titanium (Figure 3-18).

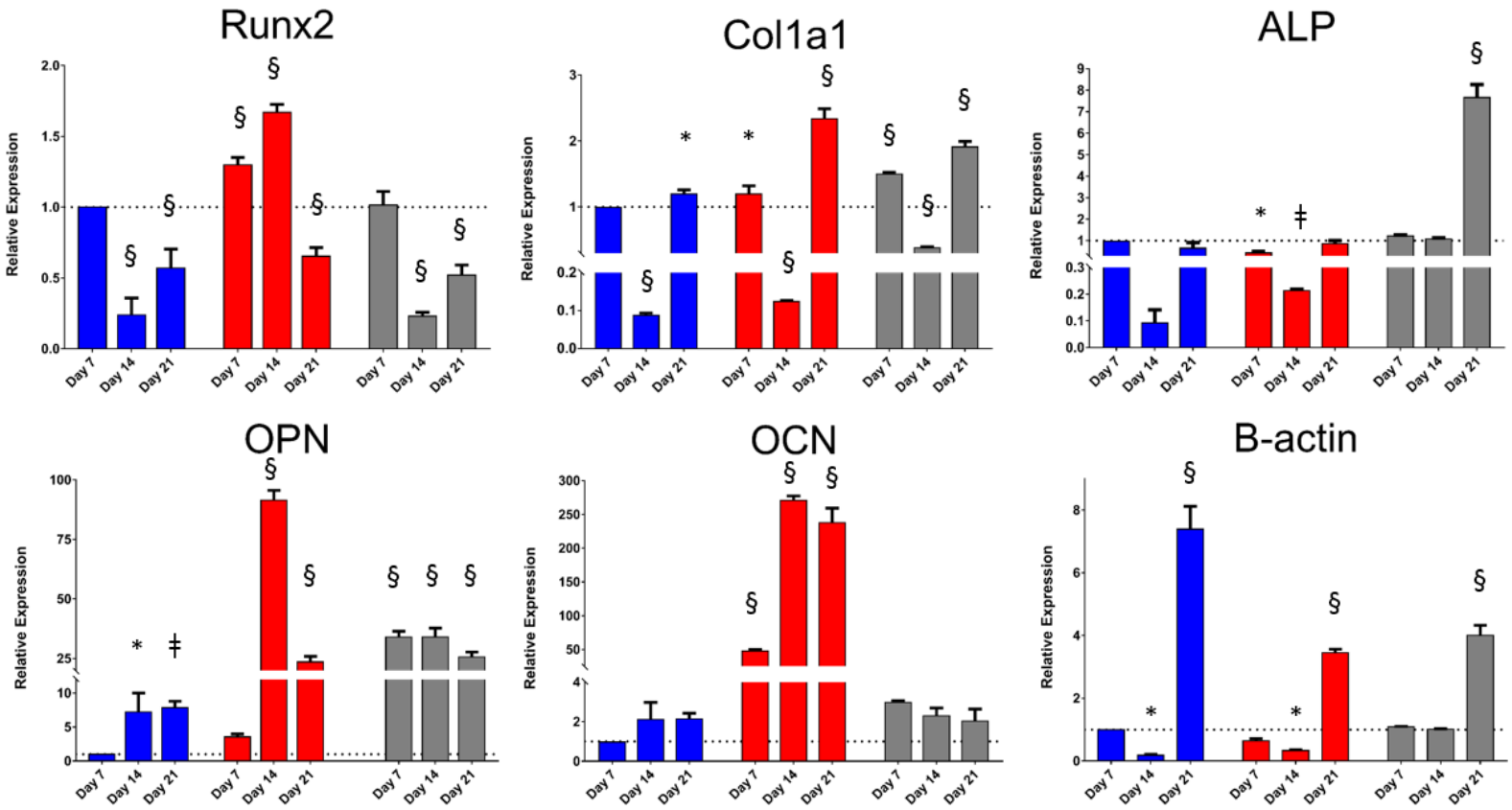

Figure 3-17 Relative expressions of Runx2, Col1a1, ALP, OPN, OCN, and β-actin at days 7, 14, and 21.

STRO-1 enriched BMSCs on TCP were cultured in basal (in blue) and osteogenic (in red) media. STRO-1 enriched BMSCs on EOS templates were cultured in basal media (in grey). Relative expression of each gene marker at all time-points was normalised against the relative expression of the same marker from basal media day 7 samples. (= $p < 0.05$, ǂ = $p < 0.01$, § = $p < 0.001$.)*

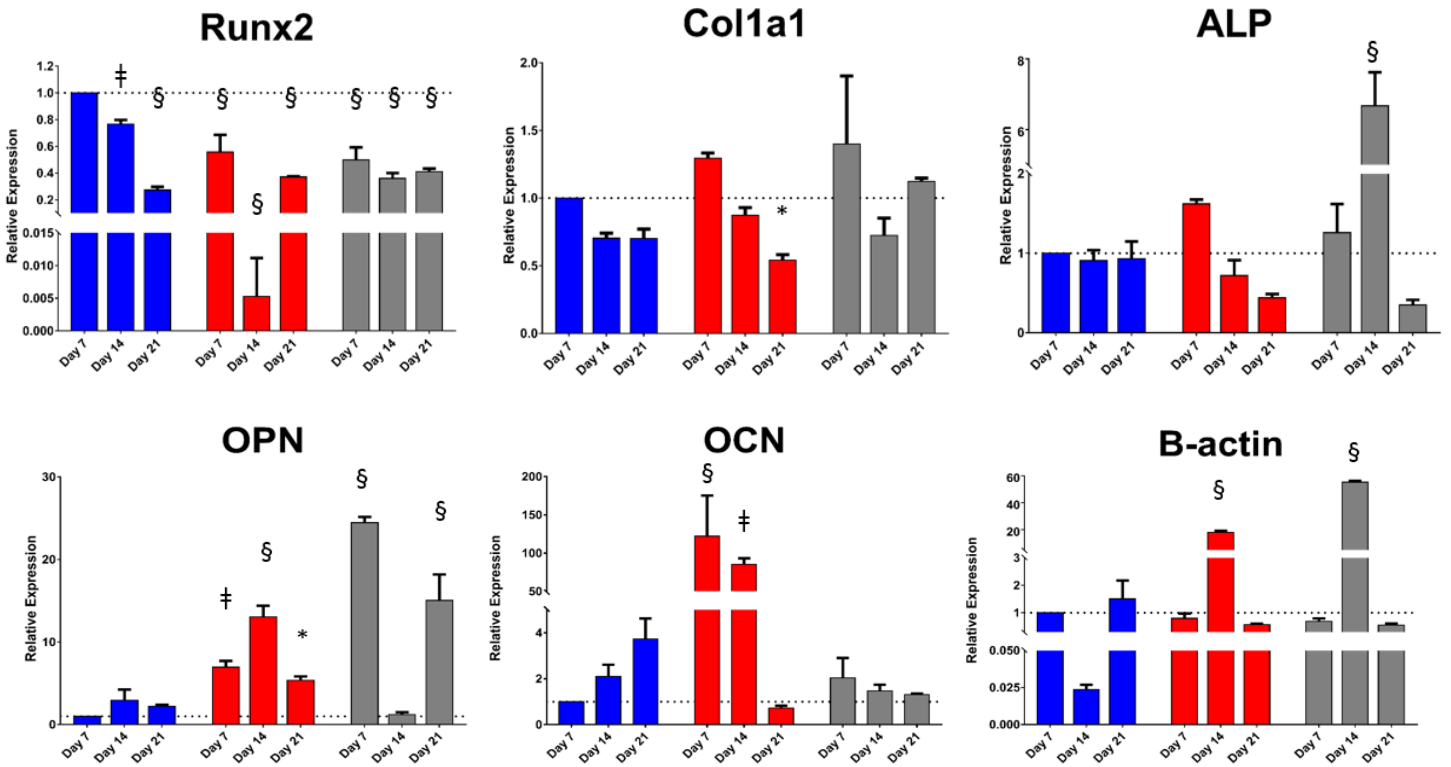

Figure 3-18 Relative expressions of osteogenic differentiation markers Runx2, Col1a1, ALP, OPN, and OCN, and the cytoskeletal marker, β-actin, at days 7, 14, and 21.

STRO-1 enriched BMSCs seeded on TCP were cultured in basal (in blue) and osteogenic (in red) media while those on UV titanium templates were cultured in basal media (in grey). STRO-1 enriched BMSCs cultured on UV templates demonstrated less persistent osteogenic differentiation. This difference could be a consequence of the more hydrophobic surface of UV templates resulting in poorer cell adhesion to the template surface. (= $p < 0.05$, ǂ = $p < 0.01$, § = $p < 0.001$.)*

3.2.3.5 Cell viability, proliferation, and functionality

Excellent cell viability and negligible cell death of seeded STRO-1 enriched BMSCs over the 21-day culture period on the templates was evidenced by strong Calcein AM and a negative Ethidium homodimer-1 staining (Figure 3-19). However, the WST-1 assay revealed a markedly reduced cellular proliferation of seeded STRO-1 enriched BMSCs on the EOS titanium templates at all time-points over the 21 day period in comparison to STRO-1 enriched BMSCs cultured on TCP in both basal and osteogenic media. Maximal cellular proliferation occurred at day 10 in all groups (Figure 3-19). STRO-1 enriched BMSCs cultured in osteogenic media demonstrated a reduction in cellular proliferation after seven days of culture when compared to STRO-1 enriched BMSCs cultured in basal media. Two-way ANOVA analyses with Tukey *post-hoc* testing demonstrated an extremely significant interaction (F (8, 24) = 120, h^2 = 0.048) between culture time (F (4, 24) = 504.6, h^2 = 0.01) and culture approach (F (2, 6) = 1886, h^2 = 0.849) in affecting cell proliferation ($p < 0.001$), resulting in an indistinguishable effect of each variable.

Gene marker	***Variable***	***F (DFn, DFd)***	***p value***	***h^2***
Runx2	Time	F (2, 4) = 84.76	< 0.001	0.231
	Approach	F (2, 4) = 97.34	< 0.001	0.389
	Interaction	F (4, 8) = 181.7	< 0.001	0.36
Col1a1	Time	F (2 ,4) = 1424	< 0.001	0.822
	Approach	F (2 ,4) = 89.35	< 0.001	0.096
	Interaction	F (4, 8) = 89.1	< 0.001	0.076
ALP	Time	F (2, 4) = 248.9	< 0.001	0.263
	Approach	F (2 ,4) = 656.6	< 0.001	0.348
	Interaction	F (4, 8) = 495.6	< 0.001	0.383
OPN	Time	F (2, 4) = 393.2	< 0.001	0.265
	Approach	F (2, 4) = 441.5	< 0.001	0.304
	Interaction	F (4, 8) = 638.4	< 0.001	0.425
OCN	Time	F (2, 4) = 260.1	< 0.001	0.01
	Approach	F (2, 4) = 1844	< 0.001	0.699
	Interaction	F (4, 8) = 299.4	< 0.001	0.198
	Time	F (2, 4) = 505.3	< 0.001	0.783

β-actin	Approach	F (2, 4) = 115.5	< 0.001	0.063
	Interaction	F (4, 8) = 101.8	< 0.001	0.145

Table 3-5 Two-way ANOVA analyses of the effects of culture time and culture approach on the expression of gene markers.

Seeded STRO-1 enriched BMSCs demonstrated a spindle-like morphology within 24 hours of culture, and most progressed to a stellate morphology by day 14 (Figure 3-19), irrespective of cell density. SEM image analysis and Calcein AM staining highlighted the variation in cell density on the template surface, whereby the highest density of cells were localised to the immediate vicinity of the droplet area. In general, cell density decreased from the centre to the edge of templates (Figure 3-13). This pattern emerged by day 3 and remained unchanged at day 21, suggesting limited cellular migration across the template over the culture period. STRO-1 enriched BMSCs were observed to commence formation of colony clusters by day 3, and collectively organised in a similar direction in highly confluent areas by day 14, forming sheet-like cell layers containing minimal intercellular gaps across the template surface, with most 90 µm pores in these areas appearing to be bridged by cells (Figure 3-13). In low confluency areas, cellular orientation appeared disorganised and random, with areas of the template remaining visible. STRO-1 enriched BMSCs grew into the 90 µm pores, with modest bridging of the 90 µm wide gap of each pore by day 7 (**Error! Reference source not found.**).

Figure 3-19 illustrates the ALP activity of the three groups over the 21 day period. ALP activity reached peak values at day 7 in all three groups, before falling to similar levels over the next 14 days. Two-way ANOVA analyses with Tukey multiple comparison test, revealed that the main effect for time groups yielded an F ratio of F (4, 24) = 1042, $p < 0.001$, $h^2 = 0.9894$, indicating that culture time had a significant effect on ALP activity. However, culture approach yielded an F ratio of F (2, 6) = 1.17, $p > 0.05$, $h^2 = 0.001$, indicating non-significance. The interaction effect was not significant, F (8, 24) = 1.61, $p > 0.05$, $h^2 = 0.006$. Tukey *post-hoc* analysis revealed no significant differences in ALP activity between the culture groups at each time point except at day 14, where ALP activity remained significantly higher in the EOS titanium group in comparison to the other 2 groups (basal-osteogenic = non-significant, basal-titanium = $p < 0.01$, osteogenic-titanium = $p < 0.05$) (Figure 3-20). Coupled with WST-1 results showing a markedly lower cell proliferation rate in the EOS titanium group and higher ALP gene expression over

time in STRO-1 enriched BMSCs seeded on EOS titanium, the results indicate enhanced ALP production by STRO-1 enriched BMSCs cultured on EOS titanium.

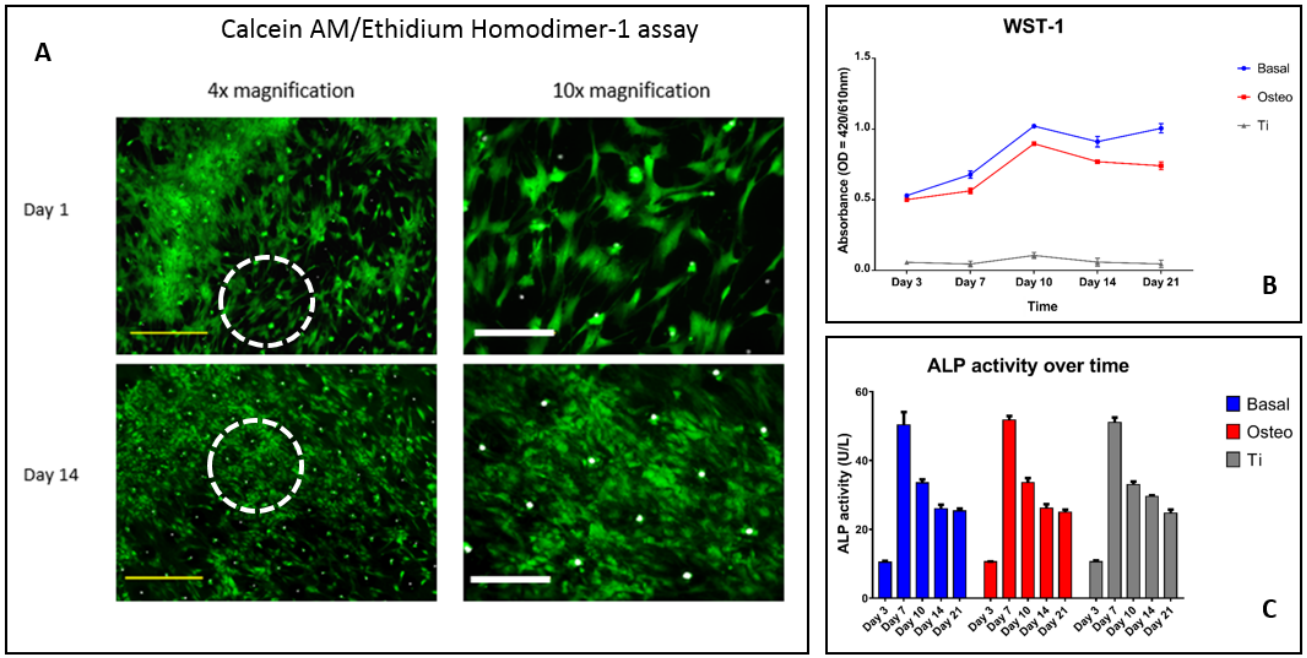

Figure 3-19 STRO-1 enriched BMSC viability, proliferation and functionality over time.

A) Merged Calcein AM, Ethidium homodimer-1, and Brightfield images of STRO-1 enriched BMSCs on EOS templates at day 1 and day 14 demonstrated good cell viability over time, with a concomitant increase in cell density and stellate morphology. Dotted white circles indicate the area visualised under 10x magnification. Yellow scale bar represents 500 µm, white scale bar represents 200 µm. B) WST-1 proliferation assay demonstrated a higher proliferative rate of STRO-1 enriched BMSCs on TCP when compared to EOS templates over the 21 day culture period ($p < 0.001$). STRO-1 enriched BMSCs cultured in osteogenic media had a lower proliferative rate compared to STRO-1 enriched BMSCs cultured in basal media between days 7 and 21 ($p < 0.001$), reflecting osteogenic differentiation under 1,25-VitD3 induction (9). C) ALP activity peaked at day 7 in all three groups, with an expected stepwise reduction over the following two weeks of culture.

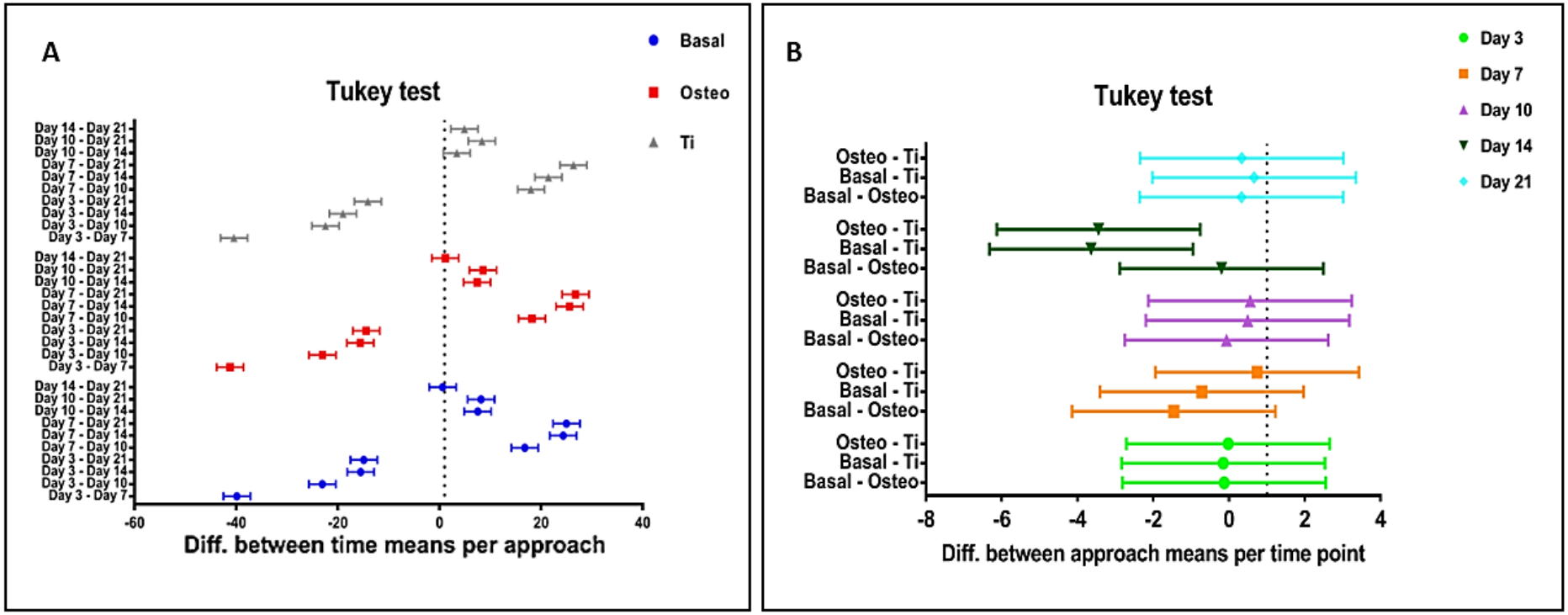

Figure 3-20 Tukey *post-hoc* 95% confidence intervals defined the significance of the individual effects on ALP activity.

A) Culture time had significant effects within each culture approach, with all comparisons demonstrating extremely significant ($p < 0.001$) changes in ALP activity, except for day 14 compared to day 21 in basal and osteogenic cohorts ($p > 0.05$). B) Culture approach however, did not demonstrate significant effect on ALP activity at each time point, except at day 14 in the basal-titanium ($p < 0.01$) and osteogenic-titanium ($p < 0.01$) groups. Culture time therefore plays a crucial role in changes in ALP activity.

3.2.4 Discussion

To summarise, the results of the above experiments demonstrated:

- *EOS titanium templates had a significantly higher wettability compared to UV titanium templates*
- *STRO-1 enriched BMSCs were able to adhere onto the inverted surface of EOS and UV titanium templates despite the short incubation time*
- *STRO-1 enriched BMSCs only grew 25 µm into the 100 µm deep pores*
- *STRO-1 enriched BMSCs developed a stellate morphology earlier in osteogenic and titanium groups*
- *Increased, as well as organised, F-actin and tubulin activity in the titanium groups occurred over time*
- *Increased OPN and OCN gene expression occurred in the osteogenic cohort, and to a lesser extent, the EOS titanium group, indicating the osteoinductive effect of titanium on seeded STRO-1 enriched BMSCs*
- *OPN and OCN upregulation was less persistent in the UV titanium group.*
- *Although the titanium templates were biocompatible, WST-1 assay showed that cell proliferation rate in the EOS titanium group was the lowest at all time-points. Cell proliferation rate in the osteogenic cohort was also found to be significantly lower than in the basal cohort*
- *ALP activity remained significantly higher in the EOS titanium group when compared to both basal and osteogenic groups at day 14*

Given the established biocompatibility of titanium, and the associated long-term health issues of utilising alloys in implants, this study examined whether commercially available medical grade IV titanium could be re-purposed as a bridging interface. Laser-generated microporous, micro-rough titanium templates facilitated rapid STRO-1 enriched BMSC adhesion, and induced early osteogenic differentiation of STRO-1 enriched BMSCs throughout a 21 day culture period, irrespective of the sterilisation method. Cellular interaction with biomaterials is crucial for the successful, long-term implantation of any medical device. Altering surface roughness can increase surface hydrophobicity, but overall, modulation of surface roughness improves cell adhesion through its effects on adhesion proteins (254, 275). Studies by Zinger *et al*, Zhao *et al*, Olivares-Navarrette *et al*, and Banik *et al* indicate that microporosity (252), micro-scale roughness (255, 261), low skewness and low kurtosis topography (276), and high surface energy (253, 272, 277) can synergistically enhance osteogenic differentiation of seeded human osteoblast-like or

MSCs. High surface energy has even been shown to improve angiogenesis (278). In contrast, while MG63 cell adhesion remained unaffected by the degree of roughness of titanium surfaces, cellular proliferation decreased with increasing surface roughness, whereas osteoblastic differentiation increased (251). The latter effect was further enhanced by 1,25-VitD3 stimulation (279). Therefore, a fundamental point to consider during the investigation of cellular reaction to a biomaterial with varying surface roughness is the cell-specific nature of such responses.

Surface composition is a key factor in determining the characteristic of any scaffold, and has been postulated to play a role in the cytocompatibility and osteoinductive effects of a biomaterial on seeded cells. Fabrication methods, as well as surface modification techniques (including biochemical modification), can alter the surface composition, which in turn, can positively, or adversely, affect the performance of an implant *in vivo* (241). It is therefore crucial to elucidate a scaffold composition beforehand, in addition to understanding the effects that modification and manufacturing techniques have on surface properties. Lincks *et al* demonstrated that MG63 cells underwent greater differentiation when cultured on pure titanium, rather than titanium alloy surfaces (251). One of the most commonly used titanium alloys in implants, Ti6Al4V, on degradation through wear and corrosion, produces wear debris *in vivo* consisting of aluminium and vanadium particles that have been linked to neurotoxicity, impaired bone remodelling, and osteoblast toxicity. With other metals such as chromium and cobalt demonstrating similar toxic effects *in vivo* (280), efforts have been made to identify new alloy combinations for use in medical implants. Ikarashi *et al* utilised a titanium alloy containing 50% zirconium, which showed better cytocompatibility than pure titanium and chromium implants (281). Additionally, alloy elements form different oxides apart from titanium oxide on the surface of implants, which could limit the formation of apatite, thereby reducing the osseointegrative capability of the implant (241). A different approach that aims to reduce ion dissolution (and therefore toxicity) is by coating the metal surfaces with a biocompatible material to reduce metal corrosion *in vivo*. Diamond-Like-Carbon coating has proven to be biocompatible, and in some studies, shown to increase the proliferation of osteoblasts and MSCs (282).

In theory, pure titanium surfaces exhibit high surface energy due to their native oxide layer. However, such surfaces adsorb inorganic anions or organic hydrocarbons within seconds of exposure to the atmosphere, altering their surface chemical composition and reducing hydrophilicity (283). This has been reported to

cause reversion to the original hydrophilicity of the material, irrespective of surface treatment (283). Sterilisation methods using ethanol or autoclaves are known to further increase the hydrophobicity of a material (277). In this study, the different modes of sterilisation used, EOS and UV, both resulted in the presence of (albeit differing) oxygen on the template surfaces, with the EOS process generating an increased oxide presence, as demonstrated by EDS mapping (Figure 3-11). The oxidising effect of EO gas could have resulted in the increased oxygen content of EOS templates. The increased presence of titanium dioxide could have improved the wettability (and indirectly, the surface energy) of EOS templates compared to UV templates, which in turn would enable better cell adhesion. Limited template quantities prevented the performance of proliferation and ALP studies in the UV titanium cohort. However, non-sustained OCN and OPN upregulation in STRO-1 enriched BMSCs seeded on UV templates suggest that surface titanium dioxide levels could influence the osteoinductivity of titanium surfaces, and that high levels of titanium dioxide may help to improve the osseointegration of titanium-based implants. These findings suggest the importance of understanding methods of sterilisation and storage of implants as interaction with the atmosphere (once removed from their protective packaging), could potentially, at least in titanium implants, affect their efficacy *in vivo*.

In general, cells prefer hydrophilic surfaces for adhesion and proliferation (256). However, the contact angle method used to measure the wettability of a material surface becomes less reliable when performed on porous substrates. Potential confounding factors such as air trapping within the pores, high scaffold porosity, and surface concavity or convexity can affect liquid dispersion across the surface, consequently producing inaccurate results. Given the 90 µm pore surface consisted mainly of pores, rather than a solid, flat titanium surface, air trapping within the pores could possibly have increased the contact angle readings obtained for both EOS and UV templates. Although the values obtained predicted poor cell adhesion and despite the inverted culture method over the 21 day period, good STRO-1 enriched BMSC adhesion on 90 µm pore surfaces was observed (Figure 3-13, Figure 3-14, Figure 3-15 and **Error! Reference source not found.**). The strength of cell adhesion was confirmed by increased cytoskeletal activity in STRO-1 enriched BMSCs seeded on EOS templates over time (Figure 3-14 and Figure 3-15) and early and persistent upregulation of β–actin (Figure 3-17), indicating that 90 µm pore surfaces of EOS templates had better wettability than predicted by contact angle tests. Differences in cytoskeletal organisation between

the superficial cellular layer and STRO-1 enriched BMSCs directly adherent on the template surface (Figure 3-14 and Video 3-1) indicate the crucial role played by the secreted ECM, as discussed in greater detail by Feller *et al* (248). Equally important is the paracrine effect of cells directly adherent on a scaffold surface on cells distal to the implant which has previously been shown to be effected by their secretion of PGE_2, OPG, and TGF-β1 (251). *In vivo*, these local factors inhibit osteoclastic activity in addition to enhancing osteoblastic activity. This effect has been shown to be augmented by the presence of 1,25-VitD3 (284). Limited template quantities in this study precluded the investigation into whether STRO-1 enriched BMSCs cultured on titanium templates under osteogenic conditions (containing 1,25-VitD3) would have demonstrated a greater augmented effect on osteogenesis. However, it is possible that immobilising such stimuli on a scaffold surface may be a viable approach in enhancing the osseointegrative capability of titanium-based devices.

The high porosity of the 90 µm pore surface could limit the spread of the centrally deposited cell-laden droplet over the template surface, which in turn, could have contributed to the constraint of cellular migration observed. Furthermore, the rate of random cell migration has been implicated in generating a uniform cell population distribution and thus, a uniform coverage of a surface (284). The reduced surface area available would have limited the rate of random cell migration, as reflected by the limited distribution of the cells at day 21. Despite the observed cellular proliferation (Figure 3-15 and Figure 3-19), the cells failed to cover the entirety of the template surface, with the vast majority of cells remaining localised to the template centre. This is in marked contrast to cells seeded on TCP, which migrated across the entire surface of the wells in basal and osteogenic conditions, achieving full confluency. This issue could be overcome by three-dimensional printing techniques, such as inkjet cell printing, which would allow for a uniform, scaffold-wide distribution of cells. AM techniques have been utilised to alternately print different biomaterials per layer, with the aim of creating discrete surface energy gradients across a bioconstruct scaffold, which may trigger different cellular activity and differentiation, making it possible to generate distinct tissue types within a single bioconstruct (285).

Seeded STRO-1 enriched BMSCs also grew into the 90 µm pores, in addition to bridging the pores, irrespective of cell density and the mode of sterilisation. This is in contrast to findings by Xue *et al* (240) who found that a critical pore size of 200 µm or higher was necessary for osteoblastic precursor cell line ingrowth into pores.

Hollander *et al* (266) had shown that 5 X 10^4 human osteoblasts cultured on direct laser forming Ti6Al4V scaffolds with 700 µm and 1000 µm pore sizes did not completely bridge the pores but developed a circular-shaped growth pattern along the rims of the pores. The same number of cells covered the entirety of the surface of scaffolds with 500 µm-sized pores. Neither study was able to determine the extent of cell growth into the pores. In our study, confocal microscopy imaging was utilised to create a three-dimensional reconstruction of the templates, allowing the measurement of the depth of cell ingrowth within the pores. Although STRO-1 enriched BMSCs were able to grow 25 µm deep into the 90 µm-sized pores, the cells were unable to penetrate the full 100 µm depth of the conical-shaped pores. This finding suggests that pore geometry, as well as pore size, are key determinants in the extent of pore bridging and cell ingrowth within porous scaffolds, thus highlighting the importance of scaffold design in the development of successful implants for bone tissue engineering.

Previous studies indicated that osteoblasts are capable of discriminating micro-scale topographical features on titanium and titanium alloy surfaces, with increased osteogenic differentiation on surfaces containing micro-scale roughness (148, 251, 261, 276). Olivares-Navarrette and colleagues demonstrated that MSCs developed osteoblastic characteristics when grown on micro-structured titanium surfaces, even in the absence of osteogenic medium supplements such as β-glycerophosphate and dexamethasone. This osteoinductive capability was more pronounced on surfaces that were more hydrophilic (286). Zhao *et al* demonstrated that MG63 cells develop more filopodia on rougher titanium surfaces compared to smooth surfaces (253). Work recently published by Banik *et al* further indicates that MSCs develop a fibroblastic morphology when seeded on smooth titanium surfaces, whereas on rough titanium surfaces, MSCs are mostly cuboidal or stellate in appearance (255). Such morphological changes have previously been shown in cells undergoing osteogenic differentiation (229, 230). The above results concur with these published data, with seeded STRO-1 enriched BMSCs demonstrating morphological, functional, and gene expression changes in keeping with early and persistent osteogenic differentiation in both the titanium and osteogenic media TCP groups. The osteoinductive effect of titanium on STRO-1 enriched BMSCs could further explain the lower proliferative rate of seeded STRO-1 enriched BMSCs compared to those cultured on TCP as previously reported (251, 253, 255).

3.2.5 Conclusions

This study has demonstrated that laser-generated microporous, micro-rough titanium templates could facilitate rapid STRO-1 enriched BMSCs adhesion, and induce early osteogenic differentiation of STRO-1 enriched BMSCs despite the seeded surface being inverted and suspended throughout a 21 day culture period. Early osteogenic differentiation resulted in a lower proliferative capacity and surface migration of seeded STRO-1 enriched BMSCs, which subsequently left exposed areas on the template and could potentially contribute to poorer long-term osseointegration *in vivo*. Pore geometry and size appeared to affect the degree of cellular overgrowth within pores as STRO-1 enriched BMSCs only grew a distance of 25 µm into 100 µm deep conical pores, highlighting the critical effect of scaffold design on device functionality. Finally, the impact of the method of sterilisation and storage on the surface properties of implants is crucial as part of quality assurance evaluation during the manufacturing process. In summary, the current *in vitro* study indicated that STRO-1 enriched BMSC-seeded microporous, micro-rough titanium could be used as a superficial template or bridging interface between an implant and the bone surface to enhance peri-implant bone wound healing and therefore, osseointegration, while minimising implant alloy-related wear debris toxicity and critically, in the longer term, improve implant safety, functionality, and longevity.

Chapter 4: Biomimetic bioinks for cell delivery

Numerous biomaterials have been created and investigated by researchers in the last fifty years, with an increasing focus towards biodegradable, biomimetic alternatives that could be used in tissue engineering. As discussed in 1.5, evidence for cell printing in bone regeneration remains limited. Most post-printing viability studies have been conducted using cell lines. In contrast, the feasibility of bioprinting STRO-1 enriched BMSCs with high viability and functionality has yet to be investigated. Furthermore, as shown in 3.2, manual seeding methods have failed to achieve uniform cell distribution, which could adversely affect osseointegration *in vivo*. Such an issue could, potentially, be resolved by bioprinting cell-laden bioinks onto a scaffold to maximise coverage. This chapter outlines the approaches taken in creating cytocompatible bioinks, using commercially available biomaterials, for cell delivery and the potential to print STRO-1 enriched BMSC-laden bioinks with retained cell viability.

4.1 Creating cytocompatible, biomimetic bioinks

4.1.1 Introduction

Hydrogels are 3D networks formed from hydrophilic homopolymers, co-polymers, or macromers crosslinked to form insoluble polymer matrices. Above specific glass transition temperatures (T_g), hydrogels are soft and elastic. As discussed in 1.6.3.2, there has been increasing interest in the use of hydrogels for biofabrication purposes given hydrogels have a high water content, which allows for the recreation of natural ECM conditions (287) through the incorporation of bioactive growth factors, drugs, or even micro- or nanoparticles containing biochemical signals for delayed or slow-release dosage. An increasing number of publications have demonstrated the successful utilisation of interpenetrating network, nanocomposite, supramolecular, and multi-material hydrogels for such purposes, with the latter approach being the most investigated to date (85, 135, 288).

Over the past decade, tremendous progress has been made in the synthesis and biofabrication of hydrogels from natural and synthetic sources for applications in the biomedical and pharmaceutical fields. Naturally-derived biomaterials, such as alginate, gelatin, fibrin, and hyaluronic acid, are useful for their cell-interactive properties and biodegradability. Poor mechanical properties, unpredictable or uncontrolled degradation kinetics, and the potential for immunogenicity limit their

functionality. The reverse is true for synthetic hydrogels, such as poly(vinyl alcohol), poly(ethylene glycol), pluronics, and polyacrylamide. Current approaches combine natural and synthetic-derived materials to overcome such drawbacks (85). Various crosslinking approaches have been utilised to create polymer networks in order to preserve their 3D structures in aqueous environments (Table 1-8). Chemically crosslinked gels (through the formation of covalent bonds) generally display better mechanical properties than physically crosslinked gels, and in addition are a more attractive option for engineering load-bearing tissues. However, residual organic solvents, photoinitiators, or chemical crosslinkers used during synthesis, could potentially be cytotoxic to seeded cells. A growing number of hydrogels utilise photo-crosslinking methods involving ultraviolet radiation to create free radicals that form covalent bonds with activated functional groups to generate a crosslinked network, with subsequent removal of unreacted polymers upon completion of crosslinking. This results in a more stable hydrogel with superior mechanical properties, allowing the hydrogel to be used as a standalone scaffold. However, free radicals generated during the process could damage DNA and impair cellular function of seeded cells. There is emerging evidence suggesting that this could be minimised by using a low-dose, long-wave ultraviolet light for such purposes (289). Such potential problems need to be considered prior to choosing the combination of biomaterials, and method, for hydrogel synthesis. Additionally, to maximise a hydrogel's ability to foster tissue growth, the biomaterial(s) must degrade *in vivo*.

Alginate remains one of the best studied biomaterials to date (290). Typically extracted from brown algae (*Phaeophyceae*) and some bacterial species, alginate has been widely used for wound dressings, tissue engineering, as well as cell and drug delivery. This is due to its non-immunogenicity, low cost, capability to form highly porous gels (which enables high diffusion rates for macromolecules), and its ready gelation in the presence of divalent ions (except Mg^{2+}) (291). Alginate is a family of linear copolymers consisting of blocks of consecutive guluronate, mannuronate, and alternating guluronate-mannuronate residues. Alginate extracted from different sources differ in guluronate and mannuronate content, as well as the block length. Gelation occurs through the exchange of sodium ions from guluronate blocks for divalent ions, which results in the stacking of these guluronate groups to form an 'egg-box' structure (Figure 4-1) (292). The guluronate to mannuronate ratio and sequence, guluronate block length, and molecular weight of the alginate used, are key factors that affect the physical properties of alginate hydrogels (291). For instance, high molecular weight alginate forms viscous gels, increasing the risk of

shear force damage to encapsulated cells during mixing and printing. Gelation rate is a critical factor in controlling alginate gel uniformity and mechanical integrity, wherein slower gelation results in greater uniformity and strength. This can be achieved by exposure to lower temperatures (which reduces the reactivity of ionic crosslinkers) or by utilising alginate sources with a higher guluronate content, which increases stiffness of the resulting hydrogel. Alginate hydrogels have been prepared by various crosslinking methods, enabling the creation of tuneable gels with differing mechanical strengths, and the potential for controlled drug release (291, 293).

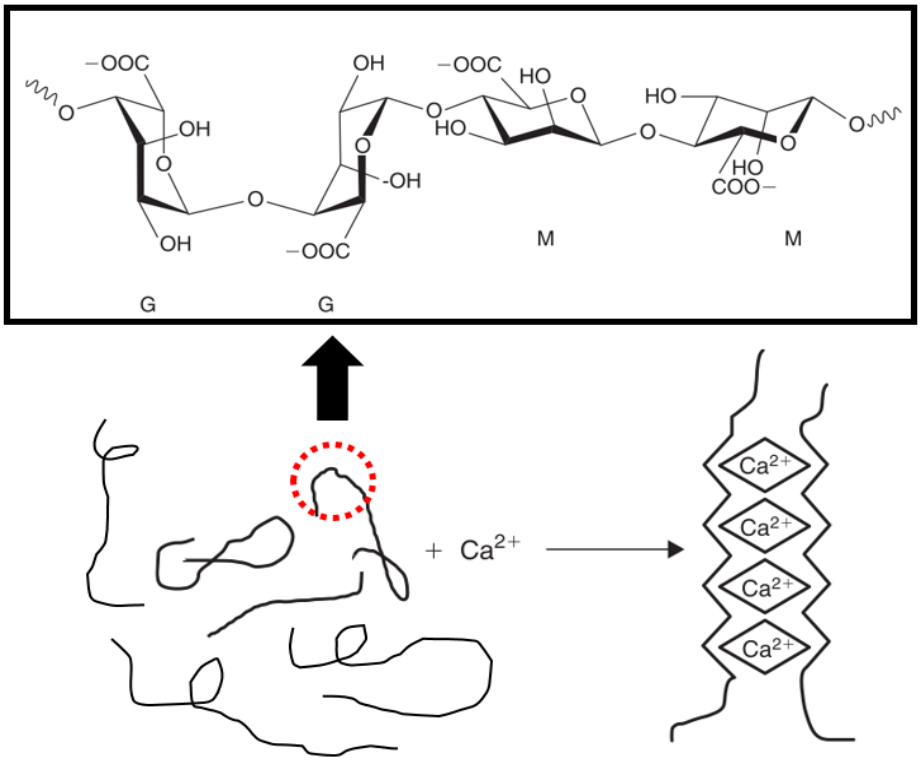

Figure 4-1 Structure of alginate and the 'egg box' model for alginate gel formation.

Alginate comprises guluronate (G) and mannuronate (M) residues. The random coils of alginate form buckled ribbon-like structures containing arrays of divalent ions, such as calcium ions, during ionic crosslinking. Modified from (292).

Despite these advantages, ion-crosslinked alginate is known to degrade in an uncontrollable and unpredictable manner. Loss of divalent ions into the surrounding media results in its subsequent dissolution. Lower molecular weight alginate is more likely to be renally excreted on degradation *in vivo* [217]. Renal clearance is the only mechanism by which alginate can be removed from the human body as mammals lack alginase, the enzyme needed to breakdown alginate. Some forms of alginate have been subjected to partial oxidisation and crosslinking using

adipic acid dihydrazide to control degradation rates through pH and/or temperature changes (294). Other methods, such as chemical crosslinking and thermal gelation, have also been examined (295). One disadvantage of alginate is its hydrophilicity, which discourages protein adsorption and thus, cellular interactions. A number of studies have attempted to incorporate peptide sequences such as RGD, to overcome this limitation, showing increased cell adhesion, proliferation and differentiation (163, 291). Alginate gels have been successfully combined with stem cells for enhancing repair and regeneration of critical-sized bone defects, other natural polymers such as chitosan and gelatin for encapsulating cells and for growth factor delivery for bone regeneration, and also with inorganic materials, such as HAP, to enhance bone formation *in vivo* (291).

Gelatin is a cytocompatible biomaterial that has been used to promote cell adhesion for a number of cell types (296). Gelatin is formed by the hydrolysis of collagen from its triple-helical structure to single-stranded polymeric chains of different amino acids (Figure 4-2). The amino acid composition and sequence in the single chains varies depending on the origin of the gelatin, which in turn, influences its final properties. The average molecular weight of gelatin is between 15 and 400 kDa (297). The manufacturing procedure of gelatin involves three stages: 1) pre-treatment of the raw material, 2) gelatin extraction, and 3) purification or drying of the product. Two types of gelatin are produced: type A gelatin, with an isoelectric point of 9.0, is derived from acid-cured animal tissue prior to undergoing thermal denaturation, while type B, with an isoelectric point of 5.0, is from lime-cured animal tissue (294). With the source being animal tissue, there is a very small risk of transmissible spongiform encephalopathies and as such, gelatin for human use remains under strict manufacturing regulations worldwide. The animal source or method of procuring could also be an issue for some religious or dietary groups.

The behaviour of a gelatin solution depends on temperature, concentration, pH, and preparation method. Gelatin solutions form gels at temperatures below 30 °C; uncrosslinked gels return to a liquid form above 32°C. During the gelation process, locally ordered regions among gelatin molecules take place and are subsequently joined by hydrogen, electrostatic and hydrophobic bonds. *In vivo*, gelatin degrades due to its matrix metalloproteinase sensitive protein sequences. The ease of gelation, and low immunogenicity, has made gelatin a commonly utilised material for hydrogels (297). The early popularity of gelatin also stemmed from the fact that collagen forms portions of native bone. Composites of gelatin, fibrin, hyaluronic acid, and/or collagen have been used in bone tissue engineering to

release growth factors and anti-inflammatory compounds, demonstrating superior pharmacokinetic profiles of these agents *in vivo* compared to injection therapy (297, 298). The Bloom number indicates strength of gelation of a gelatin solution of known concentration, which is proportional to the average molecular mass of the proteins. A myriad of approaches, typically involving chemical modification, have been required to address the inherent mechanical weakness of gelatin-based hydrogels. Gelatin methacrylate is one such example. Billiet *et al* were able to 3D print a macroporous, 10 – 20% gelatin methacrylate scaffold encapsulating HepG2 cells (a hepatocarcinoma cell line), with 97% cell viability (299).

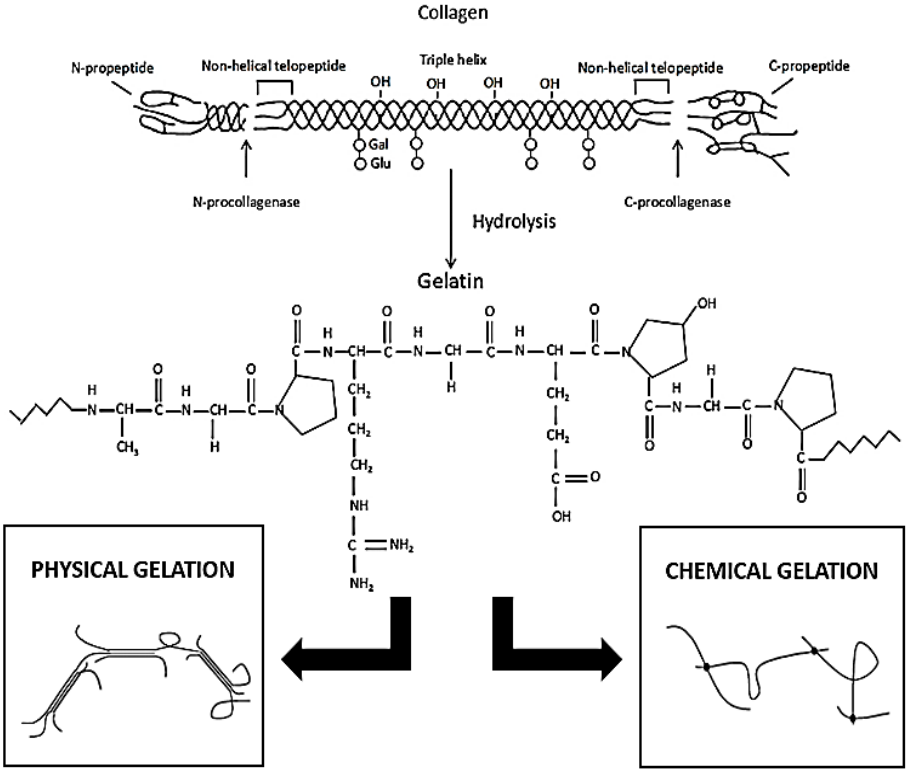

Figure 4-2 Chemical structure of gelatin and the structure of gelatin gels.

Gelatin is derived from collagen hydrolysis and forms triple helices with small random coil areas when exposed to low temperatures (physical gelation). These coil areas are larger in chemical gelatin gels, which can be obtained by transglutaminase, catalysed covalent crosslinking. Modified from (300).

Glycerol (formula: $C_3H_8O_3$) is a water soluble, colourless, odourless, viscous liquid. Glycerol is widely used as a lubricant, humectant (due to its hygroscopic nature) (301) and cryoprotectant (amongst other uses) in various industries. *In vivo*, glycerol is metabolised to glyceraldehyde 3-phosphate prior to undergoing glycolysis or gluconeogenesis (depending on physiological conditions), thus

providing energy for cellular metabolism. Furthermore, glycerol is a precursor for triglyceride and phospholipid synthesis in liver and adipose tissues, and is biocompatible *in vivo* (302). Wang *et al* added dextran-40 and 2.5% glycerol as a cryoprotectant and humectant component of cell-laden alginate/gelatin/fibrinogen hydrogels, with good cellular revival post-freezing (303). Kang and colleagues had optimised a printable hydrogel for bone tissue engineering composed of 3 mg/ml hyaluronic acid (HA), 20 mg/ml fibrinogen, 35 mg/ml gelatin, and 10% v/v glycerol, that delivered 5 X 10^6 per ml of human amniotic fluid stem cells with a cell viability of 91% at day 1 (69).

Fibrinogen is a 340 kD dimeric glycoprotein, with each dimer composed of 3 distinct chains, Aα, Bβ, and γ chains and joined together by six disulphide bridges. Fibrinogen is the soluble inactive precursor of the fibrin monomer, a vital insoluble haemostatic component of the coagulation cascade. Fibrin formation is initiated by thrombin, which is released in response to injury. The homogeneity of fibrin mesh formation (and therefore gel compaction) increases as the thrombin concentration decreases (304, 305). The fibrin network serves as a scaffold for tissue repair *in vivo*, by allowing macrophage, fibroblast, platelet and neutrophil infiltration and aggregation, which in turn, enables the deposition of FN, collagen and other ECM components (Figure 4-3). Fibrin has numerous binding sites for growth factors, integrins ($\alpha_{IIB}\beta_3$, $\alpha_v\beta_3$, $\alpha_M\beta_2$, $\alpha_x\beta_2$) and other signalling factors, which allow for the direction of cell behaviour. Fibrinopeptides A and B (released during fibrin formation), in addition to fibrin degradation products (created by plasmin-mediated fibrinolysis), Fragments D and E, are bioactive, contributing to tissue repair through chemotactic, mitotic, and pro-angiogenic stimulation. *In vivo*, the degradation rate of fibrin is controlled by aprotonin, a proteinase inhibitor (294). Since fibrin was first purified in large amounts in the 1940s, fibrin versatility has been demonstrated through its use in a wide variety of biomedical applications, from scaffolds for tissue engineering (77), to stem cell delivery and differentiation (306, 307), as well as in wound repair as a sealant (294, 308, 309). Alteration of fibrin polymerisation through altering pH (77), sodium chloride (310) and thrombin concentration (309), incorporation of poly(ethylene glycol) (311) and other polymers (312) have been utilised to create desirable properties for bone tissue engineering uses (77). Additionally, thrombin exerts a non-concentration dependent enhancement on osteoblastic proliferation (304), while fibrin supports osteoblast differentiation and bone healing (313).

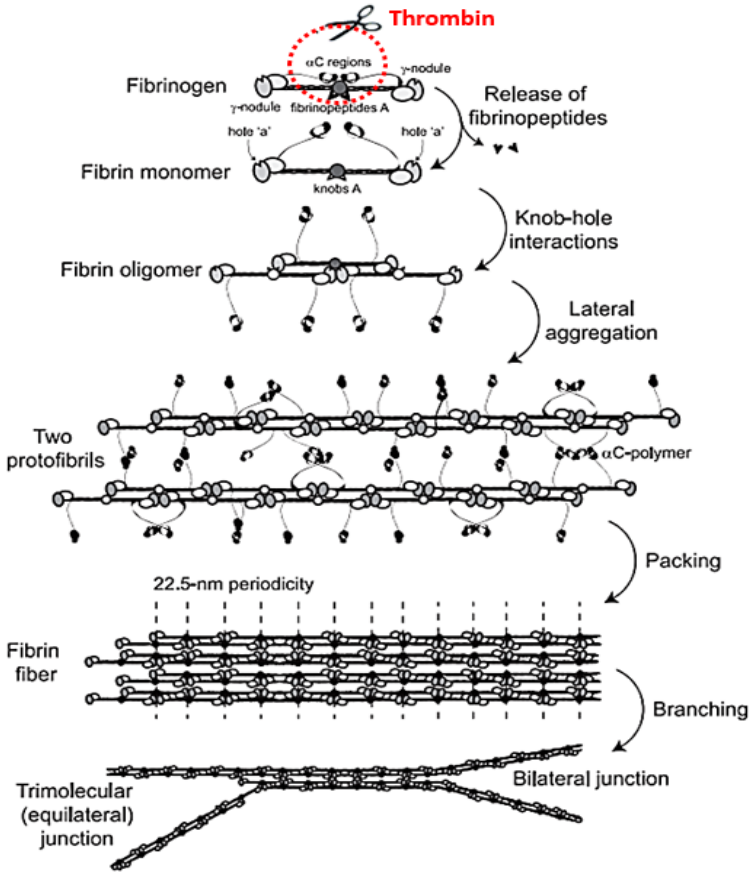

Figure 4-3 Fibrin formation and polymerisation *in vivo*.

Fibrinopeptides are released by thrombin cleavage from fibrinogen, which results in the formation of monomeric fibrin-containing exposed knobs and the partial dissociation of αC regions. Monomeric fibrin self-assembly occurs through knob-hole interactions, which result in the formation of two-stranded fibrin protofibrils. Homophilic αC-αC interactions within and between protofibrils causes lateral aggregation of protofibrils, which become packed into a fibre with a 22.5 nm periodic cross-striation due to the paracrystalline arrangement. The branching of fibres finally forms the fibrin network. Adapted from (314).

Although alginate, gelatin, glycerol, and fibrin have all been shown to be printable and cytocompatible, these biomaterials require the addition of stimulatory factors to improve their functionality (other than as a delivery system). Over the past decade, there has been increasing interest in adopting a biomimetic approach to improve bone tissue regeneration by re-creating the native bone ECM (315, 316). Cell phenotype is specified by environmental cues embedded in the composition and architecture of ECM (317). As highlighted in 1.1, native bone ECM is a nanocomposite, which closely surrounds resident cells in bone, regulating their proliferation, migration and differentiation. The ECM also provides mechanical support and aids in cell recruitment via integrin interactions. Recently, promising

results have been obtained through the utilisation of decellularised ECM derived from bone, cartilage and teeth in bone regeneration studies (318). There is increasing evidence the regenerative properties of synthetic biomaterials could be enhanced when combined with ECM molecules such as collagen, self-assembly peptides and glycosaminoglycans (319).

Fibronectin (FN) is a multi-functional ECM glycoprotein composed of two almost identical disulphide-bound polypeptides of molecular weight 240 to 270 kDa (Figure 4-4). FN is secreted by cells as a soluble compact dimer that undergoes conformational change and assembles into short fibrils that are subsequently converted into insoluble, dense, multimeric fibril networks through binding of the $\alpha 5\beta 1$ integrin receptor at cell surfaces. Integrins link FN fibrils to actin, thereby influencing intracellular Rho activity. This connection is crucial for FN fibrillogenesis, which provides cells with firm substrate attachment. Different sets of repeats make up domains within FN that enable binding to extracellular and cell surface molecules such as collagen, fibrin, integrins, glycosaminoglycans, syndecans, and FN itself (Figure 4-4) (320). FN fibrils are rearranged and recycled by cell movement, cell density and degradative processes. This, in turn, mediates matrix assembly. There is also evidence that FN is synthesized and deposited during tissue repair (where early recruitment of osteoblast precursors occurs). Lower FN density (~48 ng/cm^2) when used as a coating for polycaprolactone (PCL) scaffolds elicited greater Col1a1 and ALP gene expression and higher cytoskeletal spreading of human MSCs (321). Zhang *et al* found that a HAP composite layer containing 20 µg/ml FN and 100 pg/ml BMP-2 enhanced ALP and OCN gene expression and ALP activity in MC3T3-E1 cells (322).

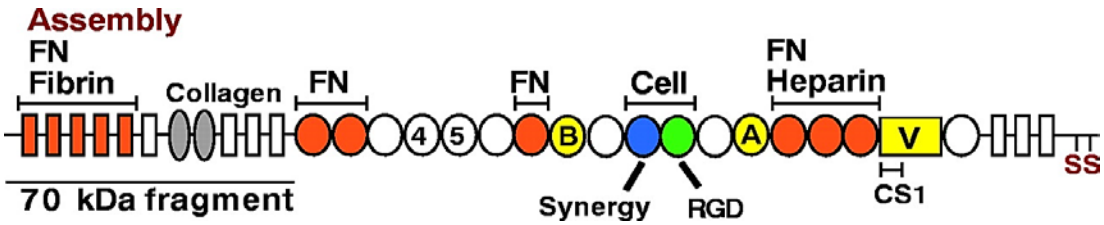

Figure 4-4 Domain structure of fibronectin.

Schematic representation of the fibronectin glycoprotein, demonstrating sets of repeats that constitute the binding domains for fibrin, collagen, heparin, and cells within its structure. Fibronectin consists of type 1 (rectangles), type II (ovals) and type III (circles) repeats. Fibronectin binding sites and the assembly domains are highlighted in orange. SS indicates C-terminal cysteines that form the dimer. Reproduced from (320)

Hyaluronan, or hyaluronic acid (HA), is a highly hydrophilic, non-sulphated glycosaminoglycan with a molecular weight range of 1 kDa to above 2 MDa. *Streptococcus zooepidemicus* is most often used for the production of HA today. Repeating disaccharide units of pyranose rings interconnected by β1,3 bonds form the polymeric chain of HA, and these repeating units are bonded with a β1,4 glycosidic bond within the chain between N-acetyl-D-glucosamine and D-glucuronic acid (Figure 4-5) (323). Each glucoronate unit (with its carboxylate group) carries an anionic charge, which is balanced with mobile cations such as Na^{+}, Ca^{2+} and Mg^{2+}. Alterations in pH and ionic strength changes the overall charge, which in turn influences the organisation of the chains and their interaction with their surroundings. This is reflected by the insolubility of HA in water when converted into an uncharged polymer. When HA is dissolved in water, molecules of water form hydrogen bonds between the carboxy- and acetamido-groups, forming single-strand left-handed helices consisting of two disaccharide residues per turn. This arrangement of the polymeric chain results in regular alternating areas with polar functional groups and hydrophobic patches, the latter allowing for the formation of duplexes in water, generating a β-sheet tertiary structure (Figure 4-5). HA molecules in solution have been shown to form an infinite mesh (consisting of filaments of differing width) possessing non-Newtonian viscoelastic property. Establishment of this network is dependent on the molecular weight and concentration of HA used, and is further influenced by the ionic strength of body fluid *in vivo*. This meshwork in turn reduces the diffusion and flow of solutes like proteins and low molecular weight compounds (323, 324).

HA is found in nearly all tissues in humans, with a total content of about 15 g in a 70 kg individual. The largest amount is present in musculoskeletal tissue and skin. *In vivo*, daily HA turnover is 5 g, and is achieved through hyaluronidases and reactive oxygen species (324). This turnover is raised during infection and chronic inflammation, increasing tissue fragility, as HA binds to proteoglycan aggrecan to form large aggregates that interact further with collagen and other ECM components to stabilise tissue integrity. Furthermore, HA regulates focal adhesion kinases, protein kinase C, and MAP kinase which are involved in ECM remodelling (325). HA has been shown to facilitate stem cell migration from their original niche to distant sites within the developing organism. HA also influences wound healing and the macrophage response in inflammation by interacting with cell-associated proteins, such as CD44 and CD168, to stimulate signal transduction pathways that facilitate cell adhesion and cell locomotion respectively (292, 323, 325). The physicochemical

and biological properties of HA have been shown to be molar mass-dependent (323). Of particular interest is the finding that low molecular weight HA not only modulates the inflammatory response *in vivo*, but also promotes angiogenesis (323, 324). Such varied functionality has seen HA utilised in viscosurgery, viscoprotection and viscosupplementation (in particular in osteoarthritis as joint synovial fluid replacement therapy). Although HA is a major ECM component, its non-adhesive nature limits its use in applications where cell spreading is required, and therefore, HA is often used in combination with other biomaterials such as gelatin and alginate to improve their mechanical and biological properties (296). HA can be chemically modified by several methods and has been used in bone tissue engineering to create biodegradable scaffolds (324, 326), for cell (326) or controlled drug delivery (292, 324), and as a stimulatory coating on existing metallic implants (324).

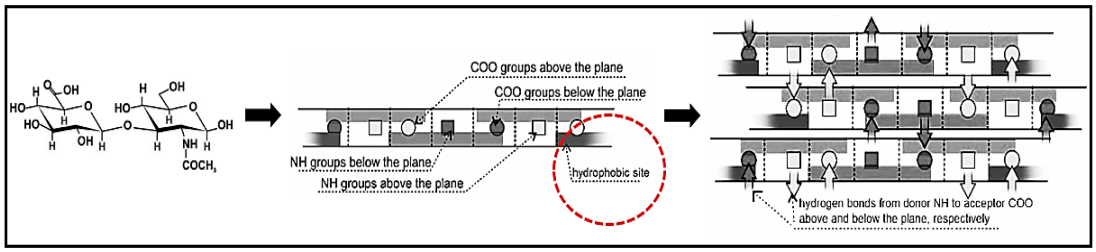

Figure 4-5 Structure of hyaluronic acid.

The molecular formula of a HA disaccharide unit, and the secondary and tertiary structure of HA when dissolved in water. Adapted from (324).

Naturally derived biomaterials possess a unique viscoelastic property, whereby their elastic modulus strengthens the more deformed the material becomes (otherwise known as ‘strain stiffening’). Synthetic materials usually comprise of hydrophilic polymer chains that become fully extended in aqueous media, causing the materials to become brittle. Combining natural and synthetic materials can be used to resolve this issue (85). Increased stiffness of a scaffold or matrix has been shown to improve osteogenesis (327). Stiffness, or elastic modulus, of such gels can be adjusted by varying the ratios of the components and/or the concentrations of each component, and by the addition of crosslinking agents to the mixture (during or after bioprinting) (86, 328-331). Naturally-derived matrices are mostly enzymatically degraded *in vivo*, allowing cells to remodel their surrounding environment (288). This is necessary for cells to spread and proliferate, as shown by Lutolf and co-workers, who demonstrated that bone regeneration is affected by the proteolytic sensitivity of the hydrogel matrix (332). As such, cell behaviour is strongly influenced by the degradation properties of the scaffold as scaffold

degradation allows for the deposition of new ECM by cells as well as the formation of new tissue. Selecting such materials enables the generation of a tuneable, composite gel, thus meeting the requirements of the biofabrication window. The integrated approach of this project centred upon first determining suitable combinations of these biomaterials for the synthesis of tuneable, cytocompatible bioinks that could then be printed using the 3DDiscovery bioprinter.

As stated in 1.9, the hypotheses of this thesis are:

1) Human STRO-1 enriched BMSCs possess, and retain, the capacity for osteogenesis when seeded onto scaffolds, and are therefore a suitable cell type for use in bone reparation.

2) Biomaterials can be combined to generate tuneable bioinks, which can be used to deliver STRO-1 enriched BMSCs with high viability and functionality.

3) 3D printing methods are capable of manufacturing porous scaffolds of clinically relevant size with high resolution and reproducibility.

4) STRO-1 enriched BMSCs, biomimetic bioinks, and 3D printed polycaprolactone-based scaffolds can be combined to create an integrated bioconstruct for use in bone repair.

In conjunction with the above hypotheses, the aims of this research project are:

1) To confirm the osteogenic potential of STRO-1 enriched BMSCs.

2) To elucidate the osteoinductive capabilities of established biomaterials, such as titanium and polycaprolactone (amongst others), in order to identify potential combinations for the generation of composite scaffolds and/or bioinks for use in bone tissue engineering.

3) To design novel porous scaffolds that mimic natural bone architecture.

4) To investigate the feasibility of utilising 3D printing techniques to accurately and reproducibly manufacture scaffolds according to their design.

5) To determine the possibility of 3D printing cell-laden bioinks.

6) To develop methods for integrating 3D printed scaffolds, biomimetic bioinks, and STRO-1 enriched BMSCs, with the objective of creating functional bioconstructs for use in bone reparation.

4.1.2 Materials and Methods

4.1.2.1 Manufacture of hydrogels

2.16% w/v sodium chloride solution was made by dissolving 1.08 g of sodium chloride (Sigma Aldrich, UK) in 50 ml of deionised water. 100 mM of calcium chloride was made by dissolving 0.2775 g of calcium chloride dihydrate (Sigma Aldrich, UK) in 25 ml of deionised water. These stock solutions were sterile-filtered using a 0.22 µm filter and were diluted as required.

8% w/v alginate solutions were made by dissolving 4 g of alginic acid sodium salt from brown algae, low viscosity (Sigma Aldrich, UK) in 50 ml of sterile DPBS (pre-warmed to 37°C) under magnetic stirring for 1 hour in sterile conditions. This particular hydrophilic alginate salt, comprising of guluronate and mannuronate residues at about a 1:4 ratio, was chosen for its low viscosity properties: a 1% w/v solution has a 4 – 12 MPa.s viscosity (data provided by Sigma Aldrich). This alginate was used by Wüst *et al* to create a tuneable composite hydrogel for bone bioprinting (328).

10% w/v gelatin solutions were made by dissolving 5 g of Type A gelatin from porcine skin (Sigma Aldrich, UK) in 50 ml of sterile DPBS (pre-warmed to 37°C) under magnetic stirring for 10 minutes and kept at 37°C for 2 hours to remove any bubbles. The two solutions were subsequently mixed in a 1:1 ratio to generate a 4% w/v alginate and 5% w/v gelatin hydrogel solution. When different working weight amounts of either solution was required, the appropriate dilutions were carried out by adding the required volumes of DPBS to achieve the desired concentrations.

100 µl of glycerol (Sigma Aldrich, UK) was added to every 0.9 ml of 4.5% w/v alginate solution to create a 4% w/v alginate, 10% v/v glycerol hydrogel solution whereas 100 µl of the stock solution of fibrinogen and 100 µl of glycerol were added to 0.8 ml of 5% w/v alginate solution to generate a 4% w/v alginate, 10% v/v glycerol and 10 mg/ml fibrinogen hydrogel solution. 5% w/v gelatin-based equivalent hydrogel solutions containing 10% v/v glycerol, and 10% v/v glycerol and 10 mg/ml fibrinogen were created in a similar manner.

100 mg/ml stock solution of fibrinogen was prepared by dissolving 250 mg of human fibrinogen (Sigma Aldrich, UK) in 2.5 ml of sterile-filtered 2.16% w/v sodium chloride solution. 100 µl of the stock solution of fibrinogen and 20 mg of mPEG-

Succinimidyl Valerate, M_w = 5000 g/mol (Laysan Bio, Inc., USA) were added to every 0.9 ml of 4.4% w/v alginate and 5.5% w/v gelatin solution to create a 4% w/v alginate, 5% w/v gelatin, 10 mg/ml fibrinogen and 20 mg/ml mPEG-Succinimidyl Valerate hydrogel solution. The addition of mPEG-Succinimidyl Valerate to the mixture was based on work done by Rutz and colleagues, who had combined gelatin, fibrinogen and mPEG-Succinimidyl Valerate successfully to form a printable bioink (329). The changes to the ratio of the components was aimed at incorporating alginate into the mixture, and to generate a higher viscosity hydrogel by increasing the mPEG-Succinimidyl Valerate component in the original design.

500 µg/ml stock solution of FN was prepared by dissolving 1 mg of human FN (Sigma Aldrich, UK) in 2 ml of sterile-filtered 2.16% w/v sodium chloride solution.

4.1.2.2 Hydrogel swelling test

1x PBS, SBF, and basal medium were prepared as described in 2.1. Each 5 mm by 2 mm hydrogel disc was made from 100 µl of 4% w/v alginate, 4% w/v alginate and 10% w/v glycerol, 4% w/v alginate, 10% w/v glycerol and 10 mg/ml fibrinogen, 5% w/v gelatin, 5% w/v gelatin and 10% w/v glycerol, 5% w/v gelatin, 10% w/v glycerol and 10 mg/ml fibrinogen solutions using customised moulds (see 2.4.2). The filled moulds were kept at 4°C for 30 minutes. Ionic crosslinking in a solution of 100 mM calcium chloride was performed for 15 minutes for all alginate-containing groups. No cells were added in any of the groups for this test.

Hydrogel swelling was assessed by measuring the wet weight of each hydrogel disc over a 28 day period following immersion in 1x PBS (without Ca or Mg), SBF, or basal media containing 22.5 mM calcium chloride. Hydrogels containing fibrinogen had 5 units per ml human thrombin added to their respective immersion liquids. The immersion liquids were changed weekly. Swelling at 21°C and 37°C of the various hydrogels immersed in each liquid (n = 3 per group) was measured at days 3, 7, 14, 21, and 28, by weighing the wet hydrogels at each time point using an electronic balance. Excess liquid was removed from each gel using sterile filter paper prior to weighing.

The swelling ratio was calculated as the ratio of the measured hydrogel wet weight over time, with respect to the initial hydrogel wet weight. In comparison to the classical hydrogel swelling assessment, whereby the swelling of dry hydrogel discs is measured over a three day period following immersion in 1x PBS or deionised water at 21°C, this approach (based on work by Wüst and colleagues (328))

enables a closer approximation of the behaviour and properties of each hydrogel when exposed to experimental conditions during 3D bioprinting and subsequent culture at 37°C over an extended time in *in vitro* and *in vivo* experiments.

A second hydrogel swelling test was performed on 5 mm by 2 mm hydrogel discs made from 100 µl of 10% w/v alginate, 0.5% w/v HA, 10 mg/ml fibrinogen and 20 µg/ml FN, 6% w/v gelatin and 0.75% w/v HA, and 8% w/v gelatin and 1% w/v HA solutions using customised moulds (see 2.4.2). The filled moulds were kept at 4°C for 30 minutes. Ionic crosslinking in a solution of 100 mM calcium chloride was performed for 15 minutes for all alginate-containing groups. No cells were added for this test. Hydrogels were cultured at 37 °C, 5% CO_2 in basal media containing 2.5 mM calcium chloride and 1 U/ml human thrombin (Sigma Aldrich, UK).

4.1.2.3 MG63 cell viability post-encapsulation

MG63 cells were obtained from Taipei Medical University and cultured as described in 2.2. These cells were pre-labelled using PKH-26 (Red) Fluorescent cell membrane labelling kit, as summarised in 2.6.2. 1 X 10^6 PKH-26 (Red)-labelled MG63 cells were suspended in 1 ml of 4% w/v alginate and 5% w/v gelatin and 4% w/v alginate, 5% w/v gelatin, 10 mg/ml fibrinogen and 20 mg/ml mPEG-Succinimidyl Valerate solutions. Each 5 mm by 2 mm hydrogel disc was made from 100 µl of each cell-laden solution using the customised moulds (see 2.4.2). The filled moulds were kept at 4°C for 30 minutes, before performing ionic crosslinking in a solution of 100 mM calcium chloride for 15 minutes. Triplicates of 4% w/v alginate and 5% w/v gelatin hydrogels were cultured in basal media containing 22.5 mM calcium chloride, while 4% w/v alginate, 5% w/v gelatin, 10 mg/ml fibrinogen and 20 mg/ml mPEG-Succinimidyl Valerate hydrogels were cultured in basal media containing 22.5 mM calcium chloride and 5 U/ml human thrombin (Sigma Aldrich, UK) to activate fibrin formation. Hydrogels were cultured for 21 days in a humidified incubator at 37°C, 5% CO_2. Media changes were done every 3 to 4 days. Triplicate images at each time-point were used for cell counts, which was performed using the Fiji cell count plug-in.

4.1.2.4 STRO-1 enriched BMSC viability post-encapsulation

The initial aim for these experiments was to investigate the cytocompatibility of several biomaterials on STRO-1 enriched BMSCs. Hydrogel composition for this phase of experiments was adjusted based on the results obtained in 4.1.2.3, and on

the composite hydrogel developed for bone constructs by Kang *et al* (69). STRO-1 enriched BMSCs from the bone marrow of a 76 year old male patient were isolated and cultured according to protocols described in 3.1.2.1 and 3.1.2.2. These cells were pre-labelled using PKH-26 (Red) Fluorescent cell membrane labelling kit, as summarised in 2.6.2. 1 X 10^6 cells were suspended in 1 ml aliquots of 4% w/v alginate, 4% w/v alginate and 10% v/v glycerol, and 4% w/v alginate, 10% v/v glycerol and 10 mg/ml fibrinogen solutions. Each 5 mm by 2 mm hydrogel disc was made from 100 µl of each cell-laden solution using customised moulds (see 2.4.2). The experimental set-up was otherwise as described in 4.1.2.3.

Following on from results obtained from the above experiments, adjustments were made to the composition of hydrogels used in the next phase of experiments, which were focused on creating a biomimetic hydrogel for cell encapsulation purposes that was printable using the 3DDiscovery. As alginate is bioinert, it is necessary to incorporate bioactive agents to improve the functionality of alginate-based hydrogels. The composition of gelatin-based hydrogels was similarly adjusted to improve their printability. In both cases, HA was used to substitute for glycerol given its proven functionality and physicochemical properties. Additional hydrogel compositions were created based on previous studies by Wust *et al* (328), Kang *et al* (69) and Zhang *et al* (322), the properties of which are summarised in **Table *4-1***.

Hydrogel composition		**Crosslinking method (post-deposition)**	**Printability**	
			Extrusion	Inkjet
Low viscosity alginate	**2% w/v**	100 mM $CaCl_2$	-	+
	4% w/v		-	++
	10% w/v		+	+++
4% w/v alginate, 5% w/v gelatin		100 mM $CaCl_2$ and cooling to 4°C	+	++
10% w/v alginate, 0.5% w/v HA, 10 mg/ml fibrinogen		100 mM $CaCl_2$	+	++
10% w/v alginate, 0.5% w/v HA, 10 mg/ml fibrinogen, 20 µg/ml fibronectin		100 mM $CaCl_2$	+	+++
Gelatin	**2% w/v**	None	-	+
	6% w/v		-	++
	8% w/v		+	+++
5% w/v gelatin, 0.5% w/v HA		None	-	+

6% w/v gelatin, 0.75% w/v HA	None	-	++
8% w/v gelatin, 1% w/v HA	None	+	+++

Table 4-1 Hydrogel compositions and their printability using the 3DDiscovery.

The printability of various hydrogel compositions is indicated by a negative (-) or positive (+) sign, with an increasing ease in printing indicated by additional positive signs.

The next phase of experiments involved testing the cytocompatibility of the most printable cohort of hydrogels (based on the findings in Table 4-1), and to elucidate the effects of increased hydrogel viscosity and lower Ca^{2+} availability for alginate hydrogels on cell viability post-encapsulation. STRO-1 enriched BMSCs were isolated from the bone marrow of a 70 year old female patient, and cultured according to protocols described in 3.1.2.1 and 3.1.2.2 prior to being pre-labelled using PKH-26 (Red) Fluorescent cell membrane labelling kit, as summarised in 2.6.2. 1 X 10^5 cells were suspended in 1 ml of 10% w/v alginate, 0.5% w/v HA, 10 mg/ml fibrinogen and 20 µg/ml FN, 6% w/v gelatin and 0.75% w/v HA, and 8% w/v gelatin and 1% w/v HA solutions. 100 µl of each cell-laden solution was manually pipetted onto the TCP of a 24-well plate. The plates were kept at 4 °C for 30 minutes to enable physical crosslinking. Ionic crosslinking of alginate-based bioinks was then performed by incubating the bioinks in 100 mM calcium chloride for 15 minutes. All cell-laden cohorts were cultured in a humidified incubator at 37 °C, 5% CO_2 for 7 days in basal media containing 2.5 mM calcium chloride and 1 U/ml human thrombin to match *in vivo* conditions. Media was changed every 3 days.

4.1.3 Results

4.1.3.1 Hydrogel swelling test

Hydrogel swelling was maximal within the first three hours of incubation for all four types of hydrogels. The size of alginate-based hydrogels appeared to equilibrate by day 3 (see Figure 4-6). 4% w/v alginate, 10% v/v glycerol and 10 mg/ml fibrinogen gels had the highest swelling ratios of the three alginate-based gels, irrespective of incubation temperature, when cultured in αMEM containing 22.5 mM calcium chloride. Alginate-based hydrogels demonstrated similar swelling patterns and degradation rates when cultured in αMEM containing 22.5 mM calcium chloride, no matter the incubation temperature (Figure 4-7). While alginate-based hydrogels only began to degrade after 3 days of incubation, 5% w/v gelatin and 10% v/v glycerol hydrogels degraded within 24 hours of culture at both temperatures,

with debris seen within the wells. 5% w/v gelatin, 10% v/v glycerol and 10 mg/ml fibrinogen hydrogels, when incubated at 37°C in αMEM with 22.5 mM calcium chloride, were too fragile to weigh at day 3. The same gels were also too fragile to weigh from day 1 of incubation in 1x PBS or SBF, but were observed to be more swollen in 1x PBS, compared to SBF. By day 8 hydrogels in this group had disintegrated. Results of the hydrogel swelling test are summarised in Table 4-2.

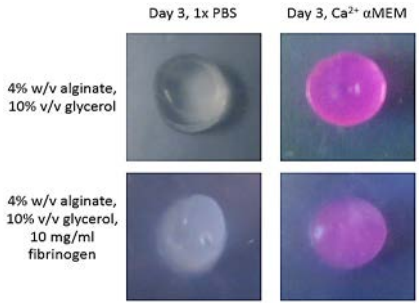

Figure 4-6 Hydrogel swelling at day 3.

Alginate-based hydrogel discs in 1x PBS and αMEM containing 22.5 mM calcium chloride kept at 21 °C retained their shape and structural integrity.

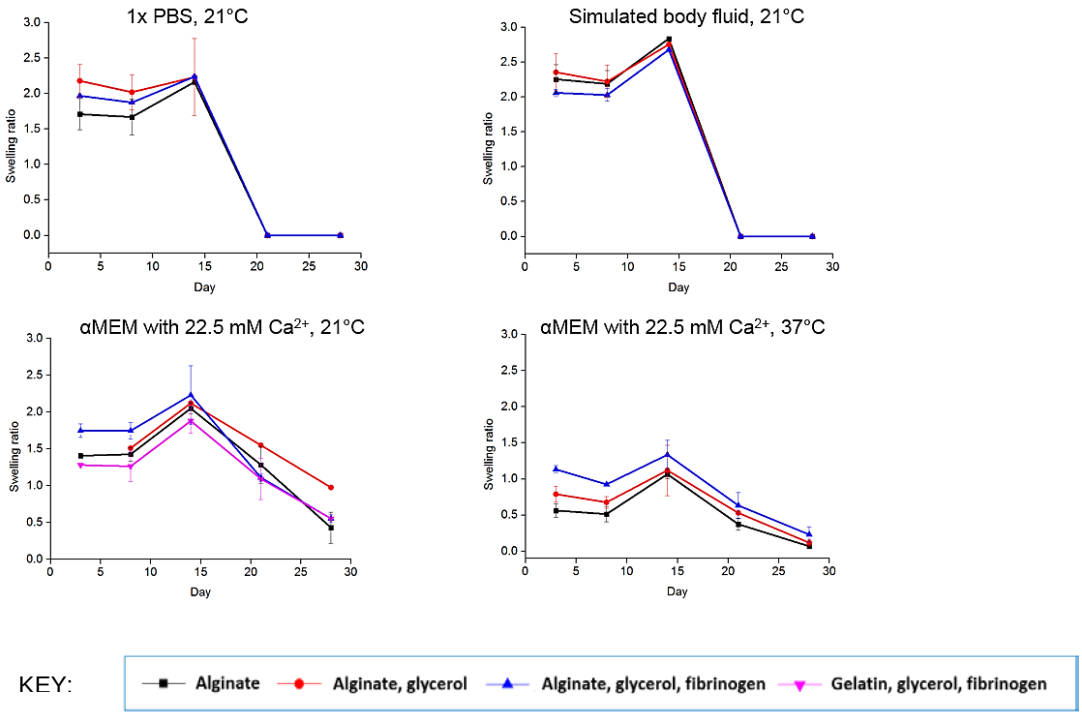

Figure 4-7 Hydrogel swelling test under different culture conditions.

The hydrogel swelling test demonstrated the most significant condition influencing swelling (and degradation) of alginate- and gelatin-based hydrogels was temperature.

Hydrogel composition	Time at peak swelling		Maximum swelling ratio		Time of earliest complete degradation	
	21 °C	37 °C	21 °C	37 °C (αMEM)	21 °C	37 °C (αMEM)
4% w/v alginate	Day 14	Day 14	2.84, in SBF	1.07	Day 21, in SBF, 1x PBS	Day 28
4% w/v alginate, 10% v/v glycerol	Day 14	Day 14	2.76, in SBF	1.12	Day 21, in SBF, 1x PBS	Day 28
4% w/v alginate, 10% v/v glycerol, 10 mg/ml fibrinogen	Day 14	Day 14	2.68, in SBF	1.34	Day 21, in SBF, 1x PBS	Day 28
5% w/v gelatin, 10% v/v glycerol	Day 1	Day 1	N.A.	N.A.	Day 1, all media	Day 1
5% w/v gelatin, 10% v/v glycerol, 10 mg/ml fibrinogen	Day 14	Day 1	1.88, in αMEM	N.A.	Day 8, in SBF, 1x PBS	Day 1

Table 4-2 Summary of hydrogel swelling test results.

Alginate-based hydrogels had completely degraded by day 21 when incubated in SBF or 1x PBS at 21°C.

Alginate and gelatin-based hydrogels in the second swelling test degraded within 6 hours of incubation at 37 °C. Maximal swelling for alginate-based hydrogels occurring at 3 hours, and gelatin-based hydrogels at 1 hour post-incubation.

4.1.3.2 MG63 cell viability following hydrogel encapsulation

Cell-laden hydrogels were successfully made using the customised moulds. PKH-26 (Red)-labelled MG63 cells had higher initial viability following encapsulation in 4% w/v alginate, 5% w/v gelatin hydrogels compared to 4% w/v alginate, 5% w/v gelatin, 10 mg/ml fibrinogen, 20 mg/ml mPEG-Succinimidyl Valerate hydrogels. Cell numbers had decreased by day 21 in both hydrogels (Figure 4-8, Table 4-3). Both hydrogels achieved maximal swelling on visual inspection by day 3, but did not significantly degrade over 21 days of culture. MG63 cells remained trapped within both hydrogels, maintaining their spherical morphology over the culture period, with some cells forming larger sized spheroid bodies (highlighted by yellow dotted circles in Figure 4-8). PKH-26 (Red) signal was present throughout the 21 day culture.

Hydrogel composition	Mean cell count		
	Day 3	Day 10	Day 21
4% w/v alginate, 5% w/v gelatin	432 ± 16	229 ± 17	202 ± 16
4% w/v alginate, 5% w/v gelatin, 10 mg/ml fibrinogen, 20 mg/ml mPEG-Succinimidyl Valerate	183 ± 11	298 ± 28	88 ± 12

Table 4-3 MG63 cell survival over culture time in different hydrogels.

4.1.3.3 STRO-1 enriched BMSC viability following hydrogel encapsulation

STRO-1 enriched BMSCs encapsulated in 4% w/v alginate and 10% v/v glycerol, and 4% w/v alginate, 10% v/v glycerol and 10 mg/ml fibrinogen hydrogels remained spherical at day 28 (Figure 4-9). In contrast, STRO-1 enriched BMSCs encapsulated in 4% w/v alginate proliferated and changed in morphology over the 28 day culture period. 4% w/v alginate hydrogels disintegrated within 24 hours of culture, with debris seen at the bottom of each well (Figure 4-10). A reduction in PKH-26 (Red) signal was observed only in this group over the 28 day culture period (Figure 4-10).

STRO-1 enriched BMSCs encapsulated in 10% w/v alginate, 0.5 mg/ml HA, 10 mg/ml fibrinogen and 20 µg/ml FN, 6% w/v gelatin and 0.75% w/v HA, as well as 8% w/v gelatin and 1% w/v HA were all viable in basal and osteogenic conditions at day 7 (Figure 4-11). These hydrogels degraded within 24 hours of culture. However, a few cells remained spheroidal in morphology in the alginate-composite hydrogel.

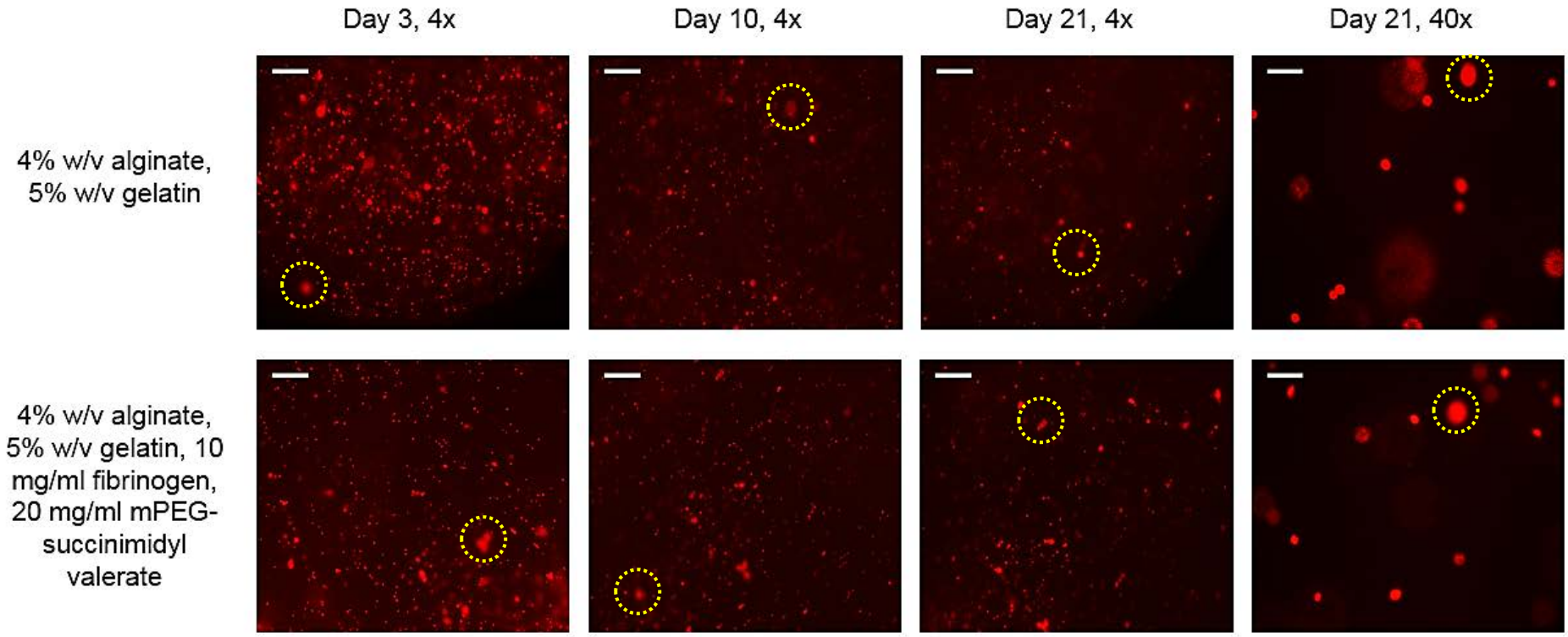

Figure 4-8 Morphological appearance of encapsulated MG63 cells cultured over 21 days.

Encapsulated MG63 cells retained their PKH-26 (Red) label and remained spherical in appearance over the 21 days of culture. Yellow dotted circles highlight the presence of spheroid bodies that were larger than the size of single MG63 cells. Scale bars in 4x magnification images represent 500 µm. Scale bars in 40x magnification images represent 50 µm. Images taken using an Olympus IX microscope, with 4x and 40x objectives, and a TRITC filter.

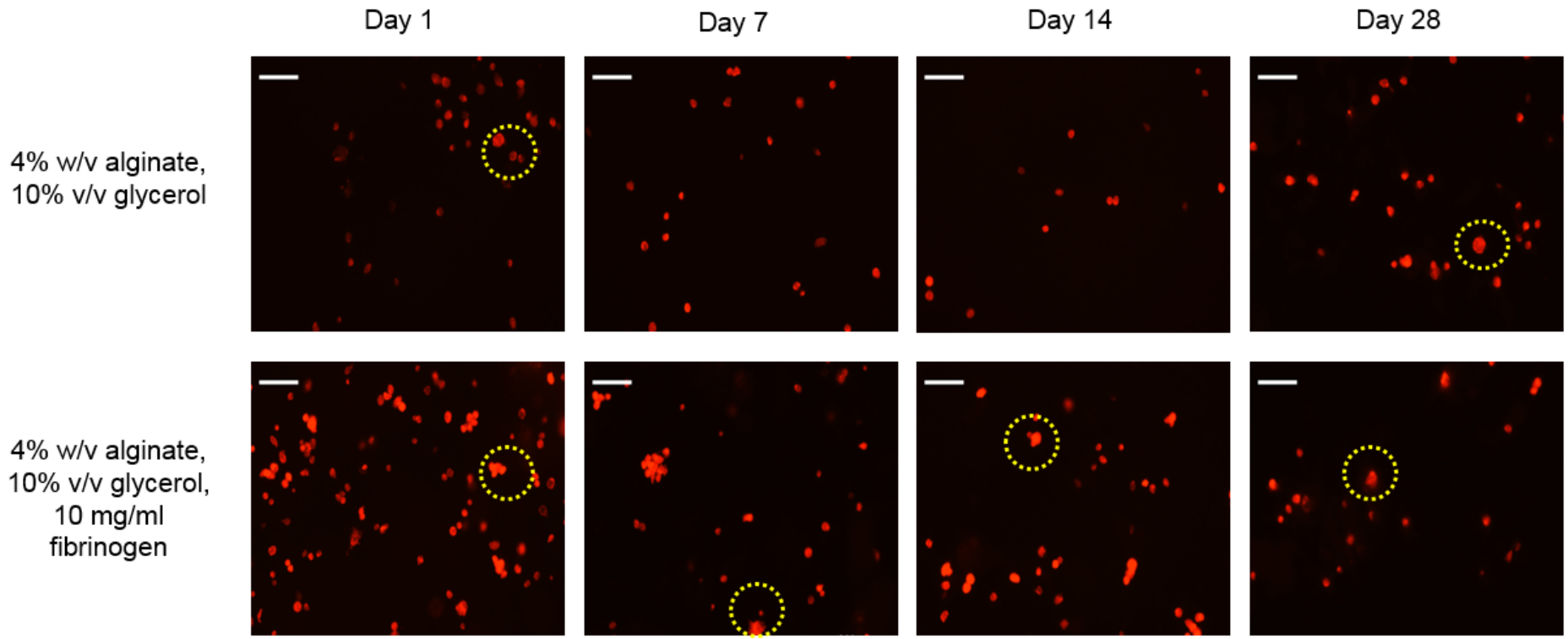

Figure 4-9 Morphological appearance of hydrogel-encapsulated STRO-1 enriched BMSCs cultured in basal media over 28 days.

The spherical appearance of PKH-26 (Red)-labelled STRO-1 enriched BMSCs encapsulated in 4% w/v alginate and 10% v/v glycerol, and 4% w/v alginate, 10% v/v glycerol and 10 mg/ml fibrinogen hydrogels is suggestive of anoikis, with progressive apoptosis over time (particularly in the latter group). Yellow dotted circles highlight the presence of spheroid bodies that were larger than the size of single STRO-1 enriched BMSCs. Scale bars represent 100 µm. Images taken using a Nikon Eclipse Ti microscope, with a 10x objective, and a TRITC filter.

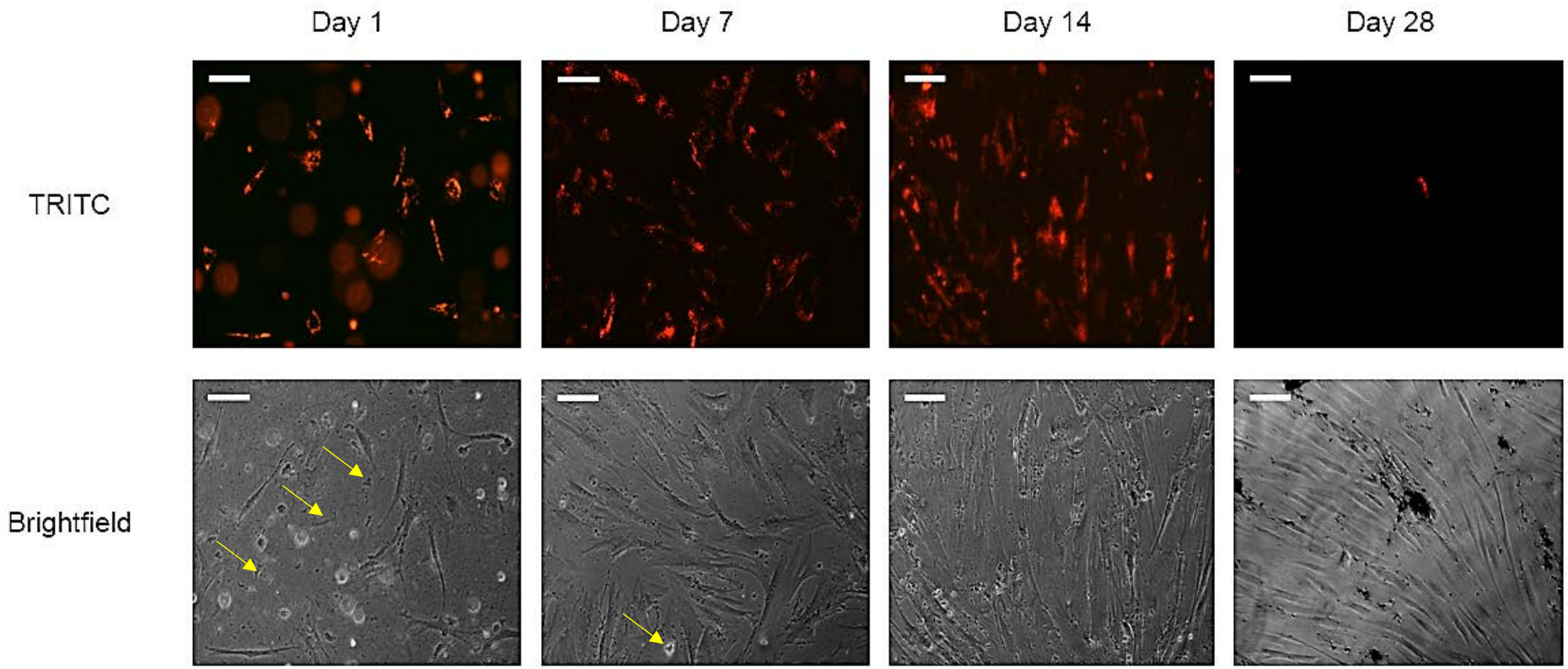

Figure 4-10 Morphological appearance of 4% w/v alginate-encapsulated STRO-1 enriched BMSCs cultured in basal media over 28 days.

PKH-26 (Red)-labelled STRO-1 enriched BMSCs encapsulated in 4% w/v alginate hydrogels demonstrated cell survival, proliferation, and migration, which matched the reduction in PKH-26 (Red) signal intensity over time (TRITC images). Alginate debris (highlighted by yellow arrows) from hydrogel degradation in vitro can be seen in the background of the Brightfield image at day 1. Scale bars represent 100 µm. Images taken using a Nikon Eclipse Ti microscope, with a 10x objective, and a TRITC filter.

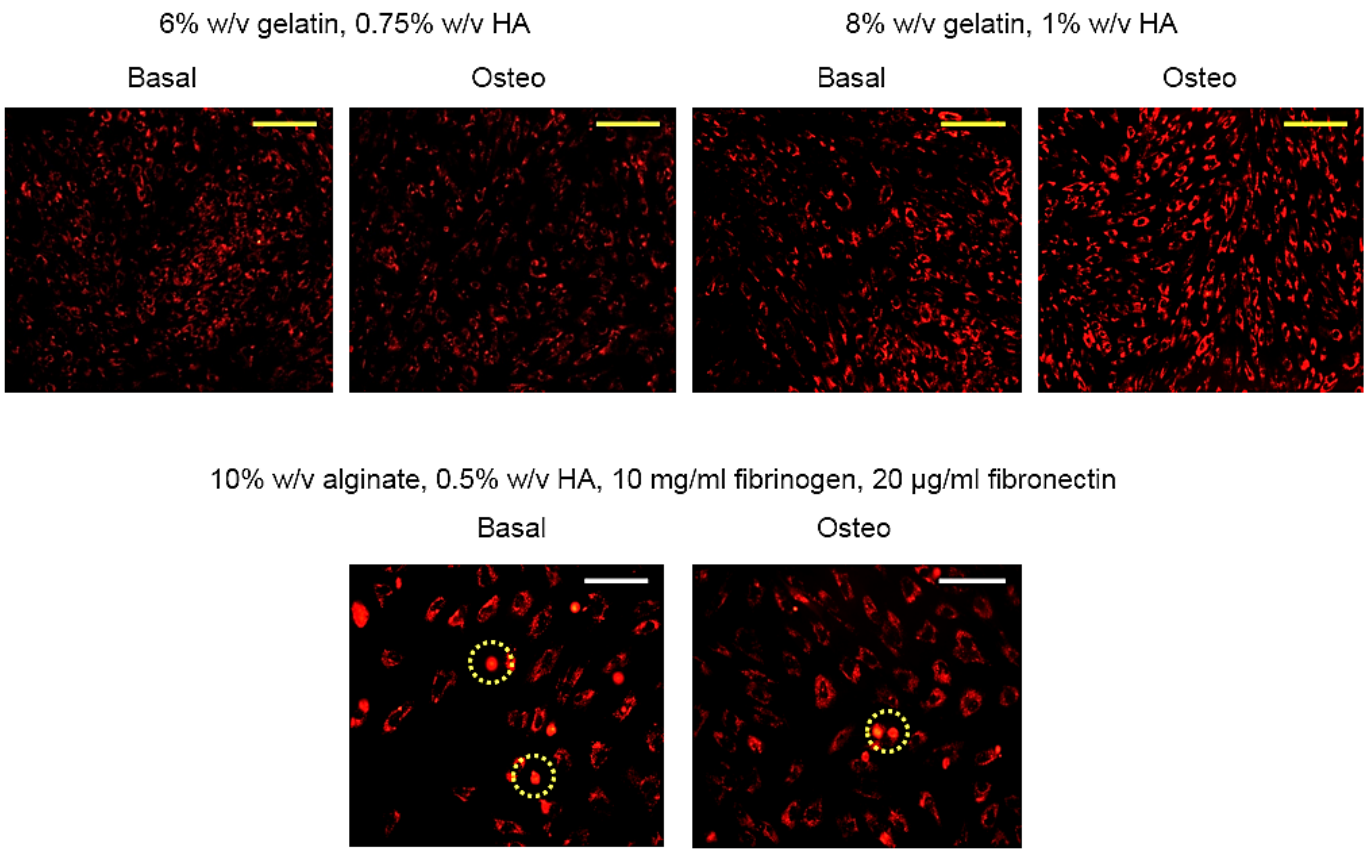

Figure 4-11 Morphological appearance of STRO-1 enriched BMSCs encapsulated in alginate- and gelatin-composite hydrogels at day 7.

PKH-26 (Red)-labelled STRO-1 enriched BMSCs were viable in basal and osteogenic conditions at day 7, following encapsulation in viscous hydrogels comprising of alginate or gelatin as the base biomaterial. Some cells remained spheroidal in morphology (yellow dotted circles). Yellow scale bars represent 200 µm, white scale bars represent 100 µm. Images taken using an Olympus IX microscope, with 10x and 20x objectives, and a TRITC filter.

4.1.4 Discussion

The experiments completed so far show:

- *Higher calcium concentrations slowed the degradation rate of alginate-based hydrogels, with alginate-based hydrogels degrading more slowly than gelatin-based hydrogels in general.*
- *Increasing incubation temperatures increased the degradation rate of both alginate- and gelatin-based hydrogels.*
- *MG63 cells and STRO-1 enriched BMSCs can survive hydrogel encapsulation, but their viability is reduced by increasing hydrogel stiffness and a slower rate of hydrogel degradation in culture.*

Alginate-based hydrogels in basal media containing 22.5 mM calcium chloride demonstrated decreased swelling ratios when incubated at 37°C, and only began to degrade after 3 days. Notably, the same hydrogels had disintegrated within 24 hours when incubated at 37°C in 1X PBS and SBF. Both solutions had much lower calcium concentrations (0 and 2.2 mM respectively). The more rapid dissolution of alginate-based hydrogels at 37°C was due to the greater reactivity of calcium ions, which caused faster crosslinking and generated less ordered networks, resulting in poorer mechanical stiffness (291). The alginic acid used to make the hydrogel solution contains a lower content of guluronate residues, which further contributed to lower hydrogel stiffness (291). The more organised network structure of hydrogels kept at 21°C enabled them to increase in size without fragmenting. The lower swelling ratios observed with alginate-based hydrogels incubated in basal media containing 22.5 mM calcium chloride (when compared to those incubated in 1X PBS and SBF) was a result of a greater degree of ionic crosslinking coupled to a slower loss of calcium ions into surrounding medium. The superior mechanical integrity of the hydrogels in this group was evidenced by their slower degradation rate at 21°C and 37°C. The hygroscopic effect of glycerol could account for the higher swelling ratios observed in glycerol containing hydrogels.

Gelatin-based, non-fibrinogen containing hydrogels disintegrated within the first 24 hours of the swelling test performed at 21 °C and 37 °C. Unmodified gelatin degrades at temperatures above 32°C, causing gel dissolution. Gelatin degradation depends on the processing conditions for its manufacture, the extraction and purification processes, as well as the crosslinking method utilised for gelation. Gelatin hydrogels are formed by physical crosslinking in water above 2% w/v, and at

temperatures below 30°C. Aggregated gelatin molecules undergo conformational changes to form a triple helix, with intermolecular hydrogen bonds forming between large fractions of gelatin chains (Figure 4-2) (333). Increased temperatures and incubation duration accelerate gelatin degradation by breaking non-covalent bonds, resulting in the destruction of the physical network (334). The osmotic effect of glycerol further weakened the stability of the gelatin network through increased water absorption. Although the addition of fibrinogen to this mixture (hydrolysed to insoluble fibrin by added thrombin) and to a lesser extent, HA, improved the stability of the gelatin network, it remained an insufficient measure (at the concentrations used) in preventing the early dissolution of these gels, particularly when incubation temperatures increased (Figure 4-7, Figure 4-11, Table 4-2).

Reduced cell viability post-alginate composite hydrogel encapsulation was noted in MG63 and STRO-1 enriched BMSC cohorts that were cultured in 22.5 mM containing media, with the exception of 4% w/v alginate-encapsulated STRO-1 enriched BMSCs. Combining alginate and gelatin meets the osmolar requirements of cells and maintains their viability while improving the stability of the hydrogel by maintaining the initial bonding between layers due to the gelation of gelatin and the ionic crosslinking of alginate by calcium chloride. Hydrolytic conversion of fibrinogen to fibrin performs a similar mechanical function. The thickness and higher stiffness of the encapsulating hydrogels could have reduced nutrient and oxygen diffusion. Signal intensity of the PKH-26 (Red) dye should have steadily diminished over time as the cells proliferated (as observed in Figure 4-10) or underwent apoptosis. PKH Linkers have been successfully utilised for live cell tracking *in vitro* and *in vivo*, with no effect on biological or proliferative ability, and with minimal transfer from labelled cells to host cells. PKH-26 (Red) labelling demonstrated the persistent spherical morphology of encapsulated cells through its binding to their cell membranes. An unchanged morphological appearance suggests encapsulated cells were unable to degrade sufficiently the surrounding matrix, and remained localised to their position during the culture period, thus limiting their capacity to migrate and differentiate. This finding was similar to those found by Fedorovich and colleagues (66, 78), and may indicate some encapsulated cells undergo anoikis (apoptosis in response to inappropriate cell-matrix interactions), when these cells are unable to spread out within a matrix after a period of time has elapsed (288). Cells normally sense their location through interactions with their ECM and neighbouring cells, even during migration. Induction of anoikis occurs when cells lose attachment to the ECM or on adherence to the wrong matrix type (although the latter is more relevant *in vivo*)

(335). STRO-1 enriched BMSCs demonstrated a more rapid decrease in cell numbers compared to the MG63 cohort following encapsulation. Cell lines and tumour cells are more resistant to anoikis, whereas stem cells are exquisitely sensitive to anoikis (335). The glycerol concentration used could also have impaired adhesion and/or proliferation of STRO-1 enriched BMSCs, thereby increasing the chances for anoikis and apoptosis of encapsulated cells (336).

In the second series of experiments, the viscosity of the hydrogel solutions was increased further by increasing the amount of alginate and gelatin, but also by the addition of fibrinogen, FN and HA to the alginate-based hydrogels, and by the addition of HA to gelatin-based hydrogels. The survival of the encapsulated cells suggest the cytocompatibility of the biomaterials added and in spite of the increase in hydrogel viscosity. However, the spheroidal appearance of a few encapsulated cells suggested that high viscosity alginate-composite hydrogels (although more bioprintable) could impair the adhesion growth of a small proportion of encapsulated cells, in keeping with initial findings in this chapter, and that of work done by Gudapati *et al* (337). The increase in hydrogel viscosity did not prevent alginate- or gelatin-based hydrogel degradation within 24 hours of incubation at 37 °C. The increased fragility of alginate-composite hydrogels was induced by decreasing Ca^{2+} concentration in culture media from 22.5 to 2.5 mM. Additionally, the polyanionic, hydrophilic nature of HA in solution accelerated hydrogel swelling and further reduced Ca^{2+} ion availability for alginate crosslinking. This increased rate of hydrogel degradation enabled the early release of encapsulated cells, which proliferated steadily over seven days of culture, thereby demonstrating hydrogel degradation rate plays a key role in determining cell viability post-encapsulation.

4.1.5 Conclusions

Hydrogel stiffness and degradation can be controlled by adjusting the molecular weight of the organic component used, the protein content, or through crosslinking methods. However, improvements in hydrogel stability and mechanical functionality were observed to have an adverse effect on cell viability, proliferation and migration. The above experiments indicated that culture conditions play a significant role in the mechanical integrity as well as the degradation rate of alginate- and gelatin-based hydrogels, and that rapid hydrogel degradation is necessary for the delivery of encapsulated STRO-1 enriched BMSCs with good viability. The next series of experiments were performed to investigate the possibility of bioprinting similar cell-laden bioinks and the effects of bioprinting on cell viability.

4.2 Bioprinting cell-laden bioinks

4.2.1 Introduction

3D printing methods and modifications in bioink compositions have become progressively more effective in ensuring not only cell viability, but functionality post-printing (288). The ability of 3D printing methods to deliver multiple cell types and biological components in a controlled fashion with spatial accuracy might help overcome the limitations of manual cell seeding methods (78, 84, 85, 135, 288). However, choices, to date, remain limited for effective bioinks for bioprinting purposes (338).

Biofabrication of osteochondral tissues requires the printing of hydrogels stacked in a multi-layered manner. Biofabricating stacked constructs using different types of hydrogels often results in inter-layer mixing, and therefore, a loss of the interface between stacked layers (as a consequence of the highly fluid nature of the solutions used). Additionally, in order to reduce cellular damage by shear forces during the printing process, cells are normally encapsulated with readily flowable, cytocompatible bioinks that are typically gelatin, alginate and/or HA-based (339). Treatment with chemicals or physical stimuli is often necessary to improve the mechanical integrity of the construct, but this could result in undesirable side-effects in other hydrogel layers and cytotoxicity to encapsulated cells. For instance, high calcium concentrations are used to induce ionic crosslinking in alginate hydrogels, which can cause cytotoxicity on prolonged exposure (337). This difficult balance between achieving structural integrity and cytocompatibility of the final construct is termed as the ‘biofabrication window’ (288).

Matching a hydrogel’s characteristics with the physicochemical demands of the biofabrication process, which in part, is due to the current limitations of AM technology, has been a major challenge (84, 135). The selected AM method directly influences the choice of biomaterials, and therefore, the properties of the bioink (340). As discussed in 1.5 and listed in Table 1-5, each AM technique has its specific advantages and disadvantages. To date, no single AM technique has met every criteria of the ‘biofabrication window’. Figure 4-12 summarises this interplay between the bioprinter, the hydrogel bioink, and cell viability post-printing.

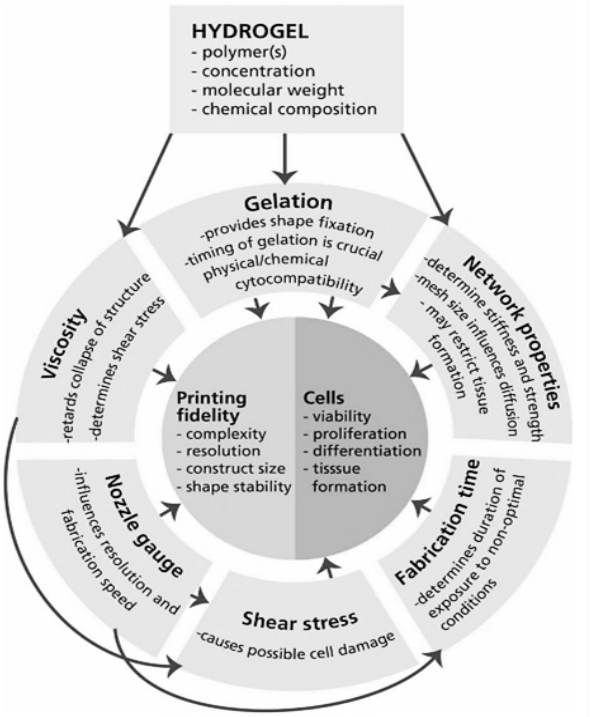

Figure 4-12 The interplay between hydrogel composition, material properties, printing parameters, and bioprinter limitations.

Several factors determine whether printed cells remain viable and functional post-printing, and whether the bioconstruct is sufficiently stable to use for in vitro or in vivo studies. Adapted from (84).

No studies have yet generated heterogeneous cell-encapsulated constructs by stacking printable ECM-mimetic biomaterials (341). Alginate and gelatin have been shown to be cytocompatible, non-immunogenic, and tuneable for printing purposes, but they lack significant mechanical properties for load-bearing function. Furthermore, these biomaterials do not promote normal cellular function as seen with native ECM. Studies have shown that hydrogels derived from natural ECM (particularly when based on the ECM composition in the tissue of interest) can enhance tissue regeneration by providing the necessary biochemical cues to induce cell differentiation and migration to a defect site (318). Some reports have indicated that uncrosslinked or degraded ECM molecules encapsulated within hydrogels may be released over time to form a gradient, directing the migration of cells near ECM hydrogels (321, 342).

Given that native bone ECM is primarily composed of collagen type I fibrils, in addition to the crucial structural and homoeostatic roles of glycosaminoglycans present such as heparan sulphate (HS) even during the initial repair phase of

fracture healing, a sensible approach would be to incorporate collagen type I and HS in any artificially created biomimetic bioink to enhance the mechanical integrity and regenerative functionality of such bioink(s). This approach was therefore investigated in this phase of bioink development. Collagen comprises of glycine-proline-hydroxyproline polypeptide repeats. The triple helix in collagen type I is approximately 300 nm in length and 1.5 nm in diameter, and is formed as a heterotrimer of two identical α_1(I)- and α_1(II)-chains and one α_2(I)-chain with ~1000 amino acids (see Figure 4-2). Hydrogen bonds link the α–chains together. Collagen molecules self-assemble into a supramolecular form via a quarter-stagger pattern of five triple helical molecules. Telopeptides (composed of non-helical regions about 20 amino acid residues in length) play a key role in fibrillogenesis, contributing to the stabilisation of mature collagen molecules through crosslink formation mediated enzymatically (lysine hydroxylase and lysyl oxidase) or non-enzymatically (glycation- or oxidation-induced advanced glycation end-products). Collagen type I is commonly extracted from bovine tendons and is biodegradable, cytocompatible, hydrophilic and stable *in vivo*. Collagen hydrogels are formed at low concentrations (<3 mg/ml). Injectable collagen type I gels and implanted sponges demonstrate low antigenicity (343). Composite scaffolds consisting of electrospun PCL, nano-HAP and collagen type I (344), fibrinogen, fibronectin and collagen type I (307), HA and collagen type I (342, 345), and HAP and collagen type I (346) have been studied as bone tissue engineering substrates. Collagen type I has been shown to support osteoblast as well as osteoclast (and chondrocyte) attachment and differentiation *in vitro* and *in vivo* (343, 347), with several collagen products currently being marketed as guided bone regeneration membranes (348).

HS forms an important part of the organic component of native bone ECM, operating structurally as well as protecting signalling factors from proteases while potentiating the presentation of these factors to cell surface receptors (Figure 4-13). HS has a molecular weight of up to 70 kDa and is a variably sulphated, polyanionic, linear polysaccharide composed of 40 to 300 disaccharide units of N-acetyl glucosamine and alternating uronic or L-iduronic acid. *In vivo*, HS synthesis occurs in the Golgi apparatus and degradation occurs via intracellular and extracellular heparanase (349). HS expression is developmental stage- and tissue-specific, indicating that various isoforms exist to perform specific binding functions. HS is covalently complexed to a protein core and can be found attached to cell surfaces as syndecans and glypicans, in the ECM as perlecans (350), or in secretory vesicles as serglycin (351). There is increasing evidence that HS and HS-mimetics

(created from dextran derivatives) may regulate the early stages of repair and regeneration of bone tissue after injury through the modulation of growth factors involved in osteoblastogenesis, osteoclastogenesis and bone remodelling (352, 353). Indeed, studies have suggested the type of HS used can positively or negatively influence the crosstalk between the bone surface and marrow cells, which in turn, could interfere with bone remodelling and formation (354). Jackson *et al* showed 5 µg, rather than 50 µg doses of HS, induced a greater increase in Runx2, ALP and VEGF gene expression (350). HS has been reported to regulate the mesenchymal niche of haematopoietic stem cells (349) and inflammation (355).

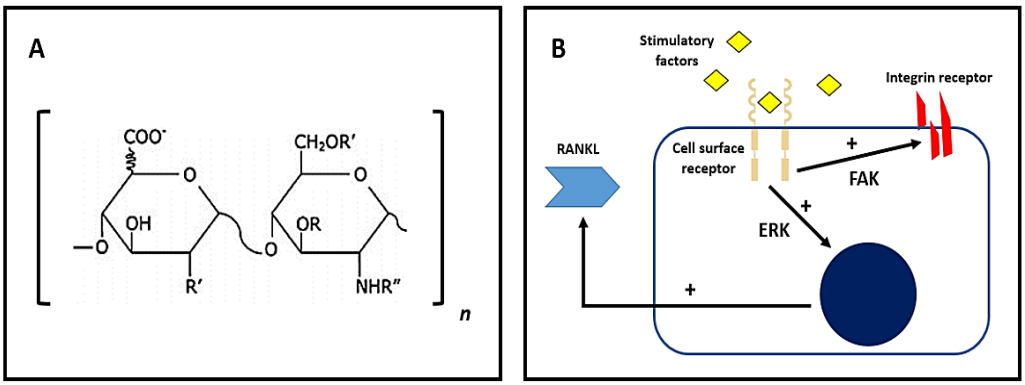

Figure 4-13 Heparan sulphate.

A) The disaccharide repeats comprising HS. B) Stimulatory factors such as Wnt, BMP-2, fibronectin, collagen type I and VEGF bound to HS become liberated from the ECM and mass action enables binding to high affinity cell surface receptors, which dimerise, triggering ERK and focal adhesion kinase pathways. This induces cell proliferation and differentiation and integrin receptor activation respectively. Upregulation of RANKL also occurs, stimulating osteoblast (and osteoclast) maturation. Adapted from (350) and (352).

Cells printed using laser-assisted and thermal inkjet techniques have been shown to have high viability in addition to retaining their phenotype post-printing (71, 356). Having demonstrated the cytocompatibility of biomimetic biomaterials through conventional seeding methods in 4.1, two of the three main AM methods for printing cell-laden bioinks (the compositions of which were based on the most printable hydrogel compositions in 4.1**Table 4-1**), microcontact extrusion and droplet jetting (see 1.5), were utilised to determine which method, if any, was capable of printing cell-laden bioinks with good cell viability, resolution and reproducibility. Composition of the tested bioinks was further adjusted in lieu of the above evidence in order to improve the functionality of the bioinks for cell delivery purposes.

As stated in 1.9, the hypotheses of this thesis are:

1) Human STRO-1 enriched BMSCs possess, and retain, the capacity for osteogenesis when seeded onto scaffolds, and are therefore a suitable cell type for use in bone reparation.

2) Biomaterials can be combined to generate tuneable bioinks, which can be used to deliver STRO-1 enriched BMSCs with high viability and functionality.

3) 3D printing methods are capable of manufacturing porous scaffolds of clinically relevant size with high resolution and reproducibility.

4) STRO-1 enriched BMSCs, biomimetic bioinks, and 3D printed polycaprolactone-based scaffolds can be combined to create an integrated bioconstruct for use in bone repair.

In conjunction with the above hypotheses, the aims of this research project are:

1) To confirm the osteogenic potential of STRO-1 enriched BMSCs.

2) To elucidate the osteoinductive capabilities of established biomaterials, such as titanium and polycaprolactone (amongst others), in order to identify potential combinations for the generation of composite scaffolds and/or bioinks for use in bone tissue engineering.

3) To design novel porous scaffolds that mimic natural bone architecture.

4) To investigate the feasibility of utilising 3D printing techniques to accurately and reproducibly manufacture scaffolds according to their design.

5) To determine the possibility of 3D printing cell-laden bioinks.

6) To develop methods for integrating 3D printed scaffolds, biomimetic bioinks, and STRO-1 enriched BMSCs, with the objective of creating functional bioconstructs for use in bone reparation.

4.2.2 Materials and Methods

4.2.2.1 Manufacture of bioinks

4.5 g of sodium chloride was dissolved in 100 ml of sterile αMEM (Lonza, Switzerland) to form the basic component of the bioink. 1 g of human fibrinogen (Sigma Aldrich, UK) was dissolved in 25 ml of sterile-filtered αMEM containing 4.5% w/v sodium chloride (warmed to 37 °C). 1 mg of human FN (Sigma Aldrich, UK) was

dissolved in 6.25 ml of sterile-filtered αMEM containing 4.5% w/v sodium chloride at 37 °C for 30 minutes on a rotator-shaker. The stock solution was sterile-filtered using a 0.22 µm filter. 15 mg of lyophilised human type I collagen (Advanced BioMatrix, USA) was dissolved in 3 ml of sterile-filtered 0.01 M hydrochloric acid. 1 mg of heparan sulphate sodium salt from bovine kidney (Sigma Aldrich, UK) was dissolved in 1 ml of αMEM containing 4.5% w/v sodium chloride.

In order to test the printability of a (sprayable) biomimetic bioink by, and the cytocompatibility of, droplet jetting, 3% w/v alginate made by dissolving 750 mg alginic acid sodium salt from brown algae, low viscosity (Sigma Aldrich, UK) in 25 ml of αMEM containing 4.5% w/v sodium chloride, was used. Once printing parameters were established, a 50 ml volume of a biomimetic bioink consisting of 3% w/v alginate, 5 mg/ml fibrinogen, 20 µg/ml FN, 100 µg/ml collagen, 5 µg/ml HS, and 1% w/v HA was made inside a microbiological safety cabinet as follows: 500 mg of high molecular weight HA (3D Global Inc., Taiwan) was added to 30 ml of αMEM containing 4.5% w/v sodium chloride under constant stirring at 800 rpm using a digital overhead stirrer. The solution was kept at 37 °C by keeping the beaker on a heating plate. 1500 mg of alginic acid sodium salt from brown algae, low viscosity (Sigma Aldrich, UK) was subsequently added to the mixture before 0.25 ml of the HS stock solution was also added. 6.25 ml of FN stock solution followed, along with 6.25 ml of the stock solution of fibrinogen. 1 ml of the collagen stock solution was finally added to the mixture, which was stirred for a further hour at 500 rpm and at 37 °C. Bioink pH was corrected to 7.5 using sterile-filtered 1 M sodium hydroxide. The bioink volume was adjusted with αMEM containing 4.5% w/v sodium chloride to make a final volume of 50 ml.

4.2.2.2 MG63 cell viability post-bioprinting

MG63 cells obtained from Taipei Medical University were cultured as described in 2.2. These cells were pre-labelled using PKH-26 (Red) Fluorescent cell membrane labelling kit, as summarised in 2.6.2. Alginate and gelatin stock solutions were made as described in 4.1.2.1. 1 X 10^6 PKH26 (Red)-labelled MG63 cells were mixed (in a 3 ml sterile printing syringe) with 1 ml of 4% w/v alginate, 5% w/v gelatin solution to generate a printable cell-laden bioink. A 10 by 10 by 0.4 mm square grid pattern was bioprinted by microextrusion, with the following settings assigned to the design: a feed rate of 3.5 mm/s, pore size of 0.8 mm, and a layer height of 0.2 mm. The CF-300H printhead was kept at 37°C. A microvalve opening time of 180 µs, with a dosing distance of 0.1 mm, and a pressure setting of 0.8 bars were applied. A

microcontact needle (with a 0.18 mm internal diameter) was used to print the cell-laden bioink onto a sterile petri dish that was kept at 4°C (using the custom cooling device in 2.3.1). This printed grid was crosslinked for 15 minutes in a 100 mM calcium chloride solution. Using a humidified incubator set at 37°C, 5% CO_2, the printed square grid was cultured for 21 days in basal media containing 22.5 mM calcium chloride (changed every 3 days). Triplicate images at each time-point were used for cell counts, which was performed using the Fiji cell count plug-in.

4.2.2.3 STRO-1 enriched BMSC viability post-bioprinting

3% w/v alginate (coloured with green food colouring) was used to ascertain the 3DDiscovery bioprinter settings required for droplet jet printing of bioinks. A 10 mm circular pattern, with fill lines set 1 mm apart and edges stripped, and a build height of 0.2 mm was designed in BioCAD to generate a double layer hydrogel. A feed rate of 5 mm/s, microvalve opening time of 180 µs, dosing distance of 0.5 mm, and a pressure setting of 0.2 bars were applied. The CF-300H printhead was kept at 37°C while ambient room temperature during the printing process was 21 °C. Ambient humidity was 70%. A jetting adapter (with a 0.3 mm internal diameter) was used to print the 3% w/v alginate bioink onto a petri dish.

STRO-1 enriched BMSCs from the bone marrow of a 70 year old female patient was isolated and cultured according to protocols described in 3.1.2.1 and 3.1.2.2. These cells were pre-labelled using PKH-26 (Red) Fluorescent cell membrane labelling kit, as summarised in 2.6.2. 1.5 X 10^5 PKH26 (Red)-labelled STRO-1 enriched BMSCs were mixed (in a 3 ml sterile printing syringe) with 3 ml of the biomimetic bioink (described in 4.2.2.1, and coloured with blue food colouring) to generate a printable cell-laden bioink. An 8 mm diameter circular fill pattern, with fill lines set 0.9 mm apart and edges stripped, and a build height of 0.06 mm, was designed in BioCAD to generate a monolayer of hydrogel lines by using the droplet jet deposition printhead of the 3DDiscovery bioprinter. The CF-300H printhead was fitted with a sterilised cell agitator which enabled constant stirring of the cell-laden bioink within the printing syringe. The CF-300H printhead was kept at 37°C while ambient room temperature during the printing process was 20 °C. The feed rate was set at 3.5 mm/s. A microvalve opening time of 140 µs, with a dosing distance of 0.5 mm, and a pressure setting of 3.1 bars were applied. A jetting adapter (with a 0.3 mm internal diameter) was used to print the cell-laden bioink onto a sterile 24-well plate. Half of the printed lines were crosslinked for 15 minutes in 100 mM calcium chloride. The remaining half were immediately immersed in culture media. Using a

humidified incubator set at 37°C, 5% CO_2, the printed lines (crosslinked and uncrosslinked) were cultured for 7 days in basal or osteogenic media (which were changed every 3 to 4 days). Similar volumes of cell-laden biomimetic bioinks were manually pipetted onto TCP, left uncrosslinked, and cultured in basal and osteogenic media as comparative control groups.

4.2.3 Results

4.2.3.1 MG63 cell viability post-bioprinting

The cell-laden 4% w/v alginate, 5% w/v gelatin square mesh was observed to contract in size during the crosslinking step described in 4.2.2.2, and did not return to its original printed size during culture. The extruded hydrogel degraded minimally (mainly along the edges of the square mesh) during the 21 days of culture (Figure 4-14 and Figure 4-15). At day 3, printed fibres of cell-laden bioink measured 460.74 ± 14.44 µm while pore sizes measured 187.52 ± 13.44 µm. These printed fibres increased in size to 604.68 ± 16.16 µm while pore sizes reduced to 128.8 ± 6.4 µm at day 21. Distinct rows of MG63 cells could be seen post-printing (unlike the random distribution with the moulded hydrogels). An initial increase in PKH-26 (Red) signal occurred by day 7 but cell numbers declined by day 21 (**Table 4-4**). Morphological changes were not observed at all time-points (Figure 4-15). Spheroid bodies, ranging from 30 to 60 µm in diameter (which were also present in similar hydrogels created using customised moulds, see Figure 4-8), were observed to form within the printed hydrogel over time (Figure 4-15).

Hydrogel composition	**Mean cell count**			
	Day 3	Day 7	Day 14	Day 21
4% w/v alginate, 5% w/v gelatin	425 ± 8	484 ± 25	487 ± 23	342 ± 24

Table 4-4 MG63 cell survival over culture time post-bioprinting.

4.2.3.2 STRO-1 enriched BMSC viability post-bioprinting

Droplet jetting was successfully used to print bilayers of 3% w/v alginate bioinks with good resolution. Overall printed geometry and designed porosity were maintained despite no crosslinking being performed post-printing (see Figure 4-14 and Video 4-1). Droplet jetting also reproducibly printed monolayers of the biomimetic cell-laden bioink, generating parallel ‘lines’ of cell-laden bioink to produce a circular pattern on TCP of each well (Figure 4-14, Figure 4-16 and

Video 4-1). These parallel fibres were formed by individual droplets coalescing with each other, creating the ‘caterpillar-like’ pattern seen in the lower magnification images in Figure 4-16. Three hours post-bioprinting, the crosslinked printed fibres had a width of 781.49 ± 12.97 µm, while the gaps between the printed fibres were 173.42 ± 14.12 µm at their narrowest and 276.2 ± 18.57 µm at their widest. Encapsulated STRO-1 enriched BMSCs appeared to be widely distributed throughout the bioprinted biomimetic bioink, with no spheroid bodies seen at day 7. By day 1, printed fibres that were not crosslinked post-bioprinting had disintegrated in both basal and osteogenic conditions, releasing encapsulated cells into the wells. Crosslinked printed fibres degraded more slowly, as demonstrated by the presence of debris in basal and osteogenic conditions at day 7 (Figure 4-17). Although printed STRO-1 enriched BMSCs retained a spherical morphology in all cohorts at day 7, cell proliferation only increased in crosslinked and uncrosslinked cohorts cultured under osteogenic conditions. This finding was mirrored in manually pipetted STRO-1 enriched BMSC-laden bioinks cultured under osteogenic conditions, where cell numbers increased, and developed a spindle-like morphology (Figure 4-18).

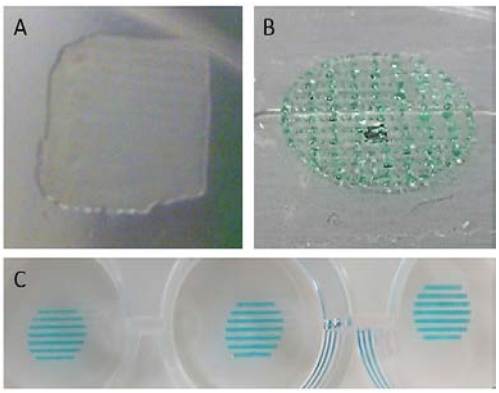

Figure 4-14 3DDiscovery-printed multi-material bioinks.

A) Microcontact extrusion was used to deposit a 4% w/v alginate, 5% w/v gelatin hydrogel encapsulating MG63 cells to form a 10 by 10 by 0.4 mm square meshwork, which retained its printed shape after 21 days in basal media. B) Droplet jetting was used to print a double layer of a 3% w/v alginate bioink with precision. C) Droplet jetting also reproducibly printed monolayers of 3% w/v alginate, 5 mg/ml fibrinogen, 20 µg/ml FN, 100 µg/ml collagen, 5 µg/ml HS, 1% w/v HA bioink containing STRO-1 enriched BMSCs every 16 seconds.

Gel printing.mov

Video 4-1 Droplet jetting of alginate-based hydrogels.

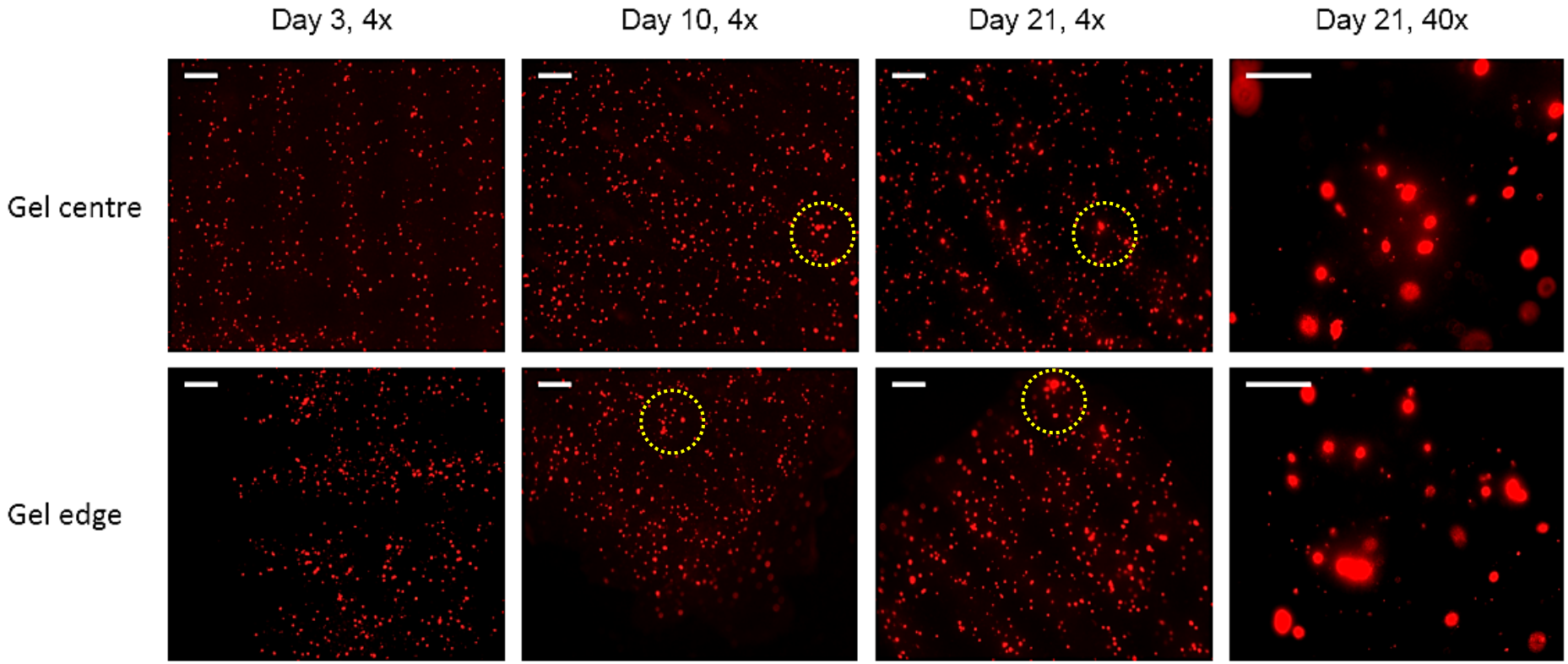

Figure 4-15 3D printed MG63 cell-laden 4% w/v alginate, 5% w/v gelatin bioinks over time.

Encapsulated MG63 cells remained spherical in morphology during the 21 days in basal culture, with some larger sized spheroid bodies readily spotted within the printed hydrogel by day 10 of culture (yellow dotted circles). The printed hydrogel underwent partial degradation over the 21 days, but retained its overall meshwork shape as shown above. Scale bars in 4x magnification images represent 250 µm while scale bars in 40x magnification images represent 50 µm. Images taken with an Olympus IX microscope with 4x and 40x objectives, and a TRITC filter.

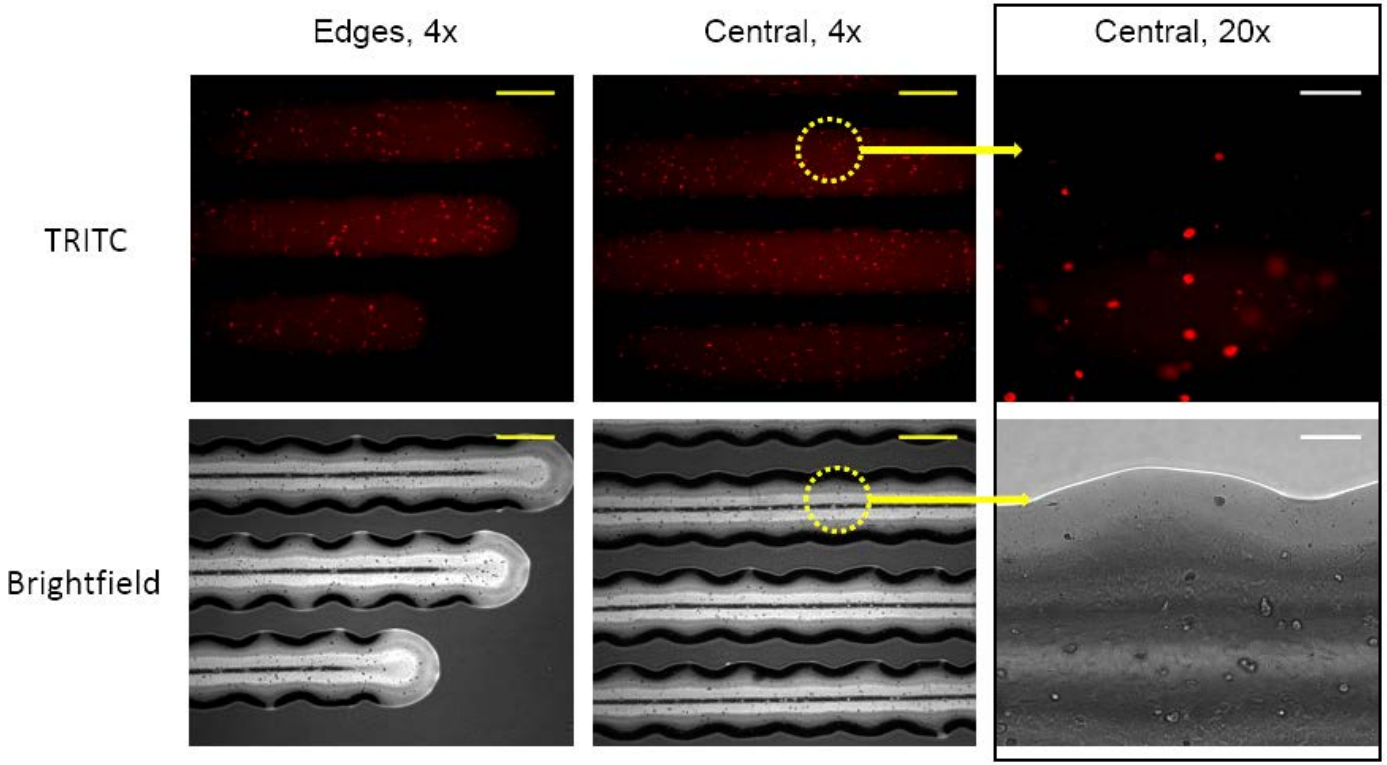

Figure 4-16 Bioprinted STRO-1 enriched BMSC-laden biomimetic bioink at day 0.

Printed fibres of cell-laden bioink retained their shape three hours post-printing, with encapsulated PKH-26 (Red)-labelled STRO-1 enriched BMSCs remaining spherical in shape (yellow dotted circles, 20x magnification images). Encapsulated cells appear fairly well distributed throughout the bioink. Yellow scale bars represent 500 µm while white scale bars represent 100 µm. Images taken using an Olympus IX microscope with 4x and 20x objectives, and a TRITC filter.

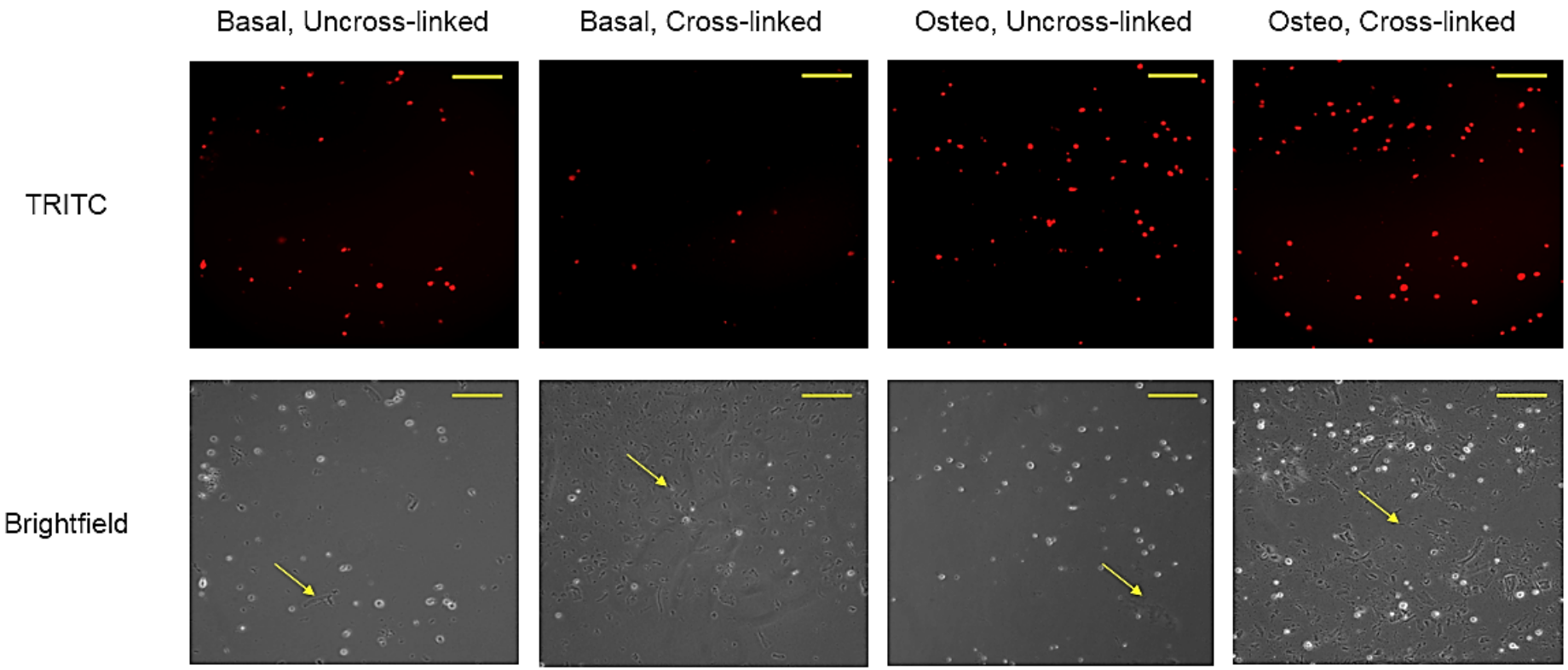

Figure 4-17 3D printed STRO-1 enriched BMSC-laden biomimetic bioink in different culture conditions at day 7.

Bioinks that underwent crosslinking prior to culture in both basal and osteogenic conditions degraded more slowly over time, with hydrogel debris (indicated by yellow arrows) easily visible at day 7 when compared to uncrosslinked bioinks. Cell survival and proliferation appeared to be reduced in basal conditions compared to osteogenic conditions. Yellow scale bars represent 200 µm. Images taken using an Olympus IX microscope with 10x objective, and a TRITC filter.

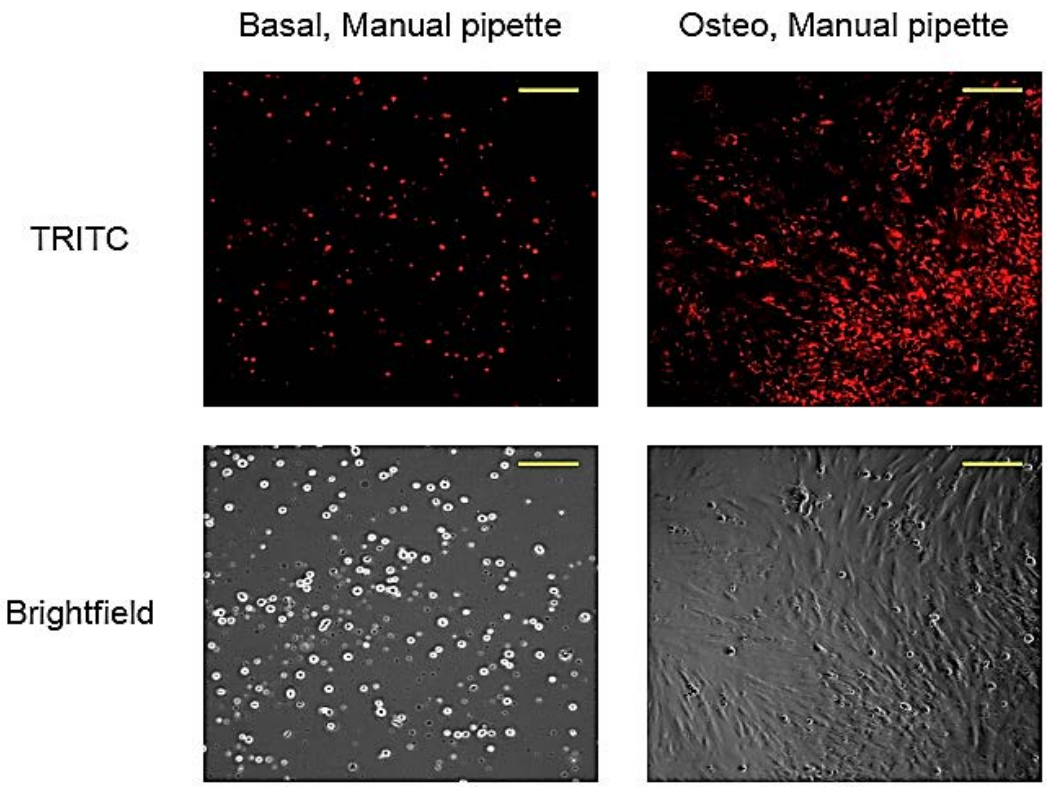

Figure 4-18 Pipetted (manual deposition) STRO-1 enriched BMSC-laden biomimetic bioinks at day 7.

Encapsulated STRO-1 enriched BMSCs cultured in basal media remained spherical in appearance at day 7. However, encapsulated cells cultured in osteogenic media demonstrated cell proliferation in addition to undergoing morphological changes by the same time point. Yellow scale bars represent 200 µm. Images taken using an Olympus IX microscope with a 10x objective, and a TRITC filter.

4.2.4 Discussion

The experiments above demonstrated:

- *The droplet jetting mode of the 3DDiscovery bioprinter can rapidly print bioinks with good resolution and reproducibility.*
- *The biomimetic bioink is printable and cytocompatible.*
- *MG63 and STRO-1 enriched BMSCs can survive encapsulation and bioprinting.*
- *Bioprinted cells remained spherical in morphology despite hydrogel degradation.*

3DDiscovery droplet jetting (and to a lesser extent, microcontact printing) demonstrated good resolution and reproducibility for bioprinting the generated bioinks. The adopted settings could be readily adjusted to reduce the volume of

deposited bioink to further improve the bioprinting resolution. Unlike microcontact printing, droplet jetting does not require the bioink to possess a high viscosity in order to accurately deposit the bioink onto a substrate (340). 3% w/v low viscosity alginate and biomimetic bioinks possessed sufficient viscosity for droplet jetting (but not microcontact printing) to build the designed geometries and porosities. Irrespective of the AM method applied, the low viscosity of these jetted bioinks would have reduced the stiffness of formed hydrogel layers, which could preclude the building of a clinically relevant-sized construct unless other crosslinking approaches were utilised (295). As osteogenic commitment of MSCs occurs at intermediate elastic microenvironments (11 to 30 kPa) (357), rheometric calibration of bioink viscosity could guide the adjustment of bioink composition so as to match printing requirements as well as direct the generation of a specific type of tissue (Figure 4-19). Such an approach has successfully created larger printed hydrogel-based constructs for use in tissue engineering (328, 329, 358).

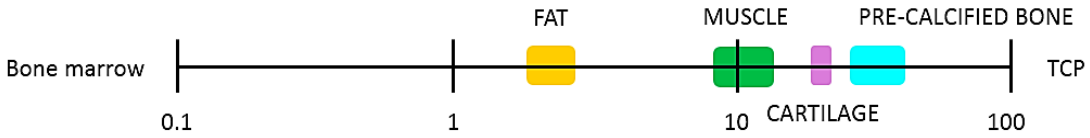

Figure 4-19 Elastic modulus scale of tissues in kPa.

Creating hydrogels with a similar elastic modulus could enhance MSC differentiation into the tissue of interest. Modified from (359).

Bioprinted MG63 cells remained viable but retained a spherical appearance and were unable to spread at all time points. Encapsulated cells adhere in three dimensions in hydrogels, resulting in a rounded morphology with no polarity being induced by cell-matrix interactions (287). Although polymer fraction solutions of greater than 5 wt% aid printability, such viscous solutions can reduce cell viability (329). This could be attributed to a reduced oxygen tension over time caused by low oxygen diffusivity through a viscous material [61, 139]. Studies have also shown that cell proliferation is reduced in 3D environments with a higher stiffness (150). Markusen and colleagues did not observe human MSC proliferation following MSC encapsulation within 1 wt% RGD-alginate beads after two weeks of culture, despite the encapsulated MSCs displaying metabolic activity (360). Similar findings were obtained by Maia *et al* with 2 wt% RGD-alginate (361), and Duggal *et al* using 1.8 wt% RGD-alginate (362). Duggal *et al* found that genes associated with early development, intracellular signalling and cell shape were downregulated upon MSC

immobilisation in RGD-alginate (362). Maia *et al* also demonstrated that the metabolic activity of encapsulated MSCs decreased as time progressed, while dsDNA content remained the same from day 4 onwards, indicating non-proliferation of encapsulated MSCs (361). Fully encapsulated cells are often sterically hindered in their spreading and migration due to the confinement of the surrounding matrix, with cell movement through a 3D environment having nanoscale pore sizes being reliant on the proteolytic activity of the cell (337). As mammalian cells lack alginase, encapsulated cells are dependent on hydrogel degradation in order to migrate.

Results obtained in 4.1.3.2 and 4.1.3.3 further suggested that an earlier cell release from encapsulation might improve cell viability and functionality. Several approaches can improve the mechanical attributes of alginate (339), but few methods (as discussed in 4.1.1) allow for better control over the degradation rate of alginate-based gels. In these experiments, prolonged STRO-1 enriched BMSC entrapment was avoided by reducing alginate concentration and by the addition of HA to the bioink composition. Reduced calcium concentrations in the culture media further accelerated hydrogel degradation. Despite this, bioprinted STRO-1 enriched BMSCs did not proliferate or show any morphological changes at day 7. Neither crosslinking nor culture conditions affected STRO-1 enriched BMSC behaviour post-bioprinting. The short culture period employed was not ideal, and may have precluded the possibility that bioprinted cells could proliferate or even differentiate at a later time point. Wu *et al* also noted that accelerating alginate degradation did not improve cell-cell or cell-matrix interactions in extrusion bioprinted hydrogels (363).

This static cell behaviour post-bioprinting suggests that mechanical forces applied to the cell-laden bioink could potentially contribute to a delayed recovery and functionality of encapsulated cells. In this study, the use of a stirring mechanism within the printing cartridge to minimise cell sedimentation during bioprinting could have compounded shear strain on the bioprinted STRO-1 enriched BMSCs. Droplet jetting consists of five stages: i) pressure generation, ii) flow through the orifice, iii) droplet formation and propagation to the substrate, iv) impact with the substrate, and v) recovery of the jetting mechanism to its original configuration (356). Each stage subjects the bioink to physical conditions that may damage encapsulated cells. Hydrostatic and inertial forces exerted during pressure generation, droplet formation and recovery are smaller than those due to shearing through the orifice and impact with the substrate (356, 364). Factors such as bioink rheology, orifice diameter, droplet volume and jetting velocity determine the level of shear strain (and

therefore cell damage) (356, 364). However, Blaeser *et al* found that the viability of 0.5 to 1.5 wt% alginate-encapsulated human MSCs bioprinted by drop-on-demand deposition were not only unaffected by short-term exposure to shear stresses of less than 10 kPa, but that cell proliferation increased during 7 days of culture. MSC survival and functionality, but crucially not phenotype, were only affected when a stress threshold was exceeded during the bioprinting process (364).

The observed static cell morphology could also be due to the low STRO-1 enriched BMSC density used. Cell densities in most bioprinting studies range from 1 to 100 million cells per ml of bioink. Hydrogels formed by STRO-1 enriched BMSC-laden biomimetic bioinks, which had a cell density of 5×10^4 cells/ml, contained no spheroid bodies, unlike the MG63-laden bioinks which had a cell density of 1×10^6 cells/ml. Hong *et al* had reported that bioprinted 3 wt% HA-PEG containing 1×10^8 cells/ml of human MSCs formed large spheroids through cell aggregation (150). Migration speed and cell differentiation are different for single cells as well as for different cell types in a 3D matrix (150). Higher cell densities have been shown to promote cell-cell interactions necessary for improved viability and osteogenic differentiation (361). Some studies also indicated a cell type- (and possibly even cell passage-) dependent plateau effect on culture maturation exists, whereby further increments in cell density no longer stimulated proliferation or differentiation (365). Additionally, Huebsch and colleagues showed that cell phenotype commitment was not correlated to cell morphology in 3D culture, but rather in response to 3D matrix rigidity, which regulates integrin binding and the reorganisation of adhesion ligands on the nanoscale (357).

4.2.5 Conclusions

Alginate- and gelatin-based bioinks are biodegradable *in vitro* and their functionality could be improved through the addition of ECM components without toxicity to encapsulated cells. However, naturally derived biomaterials lack the necessary mechanical properties. Although a myriad of techniques exist to partially resolve this issue, increasing hydrogel stiffness decreases cell viability and functionality. Designing the bioink to degrade rapidly and minimising the shear strain exerted on encapsulated cells are vital in achieving cell viability and functionality post-bioprinting. These initial experiments highlight the difficulties in meeting the requirements of the ‘biofabrication window’. Further research is needed to elucidate the optimal initial cell density, viscoelasticity and degradation kinetics of bioinks for each mode of bone bioprinting.

Chapter 5: Integrated 3D printed scaffolds for bone repair

Although hydrogels can be used to encapsulate cells with reasonable viability, the functionality of these cells remains unclear, being dependent on the porosity, composition, and the degradation rate of the hydrogels (366). Improving the mechanical properties of hydrogels appeared to be detrimental to the survivability of encapsulated cells. Furthermore, the effect of shear strain forces during any bioprinting process on cell viability and functionality, as indicated by the experiments above, appears a significant challenge. Such issues limit the use of hydrogels as stand-alone, cell-laden scaffolds for bone tissue engineering. This chapter proposes an alternative approach to meet these pre-requisite structural qualities, by first designing and confirming the feasibility of utilising extrusion printing to reproducibly build scaffolds composed of a biodegradable biomaterial (with the potential for implantation *in vivo*). The ultimate goal of these experiments was to produce an integrated bioconstruct consisting of STRO-1 enriched BMSCs deposited onto biomimetic-coated 3D printed scaffolds for use in bone reparation.

5.1 Development of 3D printed scaffolds for structural and cell support

5.1.1 Introduction

Scaffolds play a central role in tissue engineering today. Although there is a consensus on the key qualities a scaffold should possess (as listed in Table 1-4 and Table 1-11), there is no clear definition of an ideal cell-scaffold construct for any specific tissue type. The appropriate design of a scaffold, in combination with cells and/or growth factors to the defect site, remains the current approach in creating a bone tissue engineered construct. Several studies have indicated that scaffold geometry affects biological responses including: i) cell seeding efficiency, ii) cell proliferation, and iii) tissue formation (367) while high scaffold porosity has an adverse effect on mechanical functionality (367, 368). Therefore, a construct should possess surface properties and sufficient open porosity to support cell migration, growth and differentiation, while guiding tissue development and organisation into a mature state (see Figure 5-1) (369). Scaffold degradation and resorption kinetics based on the mechanical properties, molecular weight, mass loss and tissue development need to be factored into the scaffold design process, as highlighted in Figure 5-2 (370). The latter is of particular importance in bone tissue engineering, as although a scaffold need not provide total mechanical equivalence to the tissue of interest, its stiffness and strength should be sufficient to support and transmit forces

to the host tissue, in addition to maintaining an adequate structural integrity during *in vitro* and *in vivo* growth and remodelling. Current bone graft substitute materials in clinical use are predominantly ceramic- and bioglass-based, while dental and prosthetic implants are typically metallic (alloy)-based. However, none of these biomaterials, when used in isolation and irrespective of the manufacturing technique, retain the necessary characteristics for an optimal bone scaffold for bone regeneration.

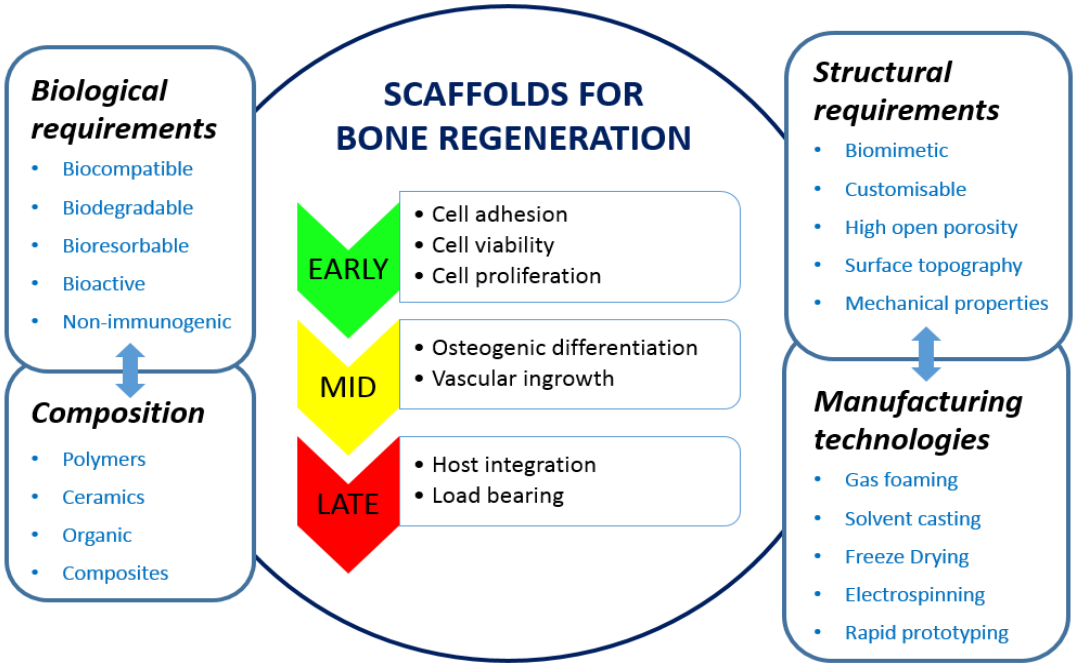

Figure 5-1 Properties of an ideal scaffold for bone tissue engineering.

Adapted from (369).

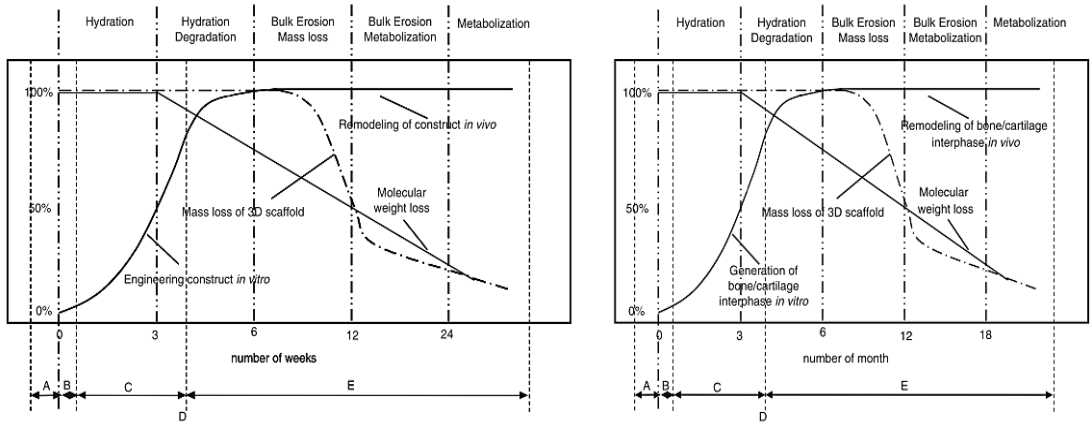

Figure 5-2 The complex relationships between mass loss of the 3D scaffold and molecular weight loss against time for tissue engineering a construct.

Reproduced from (370).

As summarised in Figure 5-1, a crucial factor in scaffold design is the choice of biomaterial, which not only defines the physicochemical properties of the scaffold, but also determines the manufacturing approach(es) that could be utilised. For this study, polycaprolactone (PCL) was chosen for its *in vitro* and *in vivo* biocompatibility and efficacy, and the appropriate mechanical properties of PCL (see Figure 5-3) (371). PCL has already received US Food and Drug Administration approval for its use in medical and drug delivery devices. PCL is a semi-crystalline linear aliphatic polyester first synthesised by the Carothers group in the 1930s (372). Today, PCL is synthesised by ring-opening polymerisation of ε-caprolactone using cationic, anionic and coordination catalysts, or via free radical ring-opening polymerisation of 2-methylene-1-3-dioxepane (372). Achieving high molecular weights, and control of the average weight, distribution, as well as the polymer architecture, are difficult.

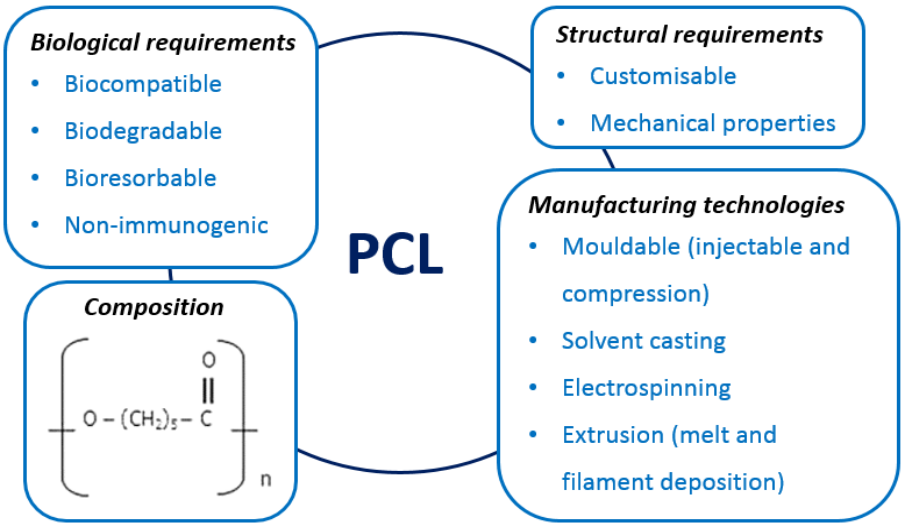

Figure 5-3 Polycaprolactone (PCL) properties that make it a suitable biomaterial for use in scaffold fabrication (372).

Depending on the molecular weight of PCL, and whether PCL is blended with other biomaterials, biodegradation *in vivo* can take months to years (373-375), making PCL an attractive material for use as a long-term implant, given PCL scaffolds can provide the necessary support for cell invasion and mechanical reinforcement (376). The slow degradation rate of PCL is due to its hydrophobicity and high crystallinity. *In vivo*, PCL degrades in two stages, irrespective of the specimen shape (372). Molecular weight reduction, at a linear rate through random bulk hydrolytic ester cleavage, occurs prior to a surface erosion process (through a diffusion loss of oligometric species from its bulk) which eventually results in implant fragmentation (372). PCL degrades to 6-hydroxylcaproic acid, which is metabolised

via the citric acid cycle, or removed by renal excretion. Additionally, the slower degradation rate makes PCL less likely to cause extreme pH changes in the local microenvironment, making PCL more cytocompatible than PLLA or PLGA (both of which degrade at faster rates *in vivo*) (372).

Despite these advantages, PCL lacks biological recognition sites to provide cues for cell adhesion and proliferation. The inherent hydrophobicity of PCL further reduces cell adhesion (377). Blending polymers or bioactive molecules onto, or mixed into, PCL scaffolds have been attempted to resolve this issue, with composites such as PCL-hydroxyapatite (344), PCL-β-tricalcium phosphate (376), PCL-chitosan (378), and more recently, PCL-alginate (379), being studied to determine their potential for bone biofabrication. Surface modification (usually employed as a post-processing technique) utilising sodium hydroxide treatment (372), plasma functionalisation (377), chemical conjugation with synthetic peptides such as Arg-Gly-Asp (380) or growth factors such as BMP-2 (159), protein coating of the scaffold through FN adsorption (321), electrospun collagen and nano-HAP (344), or a combinatorial approach (381), have been attempted to improve the hydrophilicity and osteoconductivity of PCL-based scaffolds. Fu *et al* incorporated PCL into a triblock co-polymer with poly(ethylene glycol), nano-HAP and collagen to form an injectable, thermosensitive hydrogel which guided bone regeneration (382), confirming the versatility of PCL as a biomaterial for use in bone tissue engineering.

From the perspective of clinical translation, AM methods are an increasingly attractive approach as scaffolds must be manufactured under Good Manufacturing Practice conditions at an economic cost (54, 383-385). As such, a key consideration during the scaffold design process must be the capability of the fabrication method to reproduce any design with high fidelity. In an ideal scenario, it should be possible to utilise any AM method to fabricate identical constructs using the same design. However, in reality, this is not the case. Indeed, production fidelity and scaffold properties are typically constrained by the AM method available. As scaffolds were fabricated using the 3DDiscovery bioprinter in this project, the choice of biomaterials was limited to those that could be used in extrusion and jet deposition printing. PCL remained an attractive option, given its low glass transition temperature of -60°C and a melting temperature of 59 – 64°C (372), properties which were suitable for fabricating a 3D geometric scaffold with a controllable, interconnected porosity using the precision extrusion deposition technique of the 3DDiscovery bioprinter. Although Shor *et al* had utilised a similar system to fabricate a PCL scaffold with a 0°/90° fill

pattern and a 350 µm average pore size (386), the reported 64.72% total porosity was based on a cross-section of, rather than the whole, µCT-reconstructed scaffold. One major constraint of using thermoplastic polymers in an extrusion-based system is that the pore openings of fabricated scaffolds are often not consistent in three dimensions. Pores facing the z-axes are formed between inter-crossing material fibres and are user-defined. Pores in x- and y-axes are formed from voids created by stacked biomaterial layers, with a resulting restriction of pore sizes by fibre thickness. Pore morphology often lacks variation in x-, y-, and z-axes, particularly in scaffolds with a 'standard' 0°/90° fill pattern (372). External pores were typically smaller in size when compared to internal pore sizes (367). Despite these limitations, the extrusion deposition method allows for the fine-tuning of fibre diameter, height and distance between fibres, thereby enabling the generation of pore gradients and complex geometries otherwise not possible with conventional manufacturing techniques, in addition to maintaining a homogeneous fabrication of scaffolds (367).

Therefore, the following initial experiments were conducted to identify the printing parameters that would allow the 3DDiscovery bioprinter to reproducibly 3D print different PCL scaffolds with varying geometries and porosities. The effects of printing parameters and conditions, as well as the different fill patterns, on overall surface topography, scaffold porosity and architecture were analysed. Non-modified 3D printed PCL scaffolds were seeded with STRO-1 enriched BMSCs to determine cell adhesion and survival.

As stated in 1.9, the hypotheses of this thesis are:

1) Human STRO-1 enriched BMSCs possess, and retain, the capacity for osteogenesis when seeded onto scaffolds, and are therefore a suitable cell type for use in bone reparation.

2) Biomaterials can be combined to generate tuneable bioinks, which can be used to deliver STRO-1 enriched BMSCs with high viability and functionality.

3) 3D printing methods are capable of manufacturing porous scaffolds of clinically relevant size with high resolution and reproducibility.

4) STRO-1 enriched BMSCs, biomimetic bioinks, and 3D printed polycaprolactone-based scaffolds can be combined to create an integrated bioconstruct for use in bone repair.

In conjunction with the above hypotheses, the aims of this research project are:

1) To confirm the osteogenic potential of STRO-1 enriched BMSCs.

2) To elucidate the osteoinductive capabilities of established biomaterials, such as titanium and polycaprolactone (amongst others), in order to identify potential combinations for the generation of composite scaffolds and/or bioinks for use in bone tissue engineering.

3) To design novel porous scaffolds that mimic natural bone architecture.

4) To investigate the feasibility of utilising 3D printing techniques to accurately and reproducibly manufacture scaffolds according to their design.

5) To determine the possibility of 3D printing cell-laden bioinks.

6) To develop methods for integrating 3D printed scaffolds, biomimetic bioinks, and STRO-1 enriched BMSCs, with the objective of creating functional bioconstructs for use in bone reparation.

5.1.2 Materials and Methods

5.1.2.1 Manufacture of PCL prototype scaffolds

PCL (average M_w = 80000 g/mol) was purchased from Sigma Aldrich, UK. 3 mm-sized PCL beads were added to the melt extrusion tank of the 3DDiscovery bioprinter and heated to 110°C for 2 hours. Precision extrusion deposition via the HM-300H printhead was performed at ambient temperatures of 25°C and a humidity of 55%. A needle tip with a 0.51 mm internal diameter was used for printing a 10 by 10 by 1.32 mm square mesh scaffold designed in BioCAD. Printing parameters were set at a feed rate of 5 mm/s, pressure of 2 bars, a screw revolution rate of 14 revolutions per second, printing temperature of 90°C, and a layer thickness of 0.33 mm. The first layer was printed by depositing PCL in fill lines spaced 1 mm apart and set at a 0° angle, followed by fill lines at a 90° angle. This building pattern was repeated until a total build height of 1.32 mm was reached.

A needle tip with a 0.18 mm internal diameter was used to print a cylindrical scaffold with a central hollow that was designed in BioCAD, with a total build height of 3.2 mm, an outer diameter of 8 mm, and an inner diameter of 3 mm. This design was based in part on the biphasic key design published by Holmes *et al* (383). Printing parameters were set at a feed rate of 5 mm/s, pressure of 2.8 bars, a screw

revolution rate of 19 revolutions per second, printing temperature of 110°C, and a layer thickness of 0.16 mm. The first layer involved printing both circles followed by fill lines at a 60° angle, with their edges stripped. This was followed by further circular patterns but with fill lines at a 150° angle for the next layer, then 90°, and 0°. Fill lines were set 0.9 mm apart to generate scaffold porosity. In between each layer, an outer and inner ring pattern were deposited to create a gap between layers, thus increasing the porosity of the construct. These layers were designated as a group, which was re-printed until the total build height was achieved.

For both printing processes, a custom cooling device (set at -10°C, refer to 2.3.1) with an attached glass slide were used as the printing stage onto which the PCL bioink was deposited to generate each construct. Double-sided adhesive tape was applied to the glass slide to increase the adhesion of PCL fibres during the building of the first layer for each construct. All scaffolds were UV-sterilised for 2 hours prior to use for any experiment.

5.1.2.2 Structural analyses of 3D printed prototype PCL scaffolds

Qualitative assessments of the macro-, and micro-structure of the PCL prototype cylinder construct was acquired by scanning electron microscopy (SEM, FEI Quanta 200, Thermo Fisher Scientific, USA). Cell-free constructs were analysed with the addition of a 7 µm-thick gold-palladium coat. The working distance for visualisation was between 9.42 and 9.71 mm, with a spot size of 3 nm, and an accelerating voltage of 10 kV under high vacuum conditions. Higher magnification images were captured using a working distance of 9.64 mm, a spot size of 5.0 nm, and an accelerating voltage of 20 kV under high vacuum conditions. No critical drying step was required, as the imaged constructs did not contain any cells. As PCL scaffolds are opaque, it was possible to utilise the 561 and 633 nm wavelength lasers in the reflectance mode of confocal microscopy to directly assess the non-coated surface appearance of the deposited fibres of both (acellular) prototype PCL scaffolds. Reflectance mode imaging was performed using a Leica SP8 Confocal Microscope. 3D image reconstructions were undertaken using Leica Application Suite X.

The porosity and architecture of both 3DDiscovery-printed PCL scaffolds were further analysed using a Skyscan1176 µCT scanner (Bruker Corporation, USA). Each square mesh scaffold was placed into an empty 15 ml Falcon tube and fixed in position within the µCT scanner. After flat-field correction was carried out, the µCT scan was performed without a filter applied, at a pixel resolution of 8.78

µm, a current of 600 µA, voltage of 40 kV, rotation step of 0.3°, and with frame averaging switched off. Image reconstruction was performed with the accompanying NRecon software, having first selected an appropriate region of interest (ROI) to encompass the entire scaffold in every image slice, and then applying an angular step of 0.3°, no smoothing, beam hardening correction of 30%, and ring artefact correction of 9. Similar scanning and reconstruction settings were applied for each prototype PCL cylinder, which was contained in an empty 1.5ml Eppendorf tube.

Reconstructed images were loaded in Dataviewer (version 1.5.4.0, Bruker Corporation, USA) to align images in the coronal, sagittal and transverse axes. These axial images were centred and saved as a volume of interest dataset. CTAn software (version 1.16.4.1, Bruker Corporation, USA) was then used to perform volume and surface rendering, and 3D analysis, which involved the measurement of PCL volume, the total volume of the construct, the degree of open, closed and total porosity, as well as the average range distribution of PCL fibre thickness from the reconstructed 3D dataset. Firstly, a volume of interest dataset was loaded and the top and bottom references set. An appropriate ROI was applied to an image slice, adjusted to fit, and then interpolated throughout the entire volume. For the prototype PCL cylinder a second ROI was drawn by holding down the control, shift, and right-click mouse buttons to exclude the central hollow area from the final analysis. This new dataset was saved and the new volume of interest was loaded before adjusting the grayscale histogram to a lower threshold setting of 30, and an upper threshold setting of 150. 3D analysis was performed for each scaffold. The rendered dataset was opened in CTVox software (version 3.1.1 r1191, Bruker Corporation, USA) to create 3D reconstructions of the PCL scaffolds for export.

Following method note MN060 (Bruker Corporation, USA) and using the second saved volume of interest dataset per construct, surface meshes for open and closed pore models were created in CTAn software to analyse open and closed porosities per construct. CTVol software (version 2.3.2.0, Bruker Corporation, USA) illustrated the open and closed porosity 3D maps generated from the analyses.

5.1.2.3 STRO-1 enriched BMSC isolation and culture

STRO-1 enriched BMSCs were isolated from human bone marrow samples from two male patients, aged 76 and 84, and cultured as described in 3.1.2.1 and 3.1.2.2. Cells of P1 or 2 were used for the experiments.

5.1.2.4 Manufacture of bioinks for cell encapsulation and delivery

4% w/v alginate, 4% w/v alginate, 10% v/v glycerol, and 4% w/v alginate, 10% v/v glycerol and 10 mg/ml fibrinogen bioinks were manufactured as described in 4.1.2.1. Bioinks were maintained at room temperature prior to use.

5.1.2.5 Determination of cell viability, proliferation and migration

This series of experiments were conducted in conjunction with experiments described in 4.1.2.4. To determine seeded STRO-1 enriched BMSC viability, proliferation and migration on these 3D printed PCL scaffolds, PKH-26 (Red) labelling of STRO-1 enriched BMSCs was performed, as per the protocol described in 2.6.2. 1 ml of 4% w/v alginate, 4% w/v alginate, 10% v/v glycerol, and 4% w/v alginate, 10% v/v glycerol, 10 mg/ml fibrinogen solutions were used to encapsulate 1 X 10^5 STRO-1 enriched BMSCs. 100 µl of each cell-laden mixture was manually deposited onto the surface of the square mesh patterned PCL scaffolds using a P-1000 pipette. The seeded scaffolds were placed into a well of a 12-well Corning® plate, which was transferred to a humidified incubator at 37°C, 5% CO_2 for 25 minutes before basal media containing 2.5 mM calcium chloride was added to each well. Scaffolds containing fibrinogen had 1 U/ml of human thrombin (Sigma Aldrich, UK) added to the basal media containing 2.5 mM calcium chloride. Seeded scaffolds were cultured for 21 days, with media changed every 3 to 4 days.

At day 21, F-actin staining of the seeded cells was performed as detailed in 2.6.3. The scaffolds were rinsed thrice with 1x PBS before 2 µg/ml of HCS CellMask™ Deep Red stain (diluted in 1x PBS) (Thermo Fisher Scientific, USA) was added. The scaffolds were incubated in the dark at room temperature for 30 minutes before being rinsed three times in 1x PBS and visualised using a Nikon Eclipse T*i* microscope with TRITC and Cy5 filters, and 4x and 20x objectives.

5.1.3 Results

5.1.3.1 3D-printing of prototype PCL scaffolds

The various designs created using BioCAD, were reproducibly printed using the printing parameters described in 5.1.2.1, with a build time of 4.5 minutes for the PCL square mesh and 17 minutes for the prototype PCL cylinder (Video 5-1 and Figure 5-4). A higher degree of design fidelity and control of the placement of

printed PCL fibres was achieved through the use of the custom cooling device, which enabled the molten PCL to solidify at a faster rate post-deposition.

Prototype PCL cylinder.mov

Video 5-1 3DDiscovery printing of a prototype PCL cylinder.

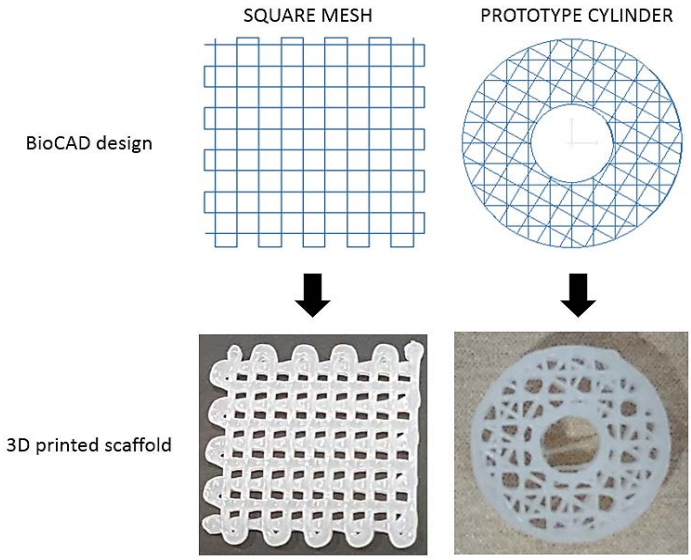

Figure 5-4 PCL prototype scaffolds designed in BioCAD and fabricated using the 3DDiscovery bioprinter.

The 3DDiscovery bioprinter was able to reproducibly print the standard square mesh design as well as a more complex hollow cylinder pattern.

5.1.3.2 Structural analyses of 3D printed prototype PCL scaffolds

SEM images of the PCL constructs highlighted the layer-by-layer generation of the constructs and confirmed the high resolution of precision extrusion deposition printing, which built a hollow cylinder with complex pore geometry. Deposited PCL fibres in the prototype PCL cylinder measured 302.9 ± 16.13 µm in diameter, while the pores within a layer measured 491.11 ± 47.52 µm in size. SEM images suggest deposited PCL fibres had a smooth surface appearance (Figure 5-5A to C). However, microgrooves along the directionality of the PCL fibre deposition could be seen in 500x magnification images (Figure 5-5D). Confocal microscopy images using reflectance mode revealed a marked variation in surface topography of the deposited PCL fibres for the two constructs. Some deposited fibres possessed 1 to

4 µm-wide grooves along the deposition direction, as was observed in the higher magnification SEM images. These microgrooves were observed in fibres deposited in straight fill patterns, which were printed at faster speeds (Figure 5-6A and B). However, in areas with greater curvature and at points of fibre intersection in both constructs, confocal microscopy images revealed that the surface appearance in these areas was significantly rougher (Figure 5-6C). The longer printing time for the prototype PCL cylinder was not just a result of its larger dimensions, but also the greater non-linearity of the design, which required the 3DDiscovery bioprinter to reduce its printing speed to achieve accuracy and conformity to the intended shape.

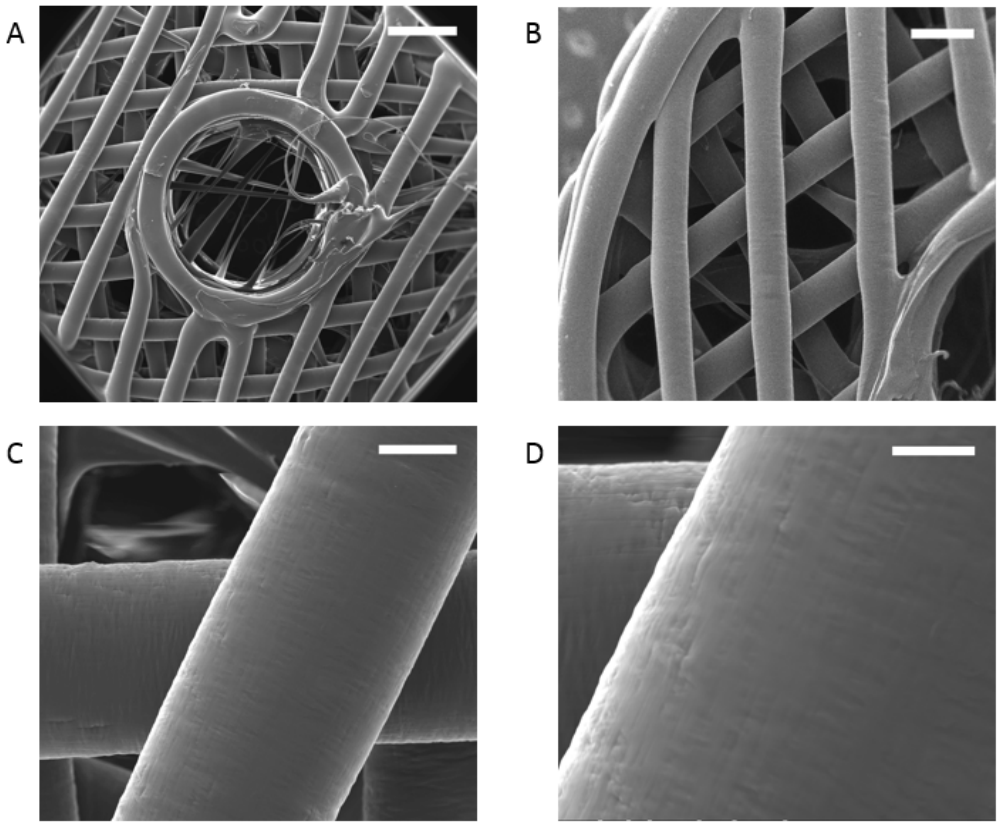

Figure 5-5 Scanning electron microscopy images of the prototype PCL cylinder.

A) 20x magnification view of the prototype PCL cylinder, demonstrating the fill pattern designed around a hollow centre. Fine fibres in the central hollow area were due to the viscoelastic property of PCL, and formed as the needle tip stopped and restarted depositing material when it reached the boundaries of the hollow centre. Scale bar represents 1 mm. B) 40x magnification view illustrates the regularity of the printed PCL fibres and the complex porosity generated by the design. Scale bar represents 500 µm. C) 100x magnification view suggests the printed PCL fibres had a smooth surface topography. Scale bars represent 200 µm. D) However, 500x magnification view shows microgrooves on the fibre surface. Scale bar represents 50 µm.

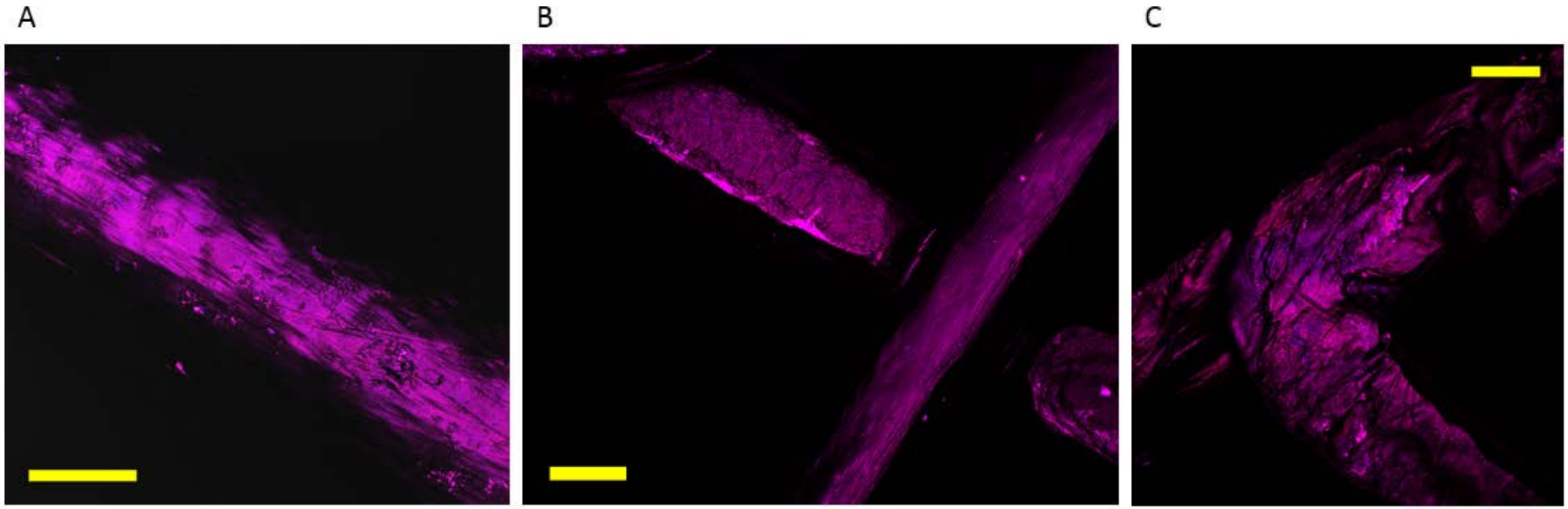

Figure 5-6 Confocal microscopy (reflectance mode) images of the surface topography of bare PCL fibres in the PCL square mesh (A) and the prototype PCL cylinder (B and C).

The reflectance mode images demonstrate the presence of microgrooves in the surface of deposited PCL fibres in both constructs. The images highlight the variations in surface topography as a consequence of changes in the geometry of the design. Scale bars represent 100 µm in all images.

µCT 3D analyses of the reconstructed PCL square mesh and prototype PCL cylinder showed a consistent layer-by-layer distribution of the PCL fibres (Figure 5-7 and Figure 5-8). Table 5-1 summarises the 3D analyses results for both constructs.

Subject	Average fibre thickness (mm)	Mean PCL volume/Total volume (%)	Mean open porosity (%)	Mean closed porosity (%)	Mean total porosity (%)	Average open pore volume (mm^3)
PCL Square Mesh	0.378 ± 0.041	52.96 ± 4.26	47.035 ± 2.11	0.015 ± 0.052	47.044 ± 2.43	55.303 ± 2.01
Prototype PCL cylinder	0.341 ± 0.08	57.31 ± 6.2	42.38 ± 6.21	0.539 ± 0.60	40.82 ± 6.79	60.148 ± 12.46

Table 5-1 Summary of CT analyses of the architecture of the PCL square mesh and prototype PCL cylinder.

Sagittal cross-section views show pore geometry could be varied by altering the fill pattern orientation from 0°/90°, which produced uniform, columnar pores (Figure 5-7B), to 60°/150°/90°/0°, which generated complex, trabecular-like pores (Figure 5-8B). Mean open porosity reduced by about 5% while mean closed porosity rose by about 0.5% when the fill pattern changed to 60°/150°/90°/0°. Open pore volume was more variable in the prototype PCL cylinder. A mean 6% reduction in total porosity of the prototype PCL cylinder was offset by a mean 5.5% increase in bone volume. Despite the prototype PCL cylinder displaying slightly thinner PCL fibres on average, it had a wider range of fibre thickness when compared to the PCL square mesh (Figure 5-9). Figure 5-10 maps the different pore distributions of the PCL square mesh and prototype PCL cylinder. Although the open pore network in both constructs consisted of larger sized pores, a proportion of open pores in the prototype PCL cylinder (but absent in the PCL square mesh) were larger than 1 mm in size. Closed pores in both constructs were irregularly shaped, and small to medium-sized. Closed pores of the PCL square mesh appeared to be randomly distributed, whereas a significant proportion of the closed pores of the prototype PCL cylinder were found along the outer and inner ring areas. The lack of porosity of the outer and inner ring surfaces of the prototype PCL cylinder was also visible in the µCT reconstruction image, as seen in Figure 5-8C.

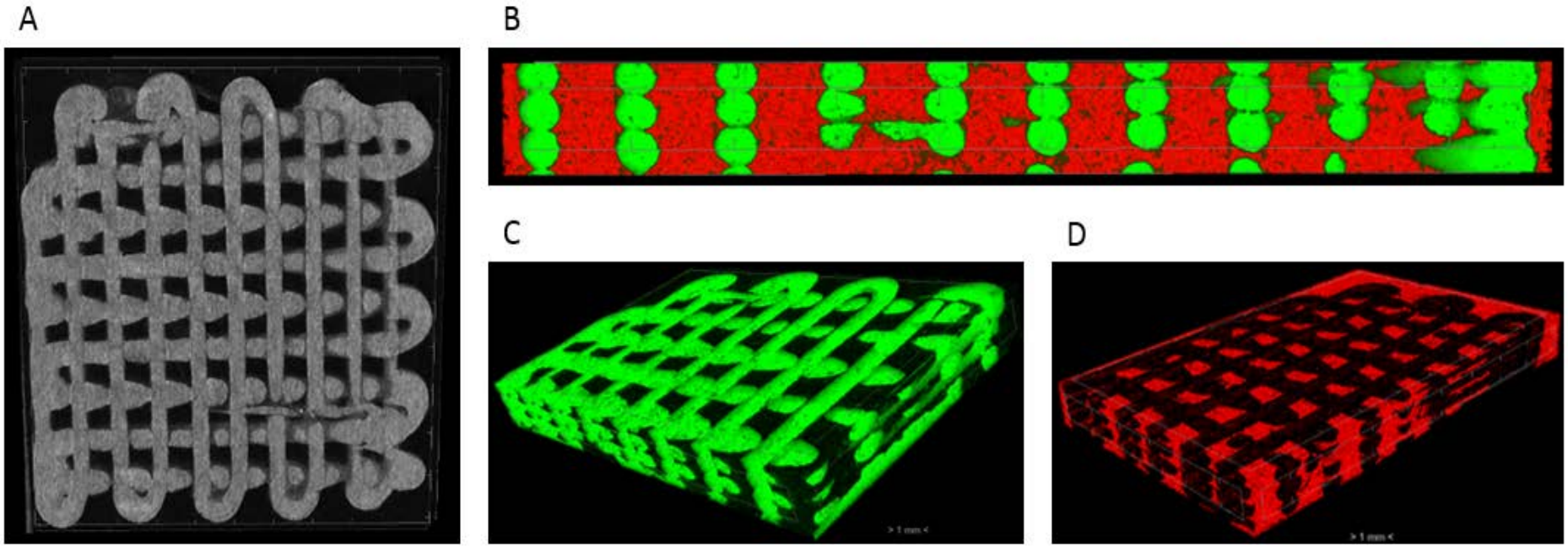

Figure 5-7 µCT reconstructed images of the PCL square mesh.

A) 3D reconstructed grayscale image highlighting the porosity of the printed construct. B) Sagittal view of the printed construct shows the spaces (shown in red) within the construct occur primarily between the columns of deposited PCL fibres (shown in green). C, D) Oblique view of the square mesh (shown in green) illustrates the uniformity of the layer-by-layer printing process. The design pattern generated relatively uniform pore geometries, which extend from the top to the bottom of the construct (shown in red).

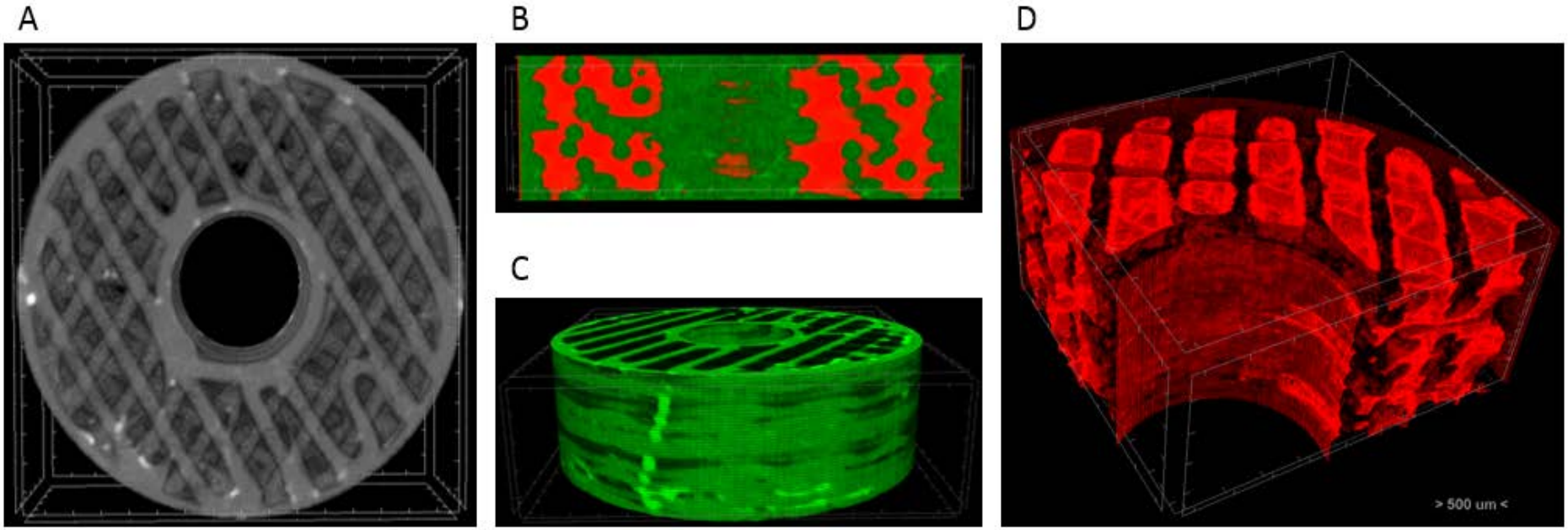

Figure 5-8 µCT reconstructed images of the prototype PCL cylinder.

A) 3D reconstructed grayscale image of the prototype cylinder demonstrates the printing resolution of the 3DDiscovery in building a construct with varied pore geometry. B) Sagittal view of the prototype cylinder illustrates the complexity of the network of interconnected spaces (shown in red) within the construct. C) Oblique view of the prototype cylinder (shown in green) illustrating the regular layer-by-layer deposition of the outer ring of PCL as designed. The design however, appeared to significantly reduce the porosity of the outer ring of the construct. D) The spaces (shown in red) within the construct appear to remain connected from the top to the bottom of the construct despite the complexity of the design.

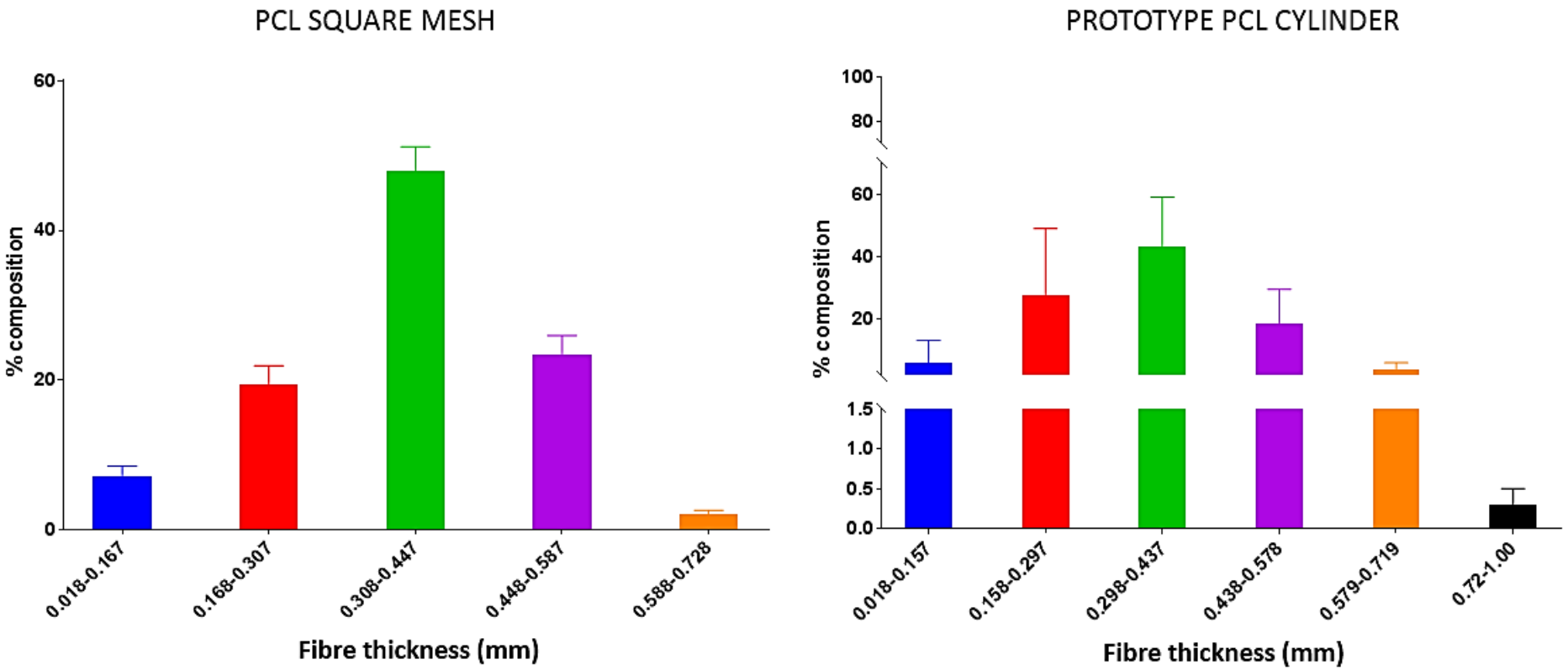

Figure 5-9 Fibre thickness distribution in the PCL square mesh and prototype PCL cylinder.

The complex fill pattern used to generate the prototype PCL cylinder resulted in a greater number of deposited fibres intersecting between layers and with the outer and inner rings which could have contributed to a small increase in the number of larger fibres found within the prototype PCL cylinder.

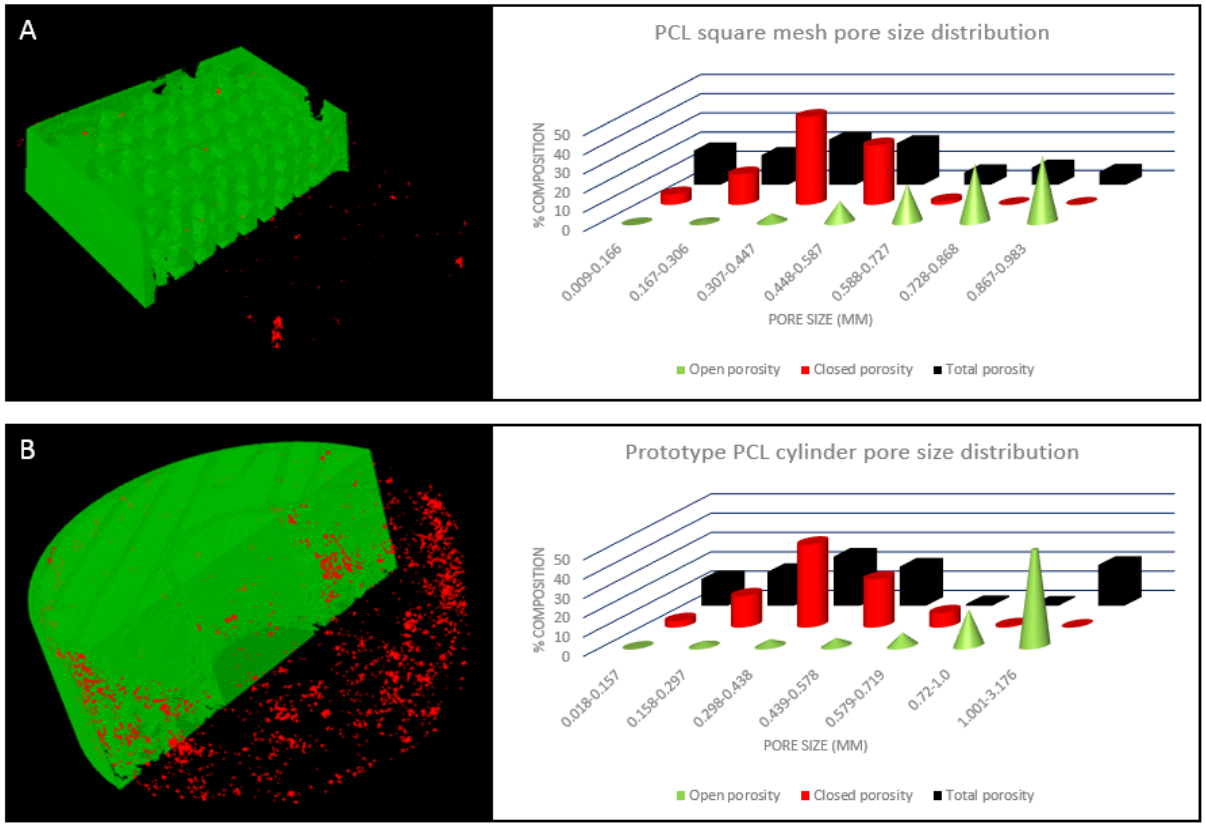

Figure 5-10 Porosity mapping of the PCL square mesh and prototype PCL cylinder.

A) The 'standard' 0°/90° fill pattern generated few areas with closed porosity (shown in red) within the printed square mesh construct. B) The more complex patterning used to create the cylinder resulted in an increase in the number of closed pores, predominantly near the outer edge of the cylinder. The overall open porosity (shown in green) within the cylinder did not appear to be significantly affected.

5.1.3.3 STRO-1 enriched BMSC viability and functionality

Cell seeding of the prototype PCL cylinder by manual droplet pipetting of cell-laden 4% w/v alginate, 10% v/v glycerol and 4% w/v alginate, 10% v/v glycerol, 10 mg/ml fibrinogen bioinks failed. Most of the bioink volumes for these two cohorts failed to permeate into the constructs. The majority of encapsulated cells deposited onto the construct surface passed through the pores onto TCP below following hydrogel degradation. Minimal cell attachment was observed by day 3, bringing about a premature termination to the experiment for these two cohorts. Although a large proportion of encapsulated STRO-1 enriched BMSCs were deposited in the pore areas of the PCL square meshes for these two cohorts, a small proportion of STRO-1 enriched BMSCs remained deposited on the fibres. Figure 5-11 illustrates the decreasing cell viability of STRO-1 enriched BMSCs encapsulated within 4% w/v alginate, 10% v/v glycerol and 4% w/v alginate, 10% v/v glycerol, 10 mg/ml fibrinogen over time. The STRO-1 enriched BMSCs remained spherical, despite both cell-laden hydrogels gradually degrading over the 21 day period. These results were similar to that obtained in 4.1.3.3.

STRO-1 enriched BMSCs encapsulated in 4% w/v alginate adhered and survived on both PCL scaffold designs for the duration of the 21 days of culture (Figure 5-12), just as observed on TCP in 4.1.3.3. F-actin organisation within adherent cells on the surface of the printed PCL fibres was irregular (Figure 5-13, TRITC and merged images), in contrast to the F-actin appearances of STRO-1 enriched BMSCs adherent on the surface of EOS titanium scaffolds (Figure 3-14). The HCS CellMask™ Deep Red stain highlighted a mixture of cell morphologies, with a few cells appearing spindle-shaped, while others were stellate-shaped (Figure 5-13, Cy5 image). A few adherent cells were observed to interact with neighbouring cells on the printed PCL scaffolds (merged image in Figure 5-13). Pore bridging by seeded STRO-1 enriched BMSCs was not observed in either construct at day 21.

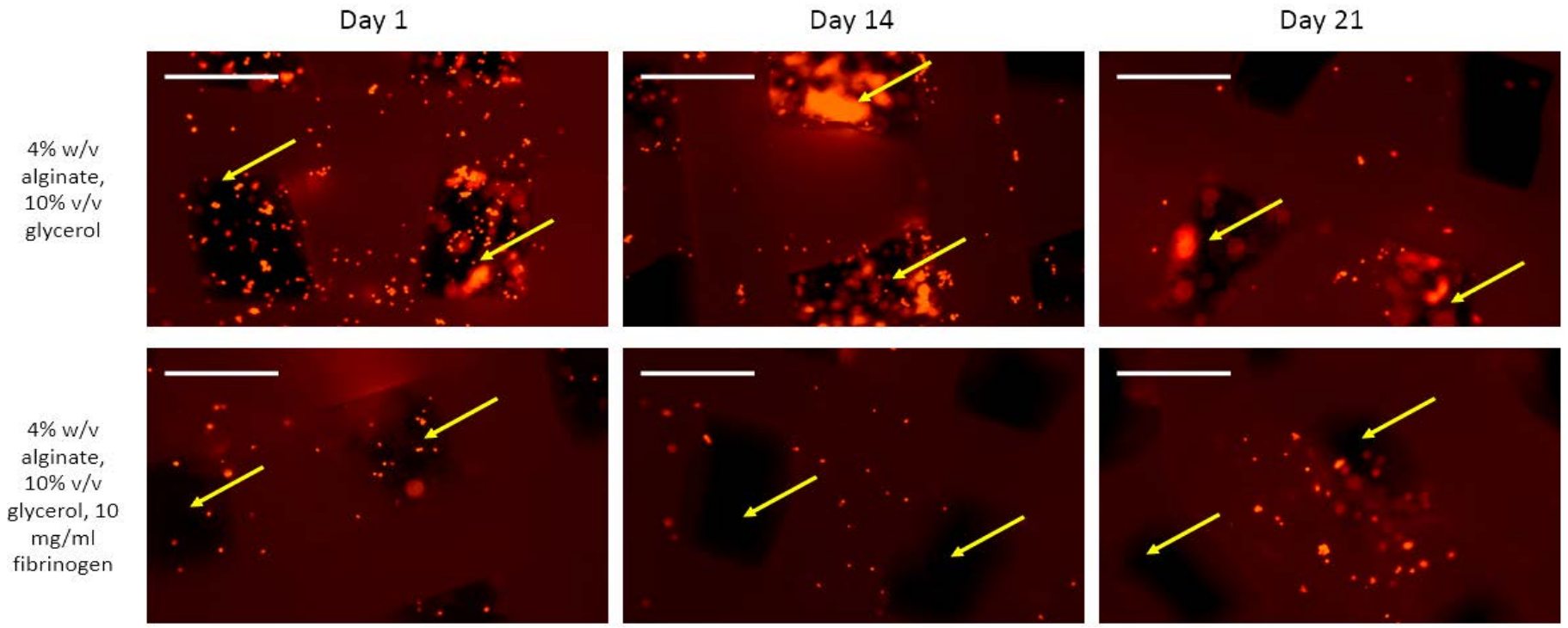

Figure 5-11 Manually deposited PKH-26 (Red)-labelled STRO-1 enriched BMSC-laden bioinks on PCL square meshes over a 21-day period.

Cell seeding was more efficient in the 4% w/v alginate, 10% v/v glycerol cohort as the bioink was less viscous and easier to manually pipette. A significant number of cells were deposited into the pores of the construct (indicated by yellow arrows). Cell viability in both cohorts decreased as time progressed. Encapsulated STRO-1 enriched BMSCs remained spherical throughout the 21 days of culture. Scale bars represent 500 µm. Images taken using a Nikon Eclipse Ti microscope, with a 4x objective and a TRITC filter.

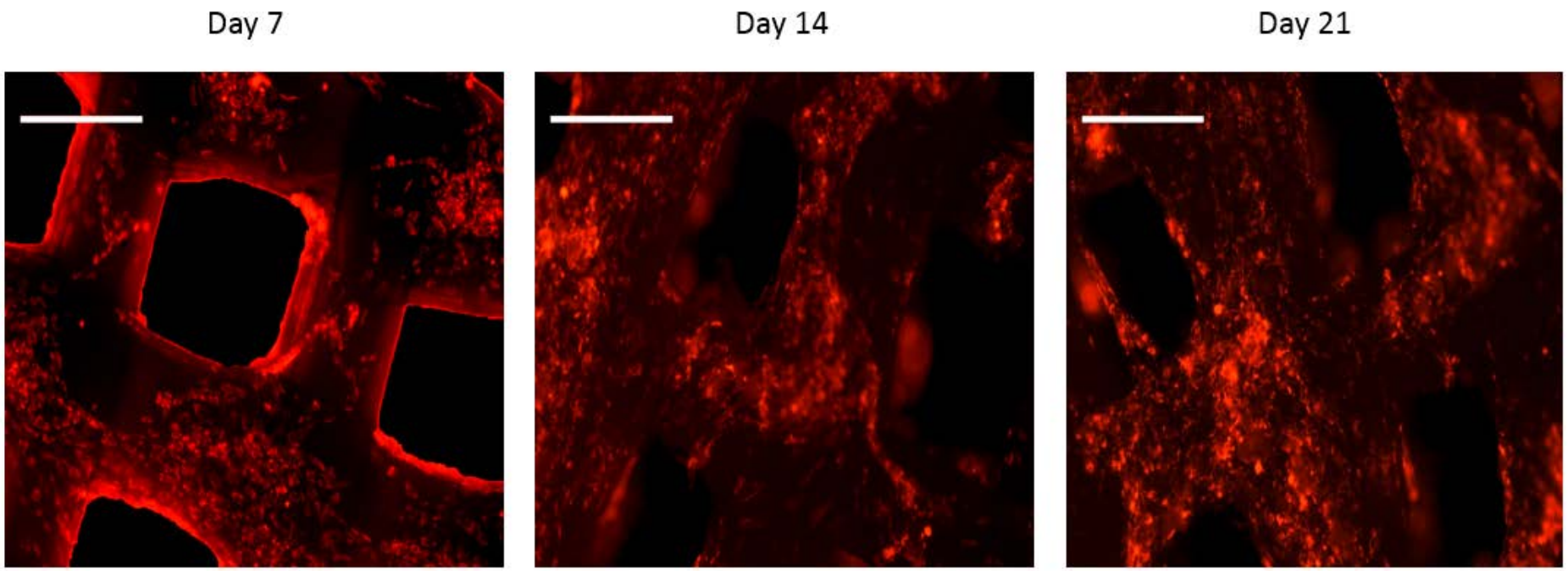

Figure 5-12 Manually deposited PKH-26 (Red)-labelled STRO-1 enriched BMSC-laden 4% w/v alginate bioink on PCL square mesh scaffolds.

PKH-26 (Red)-labelled STRO-1 enriched BMSCs encapsulated in a 4% w/v alginate bioink were viable over the 21 days. The seeded cells did not bridge the pores over the 21 day culture period. Scale bars represent 500 µm. Images taken using a Nikon Eclipse Ti microscope, with a 4x objective and a TRITC filter.

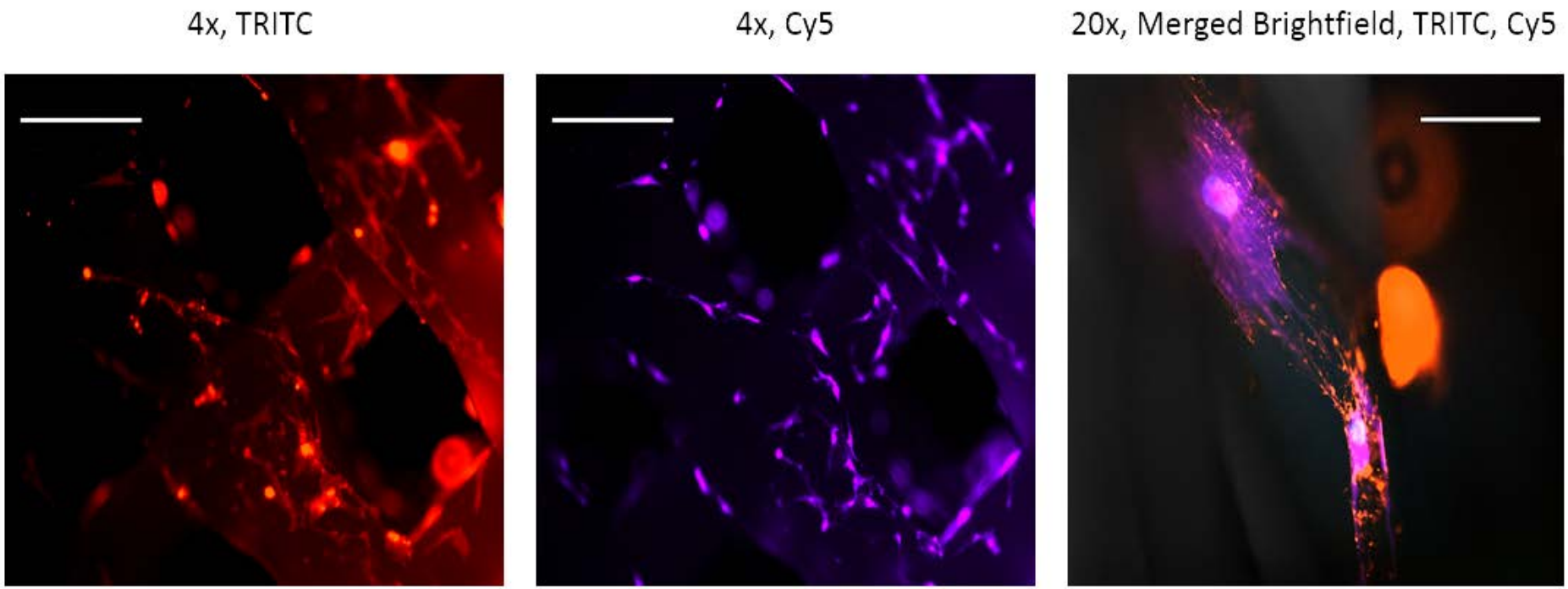

Figure 5-13 Immunocytochemical staining of seeded STRO-1 enriched BMSCs on a PCL square mesh scaffold at day 21.

Left: TRITC image showing F-actin staining of adherent STRO-1 enriched BMSCs. Scale bar represents 500 µm. Centre: Cy5 image showing the cytoplasmic and nuclear staining of adherent STRO-1 enriched BMSCs. Scale bar represents 500 µm. Right: Merged Brightfield, TRITC and Cy5 images of two adherent STRO-1 enriched BMSCs interacting with each other. F-actin organisation was irregular within each cell. Scale bar represents 100 µm. Images taken using a Nikon Eclipse Ti microscope, with TRITC and Cy5 filters.

5.1.4 Discussion

The results thus far demonstrate:

- *The 3DDiscovery bioprinter could be used to fabricate different PCL scaffolds possessing high interconnected porosity with good reproducibility.*
- *µCT can assess printing fidelity and the architecture of 3D printed constructs.*
- *4% w/v alginate-encapsulated STRO-1 enriched BMSCs were viable and adherent post-seeding onto 3D printed PCL scaffolds.*

Fabrication methods and biomaterials play a crucial role in determining the final mechanical and biological properties of any tissue-engineered construct. Most bone tissue engineering studies have, to date, focused on the creation of simplified models that are functionally similar in porosity or mechanical properties (367, 368), rather than attempting to reproduce the complex and heterogeneous architecture of bone tissue. The reasonable accuracy of *in silico* finite element analysis has led to its use as a predictive tool for *a priori* structural optimisation (387), and the creation of libraries consisting of solid, voxel, or wireframe-based unit cells (generated using CAD software or image-based design applications) that could be assembled to form complex scaffold architectures using AM methods such as selective laser sintering and stereolithography (388). More recently, Boolean operations performed on an acquired image of a defect site and the arranged stack of cellular units can be used to generate scaffolds with patient-specific external shapes with a controlled internal microarchitecture (368).

Unfortunately, these methods cannot be applied in extrusion-based systems given the scaffold interior designs generated by extrusion deposition consist of regular, continuous, lattice-like patterns (see Figure 5-14) (368). Complex pore geometries can still be achieved by changing the deposition angle between adjacent layers and by varying fibre diameter, fill line spacing and layer thickness, thereby generating 3D scaffolds with a controlled porosity, as shown by 5.1Figure 5-7 and Figure 5-8. A high interconnected porosity has been associated with improved scaffold wetting, cell seeding efficiency and homogeneity (389), cell attachment and proliferation (367) and tissue ingrowth (387). However, for a constant porosity, adjustment of the deposition pattern may adversely affect the mechanical properties of a scaffold as the fibre deposition pattern determines the number of contact points between the fibres. Several studies have demonstrated that scaffolds with a homogenous, rather than staggered, fibre spacing had a higher compressive

modulus and dynamic stiffness even if porosity was almost identical (390). Other studies have shown that scaffolds with gradient porosities improved cell seeding efficiency (367), but displayed significantly lower stiffness under compressive loading (368). Additionally, the effect of fibre orientation on cellular proliferation has not been fully ascertained (367). Customising the scaffold architecture to match conflicting biological and mechanical requirements remains a challenging issue. To date, no optimal fibre arrangements have been identified for precision extrusion deposition-fabricated constructs for use in bone tissue engineering (367).

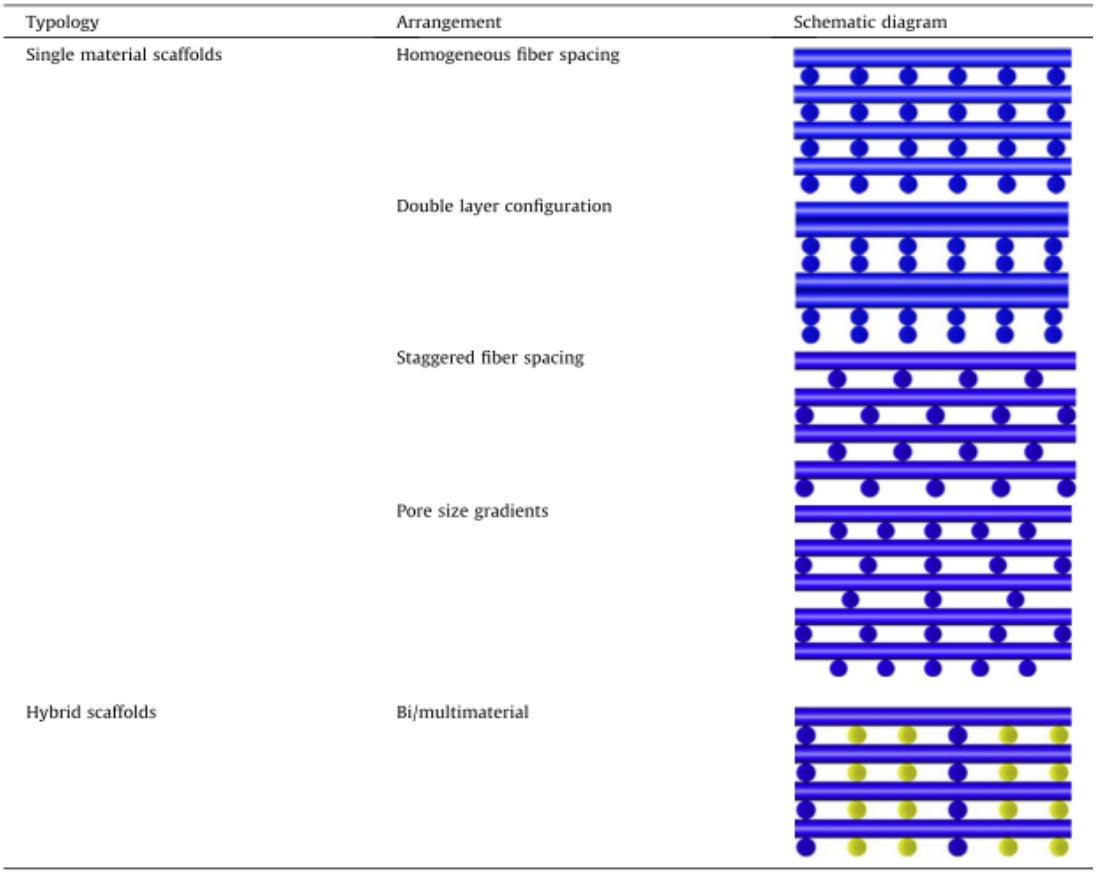

Figure 5-14 Current fibre arrangements used in extrusion-based fabrication.

Reproduced from (368).

Domingos *et al* (391) and Trachtenberg *et al* (392) have previously reported that the porosity of 3D printed PCL constructs was heavily influenced by printing parameters that controlled the size of deposited fibres, most notably the feed rate, extrusion screw speed, printing pressure and nozzle diameter. Printing parameters were optimised for precision rather than speed for both designs. As Figure 5-6 shows, printing parameters as well as scaffold geometry can affect the surface topography of the deposited fibres. Although either design could have been printed

more quickly to minimise this issue, the fabricated construct would have suffered from poor resolution, which in turn, would have adversely affected the mechanical properties, pore geometry and the degree of interconnected (open) porosity (as a consequence of the non-uniformity of build layers). Printing times were longer than desired (particularly with regards to the prototype cylinder), given that these constructs were under 20 mm in size and did not contain biological materials.

The hydrophobicity of PCL resulted in poor adhesion of the first deposited PCL layer to the printing stage, requiring the use of an adhesive tape to resolve this issue. This was a necessary intervention as the structural integrity of the printed construct relies heavily on the integrity of the first printed layer for inter-layer bonding due to the layer-by-layer process involved with the precision extrusion deposition method. The improved inter-layer bonding allowed for the precise and reproducible printing of square and cylindrical designs, as confirmed by µCT. µCT is a proven method used to perform architectural analysis of 3D printed constructs as well as in the imaging of bone tissue (182, 184, 185). Variations in pore geometry, particularly in the prototype PCL cylinder design, were visible in the reconstructed µCT images, generating a varying surface curvature in different areas of each layer and between layers. The prototype PCL cylinder design incorporated variations in pore geometry based on a review by Loh and Choong that had found improved angiogenesis, osteogenesis and osteoconductivity occurred in scaffolds with greater surface concavities and larger open pore sizes (393). The aim was to increase the possibility of vascular invasion of the scaffold, further improving the likelihood of developing a vascularised bone bioconstruct (394). The high interconnected (open) porosity confirmed by µCT demonstrated the permeability of both scaffold designs, which allowed diffusion to occur throughout the construct, thereby improving *in vivo* cell survival and proliferation within the scaffold while awaiting vascularisation from the host to occur (393, 395). Mechanical compression and yield strength testing will be necessary to ensure that the high porosity of the prototype cylinder design does not result in a more fragile construct, particularly if utilised in load-bearing situations (393, 396).

Adherent STRO-1 enriched BMSCs on the PCL square mesh that were encapsulated in both 4% w/v alginate, 10% v/v glycerol and 4% w/v alginate, 10% v/v glycerol, 10 mg/ml fibrinogen remained spherical over the 21 day culture period despite the evidence of both hydrogels gradually degrading (Figure 5-11). Cells released from the degraded hydrogels also remained spherical. These observations

indicated the occurrence of anoikis, and eventually apoptosis, as indicated by a reduction in PKH-26 (Red) signal intensity over 21 days in both cohorts. These findings were similar to results obtained when the same combination of MG63-laden hydrogels were deposited onto TCP (see 4.1.3.2 and 4.1.3.3). In contrast, STRO-1 enriched BMSCs encapsulated in 4% w/v alginate adhered and survived on the printed PCL constructs for 21 days of culture (Figure 5-12 and Figure 5-13). This was despite the fact that alginate inherently lacks cell adhesivity (291), and in spite of the inherent hydrophobicity of PCL (372). Air trapping within the complex pore geometries of the prototype cylinder further prevented the cell-laden bioinks from permeating into the construct, which accentuated the poor efficiency of manual seeding methods. Despite this issue, the low numbers of adherent cells that remained were viable, interacted with neighbouring cells on the PCL fibres and showed morphological changes, thereby confirming the cytocompatibility of PCL and alginate. Admittedly, these results reflect only on adherent cells on the surface of the scaffold, and should be interpreted with caution. However, taken together with results detailed in Chapter 4, these findings suggest that low viscosity bioinks could be used for cell delivery.

5.1.5 Conclusions

These initial experiments demonstrate the fidelity and reproducibility of the precision extrusion deposition method in fabricating porous PCL-based scaffolds of different designs. In spite of the limitations of extrusion-based fabrication, complex pore geometries and scaffold architectures could be achieved by careful scaffold design. µCT analyses highlighted the importance of scaffold geometry and further refinements that could be made to the scaffold design to improve scaffold porosity and printing efficiency. The inherent hydrophobicity of PCL, coupled with a high scaffold porosity and increased air trapping within complex pore geometries, made seeding the prototype cylinder more difficult, particularly as the cell-laden bioink viscosity increased. Furthermore, the large surface area of the cell-laden bioink and high surface tension of the PCL constructs prevented the full permeation of these bioinks. The reduced mean open porosity and poor cell seeding of the prototype PCL cylinder design indicated adjustments to the scaffold design and composition, as well as the cell seeding method, are required. Finally, by adding various stimuli, either to the printed PCL scaffold (through blending with other biomaterials), or perhaps as an intermediate, supporting layer containing such stimuli, it may yet be possible to 3D print an integrated construct for bone reparation.

5.2 Fabrication of an integrated construct for bone repair

Experiments performed in this study demonstrated the osteogenic potential of STRO-1 enriched BMSCs cultured on TCP and microporous titanium templates. The precision extrusion deposition mode of the 3DDiscovery bioprinter was capable of fabricating PCL-based constructs of different designs with a high resolution and reproducibility. Despite reasonable cell viability and substrate adhesion following encapsulation in 4% w/v (low viscosity) alginate (greater on TCP than PCL fibres), cell viability and functionality decreased as bioink viscosity and hydrogel thickness increased. Furthermore, shear stress on cells printed by microcontact printing and droplet jet deposition methods appeared to affect cell proliferation and functionality. Thus, to create an integrated construct, three key issues need to be resolved.

The first issue related to the poor cell adhesion on PCL constructs, as a result of the hydrophobic nature of PCL. As discussed in 5.1.1, the creation of composites by blending PCL with other biomaterials can overcome this issue, with some studies demonstrating the potential of such an approach for bone tissue engineering. However, the printability of custom composites may not be possible with every type of AM, with most biomaterial blends still requiring assessment and configuration prior to use in tissue engineering studies. Due to time, logistical, and equipment constraints of this project, such an approach was not practically feasible. The second issue stems from the bioinert nature of PCL and alginate, which limits their capability in aiding host tissue invasion as well as the osteogenic differentiation of seeded cells. A potential solution to these issues was to alter the surface chemistry and surface topography of the deposited PCL fibres.

The third issue pertained to the method for cell delivery. Air trapping within complex pore geometries, coupled with the large surface area of cell-laden droplets and high surface tension of the scaffold, reduced cell seeding efficiency in prototype PCL cylinder constructs (5.1). These issues could be partially resolved by altering the scaffold design (and thereby architecture) to generate a greater open porosity. Another approach to improve scaffold permeability to the bioinks is to minimise the cell-laden bioink droplet size. Droplet jet deposition (available with the 3DDiscovery bioprinter) could be configured to perform this task, but the limited availability of the 3DDiscovery bioprinter, and the need to demonstrate reproducibility with the technique, precluded this approach. An alternative method to resolve all three issues was investigated as follows.

5.2.1 Introduction

Scaffolds serve as a three-dimensional environment for cell attachment, proliferation and differentiation, allow vascular invasion, while filling bone defects and providing mechanical support during bone regeneration. The ideal scaffold in bone tissue engineering should possess a high interconnected porosity, controlled biodegradability, osteoinductive as well as osteoconductive capabilities (Table 1-4). It is therefore unsurprising that tissue engineers have focused their recent efforts on developing *in silico a priori* scaffold design approaches to generate optimal scaffold architectures, while investigating various approaches in modifying new and existing biomaterials to enhance their osteogenic or angiogenic properties key in defining the functionality of a construct (397). There is an increasing trend towards the creation of biomimetic or 'smart' scaffolds (398), whereby polymeric or ceramic-based scaffolds are modified through various processes that enable the addition of bioactive agents such as nanoparticles, compounds, growth factors or ECM proteins, with the goal of enhancing cell adhesion, differentiation as well as angiogenesis (346, 369). A literature review on 'smart' scaffolds by Motamedian *et al* (399) highlighted the vast variation in current experimental set-ups involving cell source and seeding density, biomaterials used, scaffold fabrication approaches, the type of modification(s) applied, experimental conditions and assay methods, which made the comparison of *in vitro* outcomes impossible. Despite this, the authors concluded 'smart' scaffolds had a positive effect on cell adhesion and differentiation.

One approach utilised by several studies to enhance cell adhesion involves surface modification techniques to alter surface chemistry and surface topography of PCL-based scaffolds. Surface modification (often employed as a post-processing technique) utilising sodium hydroxide (the most common method) (372), plasma treatment (377), chemical conjugation with peptides such as Arg-Gly-Asp (380) or growth factors (159), conventional surface coating through FN adsorption (321), electrospun collagen and nano-HAP (344), or a combinatorial approach (381), have been attempted to improve the hydrophilicity and osteoconductivity of PCL-based scaffolds. Physical adsorption onto a scaffold by dip- or soak-coating, covalent immobilisation onto the scaffold by chemical treatment, and directional coupling are three of the most common approaches for surface functionalisation (346). Due to its technical simplicity, physical adsorption is often used to coat surfaces. Scaffolds are soaked in a solution containing a biomimetic agent, which is passively adsorbed onto the biomaterial surface. However, the amount adsorbed is dependent on the

biochemical and biophysical properties of the scaffold as well as the biomimetic agent. Although this technique is suitable for molecules that require rapid release for biological activity, it is often necessary to use supraphysiological doses of the agent to ensure an adequate residual dose is present to influence tissue healing. Most surface coating studies that utilise physical adsorption tend to investigate the effect of one to two biomimetic agents on cell behaviour. Kang *et al* applied a 100 mg/ml fibrinogen, 10 mg/ml (high molecular weight) HA coating to 50% PCL/50% PLGA scaffolds (manufactured using solid freeform fabrication) by soaking these scaffolds for 24 hours prior to vacuum drying. This process was performed three times. 500 U/ml thrombin was then used to induce fibrin formation. Coated scaffolds that were loaded with BMP-2 were shown to stimulate bone regeneration from seeded adipose-derived stromal cells *in vivo* (400). More recently, Pati and colleagues decellularised a seeded 3D printed PCL/PLGA/TCP scaffold to generate a cell-laid, mineralised ECM 'coated' scaffold that induced an upregulation of osteogenic gene expression in newly seeded human nasal turbinate MSCs (401). Although cell-generated ECM coatings may potentially contain the necessary components to regulate the composition and organisation of native bone ECM, it remains difficult to characterise the components and optimise the cell type and cell culture times, which generate the best yield. Additionally, this method is unable to provide the cells with a uniform distribution and ideal environment to evenly deposit the osteogenic ECM coating throughout a scaffold (398). To date, no single method exists to facilitate the concomitant delivery of cells with a high viability and the addition of a multi-material ECM layer to a scaffold to generate a hybrid cell-biomatrix-scaffold construct for bone repair (402).

A key facet of tissue engineering is the delivery of cells in scaffolds for the regeneration of anatomical structures. Droplet-based cell deposition methods are increasingly used as a means of constructing or filling a variety of tissue defects due to the non-invasive, rapid yet controlled ability to deliver cells with high viability (403, 404) and precision (405). Veazey *et al* investigated the effects of different nozzle diameters and air pressures on the survival of bovine fibroblasts suspended at a density of 2×10^5 cells/ml in Hank's Balanced Salt Solution. Post-aerosol deposition (via an airbrush) viability was consistently as high as 94%, with normal growth (404). Roberts *et al* had similar results with bovine articular chondrocytes and porcine tracheal epithelial cells deposited by a custom-built, pressurised atomiser device, reporting greater than 70% viability and growth rates being comparable to cells that were deposited using conventional methods (403). Aerosols have been

routinely used to deliver small molecules as inhalable drugs, and spray coating is a well-developed method used in manufacturing thin, even layers of paint. Ahn *et al* demonstrated another use for aerosols by spraying 2% w/v calcium chloride (under constant pressure flow) to control the surface gelation of MC3T3-E1-laden, 3.5% w/v alginate bioinks deposited by robotic dispensing, achieving an 84% cell viability and a 20 by 20 by 4.6 mm-sized porous scaffold (406).

The final study was focused on determining the possibility of developing an integrated cell-scaffold construct for bone repair. Based on the earlier findings of this study, adjustments were made to the prototype PCL cylinder design and its fabrication process (5.1.2.1) to improve STRO-1 enriched BMSC seeding efficiency and attachment, as well as to generate greater external and interconnected porosity. Structural analysis methods employed in 5.1.2.2 were used to define the outcome of altering the fill pattern and fibre orientation, as well as the printing parameters, on printing fidelity, scaffold geometry and architecture. Given logistical constraints on bioprinter availability and time, an alternative approach was devised to enhance the functionality of the PCL scaffolds through surface coating using the printable bioinks developed in 4.2. Bioink composition was adapted to enable *in situ* post-deposition gelation to occur. As aerosol delivery has a similar mechanistic profile to jet deposition printing, the feasibility of utilising aerosol deposition for 1) applying an *in situ* precipitated, biomimetic coating to PCL cylinder scaffolds, and 2) delivering STRO-1 enriched BMSCs, suspended in a cell delivery bioink, with a high viability and a uniform distribution, were investigated. In order to minimise the effect of pressure on cell viability, and to ensure that bioink distribution was as similar as possible for every scaffold, identical disposable spray bottles were used for aerosol deposition of the bioinks used in surface coating and cell seeding procedures. Finally, the effect(s), if any, of the cell delivery method, the cell delivery bioink, and the biomimetic surface coating on scaffold surface topography and scaffold architecture, as well as the adhesion, proliferation, and functionality of the seeded STRO-1 enriched BMSCs (cultured in basal and osteogenic - containing 1,25-VitD3 - conditions) were elucidated.

As stated in 1.9, the hypotheses of this thesis are:

1) Human STRO-1 enriched BMSCs possess, and retain, the capacity for osteogenesis when seeded onto scaffolds, and are therefore a suitable cell type for use in bone reparation.

2) Biomaterials can be combined to generate tuneable bioinks, which can be used to deliver STRO-1 enriched BMSCs with high viability and functionality.

3) 3D printing methods are capable of manufacturing porous scaffolds of clinically relevant size with high resolution and reproducibility.

4) STRO-1 enriched BMSCs, biomimetic bioinks, and 3D printed polycaprolactone-based scaffolds can be combined to create an integrated bioconstruct for use in bone repair.

In conjunction with the above hypotheses, the aims of this research project are:

1) To confirm the osteogenic potential of STRO-1 enriched BMSCs.

2) To elucidate the osteoinductive capabilities of established biomaterials, such as titanium and polycaprolactone (amongst others), in order to identify potential combinations for the generation of composite scaffolds and/or bioinks for use in bone tissue engineering.

3) To design novel porous scaffolds that mimic natural bone architecture.

4) To investigate the feasibility of utilising 3D printing techniques to accurately and reproducibly manufacture scaffolds according to their design.

5) To determine the possibility of 3D printing cell-laden bioinks.

6) To develop methods for integrating 3D printed scaffolds, biomimetic bioinks, and STRO-1 enriched BMSCs, with the objective of creating functional bioconstructs for use in bone reparation.

5.2.2 Materials and Methods

5.2.2.1 Manufacture of bioinks

A 50 ml volume of a biomimetic bioink consisting of 3% w/v alginate, 5 mg/ml fibrinogen, 20 µg/ml FN, 100 µg/ml collagen, 5 µg/ml HS, 1% w/v HA was made inside a microbiological safety cabinet as described in 4.1.2.1. 20 µl of a red food colorant was added to the biomimetic composite bioink. The pH of this mixture was adjusted to 7.5 using sterile-filtered 1 M sodium hydroxide.

Based on results obtained in 4.2.3.2, a 100 ml volume of a (crosslinking) cell delivery bioink (GHA) consisting of 1% w/v gelatin, 1% w/v HA, 5 U/ml thrombin, 2.5

mM calcium chloride dihydrate, 1 mM magnesium chloride hexahydrate was made inside a microbiological safety cabinet as follows. This bioink composition was adjusted to enable the *in situ* precipitation of the biomimetic bioink to generate the surface coating on the PCL scaffolds. 1000 units of human thrombin (Sigma Aldrich, UK) was dissolved in 5 ml of αMEM containing 4.5 w/v sodium chloride to make a stock solution of 200 U/ml. 1000 mg of high molecular weight HA (3D Global Inc., Taiwan) was first added to 90 ml of αMEM containing 4.5% w/v sodium chloride warmed to 37 °C. 1000 mg of type A gelatin (Sigma Aldrich, UK) was added to the solution, followed by 20.3 mg of magnesium chloride hexahydrate and 36.8 mg of calcium chloride dihydrate (both Sigma Aldrich, UK). 2.5 ml of the stock solution of thrombin was finally added to the mixture under constant stirring at 800 rpm using a digital stirrer for 60 minutes. 40 µl of a blue food colorant was added to the cell delivery bioink. The pH of this mixture was adjusted to ~8 using sterile-filtered 1 M sodium hydroxide before the volume of the mixture was topped up with αMEM containing 4.5% w/v sodium chloride to make a final volume of 100 ml. 10 ml bioink aliquots were sterilised under UV light for 1 hour prior to capping the sterilised glass bottles and sealing with parafilm. All bioinks were kept at room temperature.

5.2.2.2 Manufacture of 3D printed PCL scaffolds

PCL (Capa™6800, CAS number: 24980-41-4, average M_w = 80000 g/mol) was purchased from Perstop (Sweden). 3 mm-sized PCL beads were added to the melt extrusion tank of the 3DDiscovery bioprinter and heated to 120°C for 2 hours. The switch in supplier was due to a major change in the printability of new batches of PCL purchased from Sigma Aldrich, UK, who had not disclosed a recent change in their manufacturing protocol. Precision extrusion deposition via the HM-300H printhead was performed at ambient temperatures of 21°C and a humidity of 66%.

A needle tip with a 0.26 mm internal diameter was used to print a cylindrical scaffold with a central hollow that was designed in BioCAD, with a total build height of 2.59 mm, an outer diameter of 10 mm, and an inner diameter of 4 mm. Printing parameters were set at a feed rate of 5 mm/s, pressure of 3 bars, a screw revolution rate of 14 revolutions per second, printing temperature of 102°C, and a layer thickness of 0.185 mm. The first layer involved printing fill lines at a 60° angle, with their edges stripped, to generate a ring pattern with a central hollow. This was followed by similar fill patterns but with fill lines at a 120° angle for the next layer, then 180°, 240°, 300° and finally 0°. Fill lines were set 0.9 mm apart to generate scaffold porosity. In between each layer, an outer and inner circular pattern were

also deposited to create a gap between subsequent layers, thereby increasing the overall porosity of the construct. These layers were designated as a group, which was re-printed until the total build height was achieved (Video 5-2). Double-sided adhesive tape was applied to the glass slide to increase the adhesion of PCL fibres during the building of the first layer for each construct. PCL scaffolds were washed in an antibacterial, anti-mycotic solution, rinsed in 1x PBS and UV-sterilised for 2 hours prior to being air-dried overnight in a microbiological safety cabinet.

PCL cylinder.mov

Video 5-2 3DDiscovery printing of the PCL cylinder scaffold.

Half of the sterilised scaffolds were set aside to generate biomimetic-coated PCL scaffolds. Approximately 200 to 250 µl of the red coloured biomimetic composite bioink (manufactured as described in 4.2.2.1) was deposited onto each sterilised scaffold using a sterilised disposable 30 ml spray bottle (Daiso, Japan). These scaffolds were then maintained in covered petri dishes and placed in a humidified, 37°C, 5% CO_2 incubator for 60 minutes to allow adsorption to occur. A second coating consisting of approximately 200 µl of a blue-coloured cell delivery bioink (GHA, manufactured as described in 5.2.2.1, and cell-free) was applied per scaffold using the same aerosol deposition method (Video 5-3). The scaffolds were incubated as above for 60 minutes to allow the components of the two bioinks to interact and combine. Excess bioink material was gently removed from each scaffold by blotting with sterilised filter paper. Coated scaffolds were air-dried in a microbiological safety cabinet overnight and kept in sealed sterile petri dishes.

Scaffold coating.mov

Video 5-3 Aerosol deposition of the bioinks on PCL scaffolds.

5.2.2.3 Structural analyses of 3DDiscovery-printed PCL scaffolds

Qualitative assessments of the macro- and microstructure of the non-coated and aerosol-coated PCL cylinders were acquired by scanning electron microscopy (SEM, FEI Quanta 200, Thermo Fisher Scientific, USA). Critical drying step was performed for cell-seeded PCL scaffolds as described in 2.7. No critical drying step was performed for acellular scaffolds. Both PCL scaffolds were coated with a 7 µm-

thick gold-palladium layer. Working distance for visualisation was between 9.42 and 10.04 mm, with a spot size of 5 nm, and an accelerating voltage of 20 kV under high vacuum conditions. 561 and 633 nm wavelength lasers in the reflectance mode of confocal microscopy were used to directly assess the surface appearance of deposited fibres of non-coated and aerosol-coated PCL scaffolds. Reflectance mode imaging was performed using a Leica SP8 Confocal Microscope. Three-dimensional image reconstructions were performed using Leica Application Suite X software.

Porosity and architecture of non-coated and aerosol-coated PCL scaffolds were analysed using a Skyscan1176 µCT scanner (Bruker Corporation, USA). Each PCL scaffold was placed into an empty 1.5 ml Eppendorf tube and fixed in position within the µCT scanner. After flat-field correction was carried out, a µCT scan was performed without a filter applied, at a pixel resolution of 17.55 µm, a current of 600 µA, voltage of 40 kV, rotation step of 0.5°, and with frame averaging switched off. Image reconstruction was performed with the accompanying NRecon software, having first selected an appropriate region of interest (ROI) to encompass the entire scaffold in every image slice, and applying an angular step of 0.5°, no smoothing, beam hardening correction of 30%, and a ring artefact correction of 7.

Reconstructed images were loaded in Dataviewer (version 1.5.4.0, Bruker Corporation, USA) to align images in the coronal, sagittal and transverse axes. These axial images were centred and saved as a volume of interest dataset. CTAn software (version 1.16.4.1, Bruker Corporation, USA) was used to perform volume and surface rendering, and 3D analysis, which involved the measurement of PCL volume, the total volume of the construct, the degree of open, closed and total porosity, the mean open pore volume, as well as the average range distribution of PCL fibre thickness from the reconstructed 3D dataset. A volume of interest dataset was loaded and the top and bottom references set. An appropriate ROI was applied to an image slice, adjusted to fit, and then interpolated throughout the entire volume. A second ROI was drawn by holding down the control, shift, and right-click mouse buttons to exclude the central hollow area from the final analysis. This new dataset was saved. The new volume of interest was loaded before adjusting the grayscale histogram (lower threshold setting of 30, upper threshold setting of 150). 3D analysis was performed for each scaffold. The rendered dataset was opened in CTVox software (version 3.1.1 r1191, Bruker Corporation, USA) to create 3D reconstructions of the PCL scaffolds for export.

Following method note MN060 (Bruker Corporation, USA) and using the second saved volume of interest dataset per construct, a surface mesh for open and closed pore models was created in the CTAn software to analyse open and closed porosities per scaffold. CTVol software (version 2.3.2.0, Bruker Corporation, USA) illustrated the open and closed porosity 3D maps generated from the analyses.

5.2.2.4 Isolation, culture, and seeding of human STRO-1 enriched BMSCs

As detailed in 3.1.2.1 and 3.1.2.2, STRO-1 enriched BMSCs were isolated from human bone marrow samples from two female patients (aged 62 and 77) following hip arthroplasty, with full written, informed patient consent and ethical approval (NHS England Local Research Ethics Committee, number 194/99). Culture media was changed every three to four days. Cells were passaged at 70 to 80% confluency. All experiments undertaken used cells at passage 1 or 2. Cell counts were performed as described in 2.2.

Both types of PCL scaffolds were seeded inside a microbiological safety cabinet using the same aerosol spray method employed for surface coating the PCL scaffolds. About 120 µl of the cell delivery bioink (see 5.2.2.1), containing 4 X 10^4 STRO-1 enriched BMSCs, was deposited per scaffold (Video 5-3). The spray nozzle was held approximately 5 cm away from the scaffolds, and the temperature of the cell-laden bioink was 18°C. This was followed by a 30 minute incubation of the seeded scaffolds in a sterile petri dish placed in a humidified, 37°C, 5% CO_2 incubator. The seeded scaffolds were then suspended within the well of a Corning® 24-well plate using a custom-made well insert device (see 2.4.1) and cultured for 7, 14 and 21 days in basal and osteogenic media containing 25 nM of 1,25-VitD3 (*n* = 3 per time-point). A similar number of STRO-1 enriched BMSCs suspended in basal media (manually deposited using a P-1000 pipette) and in the cell delivery bioink (deposited by the aerosol spray method) (*n* = 3 per time-point and condition) were cultured in basal and osteogenic media on TCP as controls.

5.2.2.5 STRO-1 enriched BMSC response and functionality

5.2.2.5.1 Immunocytochemical staining

Seeded scaffolds from days 7, 14 and 21 were fixed in 4% paraformaldehyde for 15 minutes prior to immunocytochemical staining as described in 2.6.3. Mouse IgG1 anti-alpha tubulin antibody was used in place of anti-vinculin antibody with no changes to the protocol steps. The final step involved incubation of the scaffolds with HCS CellMask™

Deep Red stain (2 µl per 10 ml 1x PBS; 30 minutes; Thermo Fisher Scientific, USA) which stained the cytoplasm of the seeded cells, allowing for visualisation of morphology. Stained scaffolds were kept in sterile-filtered 1x PBS prior to imaging using a Leica SP8 Confocal Microscope. 3D image reconstructions were performed using Leica Application Suite X.

5.2.2.5.2 Quantitative reverse transcription polymerase chain reaction

Seeded scaffolds (*n* = 3) and TCP controls were lysed with RNA lysis buffer (Bioline, UK) at day 7, 14, and 21 end-points using repeated freeze thaw cycles. It was not possible to use TRIzol® as the chloroform present caused the PCL to partially dissolve into a gel-like mass, which prevented RNA extraction. Otherwise, RNA purification, cDNA synthesis and RT-qPCR was performed as described in 2.5, with the exception of TATA-box binding protein (TBP) being used in place of β-actin as the housekeeping gene. Primers used are listed in Table 2-2. Relative mRNA levels were calculated using the comparative CT method, and normalised to TBP, with derived relative expression of each gene marker at all time-points normalised against the relative expression of the same marker from TCP control day 7 basal samples.

5.2.2.5.3 Cell proliferation and functionality

STRO-1 enriched BMSC proliferation at days 3, 8, 11, 15, and 21 were determined using a WST-1 cell proliferation assay (Roche, Switzerland), as per the manufacturer's protocol. A 1:10 dilution of the reagent to media was used for incubating the templates over a 3 hour period. 100 µl of the resultant mixture was plated in triplicate for each test sample in addition to a control consisting of basal media and the WST-1 reagent only (which was incubated under the same conditions). A Varioskan® Flash microplate reader (Thermo Fisher Scientific, USA) was used to read the corresponding optical densities at 420 nm, with a reference wavelength reading at 610 nm.

Triplicate culture supernatants were collected at days 8, 11, 15, and 21 for ALP activity analysis using a colorimetric assay (Abcam, UK), according to the manufacturer's instructions. Culture media was changed 24 hours prior to each assay to ensure that ALP activity measured was over a 24-hour period. Following a 1 hour incubation in the dark in a 25°C incubator, the optical density of the samples was read using a Varioskan® Flash microplate reader at an absorbance wavelength of 405 nm. Results are presented as calculated activity values based on the absolute absorbance readings, with no normalisations performed.

5.2.2.6 Statistical analysis

Values are presented as mean ± standard deviation. Two-way ANOVA analyses with *post-hoc* testing, was conducted on the influence of culture time and culture approach on cellular proliferation and ALP activity. Paired t-test analyses were performed to determine the effect of various experiment conditions on gene expression of Runx2, Col1a1, ALP, OPN, OCN, and β–actin.

5.2.3 Results

5.2.3.1 Fabrication of an integrated 3D printed PCL-based scaffold

The PCL cylinder scaffold created using BioCAD was reproducibly printed 144 times using the printing parameters described in 5.1.2.1 and 5.2.2.2 , with a reduced build time of 5 minutes and 54 seconds per scaffold (Video 5-2 and Figure 5-15). Although this design was 0.6 mm lower than the prototype design, it was 0.1 mm wider. Aerosol-coated scaffolds demonstrated a consistent level of adherent coating post-air drying, with good distribution throughout each scaffold (Video 5-3). There was some (expected) variability in the degree and uniformity of coating between scaffolds.

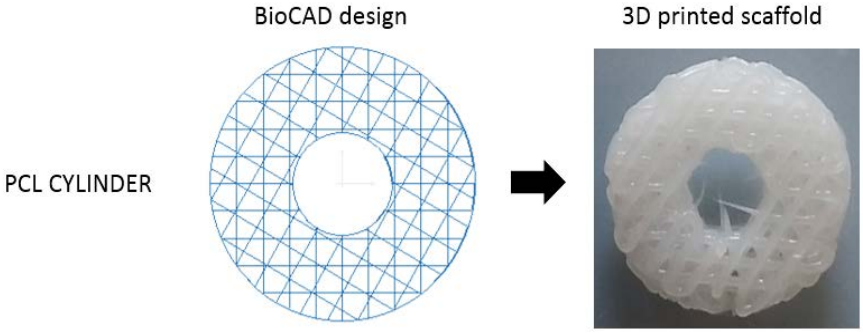

Figure 5-15 3DDiscovery-printed PCL cylinder scaffold.

5.2.3.2 Structural analyses of PCL cylinder scaffolds

SEM image analyses of the PCL scaffolds confirmed the high resolution of precision extrusion deposition printing, which was capable of building the PCL cylinder. The deposited PCL fibres in the non-coated PCL cylinder measured 342.9 ± 29.56 µm in diameter, while the pores within a layer measured 468.23 ± 48.44 µm in size. SEM images suggested the deposited PCL fibres had a smooth surface appearance (see Figure 5-16A to C). At day 7, seeded STRO-1 enriched BMSCs appeared attached to these PCL fibres as irregularly shaped bodies of varying

sizes. Deposited PCL fibres in the aerosol-coated PCL cylinders measured 298.96 ± 23.68 µm while pore sizes measured 476.22 ± 53.9 µm. In contrast, the aerosol coating process generated a rougher surface appearance, with randomly orientated microgrooves found along the majority of the length of PCL fibres (Figure 5-17).

Confocal microscopy images, using reflectance mode, further confirmed the marked difference in surface topography of the PCL fibres in the non-coated and aerosol-coated scaffolds. Deposited fibres of non-coated PCL scaffolds possessed 1 to 6 µm-wide grooves along the fibre deposition direction (Figure 5-18). At day 21, adherent STRO-1 enriched BMSCs can be seen growing within the microgrooves in a comparatively linear orientation. These linear microgrooves were replaced by a random and rougher surface topography in the aerosol-coated PCL scaffolds, with adherent cells growing within linear microgrooves (in uncoated areas of the fibres) as well as in coated areas in a typically random orientation (Figure 5-18).

Subject	Average fibre thickness (mm)	Mean PCL volume/Total volume (%)	Mean open porosity (%)	Mean closed porosity (%)	Mean total porosity (%)	Average open pore volume (mm^3)
PCL cylinder	0.34 ± 0.02	43.49 ± 5.04	56.38 ± 5.01	0.31 ± 0.105	56.3 ± 4.39	92.58 ± 14.79
Aerosol-coated PCL cylinder	0.28 ± 0.04	46.61 ± 7.42	52.97 ± 7.49	0.91 ± 0.19	55.37 ± 7.8	87.63 ± 25.52
Aerosol-deposited coating	0.11 ± 0.01	2.017 ± 0.40 (2.91 ± 0.54 mm^3)	97.98 ± 0.40	0	98.11 ± 0.44	N.A.

Table 5-2 Summary of µCT analyses of the 3D printed PCL scaffold architecture.

µCT 3D analyses of both the non-coated and aerosol-coated PCL cylinder scaffolds showed a comparatively consistent layer-by-layer distribution of the PCL fibres (Figure 5-19, Figure 5-20 and Video 5-4). Table 5-2 summarises the µCT 3D analyses results for both constructs. Sagittal cross-section views showed changes in pore geometry by altering the fill pattern orientation from 60°/150°/90°/0°, which had produced trabecular-like pores (Figure 5-8B), to 60°/120°/180°/240°/300°/0°, which generated a more organised, yet trabecular-like, porosity (Figure 5-19). Crucially, in comparison to the prototype cylinder design, the change in fill pattern of these PCL scaffolds and the removal of the outer and inner rings per layer from the

fabrication step did not affect the build integrity of the scaffolds. An increase in the mean open porosity by about 14% was observed and the mean closed porosity was reduced by about 0.22%. Average open pore volume was 32 mm^3 larger than in the prototype cylinder. Reconstructed images also showed the improvement in porosity of the outer surface of the scaffolds, even after aerosol-coating (Figure 5-20).

Figure 5-21 maps the different pore distributions of the non-coated and aerosol-coated PCL cylinders. Although the majority of the open pore network in both constructs consisted of pores greater than 0.72 mm in size, the aerosol coating process resulted in a wider range of open pore sizes, with an increase in the proportion of medium-sized pores when compared to non-coated PCL cylinders. Closed pores were randomly distributed throughout both scaffolds, and irregular in shape, with the majority of closed pores being less than 0.42 mm in size. There was a 3.5% reduction in mean open porosity while the mean closed porosity increased by 0.6% in the aerosol-coated scaffolds. Although the coating process did not result in a significant difference in the average open pore volume, pore geometry was less defined in aerosol-coated scaffolds (Video 5-4).

µCT analysis indicated that aerosol-coated PCL cylinders displayed thinner PCL fibres on average, with a higher proportion of smaller PCL fibres when compared to non-coated PCL cylinders (Figure 5-22). The average thickness of the aerosol-deposited coating was approximately 100 µm, and contributed 2% of the mean total volume of aerosol-coated scaffolds, in addition to accounting for the increased mean bone volume of aerosol-coated scaffolds. Reconstructed images from µCT scans demonstrated the aerosolised bioinks successfully permeated the PCL scaffolds, with a comparatively uniform distribution throughout the scaffold volume. The aerosol-deposition method randomly coated portions of the fibres (Figure 5-20C and Video 5-5).

Pore geometry differences.mov

Video 5-4 Aerosol coating results in differences in scaffold and pore geometry.

Virtual cross-section cPCL.mov

Video 5-5 µCT reconstruction of the aerosol-coated PCL cylinder scaffold.

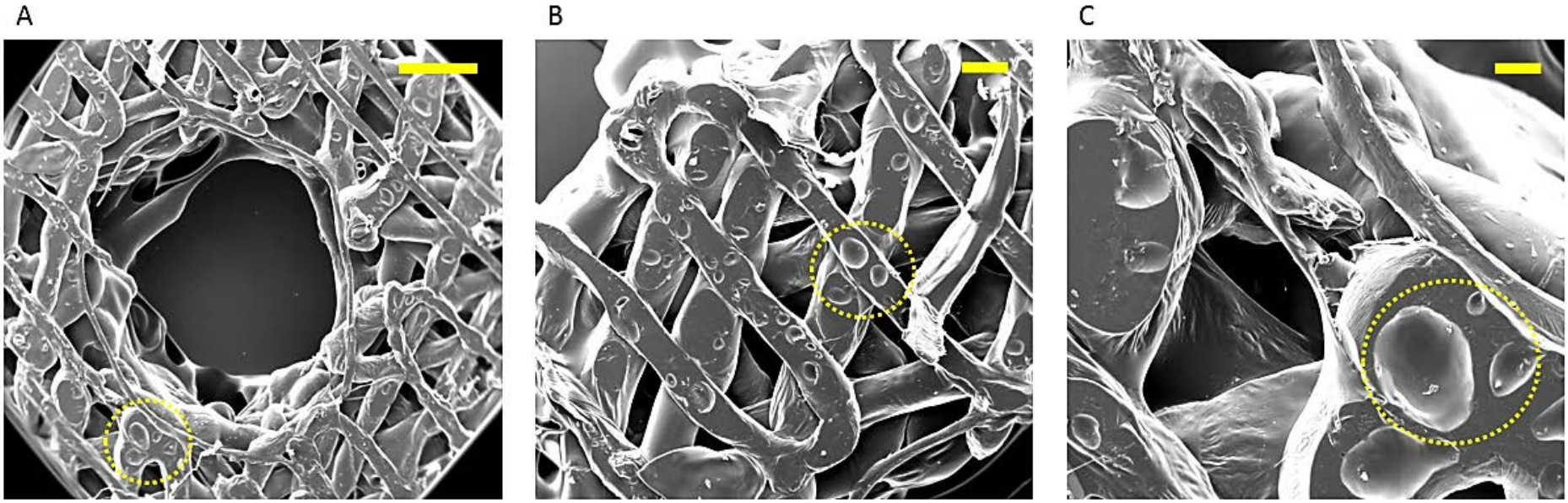

Figure 5-16 SEM images of STRO-1 enriched BMSC-seeded PCL cylinder scaffold at day 7.

The smooth appearance of the printed PCL fibres was punctuated by the presence of spheroid bodies of varying sizes (highlighted by dotted yellow circles). Scale bars represent A) 1 mm B) 500 µm and C) 200 µm.

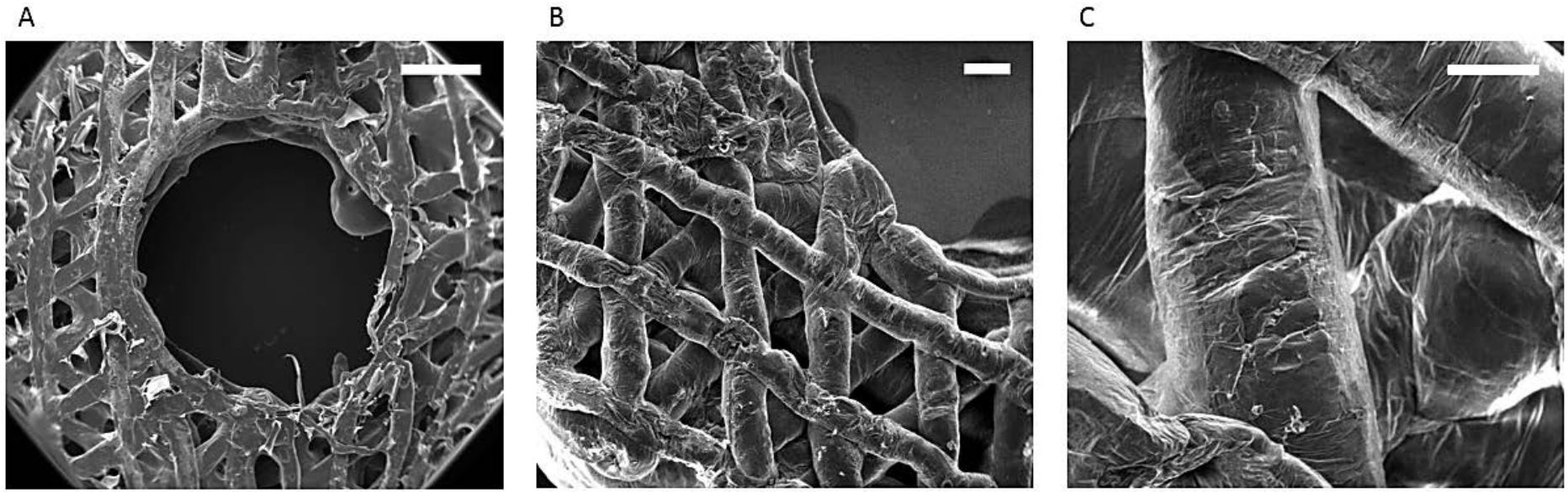

Figure 5-17 SEM images of an unseeded aerosol-coated PCL cylinder scaffold.

The aerosol spray deposition process created a rough surface topography on coated PCL fibres. At higher magnification views, the dehydrated coating applied appeared to display a 'shrink wrap' effect on the deposited PCL fibres. Scale bars represent A) 1 mm B) 500 µm and C) 200 µm.

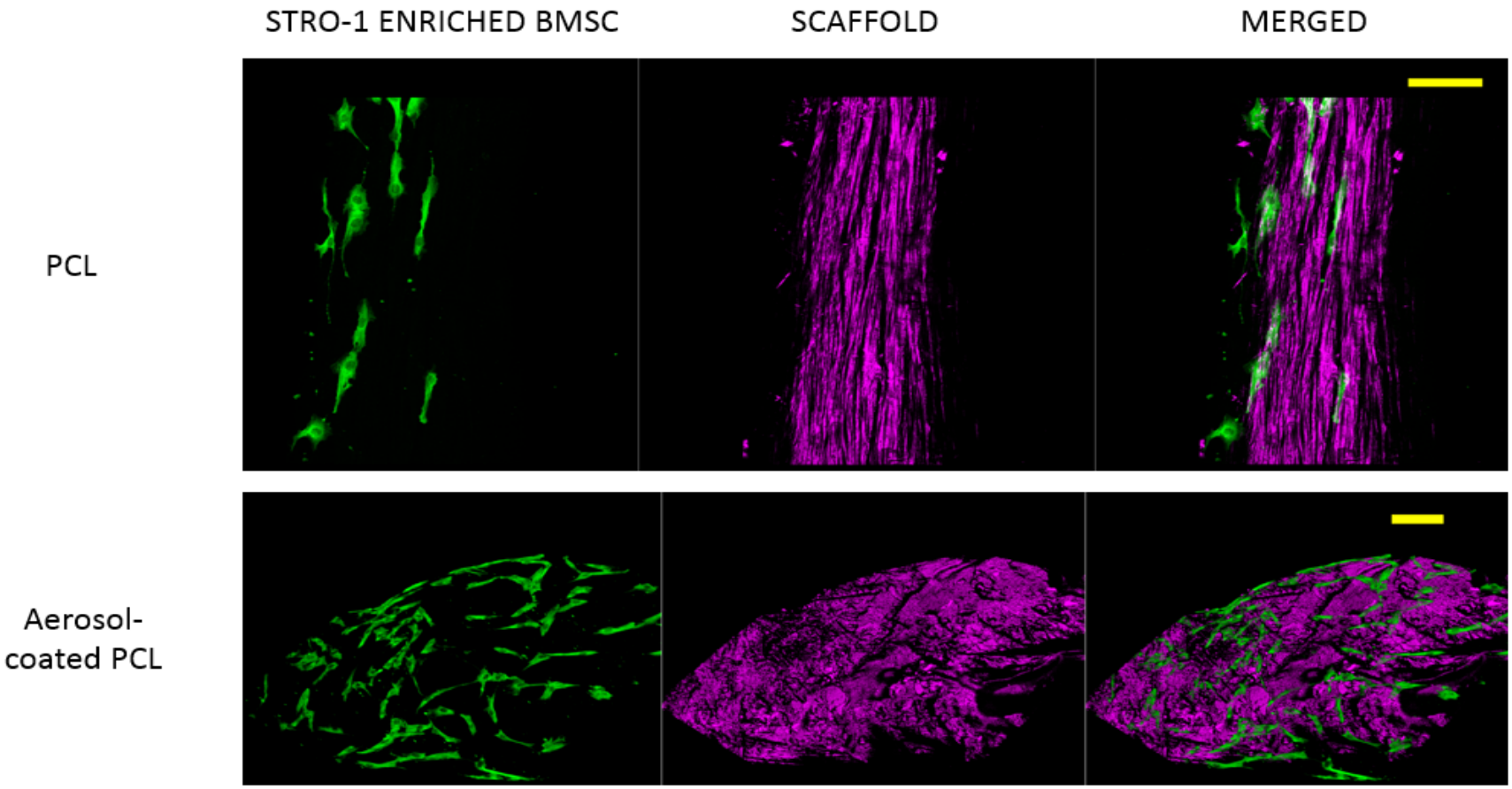

Figure 5-18 Confocal microscopy (reflectance mode) of STRO-1 enriched BMSCs seeded on both types of PCL cylinder scaffolds at day 21.

Seeded cells on non-coated PCL fibres were adherent in a linear orientation along the microgrooves present. The aerosol coating process altered the surface topography of deposited PCL fibres, with seeded STRO-1 enriched BMSCs adherent in a disorganised manner. Scale bars represent 50 µm.

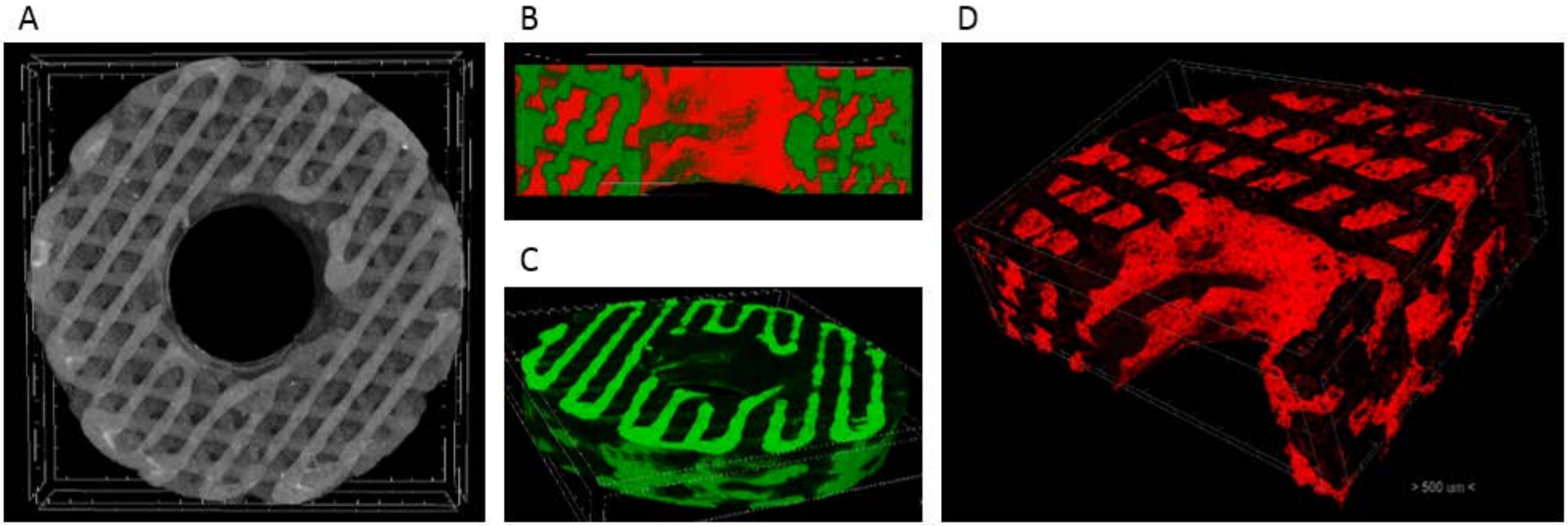

Figure 5-19 µCT reconstructed images of the non-coated PCL cylinder scaffold.

A) 3D reconstructed grayscale image illustrates the printing resolution of the 3DDiscovery in building a hollow cylinder construct. Printed PCL fibres (seen in gray) were uniformly distributed per layer as designed. B) Sagittal view of the scaffold (shown in green) demonstrates the changes in the connectivity of spaces (shown in red) within and without the scaffold compared to the prototype cylinder. C) Oblique view of the scaffold (shown in green) demonstrating a greater outer ring porosity compared to the prototype cylinder. D) The spaces within the scaffold (illustrated in red) were interconnected in a more random pattern than in the prototype cylinder.

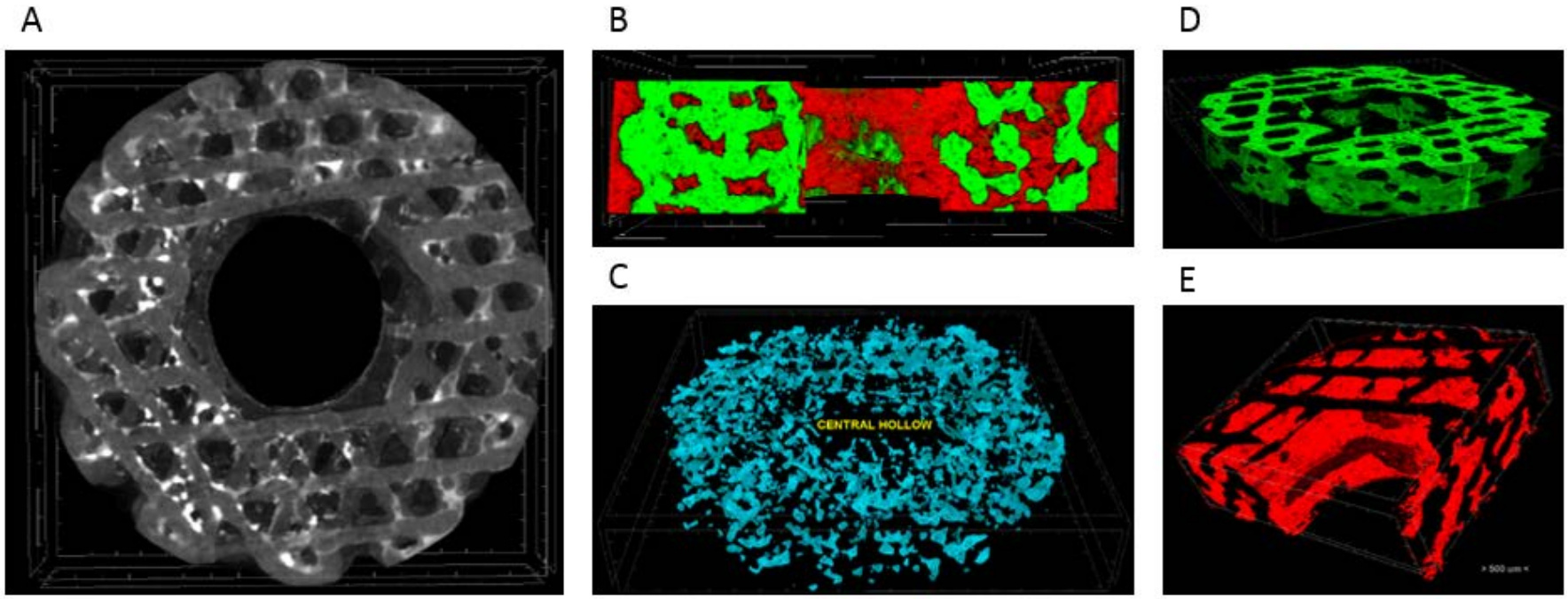

Figure 5-20 µCT reconstructed images of the aerosol-coated PCL cylinder scaffold.

A) 3D reconstructed grayscale image shows the presence of brighter areas (seen in white) within the scaffold (seen in gray). B) Sagittal cross-section view of the scaffold (shown in green) demonstrating the spaces (highlighted in red) within and without, as well as the trabecular-like appearance of the layered PCL fibres. C) The comparatively uniform distribution of the coating (shown in cyan) throughout the scaffold was evident, with the speckled patterning a reflection of the aerosol spray deposition onto the PCL fibres. D) Oblique view of the scaffold (shown in green) demonstrating that the coating process did not cause any significant changes to the overall geometry and porosity of the construct. E) The interconnected spaces within the scaffold (shown in red) were also unaffected by the coating process.

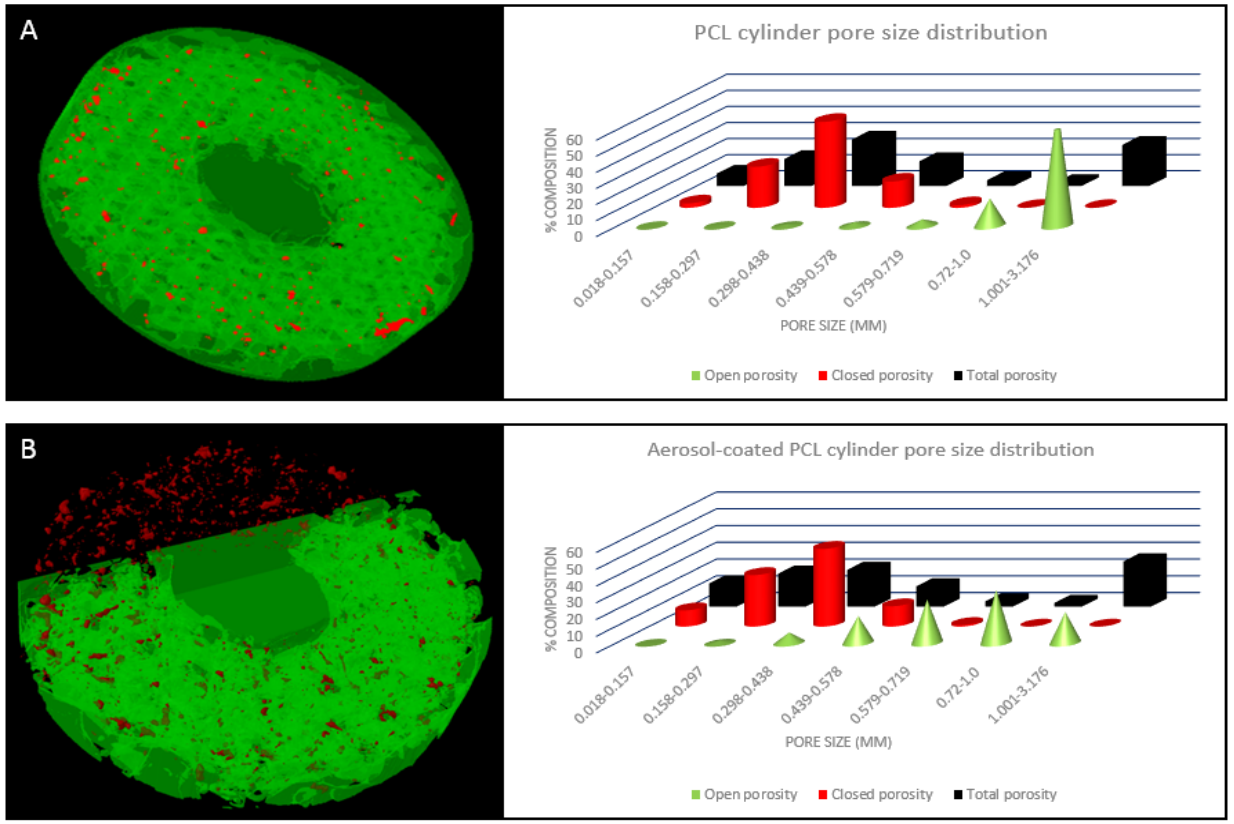

Figure 5-21 Porosity mapping comparison for non-coated and aerosol-coated PCL cylinder scaffolds.

A) The majority of the pores in the PCL cylinder scaffold were of the open type (shown in green), with closed pores (shown in red) occurring primarily at the edges or points of PCL fibre intersection. B) The coating process resulted in a clear increase in the number of closed pores, which occur throughout the aerosol-coated PCL cylinder scaffold.

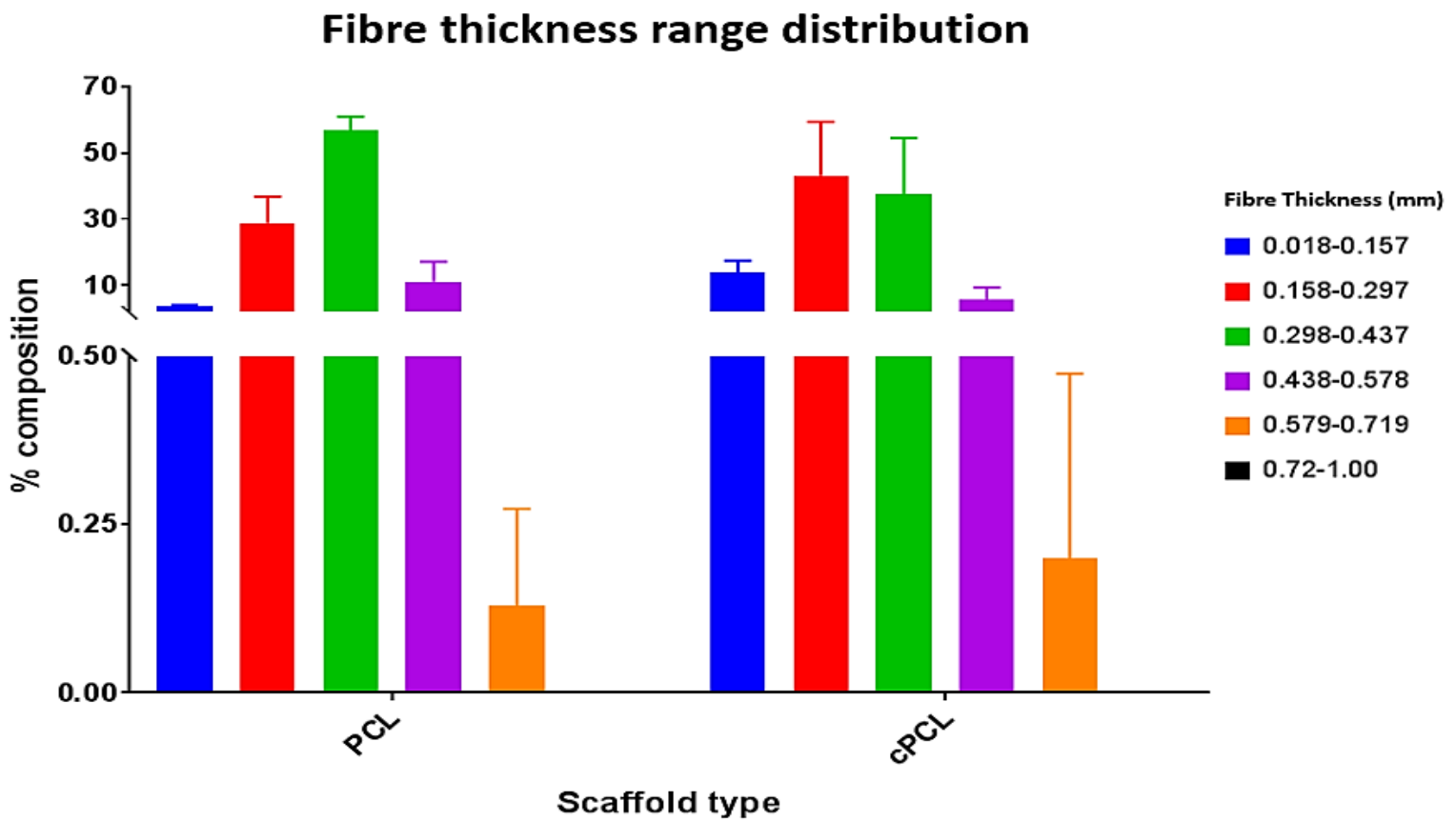

Figure 5-22 Fibre thickness distribution in PCL and aerosol-coated PCL cylinder scaffolds.

No significant differences in the overall fibre thickness between the two cohorts was found, with the aerosol-coated scaffolds demonstrating a marginally higher proportion of smaller sized fibres than non-coated scaffolds.

5.2.3.3 Cell adhesion and immunocytochemical staining

Cellular adhesion was observed in non-coated and aerosol-coated scaffolds. Osteogenic conditions appeared to increase cell proliferation in non-coated scaffolds. However, in aerosol-coated scaffolds, culture conditions did not appear to have any significant effect on cell numbers. Fewer STRO-1 enriched BMSCs were observed to adhere to non-coated PCL fibres (Figure 5-23), when compared to the aerosol-coated cohort (Figure 5-24), suggesting that the biomimetic coating applied had improved cell adhesion. α-tubulin (shown in green, Figure 5-23 and Figure 5-24) extended uniformly from the nucleus throughout the cytoplasm of STRO-1 enriched BMSCs, indicating cytoskeletal activity in response to the scaffold surface topographies of the two cohorts. This increase in signal intensity was greater in the aerosol-coated cohorts (Figure 5-24).

Although the poor seeding efficiency and low cell seeding density resulted in a non-confluent monolayer of adherent cells, it enabled a clear visualisation of the morphologies of adherent cells on the two different scaffolds. Adherent STRO-1 enriched BMSCs on non-coated PCL fibres were found predominantly in the microgrooves on the surface, and displayed smaller, spindle-like morphologies (Figure 5-18 and Figure 5-23). Cell morphology was more varied in adherent STRO-1 enriched BMSCs on aerosol-coated scaffolds, ranging from spheroidal, to spindle-like, to stellate-like morphologies (Figure 5-18 and Figure 5-24).

Confocal microscopy enabled a limited depth analysis (up to a 250 µm depth) of the seeded scaffolds without sectioning. Depth imaging demonstrated the varied curvature of the surface topography of deposited PCL fibres and revealed seeded cells were not only adherent on the flat upper surfaces of the fibres, but also on, and along the surface curvatures, and under-surface areas of the PCL fibres in both cohorts (Figure 5-25 and Figure 5-26). Depth imaging also confirmed the comparatively uniform distribution of seeded cells by the process of aerosol deposition.

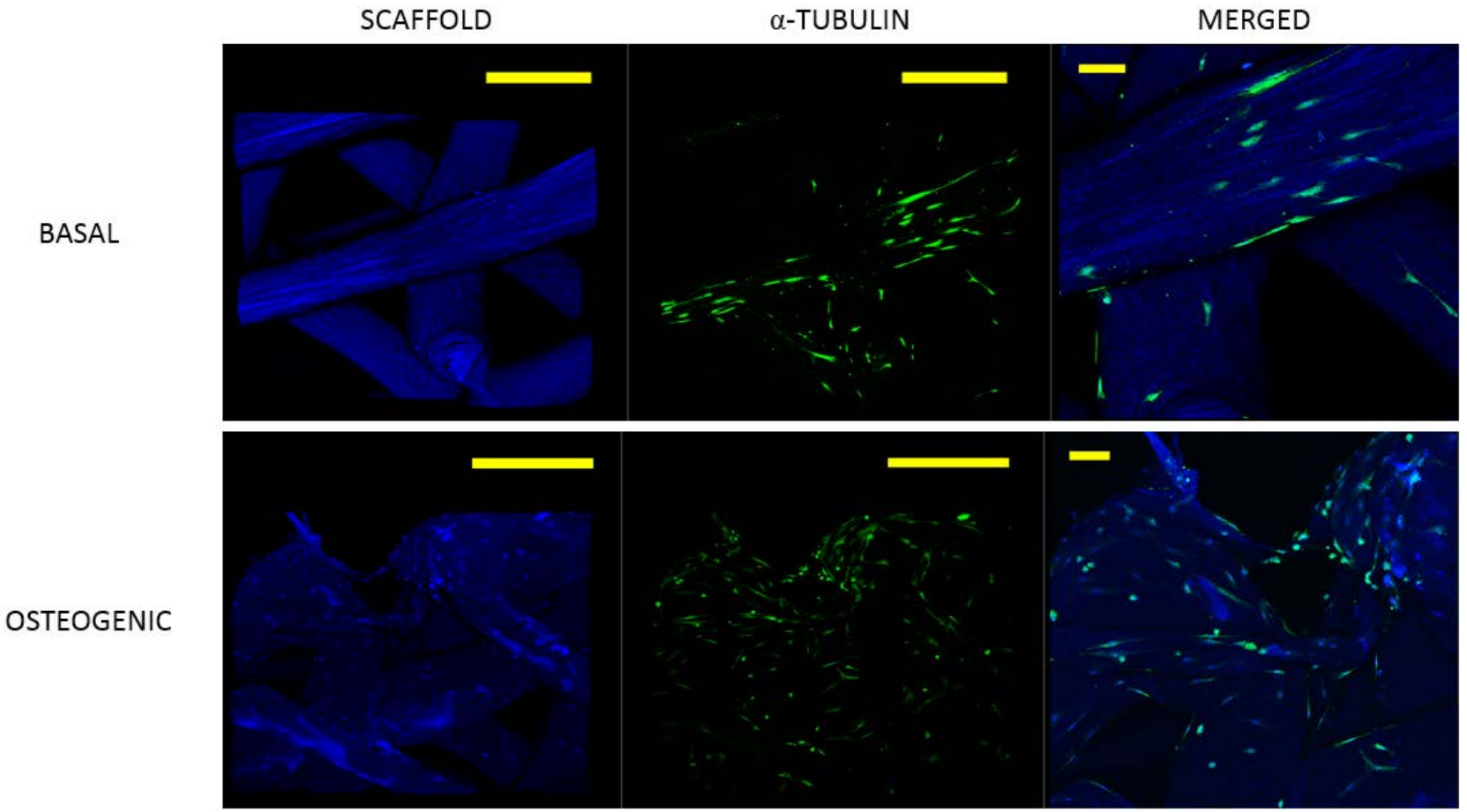

Figure 5-23 Immunocytochemical staining of seeded STRO-1 enriched BMSCs on PCL cylinder scaffolds at day 21.

Scale bars in scaffold and α-tubulin images represent 500 µm. Scale bars in magnified, merged images, represent 100 µm.

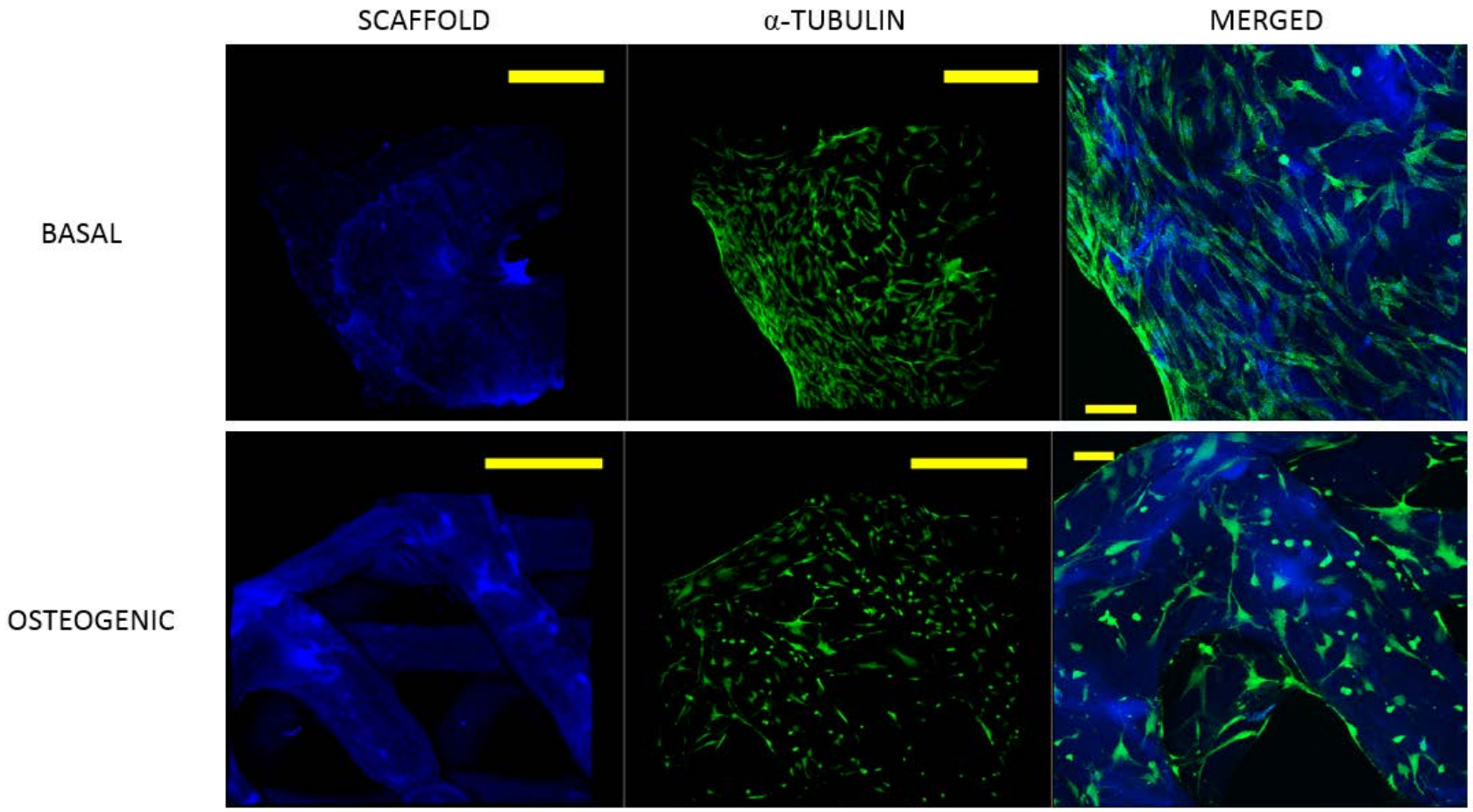

Figure 5-24 Immunocytochemical staining of seeded STRO-1 enriched BMSCs on aerosol-coated PCL cylinder scaffolds at day 21.

Scale bars in scaffold and α-tubulin images represent 500 µm. Scale bars in magnified, merged images, represent 100 µm.

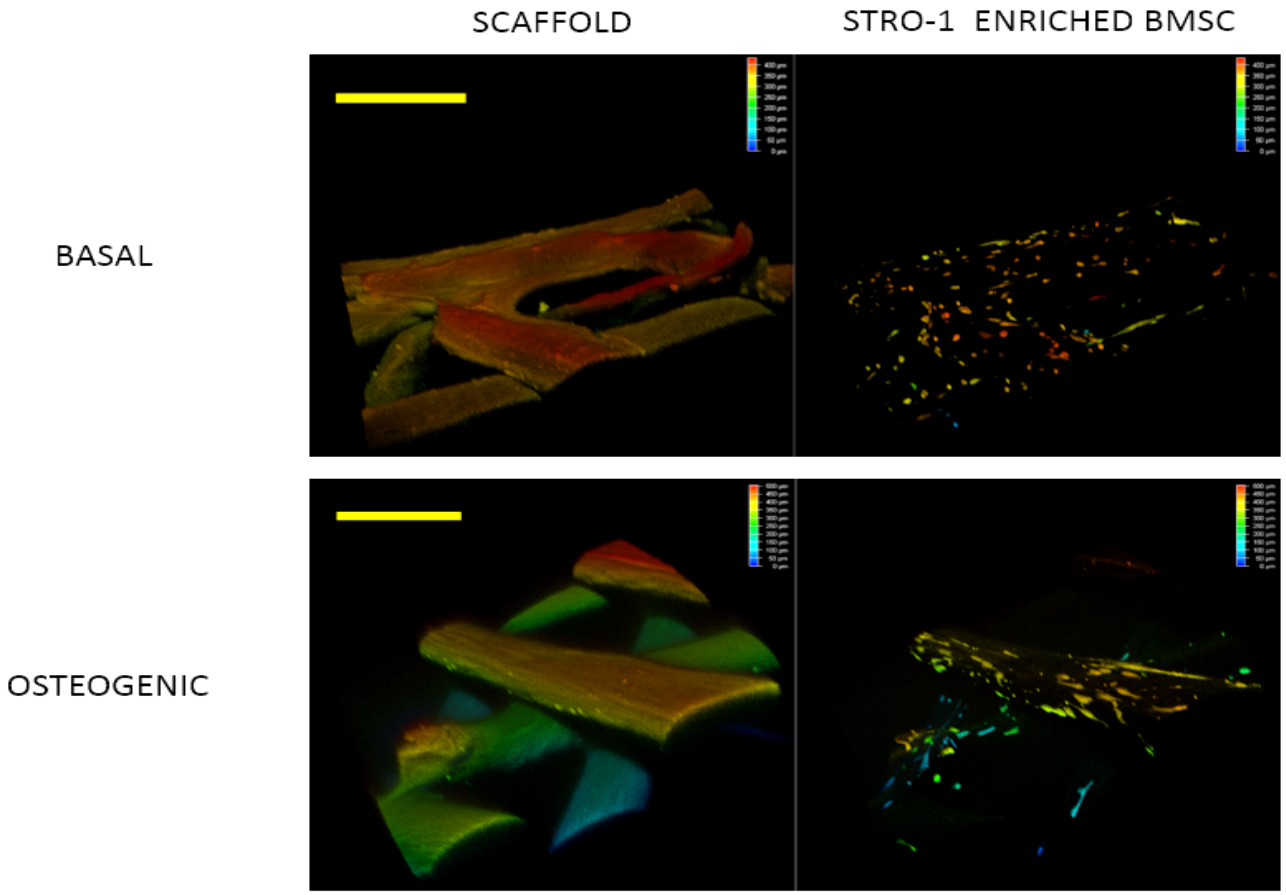

Figure 5-25 Confocal depth imaging of STRO-1 enriched BMSCs seeded on non-coated PCL cylinder scaffolds at day 21.

Adherent STRO-1 enriched BMSCs are clearly visible on depth imaging, with cells adherent throughout the convexity of the PCL fibre rather than just on the flattened areas. Scale bars represent 500 µm.

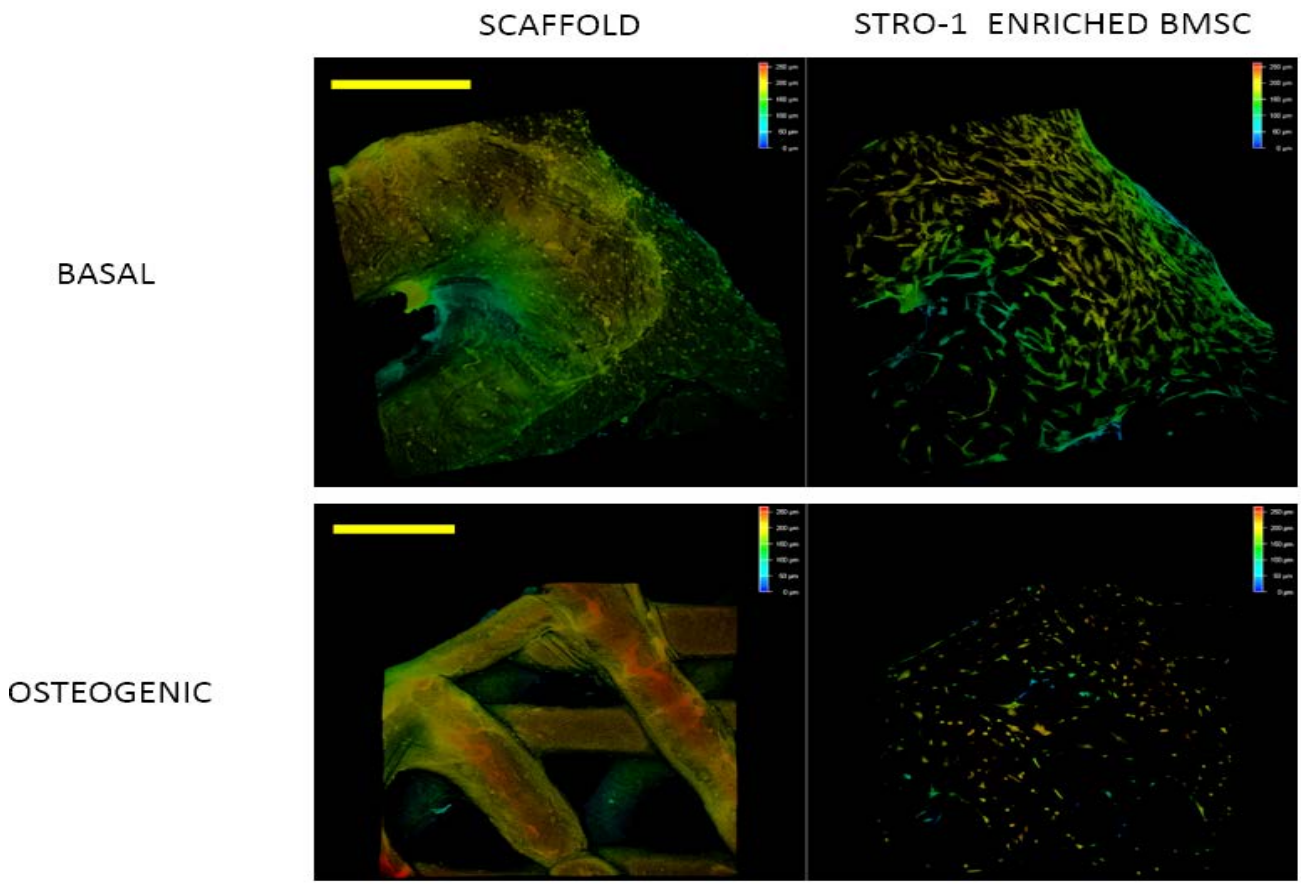

Figure 5-26 Confocal depth imaging of STRO-1 enriched BMSCs seeded on aerosol-coated PCL cylinder scaffolds at day 21.

Seeded STRO-1 enriched BMSCs were adherent on the undulating surfaces of the coated scaffolds, with adherent cells clearly visible down to a depth of 200 µm (the limit for confocal imaging solid scaffolds). Scale bars represent 500 µm.

5.2.3.4 Quantitative reverse transcription polymerase chain reaction

Insufficient quality and quantity of extracted RNA for day 7 and day 14 end-point samples for non-coated and aerosol-coated scaffolds precluded their analyses. As such, only the derived relative expression of each tested gene marker at day 21 end-points was normalised against the relative expression of the same marker from basal media day 7 samples. TBP was used as the housekeeping gene as previous studies have shown that β–actin expression changes significantly in 3D culture (274). This finding was also observed in this study, with significant differences in β–actin expression in both scaffold cohorts in both culture conditions when compared to cells cultured on TCP. STRO-1 enriched BMSCs seeded on TCP and cultured in basal and osteogenic conditions demonstrated a similar osteogenic gene expression profile to that obtained in Figure 3-4 and Figure 3-5.

The relative expression of osteogenic gene markers of STRO-1 enriched BMSCs seeded on the PCL scaffolds at day 21 are summarised in Figure 5-27. Runx2 expression was significantly downregulated at day 21 in STRO-1 enriched BMSCs seeded on aerosol-coated PCL scaffolds. Col1a1 expression was also significantly downregulated in both non-coated and aerosol-coated scaffolds. ALP expression was non-significantly elevated in non-coated and aerosol-coated PCL scaffolds cultured in osteogenic media. OPN expression in the non-coated and aerosol-coated cohorts cultured in osteogenic media (but not in scaffolds cultured in basal media) was significantly elevated at day 21. OCN expression was similarly upregulated in non-coated and aerosol-coated scaffolds cultured in basal media at day 21. The elevation in OCN (and to a lesser extent, OPN) expression in STRO-1 enriched BMSCs on aerosol-coated scaffolds cultured in osteogenic media was almost comparable to that of STRO-1 enriched BMSCs on TCP maintained in osteogenic media. Increased OPN and OCN expression indicated that STRO-1 enriched BMSCs seeded on non-coated and aerosol-coated scaffolds were induced by the scaffold to undergo osteogenic differentiation. This degree of osteoinduction was further enhanced in osteogenic media, particularly in the aerosol-coated scaffolds. Upregulation of OPN (8-fold at day 7) and OCN (3-fold at day 7) expression in STRO-1 enriched BMSCs deposited by the aerosol method onto TCP using the cell delivery bioink (GHA) and cultured in osteogenic media was observed, with OCN upregulation persistent until day 21.

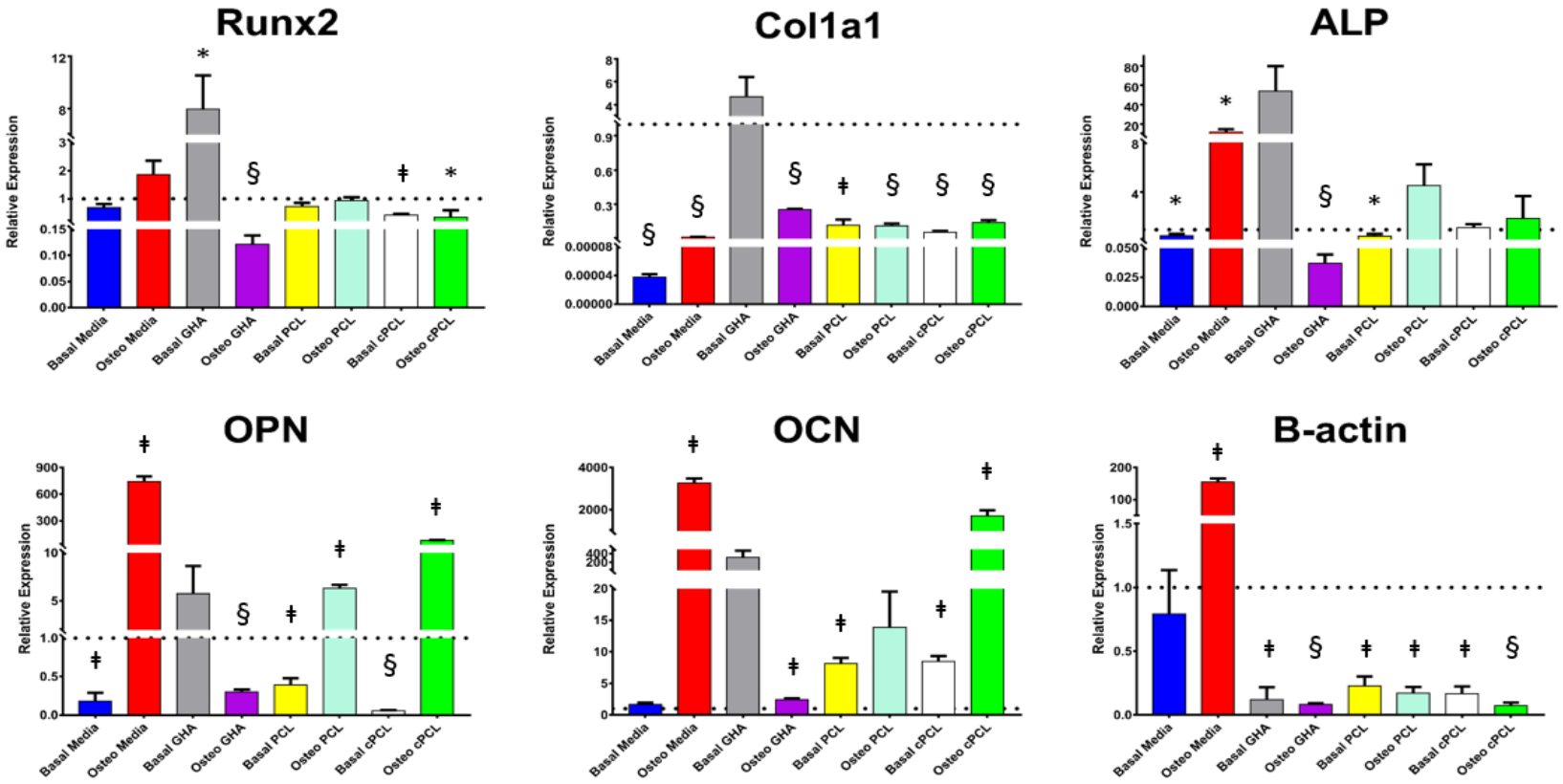

Figure 5-27 Relative expression of osteogenic gene markers of the tested cohorts at day 21.

STRO-1 enriched BMSCs on PCL scaffolds demonstrated osteogenic differentiation, which was further enhanced under osteogenic conditions. (= $p < 0.05$, ǂ = $p < 0.01$, § = $p < 0.001$.)*

5.2.3.5 Cell viability, proliferation, and functionality

Figure 5-28 summarises the WST-1 assay results for the various cohorts tested. A markedly reduced (but constant) number of seeded STRO-1 enriched BMSCs on non-coated and aerosol-coated scaffolds was observed at all time-points (irrespective of culture conditions) over the 21 day period in comparison to STRO-1 enriched BMSCs cultured on TCP in both basal and osteogenic media. No significant difference in cellular proliferation could be ascertained between non-coated and aerosol-coated scaffolds at all time-points. In contrast, maximal cellular proliferation occurred at day 21 in the four TCP cohorts. Irrespective of culture conditions, STRO-1 enriched BMSCs seeded onto TCP using aerosol deposition (GHA) demonstrated a lower proliferation rate during the first 2 weeks of culture, when compared to conventionally seeded cells. An accelerated growth phase between days 15 and 21 was more evident in the former cohort, particularly in basal conditions. STRO-1 enriched BMSCs on TCP cultured in osteogenic media had a lower cellular proliferation rate when compared to STRO-1 enriched BMSCs on TCP cultured in basal media. This finding was less evident between the PCL scaffold cohorts. Two-way ANOVA analyses with Tukey *post-hoc* testing demonstrated an extremely significant interaction ($F(28, 80) = 715.1$, $h^2 = 0.119$) between culture time ($F(4, 80) = 4009$, $h^2 = 0.096$) and culture approach ($F(7, 80) = 18801$, $h^2 = 0.785$) in affecting cell proliferation ($p < 0.001$), resulting in an indistinguishable effect of each variable.

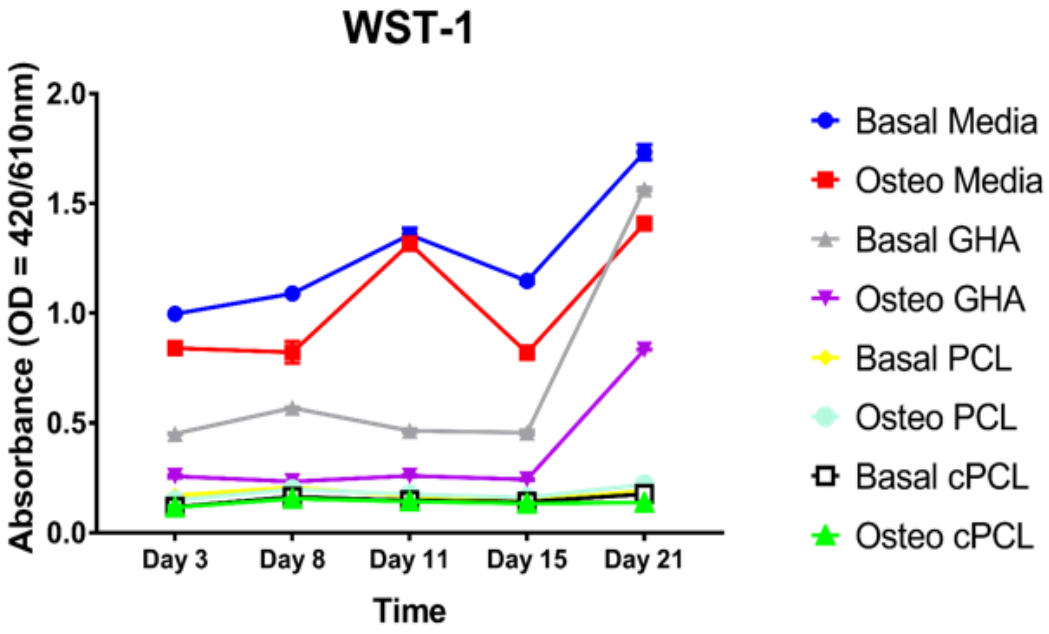

Figure 5-28 STRO-1 enriched BMSC proliferation over time in the different cohorts.

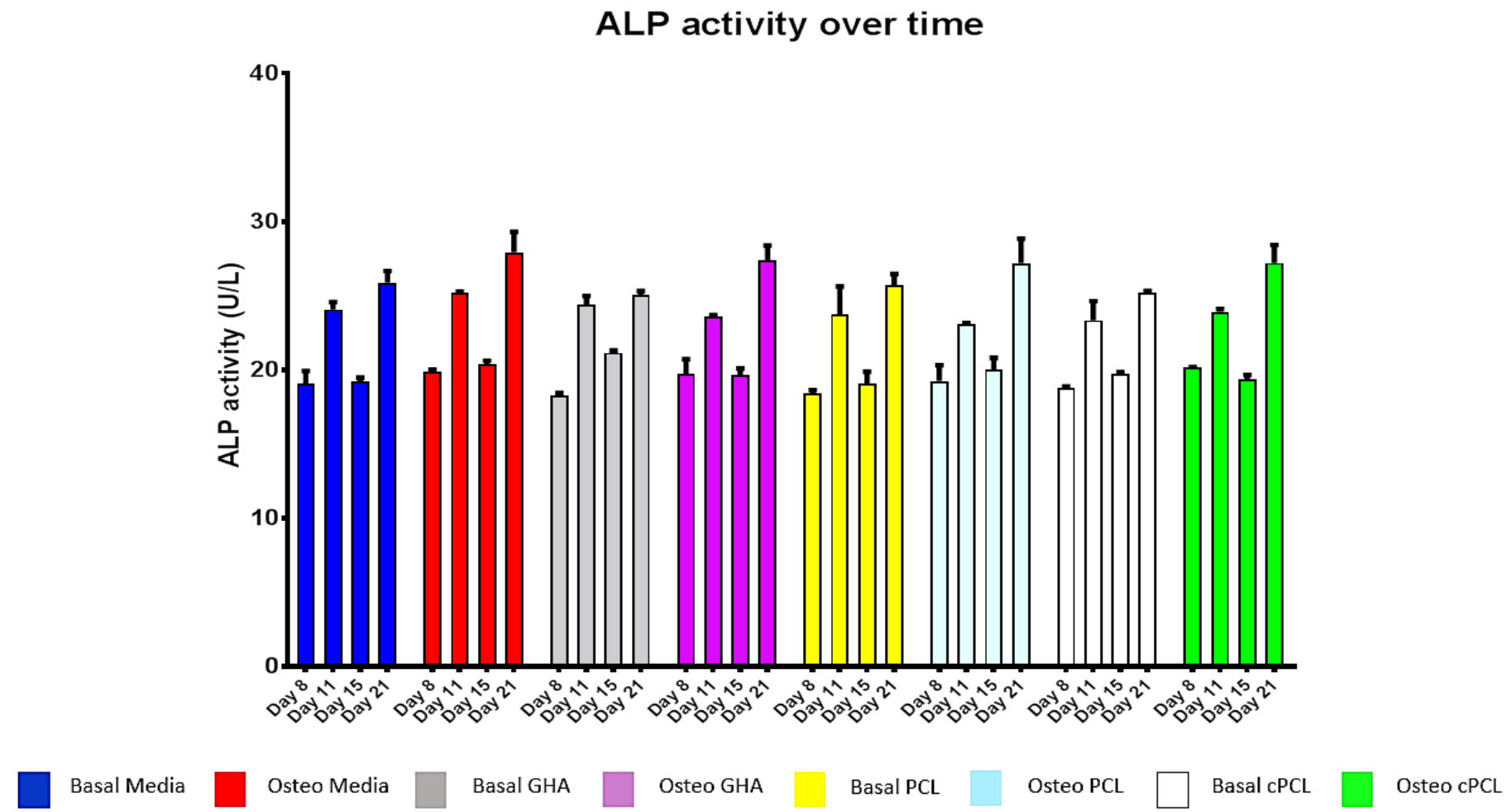

Figure 5-29 ALP activity over time in the different cohorts.

Figure 5-29 illustrates the ALP activity of the various cohorts over the 21 day period. ALP activity reached peak values at day 21 in all cohorts. Two-way ANOVA analyses with Tukey multiple comparison test, revealed that the main effect for time groups yielded an F ratio of F (3, 48) = 585.4, $p < 0.0001$, $h^2 = 0.902$, indicating that culture time had an extremely significant effect on ALP activity. Culture approach yielded an F ratio of F (7, 16) = 3.6, $p < 0.05$, $h^2 = 0.025$, indicating significance. The interaction effect was extremely significant, F (21, 48) = 3.04, $p < 0.001$, $h^2 = 0.033$. Table 5-3 summarises the cohort comparisons that had significant mean differences in ALP activity following Tukey *post-hoc* analysis. Direct comparisons between non-coated and aerosol-coated cohorts cultured in similar conditions showed the aerosol coating did not induce a significant difference in ALP activity between the two cohorts. Coupled with WST-1 results showing markedly lower cell numbers in non-coated and aerosol-coated cohorts, these results indicate an enhanced ALP production by STRO-1 enriched BMSCs cultured on both types of PCL scaffolds.

Tukey comparison test	***Mean Difference***	***p value***
Day 8 Osteogenic Media vs Day 8 Osteogenic PCL	2.129	0.026
Day 15 Basal GHA vs Day 15 Basal PCL	2.062	0.035
Day 21 Basal Media vs Day 21 Osteogenic Media	-2.039	0.038
Day 21 Osteogenic Media vs Day 21 Basal GHA	2.881	0.001
Day 21 Osteogenic Media vs Day 21 Basal PCL	2.204	0.018
Day 21 Osteogenic Media vs Day 21 Basal cPCL	2.706	0.002
Day 21 Basal GHA vs Day 21 Osteogenic GHA	-2.33	0.010
Day 21 Basal GHA vs Day 21 Osteogenic PCL	-2.151	0.023
Day 21 Basal GHA vs Day 21 Osteogenic cPCL	-2.16	0.022
Day 21 Osteogenic GHA vs Day 21 Basal cPCL	2.155	0.023
Day 21 Osteogenic PCL vs Day 21 Basal cPCL	1.976	0.050
Day 21 Basal cPCL vs Day 21 Osteogenic cPCL	-1.985	0.048

Table 5-3 Significant mean differences in ALP activity of different cohorts of seeded STRO-1 enriched BMSCs cultured over a 21 day period in basal and osteogenic media.

5.2.4 Discussion

To summarise, the results of the above experiments demonstrated:

- *Fill pattern and fibre orientation played a major role in defining the external and interconnected porosities of the scaffold architecture.*
- *Scaffold design significantly affects the printing times of the 3DDiscovery bioprinter.*
- *Aerosol deposition of bioinks and in situ gelation can be used to surface coat hydrophobic scaffolds, albeit with limited control and precision.*
- *Confocal microscopy (reflectance mode) imaging can be used to assess the surface topography of scaffolds more accurately than SEM.*
- *µCT is a useful tool for analysing the geometry and porosity of a scaffold and can be used to map the distribution of protein-coated areas within a scaffold.*
- *STRO-1 enriched BMSCs were viable and adherent to the PCL scaffolds despite the aerosol deposition, low cell numbers and seeding efficiency, the hydrophobicity of PCL and the short incubation time.*
- *Increased OPN and OCN expression occurred in the basal and osteogenic GHA and PCL cohorts, indicating the osteoinductive effect of the scaffold as well as the cell delivery bioink on seeded STRO-1 enriched BMSCs.*
- *OPN and OCN upregulation was greater in the aerosol-coated cohort cultured in osteogenic media.*
- *Although the PCL scaffolds were biocompatible, WST-1 assay showed that cell numbers and proliferation rate in all scaffold cohorts were the lowest at all time-points, irrespective of culture conditions.*
- *ALP production was significantly higher in the PCL scaffold cohorts (and marginally higher under osteogenic conditions) at all time-points when compared to TCP cohorts.*

Given the current limitations and associated long-term issues of utilising alloys in implants, and the rising demand for more effective therapeutic options for bone repair, this study examined whether an alternative biomaterial. PCL could be used. PCL has proven cytocompatibility and can be combined with other biomimetic biomaterials and STRO-1 enriched BMSCs for the fabrication of an integrated cell-scaffold construct for use in bone repair. A multi-material, biomimetic surface coating was applied to extrusion printed PCL cylinder scaffolds by simple aerosol deposition. This initial surface coating was then stabilised by the addition of a second bioink coating, which triggered *in situ* physical and ionic gelation

(Video 5-3). The final composition of the surface coating was designed to mimic the main components found in a haematoma and in the regenerative matrix of bone. The GHA bioink also served as the cell delivery bioink, and not only facilitated an improved STRO-1 enriched BMSC adhesion on hydrophobic PCL scaffolds, but also induced their early osteogenic differentiation (even in basal conditions) over a 21 day culture period (Figure 5-27). Furthermore, the multi-material, biomimetic coating enhanced the osteoinductive effect of 1,25-VitD3 on STRO-1 enriched BMSCs seeded on PCL scaffolds (Figure 5-27), thus demonstrating a similar functionality to bone ECM (315). ALP production was also significantly higher in the PCL cohorts, despite the lower cell numbers (Figure 5-29). These findings confirm the crucial role played by surface composition in enabling cellular interaction with biomaterials, which can affect the performance of an implant *in vivo* (241). The results also suggest that the osteoinductive effects of the bioinks could be adjusted by the addition of nanoparticles (407), decellularised ECM (315), growth factors (152) and/or peptide amphiphiles (402). The bioinks used in this study are tunable, allowing for optimisations to the concentrations of each component to adjust the speed and strength of coating, improve the stimulatory effect for different cell types and/or tissues, as well as the fabrication of functional graded scaffolds (constructs with gradients of bioactive agents). Adjustments to the bioink properties to enable their printability can alter the outcomes obtained in this study. Rheological studies to fully characterise the customised bioink properties are necessary prior to determining the printing parameters to be used for biofabrication (408, 409).

Confocal microscopy (reflectance mode) imaging was able to demonstrate the surface topography of deposited non-coated and coated PCL fibres (Figure 5-18) with superior resolution to SEM analysis in this study (Figure 5-16 and Figure 5-17). Coupled with the depth imaging mode, which illustrated the distribution of seeded STRO-1 enriched BMSCs (Figure 5-25 and Figure 5-26), these techniques (unlike SEM, which requires sample fixation) are non-destructive. This approach also has the potential for serial ‘live’ analysis and tracking of cell viability, migration, morphology and proliferation on 3D scaffolds (by concomitant use of ‘Live-Dead’ cell tracking systems such as Calcein AM or PKH-26 fluorescent staining). µCT and confocal microscopy (reflectance mode) imaging showed that the surface topography of PCL-based scaffolds manufactured by precision extrusion deposition system of the 3DDiscovery bioprinter was influenced by the complexity of the fill pattern, fibre orientation, and the rate of cooling of the molten (viscoelastic) biomaterial. The impact of ambient conditions (room temperature and relative humidity) cannot be

underestimated, as such factors can adversely affect the physicochemical properties (and therefore, printability) of thermosensitive materials like gelatin and alginate, or hygroscopic materials such as glycerol. Contrasting organisation and morphologies of STRO-1 enriched BMSCs adherent on the different surface topographies of the PCL scaffolds indicated that surface roughness, curvature, and skewness influence cell adhesion and cell behaviour in 3D matrices. This observation suggests that customised surface topographies could be used to enhance cell adhesion, direct cell migration and/or differentiation. One possible means of achieving this could be the creation of micro- or nanostructures within the internal bore or the aperture of printing nozzles, which would imprint specific patterns onto the extruded biomaterial fibres during printing. Printing nozzles which could generate surface concavities could also be useful, as several studies have indicated that mineralisation and bone tissue growth processes (cell adhesion, migration, morphology and spreading area) occur more readily on concave, rather than convex surfaces (393).

Cellular infiltration and colonisation of 3D porous scaffolds are influenced by many factors. Scaffold internal architecture has been shown to direct MSC migration (149) while pore sizes greater than 300 µm have also been shown to enhance vascularisation and osteogenesis *in vivo* (103). The multi-modal imaging methods employed in this study highlighted the influence of scaffold design and printing parameters on the fidelity and functionality of the fabricated construct (Figure 5-19, Figure 5-20 and Figure 5-21). µCT analyses of the PCL scaffolds demonstrated the importance of scaffold design in defining the overall and interconnected porosities, as well as the pore geometry of the fabricated construct (Table 5-1 and Table 5-2). The scaffold design could have been further improved by adopting *in silico* predictive analysis methods such as finite element analysis (387, 410) and mathematical homogenisation (411). Finite element analysis has been applied to µCT data to modulate the mechanical responses of 3D printed PCL-based scaffolds, showing good congruence with data obtained by conventional mechanical testing (412). Using this method, Ribeiro *et al* found that pore geometric configurations significantly affected the deformability of PCL scaffolds under compression (412). In this study, the sensitivity of µCT analysis was insufficient to identify a specific range within the grayscale spectrum that could isolate the adsorbed protein-PCL fibre interface layer from the applied coating layer and the PCL fibre itself. This resulted in the inclusion of the thickness of the adsorbed protein-PCL fibre interface layer in the average calculated thickness of the applied coating layer, and could account for the thinner (statistically non-significant) PCL fibres of aerosol-coated scaffolds.

µCT analysis indicated the total porosity of the PCL scaffolds was similar to trabecular bone (~50%). This improved permeability was achieved by altering the fill pattern and fibre orientation, which also created a greater external porosity. Although increasing porosity increases tissue regeneration, higher porosity is associated with decreasing mechanical functionality (387). A limitation of this study is the lack of mechanical validation of the functionality of the fabricated scaffolds, particularly if applied in load-bearing situations. Furthermore, studies performed by Olivares *et al* (387) and Melchels *et al* (389) indicated that pore size, shape and distribution are critical in the determination of mechanical stimuli and mechanical functionality of scaffolds. The constructs displayed gyroid or hexagonal pores (loaded in the transverse direction) facilitating improved fluid penetration and cell adhesion as a result of a larger surface area being subjected to mechanical stimuli. These findings were further corroborated by Bartnikowski *et al* who also observed that although scaffold architecture had a minimal effect on cell response in static culture, pore shape and architecture could induce osteogenic differentiation in perfusion culture through modifying fluid flow and therefore, the microfluidic shear forces exerted on adherent cells (413).

Interestingly, the aerosol coating process did not significantly affect the pore size or interconnectivity (Figure 5-20), indicating the robustness of the approach. Despite the differences in pore shape caused by the aerosol coating (Figure 5-19 and Figure 5-20), cell permeation was unaffected as indicated by the WST-1 results (Figure 5-28). Multi-modal imaging confirmed that the aerosol deposition method had not only improved cell deposition, but had also achieved a fairly well distributed surface coating (Figure 5-20). Aerosol-deposited STRO-1 enriched BMSCs were viable and functional (Figure 5-27 and Figure 5-29). These findings suggest the potential utility of this simple approach in clinical settings for surface coating and cell seeding of porous scaffolds manufactured by other AM methods. However, manual aerosol deposition has its limitations, as demonstrated by the imprecise and random distribution of bioinks and cells (a function of the dosing distance and air pressure applied) and its efficiency is operator-dependent (414). Another form of droplet jet deposition is inkjet printing, which could be used to improve the accuracy of surface coating and cell deposition and distribution as part of a layer-by-layer fabrication process. Nganga *et al* demonstrated the utility of inkjet printing in pattern-coating a fibre-reinforced, composite dental implant with an anti-microbial lactose-modified chitosan and silver nanoparticle layer (415). Additionally, as discussed in 1.5.3, the spatial patterning of cells and signalling factors can also be achieved by inkjet

deposition, where droplet volume and drop size can be controlled with picolitre and micrometre precision respectively by varying printing parameters (416). Although the viability of various cell types post-inkjet deposition has previously been shown to be more than 85% (340, 356, 417), printing resolution and the extent of cell viability (and functionality) post-inkjet printing are dependent on the printing parameters (see Table 5-4), the bioprinter, and the bioinks used.

Increase cell viability	Decrease cell viability
Increased nozzle diameter	Smaller droplet size
Decreased dispensing pressure	High impact velocity
Increased dosing distance	Prolonged printing times
Decreased substrate stiffness	Extremes in temperature
Decreased bioink viscosity (in general)	Increased bioink viscosity (In general)

Table 5-4 General printing parameters that determine cell viability in bioprinting.

Results obtained in 4.2.3.1 and 4.2.3.2 had shown the effects some of these parameters had on cell viability and functionality post-bioprinting. Adapted from (414) and (418).

WST-1 results in this study indicated STRO-1 enriched BMSC proliferation on 3D scaffolds was markedly reduced when low initial seeding numbers were used. Additionally, inhomogeneous cell distribution and reduced cell-cell interaction occur at low cell densities. However, increasing cell density in the bioink decreases the surface tension of the droplet and bioink viscosity (416). Increasing cell densities beyond a certain threshold could even prevent gelation (as the cells occupy a larger bioink volume fraction) and can cause an asymmetric cellular strain (416). Studies have shown that cell-laden bioinks optimised for inkjet bioprinting should have viscosities less than 10 mPa.s, and cell densities of less than one million cells per ml (416). Taking into consideration the findings above, optimisations to the current bioink compositions, cell seeding density, and printing parameters will need to be performed prior to future investigations into the feasibility of bioprinting by droplet jet deposition or other AM methods (see Table 5-5) of the biomimetic composite and cell-delivery bioinks developed in this study.

	Extrusion bioprinting	*Orifice-free bioprinting*		Inkjet bioprinting
		LIFT	**Acoustic**	
Cell density	High, cell spheroids	Medium (1 X 10^8 cells/ml)	Low (< 1.6 X 10^7 cells/ml)	Low (< 1 X 10^6 cells/ml)
Bioink viscosity (mPa.s)	30 X 10^7	1 – 300	1- 18	< 10
Resolution (µm)	200 – 1000	10 – 100	3 – 200	10 - 50
Single cell control	Medium	Medium	High	Low
Fabrication speed	Slow (10 µm/s to 700 mm/s)	Medium (200 to 1600 mm/s)	Fast (1 – 10000 droplets/second)	Fast (100000 droplets/second)
Cell viability	80 – 90%	>95%	89.8%	> 85%

Table 5-5 Bioink parameters for the most common types of bioprinting.

Adapted from (416).

5.2.5 Conclusions

Precision extrusion deposition was used to fabricate a PCL-based cylindrical scaffold with complex architecture and an interconnected porosity similar to that of trabecular bone. Aerosol deposition of a multi-material, biomimetic bioink was performed to improve the surface chemistry of untreated PCL scaffolds. The same method was successfully used to seed these scaffolds with STRO-1 enriched BMSCs, thereby generating a cell-biomatrix-scaffold construct. Despite the low cell densities used and the low proliferation rate of STRO-1 enriched BMSCs adherent on the PCL scaffolds, elevated ALP production and upregulation of OPN and OCN expression (which was most pronounced in coated cohorts cultured in osteogenic conditions) was observed. Multi-modal imaging revealed the high fidelity achieved by the 3DDiscovery bioprinter in reproducing the scaffold design, in addition to the ability of the aerosol deposition method to generate a fairly well distributed surface coating throughout the scaffold volume and to deliver STRO-1 enriched BMSCs with good viability and functionality. For the first time, confocal microscopy (reflectance mode and depth analysis) imaging was utilised to visualise surface topography and cell distribution in 3D, demonstrating the potential for ‘live’ monitoring of cell viability, migration, morphological changes and proliferation (rates) on 3D scaffolds. A note of caution applies to the fabricated PCL scaffold in this study – the printing parameters

used and their associated outcomes are specific to the 3DDiscovery bioprinter. While this may not preclude the same biomaterial or design from being fabricated by other AM methods such as selective laser sintering or filament deposition printing, outcomes may be different. There remains a need to ascertain the optimum scaffold design, cell type and density, bioink compositions and AM technique to achieve maximum printability as well as biological and mechanical functionality. However, these preliminary experiments suggest that applying the appropriate manufacturing approach(es) to fabricate different customised components (concomitantly) may enable the generation of an integrated, functional cell-scaffold construct which could potentially be used for bone reparation.

Chapter 6: Summation and future direction

6.1 Summary

Bone performs crucial physiological and structural functions in vertebrates, and is the only organ that undergoes regular remodelling of its hierarchical structure in response to mechanical stresses. This lifelong process is regulated by several mechanisms, which can be disrupted by a number of conditions, including trauma, pathology, and infection (Table 1-2). The regenerative ability of bone also declines with increasing age, resulting in inadequate self-repair and eventually, permanent defects, that can lead to a loss of function or the need for therapy. Although the current gold standard of treatment remains bone grafting, this approach has its drawbacks (Table 1-3). The limited functionality and life span of metal (alloy)-based implants used in dental and orthopaedic surgeries, coupled with recent reports of poor long-term osseointegration and possible systemic toxicities (241), have driven the urgent search for more effective, personalised therapies.

Bone tissue engineering is emerging as a promising approach to address some of these limitations in current clinical practice. The adoption of several AM techniques in bone tissue engineering has advanced both these fields of science, enabling the reproducible, yet customisable, fabrication of porous scaffolds that possess controlled geometries. Cell-free scaffolds, made from a wide range of biomaterials, have been employed in clinical settings for bone and osteochondral repair (32, 41). Poor osseointegration and tissue formation *in vivo* has seen an increasing trend over the past decade towards the incorporation of (stem) cells and bioactive factors to AM fabricated scaffolds to generate cell-scaffold-biomolecule constructs, a process termed as biofabrication (40). This approach affords the potential to precisely, and spatially, seed cells and bioactive factors in a user-defined manner, with the main aim of enhancing the osteoinductive and osteogenic capacities of the construct in directing cell differentiation and host tissue invasion. Laser-assisted, extrusion, and inkjet printing are the most common AM methods used in bone tissue engineering today (36).

Despite advances in AM and imaging technologies, current biofabricated constructs lack upscalability and *in vivo* functionality. A key limiting step is the failure to vascularise the construct, which causes tissue necrosis *in vivo* and therefore, implant failure. Slow progress towards clinical translation stems from a limited understanding of bone repair, cell behaviour in 3D culture, and the complex *in vivo*

interplay between host tissue, mechanical stimuli and cell-seeded biomaterials. The lack of standardisation of the methods and analysis approaches used in bone biofabrication studies further hampers the reproducibility and the comparison of study outcomes, as results obtained are specific to the customised bioprinters used to perform the majority of these studies. This key issue was illustrated by a recent multi-centre analysis, which found a poor correlation between *in vitro* and expected *in vivo* outcomes for biomaterials used in bone regeneration studies (419). In lieu of these problems, and to further facilitate the reproducibility of this study, established assays and imaging methods were employed (where possible) to analyse scaffold properties as well as cell viability and functionality. A commercially available bioprinter, the 3DDiscovery, was used to fabricate scaffolds. The advantages and disadvantages of the bioprinter are listed in Table 6-1.

Advantages	• High printing resolution (up to ~10 µm) • Multi-modal 3D printing capability (precision extrusion, pneumatic pressure, droplet jetting deposition, microcontact), with UV photocrosslinking available • Multiple nozzle diameter options • Wide viscosity range of bioinks printable • Temperature control available • Cell agitator available to prevent cell sedimentation during bioprinting • Possible automated mass printing of 3D constructs
Disadvantages	• Limited achievable construct size and upscalability - Fixed volumes of bioink (maximum of 10 ml per printhead) necessitating batch production of bioinks and sterile storage facilities - Fixed print stage size • Unknown bioink volume dispensed, dependent on printing parameters • Slow printhead interchange during multi-bioink printing • Complex set-up, operation and maintenance, not user-friendly - High cost (software options, equipment and maintenance) - Limited design software with restricted licence and cross-platform file type compatibility - Multiple fragile components with high damage probability - No online technical guide or troubleshooting resources

Table 6-1 Factors to consider prior to utilising the 3DDiscovery bioprinter for biofabrication.

The cell source employed in bone tissue engineering is crucial. Several cell sources have been investigated for bone tissue engineering (Table 1-9), with bone marrow-derived stem cells studied the most due to their inherent osteogenicity and ready availability. Few studies have investigated the efficacy of SSCs for bone

regeneration despite work by Robey *et al*, which indicated that although mature osteogenic cells could regenerate new bone tissue, SSCs must be present for bone turnover to occur (114). A significant drawback to utilising SSCs is their rarity, which requires *ex vivo* expansion to create sufficient numbers for use in regenerative therapies. Biofabrication studies typically use cell densities of 10^6 – 10^7 cells per ml to enhance tissue morphogenesis and function. However, high cell densities can obscure cell proliferation and migration patterns, changes in cell morphology, and may even be detrimental to cell viability in cases where there is an inadequate perfusion or vascularisation of a cell-seeded construct. Given a lack of consensus as to the optimal or minimum cell density threshold, or cell source, for use in treating critical-sized bone defects, this study focused on evaluating the suitability of utilising human SSCs for osteogenesis. An established STRO-1 isolation protocol (115) was used to enrich the population of SSCs in bone marrow obtained from patients undergoing hip arthroplasty. As human SSCs have been shown to lose their *in vivo* osteogenic ability during cell culture and passage (210), cells from passage 1 or 2 were used, which restricted the cell densities achievable per scaffold. Nevertheless, seeded STRO-1 enriched BMSCs consistently demonstrated rapid substrate adhesion, elevated ALP production, and increased osteogenic gene expression over time when cultured on TCP under 1,25-VitD3 stimulation, and on laser-generated microporous, micro-rough titanium templates under basal conditions. The latter observation highlighted the critical influence of surface properties on cellular responses, with the surface chemistry of titanium found to be affected by different methods of sterilisation and storage. These findings were in spite of the low cell seeding densities employed (1.5 X 10^4 cells per substrate), the low proliferative rate of STRO-1 enriched BMSCs in 3D culture, and the inherent biological variation among patient responses to 1,25-VitD3 stimulation (Figure 3-6 and Figure 3-7).

While the cell densities employed in this study were not optimal, it allowed for the observation of cell distribution and spreading behaviour in 3D matrices. No studies have examined the effect of cell density on STRO-1 enriched BMSCs that were fully encapsulated within a hydrogel matrix. Previous studies had indicated that different optimal cell density ranges exist for different cell types and 3D matrix compositions in promoting protein production, cell proliferation and differentiation (150, 361). Other studies indicated a cell type- (and possibly even cell passage-) dependent plateau effect on culture maturation exists, whereby further increments in cell density no longer stimulated proliferation or differentiation (365). Additionally, increasing cell density results in lower bioink viscosity and a propensity for cells to

redistribute in areas of fibre intersection, resulting in cell-free areas along the deposited fibres (409). In this study, cell-cell interaction was shown to be markedly reduced at low cell densities ($<10^5$ cells), although cell cluster formation was observed among the encapsulated cells that were in closer proximity, and as cell density increased. Encapsulated cells remained viable but retained rounded morphologies. However, as hydrogel viscosity increased and degradation rate decreased, cell viability reduced over time. Interestingly, the degradation kinetics of alginate-based hydrogels were found to be dependent on the crosslinking approach applied and ionic conditions of the culture media. When hydrogel degradation was rapid (as with 4% w/v low viscosity alginate and various gelatin-based hydrogels), encapsulated STRO-1 enriched BMSCs recovered their proliferative and migratory abilities (Figure 4-10 and Figure 4-11). Maia *et al* had also found that human MSCs entrapped within RGD-alginate hydrogels were in a non-proliferative state, but recovered their functionality when retrieved from the 3D matrices (361).

The method for cell delivery also directly affects cell distribution and cell-cell interactions on scaffolds. Conventional seeding methods often result in a focal, but uneven, distribution of cells, which could potentially lead to poor osseointegration *in vivo*. This problem was illustrated by limited STRO-1 enriched BMSC migration on hydrophobic titanium surfaces, which left exposed areas on the titanium surface. Conventional seeding methods also produce large droplet sizes, which can reduce bioink permeability even in porous scaffolds. The ability of laser-assisted and inkjet printing to deliver cells with high viability and functionality, in addition to biological components in a controlled fashion with spatial accuracy, might help overcome the limitations of manual cell seeding methods (84, 85, 288). However, choices remain limited for effective, bioprintable bioinks as matching the bioink characteristics with the physicochemical demands of the biofabrication process (the 'biofabrication window') remains a challenge (84, 135, 338). In addition, the choice of AM method directly influences the choice of biomaterials, and thus, the bioink (Figure 4-12). The droplet jetting mode of the 3DDiscovery bioprinter was used to bioprint STRO-1 enriched BMSC-laden bioinks with reproducibility. In inkjet bioprinting, the bioink rheology, orifice diameter, droplet volume and jetting velocity determine the level of shear strain, while inertial forces exerted by pressure and substrate impact further contribute to cell damage. These bioprinted cells did not proliferate or show any morphological changes after 7 days in culture despite the rapid dissolution of the hydrogel formed (Figure 4-17). Static cell behaviour post-bioprinting suggests that

mechanical forces applied to the cell-laden bioink could contribute to a delayed recovery and functionality of encapsulated STRO-1 enriched BMSCs.

Work by Blaeser *et al* indicated that MSC survival and functionality were only affected when a stress threshold was exceeded during the bioprinting process (364). Work by Chang *et al* suggested that bioprinted cells show three possible responses to damage: 1) survival with the desired phenotype and capable of proliferation, 2) survival but quiescent (as in this study), or 3) necrosis. Additionally, bioprinted cells in a quiescent state also demonstrated three additional behaviours as time passed: 1) recovery of original capability, 2) phenotypic change or dedifferentiation, or 3) cell apoptosis. Cell recovery from mechanically induced damage was observed in their study (which utilised solid freeform fabrication to bioprint hepatocytes) to occur within 24 hours post-bioprinting, with no significant improvement thereafter (418). The authors noted that different printing parameters might not equally contribute to cell viability and recovery post-bioprinting. These findings, taken in conjunction with the results of this study, elude to the need to better elucidate the interactions between different cell types and biomaterials, the optimal initial cell density and bioink viscoelasticity, as well as printing time and conditions, in order to optimise future AM approaches for engineering tissues.

Although 3% w/v low viscosity alginate and the ECM-mimetic composite bioink (consisting of alginate, fibrinogen, fibronectin, HA, collagen and HS) possess sufficient viscosity for droplet jetting, their low viscosities preclude the construction of a clinically relevant-sized construct. While rheometric calibrations could be used to guide the adjustment of bioink composition to match both printing requirements and the generation of upscalable constructs, some studies have also shown the proliferation and migration of encapsulated cells to be hindered by increasing 3D matrix stiffness (360, 361). As such, the use of hydrogels as a stand-alone, cell-laden scaffold for bone tissue engineering is limited, given that several studies have indicated that a bone tissue scaffold should ideally possess surface properties and adequate interconnected porosity to not only support cell growth and differentiation, but also a structural integrity that can support and transmit forces to the host tissue and seeded cells. Therefore, the choice of biomaterial plays a key role in scaffold fabrication. In this study, the choice of biomaterial was restricted to those suitable for extrusion and jet deposition printing. PCL was chosen as the base biomaterial for scaffold fabrication as its low glass transition temperature of -60°C, and a melt temperature of 59 – 64°C, are properties that suit the precision extrusion deposition fabrication of a scaffold with controllable, interconnected porosity. PCL has a proven

in vitro and *in vivo* cytocompatibility, controlled biodegradation, and appropriate mechanical properties for use in bone tissue engineering (Figure 5-3) (372). .

Scaffold and pore architectures have been shown to play vital roles in cell adhesion and seeding efficiency, cell viability, osseointegration, and mechanical functionality of cell-seeded constructs (367). Due to time and logistical constraints affecting the availability of the bioprinter, efforts were focused on optimising scaffold design and maximising production. The lack of cross-platform compatibility of the BioCAD software precluded the utilisation of finite element analysis to optimise the scaffold design. Instead, µCT, SEM and confocal microscopy assessments of the fidelity of fabrication to the designed geometries and the interconnected porosities achieved (through altering the geometric design) guided the evolution of the scaffold design. µCT analyses confirmed the consistency of the fabrication process, with final constructs showing a only 6% mean variation in fibre thickness. The porosity of 3D printed PCL constructs could be affected by printing parameters that control the deposited fibre size – the feed rate, extrusion screw speed, printing pressure and nozzle diameter were reported to have the most impact (391, 392). In this study, changes to these printing parameters had no effect on deposited fibre size. Instead, adjustments to the scaffold geometry and fill pattern resulted in a 14% increase in mean interconnected porosity, while the mean interconnected pore volume rose from 60.1 to 92.6 mm^3 (Table 5-1 and Table 5-2), indicating their key role in defining the interconnected porosity of precision extrusion deposition-fabricated scaffolds. As increasing construct porosity has been associated with poorer mechanical integrity (368), mechanical testing of the different fabricated constructs is necessary in order to identify the most appropriate design to develop further.

The inherent hydrophobicity of PCL resulted in poor STRO-1 enriched BMSC adhesion. Air trapping within the complex pore geometries, coupled with the large surface area of the cell-laden droplet and the high surface tension of the scaffold, further reduced cell seeding efficiency in the prototype PCL constructs. In addition, the bioinert nature of PCL and alginate limits their capability in aiding host tissue invasion and osteogenic differentiation of seeded cells. These issues were resolved in this study by the application of a simple aerosol deposition method to generate an *in situ* precipitated, ECM-mimetic, surface coating of the PCL scaffolds, as well as deliver STRO-1 enriched BMSCs encapsulated in a gelatin-HA-thrombin bioink with high viability. In spite of the limited accuracy and achievable control of the aerosol deposition approach, the widespread (albeit random) distribution of the ECM-mimetic coating and encapsulated STRO-1 enriched BMSCs were illustrated

by multi-modal imaging. Differences in pore shape were observed (Video 5-4), but the aerosol coating process did not significantly affect pore size or interconnectivity (Table 5-2). The poor cell seeding efficiency observed was due to the high scaffold porosity and the limited accuracy of the aerosol deposition method.

Despite low cell densities, and the low proliferative rate of STRO-1 enriched BMSCs adherent on the PCL scaffolds, elevated ALP production and upregulation of OPN and OCN expression were observed in non-coated and aerosol-coated PCL scaffold cohorts (Figure 5-27, Figure 5-28 and Figure 5-29). These findings suggest that the GHA bioink facilitated cell adhesion in addition to inducing early osteogenic differentiation (as observed in both the TCP GHA cohorts). Greater OPN and OCN upregulation in the aerosol-coated cohort cultured in osteogenic media suggested the ECM-mimetic coating enhanced the osteoinductive effect of 1,25-VitD3, thereby demonstrating a similar functionality to native ECM. These findings confirm the crucial role of surface composition in enabling cellular interaction with biomaterials, which can affect the performance of an implant *in vivo* (241). Concentrations of each component will need to be adjusted in order to enhance the speed and strength of coating, improve the stimulatory effect for different cell types (and/or tissues), as well as the fabrication of functional graded scaffolds. Inkjet bioprinting might improve the accuracy of the distribution of surface coating and cells, as part of a layer-by-layer fabrication. Preliminary findings from this study indicate that by minimising the jetting pressure and reducing the bioink viscosity, cell viability in inkjet bioprinting could be improved. Optimisations to the cell density and printing parameters will also be needed prior to future investigations into the feasibility of droplet jet printing (or other AM methods) of the ECM-mimetic and cell-delivery bioinks developed in this study (Table 5-4 and Table 5-5).

The contrasting organisation and morphologies of STRO-1 enriched BMSCs adherent on the different surface topographies of the PCL scaffolds (and on laser-generated, microporous, micro-rough titanium) indicated that surface roughness, curvature, and skewness influence cell adhesion and cell behaviour on 3D matrices. Confocal microscopy (reflectance mode) showed the surface topography of PCL scaffolds manufactured by precision extrusion deposition was influenced by the complexity of the fill pattern, fibre orientation, and in particular, the rate of material cooling (Figure 5-6 and Figure 5-18). This observation suggests that customised surface topographies could help to enhance scaffold adsorption of bioactive agents, improve cell adhesion, or even direct cell migration and differentiation. Further studies are needed to determine the optimal surface features for such purposes.

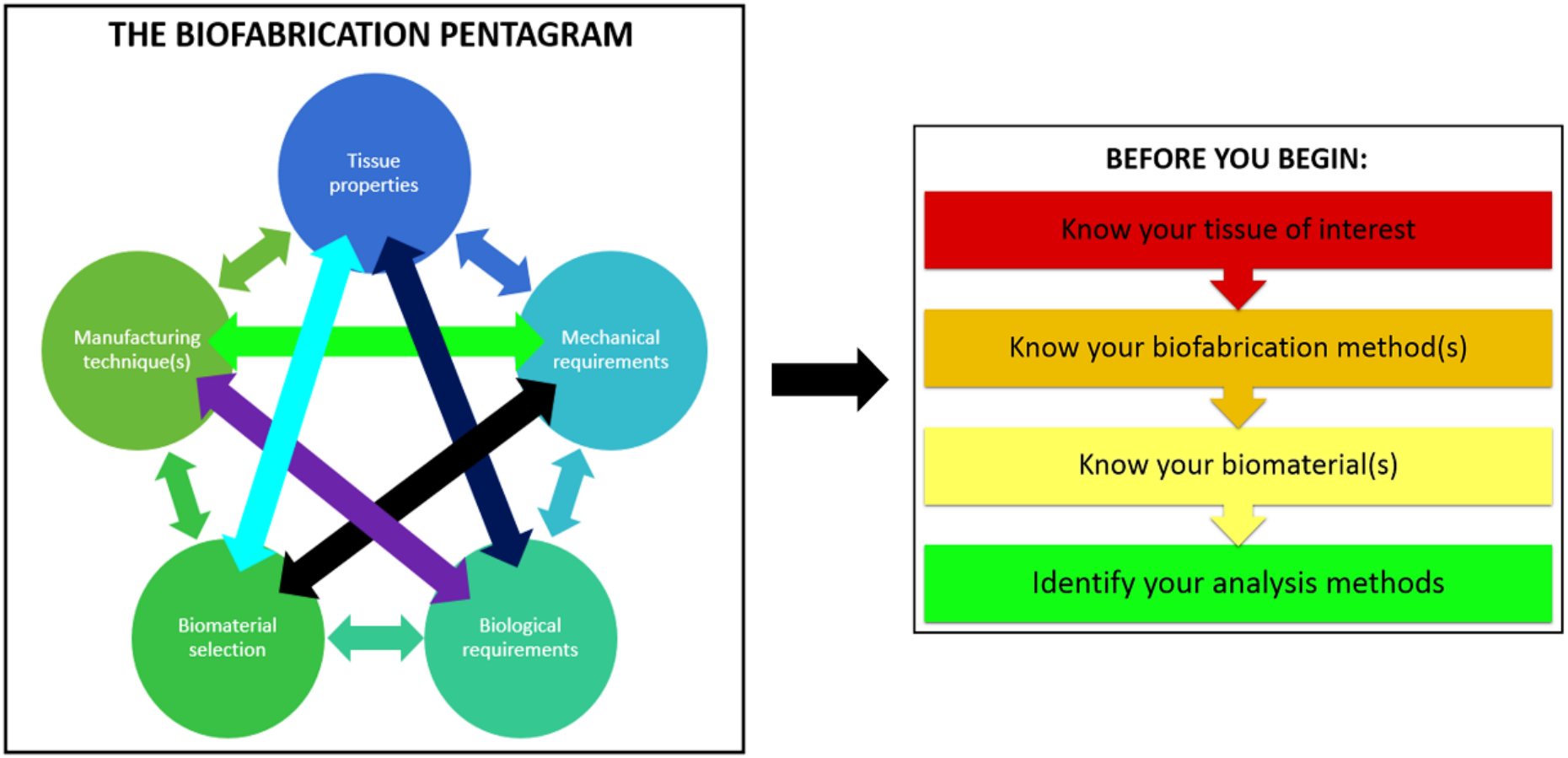

Figure 6-1 Practical rules of engagement for biofabrication.

As Figure 6-1 illustrates, understanding the complex interplay between cells, biomaterials and manufacturing techniques is fundamental for successful bone biofabrication. Existing *in silico* analysis and multi-modal imaging methods will not only aid in this endeavour, but these approaches must also be incorporated into future experimental set-ups to better enable the standardisation of methodology and the comparison of results. Advancements in these fields will only serve to expedite developments within tissue engineering. Further investigations to elucidate the optimal AM methods (and printing parameters) for each tissue type are needed, as biofabrication outcomes are AM technique-specific. Although optimisations to cell density, bioink composition, printing parameters and scaffold architecture are still required, the preliminary findings of this study suggest it is feasible to fabricate an integrated cell-scaffold for bone repair by using STRO-1 enriched BMSCs, existing biomaterials and AM methods. As discussed, *in vitro* 'successes' must be tempered with the need to also evaluate the *in vivo* performance of biofabricated constructs (followed by refinements and additional re-evaluations as indicated) before these devices can be employed in the clinical setting.

6.2 Future perspectives: through the looking glass

Since the start of 2018, there have been over 2300 publications on bone tissue engineering. Yet only eighteen involve bone or cartilage biofabrication. Despite the vast array of literature, there remains no consensus as to the optimal scaffold architecture, cell type, seeding density, biomaterial(s) or bioactive factors for use in bone tissue engineering. Methods for manufacturing and analysis have also been somewhat arbitrary. The multi-disciplinary nature of biofabrication adds to the complexity of engineering bone constructs in a reproducible manner that meets the required biological and mechanical performance, while satisfying the regulatory standards for clinical translation and commercialisation (32).

Several approaches are being investigated to develop the optimal scaffold for bone repair, from the use of multi-material composite scaffolds (407, 420), to the generation of 'smart scaffolds' that incorporate biomimetic components such as nanoparticles, drugs, growth factors, and more recently, bioactive synthetic peptides (see Table 6-2) for enhancing the osteogenic (and/or chondrogenic) and angiogenic capabilities of the construct (402). Matching the mechanical properties of a construct to that of native bone can be potentially achieved by judicious scaffold design and the appropriate combination of biomaterials. In the interim, scaffold and bioink developments will drive the creation of 'off the shelf' medical devices or

treatments for use in clinical situations such as fracture stabilisation and/or accelerated healing following traumatic or pathological fractures. Progress in these areas will enable the concomitant improvement in the efficacy of existing medical and dental implants, while providing an economically viable model until such a time that bone biofabrication becomes more cost-effective and widely available.

Synthetic peptide sequence	Equivalent molecule
REDRV, LDV	Fibronectin
DGEA, GFOGER, ^{766}GTPGPQGIAGQRGVV^{780}	Collagen type I
GLRSKSKKFRRPDIQYPDATDEDITSHM	Osteopontin
FHRRIKA	Bone sialoprotein
KIPKASSVPTELSAISTLYL	BMP-2
^{105}YKRSRYT^{111}, ^{119}KRTGQYKLGSKTGPGQK^{135}	FGF-2
YIGSR, IKVAV	Laminin
RGD	Integrin-binding proteins

Table 6-2 Synthetic peptides that could be used as alternative agents for enhancing osteogenesis and cell adhesion.

Adapted from (402).

Bone regenerative therapies have yet to achieve clinical translation because bone healing and remodelling processes remain poorly understood. The inherent biological variation of patient responses to osteogenic stimulation complicates the predictability of tissue formation. Research into these processes would be aided by providing specific access to donor medical and drug histories, which would allow researchers to better define the influential variables that could reduce the efficacy and efficiency of biofabrication. Biofabricated bone could serve as representative models that allow the *in vitro* and *ex vivo* study of normal bone development as well as bone pathologies, in addition to providing a potentially suitable environment to investigate the haematological stem cell niche and haematopoiesis. At present, limited information regarding therapeutic progress can be gathered from end point analyses using standard histological approaches and microscopy-based imaging (181). The recent development of particle-based monitoring or imaging and regenerative agents for real-time tracking of stem cells and angiogenesis, assessment of scaffold integrity and functional changes, and the potential for the

Agent	Shape	Synthesis methods	Biocompatibility	Imaging modalities	Common Applications	Disadvantages
AuNPs	Wide range and choice depends on application	Spheres: citrate reduction and Brust-Schiffrin Cages: galvanic replacement Rods: use of capping agents (i.e. CTAB)[38,192]	High: bioinert, cytocompatible and nontoxic in short-term studies. Concerns with long-term effects[147]	X-ray/CT, PA imaging, and optical imaging	Cell tracking using PA imaging, drug or biomolecule delivery	High cost and non-degradable leading to long-term toxicity, clearance issues, contrast agent transfer
IONPs	Mainly spherical	Chemical co-precipitation, sol–gel reaction, precipitation in microemulsions Hydrothermal reaction, pyrolysis[60]	High: when coated with polymers and polysaccharides (e.g. dextran), some types have FDA-approval[187]	MRI, combined MRI-nuclear imaging, magneto-motive	Cell tracking and transport, gene delivery, magnetic scaffolds	Negative MRI contrast, contrast agent transfer, high cost and time consuming MRI
CNTs	Single or multiple walled tubes	Chemical vapor deposition, arc-discharge, laser[65]	Medium: upon appropriate functionalization. Concerns over non-degradability[55,65]	Optical imaging, MRI, and PET	Scaffold enhancers, cell tracking	Can affect SC proliferation and differentiation, do not degrade
SINPs/MSNs	Spheres, hexagonal cylinders	Stöber Method, reverse microemulsion, evaporation-induced self-assembly[171]	High: low cytotoxicity for nano-sized particles	US and PET, MRI, or fluorescence by addition of contrast agents	Scaffold enhancers, drug delivery	Large size, potential to leak, additional contrast agents necessary for alternative imaging methods
PFCps	Nano or micron sized spheres	Emulsion techniques, microfluidics[45,190]	High: PFCs are inert and are rapidly cleared[150,190]	US, MRI, PA imaging	Drug, gene or gas delivery	Short lifetimes, large size of micro particles

Table 6-3 Summary of the characteristics and applications of monitoring or imaging and regenerative agents.

Reproduced from (196). Abbreviations: AuNPs = Gold nanoparticles, IONPs = iron oxide nanoparticles, CNTs = carbon nanotubes, SINPs/MSNs = silica-based particles, PFCps = perfluorocarbon particles, PA = photoacoustic imaging, US = ultrasound.

concurrent delivery of therapeutic agents is exciting. Table 6-3 summarises the characteristics and current applications of these agents (196). An added benefit of these novel agents is the ability to perform non-invasive, *in vivo* monitoring using existing clinical diagnostic modalities such as MRI, CT, PET, ultrasound and photoacoustic imaging. Adopting such an approach would help reduce the number of animals required per pre-clinical study, while enabling the serial comparison of treatment responses over time. However, access to specialist veterinary and *in vivo* imaging facilities would be required (especially for large animal studies), which might not be widely available and are expensive to perform.

Pre-operative imaging already aids the fabrication of patient-specific surgical implants (369). Guided implant surgery protocols (421) have employed AM methods to produce 3D models of the surgical area, as well as surgical splints and cutting guides as part of the virtual surgical planning process (particularly useful in cases requiring reconstructive surgery) to map out the best surgical route and ensure a good fit of the replacement implant (422). As such, biofabricated bone will be ideally suited for use in elective orthopaedic repair or replacement surgeries. Cell isolation and the fabrication of customised integrated constructs, with an in-built perfusion channel system, could be performed in advance of the planned surgery, enabling the optimisation of the constructs prior to implantation. It may be necessary to use bioreactors (for perfusion and biophysical stimulation) (93, 423, 424) and a 'part assembly' approach to achieve upscalability and generate a viable and functional biphasic integrated construct for the repair of larger defects.

Robotic automation of production and assembly phases would facilitate the possibility for upscalability and meet Good Manufacturing Practice standards (43). This approach is already utilised in automotive and pharmaceutical industries for mass production. The increasing efficacy of robotic surgery indicates the potential for precise user- or computer-controlled actions in 3D. Adapting such equipment for simultaneous multi-modal bioprinting and part assembly could enhance the flexibility and productivity of current bioprinter systems. The use of open-source design and bioprinting software would provide cross-platform compatibility and accelerate the progression and standardisation of methods within the community (245). Figure 6-2 shows a potential workflow for automated biofabrication. Although biofabrication techniques are still in its infancy, it is not inconceivable that customised, integrated osteochondral grafts, with properties more akin to native tissues than current medical implants, can be fabricated in the next few decades (369, 425).

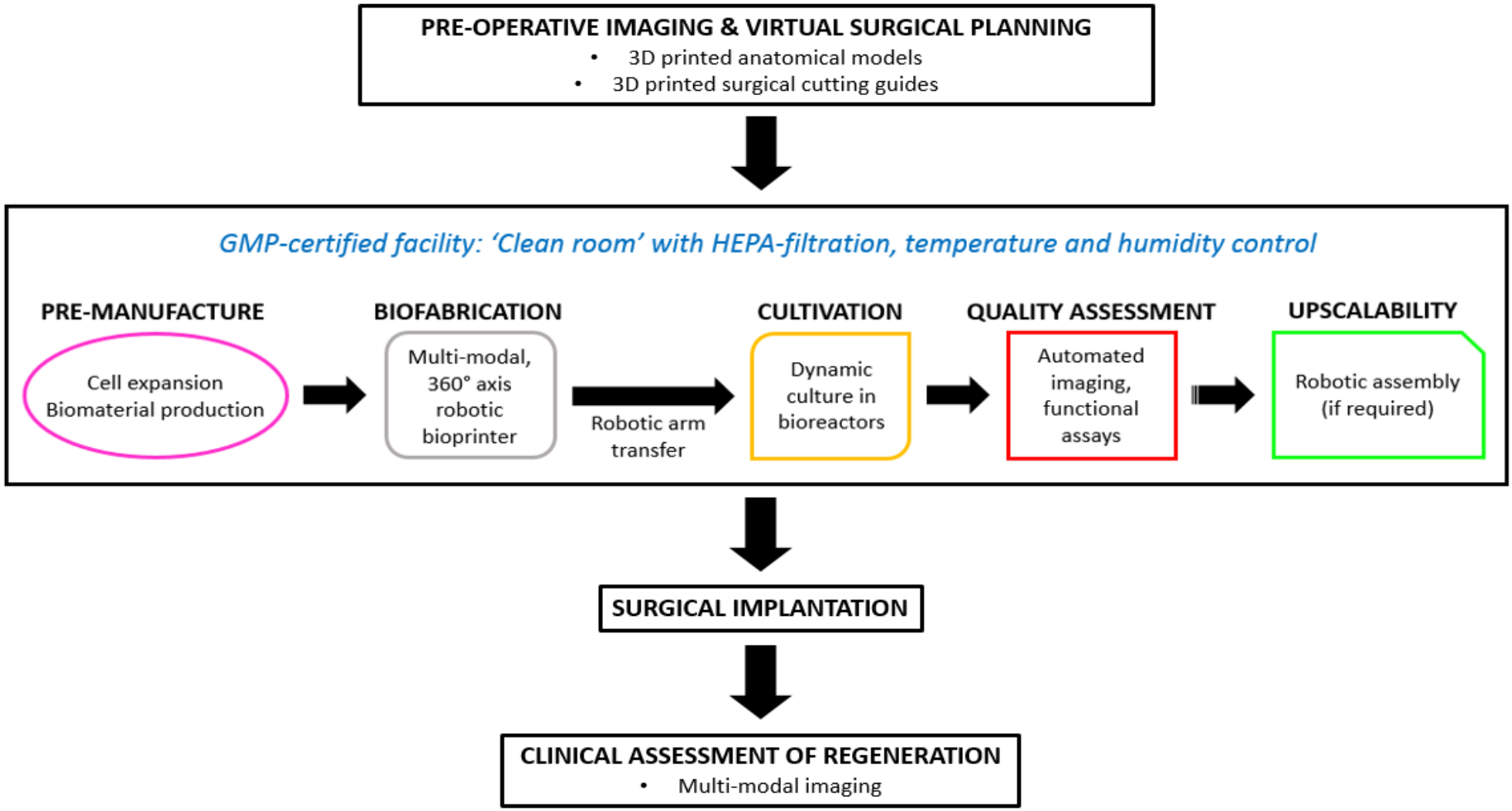

Figure 6-2 Potential pre- and post-biofabrication phases where automation could be applied to improve productivity.

References

1. Mescher A. Junqueira's Basic Histology: Text and Atlas. 12th ed: McGraw-Hill; 2009.

2. Tortora G, Nielsen M. Principles of Human Anatomy. 13th ed: Wiley; 2014. 984 p.

3. Turnbull G, Clarke J, Picard F, Riches P, Jia L, Han F, et al. 3D bioactive composite scaffolds for bone tissue engineering. Bioact Mater. 2018;3(3):278-314.

4. Rosen C, Bouillon R, Compston J, Rosen V. Primer on the Metabolic Bone Diseases and Disorders of Mineral Metabolism. 8th ed: Wiley; 2013. 1078 p.

5. Zimmermann E, Busse B, Ritchie R. The fracture mechanics of human bone: influence of disease and treatment. Bonekey Rep. 2015;4:743.

6. Henkel J, Woodruff M, Epari D, Steck R, Glatt V, Dickinson I, et al. Bone Regeneration Based on Tissue Engineering Conceptions — A 21st Century Perspective. Bone Res. 2013;1(3):216-48.

7. Wolfram U, Schwiedrzik J. Post-yield and failure properties of cortical bone. Bonekey Rep. 2016;5:829.

8. Lee H, Minematsu H, Kim K, Celil Aydemir A, Shin M, Nizami S, et al. Actin and ERK1/2-CEBPbeta signaling mediates phagocytosis-induced innate immune response of osteoprogenitor cells. Biomaterials. 2011;32(35):9197-206.

9. Aubin J. Mesenchymal Stem Cells and Osteoblast Differentiation. In: Bilezkian J, Raisz L, Martin T, editors. Principles of Bone Biology. 1. Third ed: Academic Press; 2008. p. 85-107.

10. Friedenstein A, Piatetzky-Shapiro I, Petrakova K. Osteogenesis in transplants of bone marrow cells. J Embryol Exp Morph. 1966;16:381-90.

11. Long M, Robinson J, Ashcraft E, Mann K. Regulation of human bone marrow-derived osteoprogenitor cells by osteogenic growth factors. J Clin Invest. 1995;95:881-87.

12. Modder U, Khosla S. Skeletal stem/osteoprogenitor cells: current concepts, alternate hypotheses, and relationship to the bone remodeling compartment. J Cell Biochem. 2008;103(2):393-400.

13. Purpura K, Zandstra P, Aubin J. Fluorescence activated cell sorting reveals heterogeneous and cell non-autonomous osteoprogenitor differentiation in fetal rat calvaria cell populations. J Cell Biochem. 2003;90(1):109-20.

14. Bianco P. Stem cells and bone: A historical perspective. Bone. 2015;70:2-9.

15. Bianco P, Riminucci M, Gronthos S, Robey P. Bone marrow stromal stem cells: nature, biology, and potential applications. Stem Cells. 2001;19(3):180-92.

16. Salazar V, Gamer L, Rosen V. BMP signalling in skeletal development, disease and repair. Nat Rev Endocrinol. 2016;12(4):203-21.

17. Crockett J, Rogers M, Coxon F, Hocking L, Helfrich M. Bone remodelling at a glance. J Cell Sci. 2011;124(7):991-98.

18. Itzstein C, Coxon F, Rogers M. The regulation of osteoclast function and bone resorption by small GTPases. Small GTPases. 2011;2(3):117-30.

19. Bonewald L. The amazing osteocyte. J Bone Miner Res. 2011;26(2):229-38.

20. Goggin P, Zygalakis K, Oreffo R, Schneider P. High-resolution 3D imaging of osteocytes and computational modelling in mechanobiology: insights on bone development, ageing, health and disease. Eur Cell Mater. 2016;31:264-95.

21. Zhang K, Barragan-Adjemian C, Ye L, Kotha S, Dallas M, Lu Y, et al. E11/gp38 selective expression in osteocytes: regulation by mechanical strain and role in dendrite elongation. Mol Cell Biol. 2006;26(12):4539-52.

22. Long F. Building strong bones: molecular regulation of the osteoblast lineage. Nat Rev Mol Cell Biol. 2012;13(1):27-38.

23. Loi F, Cordova L, Pajarinen J, Lin T, Yao Z, Goodman S. Inflammation, fracture and bone repair. Bone. 2016;86:119-30.

24. Einhorn T, Gerstenfeld L. Fracture healing: mechanisms and interventions. Nat Rev Rheumatol. 2015;11(1):45-54.

25. Zaidi M. Skeletal remodeling in health and disease. Nat Med. 2007;13(7):791-801.

26. Tang D, Tare R, Yang L-Y, Williams D, Ou K-L, Oreffo R. Biofabrication of bone tissue: approaches, challenges and translation for bone regeneration. Biomaterials. 2016;83:363-82.

27. Siddiqui J, Partridge N. Physiological Bone Remodeling: Systemic Regulation and Growth Factor Involvement. Physiology. 2016;31(3):233-45.

28. Delaisse J. The reversal phase of the bone-remodeling cycle: cellular prerequisites for coupling resorption and formation. Bonekey Rep. 2014;3:561.

29. Nguyen D, Burg K. Bone tissue engineering and regenerative medicine: Targeting pathological fractures. J Biomed Mater Res A. 2015;103A:420-29.

30. Boskey A. Bone composition: relationship to bone fragility and antiosteoporotic drug effects. Bonekey Rep. 2013;2.

31. Gibon E, Lu L, Goodman S. Aging, inflammation, stem cells, and bone healing. Stem Cell Res Ther. 2016;7:44.

32. Gibbs D, Vaezi M, Yang S, Oreffo R. Hope versus hype: what can additive manufacturing realistically offer trauma and orthopedic surgery? Regen Med. 2014;9(4):535-49.

33. Oryan A, Alidadi S, Moshiri A, Maffuli N. Bone regenerative medicine: classic options, novel strategies, and future directions. J Ortho Surg Res. 2014;9(18).

34. Brydone A, Meek D, Maclaine S. Bone grafting, orthopaedic biomaterials, and the clinical need for bone engineering. Proc Inst Mech Eng Part H - J Eng Med. 2010;224(12):1329-43.

35. Langer R, Vacanti J. Tissue Engineering. Science. 1993;260:920-26.

36. Kundu J, Pati F, Shim J-H, Cho D-W. Rapid prototyping technology for bone regeneration. In: Narayan R, editor. Rapid Prototyping of Biomaterials - Principles and Applications: Woodhead Publishing; 2014. p. 254-84.

37. Bose S, Roy M, Bandyopadhyay A. Recent advances in bone tissue engineering scaffolds. Trends Biotechnol. 2012;30(10):546-54.

38. Ferris C, Gilmore K, Wallace G, in het Panhuis M. Biofabrication: an overview of the approaches used for printing of living cells. App Microbiol Biotechnol. 2013;97(10):4243-58.

39. Tasoglu S, Demirci U. Bioprinting for stem cell research. Trends Biotechnol. 2013;31(1):10-9.

40. Mironov V, Trusk T, Kasyanov V, Little S, Swaja R, Markwald R. Biofabrication: a 21st century manufacturing paradigm. Biofabrication. 2009;1(2):022001.

41. Derby B. Printing and Prototyping of Tissues and Scaffolds. Science. 2012;338(6109):921-26.

42. Hutmacher D, Cool S. Concepts of scaffold-based tissue engineering-the rationale to use solid free-form fabrication techniques. J Cell Mol Med. 2007;11(4):654-69.

43. Melchels F, Domingos M, Klein T, Malda J, Bartolo P, Hutmacher D. Additive manufacturing of tissues and organs. Prog Polymer Sci. 2012;37(8):1079-104.

44. Brown J, Kumbar S, Laurencin C. Chapter II.6.7 - Bone Tissue Engineering. In: Ratner B, Hoffman A, Schoen F, Lemons J, editors. Biomaterials Science. 3rd ed: Academic Press; 2012. p. 1194-214.

45. Peltola S, Melchels F, Grijpma D, Kellomaki M. A review of rapid prototyping techniques for tissue engineering purposes. Ann Med. 2008;40(4):268-80.

46. Guillotin B, Souquet A, Catros S, Duocastella M, Pippenger B, Bellance S, et al. Laser assisted bioprinting of engineered tissue with high cell density and microscale organization. Biomaterials. 2010;31(28):7250-56.

47. Schiele N, Corr D, Huang Y, Raof N, Xie Y, Chrisey D. Laser-based direct-write techniques for cell printing. Biofabrication. 2010;2(3):032001.

48. Guillotin B, Guillemot F. Cell patterning technologies for organotypic tissue fabrication. Trends Biotechnol. 2011;29(4):183-90.

49. Fedorovich N, Schuurman W, Wijnberg H, Prins H, van Weeren P, Malda J, et al. Biofabrication of osteochondral tissue equivalents by printing topologically defined, cell-laden hydrogel scaffolds. Tissue Eng Part C Methods. 2012;18(1):33-44.

50. Fedorovich N, Wijnberg H, Dhert W, Alblas J. Distinct tissue formation by heterogeneous printing of osteo- and endothelial progenitor cells. Tissue Eng Part A. 2011;17(15-16):2113-21.

51. Shim J-H, Lee J-S, Kim J, Cho D-W. Bioprinting of a mechanically enhanced three-dimensional dual cell-laden construct for osteochondral tissue engineering using a multi-head tissue/organ building system. J Micromech Microeng. 2012;22(8):085014.

52. Khatiwala C, Law R, Shepherd B, Dorfman S, Csete M. 3D Cell Bioprinting For Regenerative Medicine Research And Therapies. Gene Ther Reg. 2012;07(01):1230004.

53. Bose S, Vahabzadeh S, Bandyopadhyay A. Bone tissue engineering using 3D printing. Mater Today. 2013;16(12):496-504.

54. O'Brien C, Holmes B, Faucett S, Zhang L. Three-Dimensional Printing of Nanomaterial Scaffolds for Complex Tissue Regeneration. Tissue Eng Part B Rev. 2014;21:103-14.

55. Tarafder S, Lee CH. 3D printing integrated with controlled delivery for musculoskeletal tissue engineering. J 3D Printing in Medicine. 2017;1:181-89.

56. Martin V, Bettencourt A. Bone regeneration: Biomaterials as local delivery systems with improved osteoinductive properties. Mater Sci Eng C Mater Biol Appl. 2018;82:363-71.

57. Koons G, Mikos A. Progress in three-dimensional printing with growth factors. J Control Release. 2019;295:50-9.

58. Nyberg E, Holmes C, Witham T, Grayson WL. Growth factor-eluting technologies for bone tissue engineering. Drug Deliv Transl Res. 2016;6(2):184-94.

59. Raina D, Qayoom I, Larsson D, Zheng M, Kumar A, Isaksson H, et al. Guided tissue engineering for healing of cancellous and cortical bone using a combination of biomaterial based scaffolding and local bone active molecule delivery. Biomaterials. 2019;188:38-49.

60. Fedorovich N, Alblas J, Hennink W, Öner F, Dhert W. Organ printing: the future of bone regeneration? Trends Biotechnol. 2011;29(12):601-06.

61. Ng J, Spiller K, Bernhard J, Vunjak-Novakovic G. Biomimetic Approaches for Bone Tissue Engineering. Tissue Eng Part B: Reviews. 2017;23:480-93.

62. Haumer A, Bourgine PE, Occhetta P, Born G, Tasso R, Martin I. Delivery of cellular factors to regulate bone healing. Adv Drug Deliv Rev. 2018.

63. Murphy S, Atala A. 3D bioprinting of tissues and organs. Nat Biotech. 2014;32(8):773-85.

64. Luo Y, Lode A, Akkineni A, Gelinsky M. Concentrated gelatin/alginate composites for fabrication of predesigned scaffolds with a favorable cell response by 3D plotting. RSC Adv. 2015;5(54):43480-88.

65. Shim J, Kim J, Park M, Park J, Cho D. Development of a hybrid scaffold with synthetic biomaterials and hydrogel using solid freeform fabrication technology. Biofabrication. 2011;3(3):034102.

66. Fedorovich N, De Wijn J, Verbout A, Alblas J, Dhert W. Three-dimensional fiber deposition of cell-laden, viable, patterned constructs for bone tissue printing. Tissue Eng Part A. 2008;14(1):127-33.

67. Fedorovich N, Haverslag R, Dhert W, Alblas J. The Role of Endothelial Progenitor Cells in Prevascularized Bone Tissue Engineering: Development of Heterogeneous Constructs. Tissue Eng Part A. 2010;16(7):2355-67.

68. Fedorovich N, Kuipers E, Gawlitta D, Dhert W, Alblas J. Scaffold porosity and oxygenation of printed hydrogel constructs affect functionality of embedded osteogenic progenitors. Tissue Eng Part A. 2011;17(19-20):2473-86.

69. Kang H, Lee S, Ko I, Kengla C, Yoo J, Atala A. A 3D bioprinting system to produce human-scale tissue constructs with structural integrity. Nat Biotechnol. 2016;34(3):312-19.

70. Guillotin B, Catros S, Keriquel V, Souquet A, Fontaine A, Remy M, et al. Rapid prototyping of complex tissues with laser assisted bioprinting (LAB). In: Narayan R, editor. Rapid Prototyping of Biomaterials - Principles and Applications: Woodhead Publishing; 2014. p. 156-75.

71. Barron J, Krizman D, Ringeisen B. Laser Printing of Single Cells: Statistical Analysis, Cell Viability, and Stress. Ann Biomed Eng. 2005;33(2):121-30.

72. Catros S, Fricain J, Guillotin B, Pippenger B, Bareille R, Remy M, et al. Laser-assisted bioprinting for creating on-demand patterns of human osteoprogenitor cells and nano-hydroxyapatite. Biofabrication. 2011;3(2):025001.

73. Catros S, Guillemot F, Nandakumar A, Ziane S, Moroni L, Habibovic P, et al. Layer-by-layer tissue microfabrication supports cell proliferation in vitro and in vivo. Tissue Eng Part C Methods. 2012;18(1):62-70.

74. Keriquel V, Oliveira H, Remy M, Ziane S, Delmond S, Rousseau B, et al. In situ printing of mesenchymal stromal cells, by laser-assisted bioprinting, for in vivo bone regeneration applications. Sci Rep. 2017;7(1):1778.

75. Cui X, Boland T. Human microvasculature fabrication using thermal inkjet printing technology. Biomaterials. 2009;30(31):6221-27.

76. Nair K, Gandhi M, Khalil S, Yan K, Marcolongo M, Barbee K, et al. Characterization of cell viability during bioprinting processes. Biotechnol J. 2009;4(8):1168-77.

77. Ahmed T, Dare E, Hincke M. Fibrin: a versatile scaffold for tissue engineering applications. Tissue Eng Part B Rev. 2008;14(2):199-215.

78. Fedorovich N, Alblas J, de Wijn J, Hennink W, Verbout A, Dhert W. Hydrogels as extracellular matrices for skeletal tissue engineering: state-of-the-art and novel application in organ printing. Tissue Eng. 2007;13(8):1905-25.

79. Gao G, Schilling A, Yonezawa T, Wang J, Dai G, Cui X. Bioactive nanoparticles stimulate bone tissue formation in bioprinted three-dimensional scaffold and human mesenchymal stem cells. Biotechnol J. 2014;9(10):1304-11.

80. Bittner S, Guo J, Melchiorri A, Mikos A. Three-dimensional Printing of Multilayered Tissue Engineering Scaffolds. Mater Today (Kidlington). 2018;21(8):861-74.

81. Gruene M, Deiwick A, Koch L, Schlie S, Unger C, Hofmann N, et al. Laser Printing of Stem Cells for Biofabrication of Scaffold-Free Autologous Grafts. Tissue Eng Part C Methods. 2011;17(1):79-87.

82. Ali M, Pages E, Ducom A, Fontaine A, Guillemot F. Controlling laser-induced jet formation for bioprinting mesenchymal stem cells with high viability and high resolution. Biofabrication. 2014;6(4):045001.

83. Bryant S, Cuy J, Hauch K, Ratner B. Photo-patterning of porous hydrogels for tissue engineering. Biomaterials. 2007;28:2978-86.

84. Malda J, Visser J, Melchels F, Jüngst T, Hennink W, Dhert W, et al. 25th Anniversary Article: Engineering Hydrogels for Biofabrication. Adv Mater. 2013;25(36):5011-28.

85. Annabi N, Tamayol A, Uquillas J, Akbari M, Bertassoni L, Cha C, et al. 25th Anniversary Article: Rational Design and Applications of Hydrogels in Regenerative Medicine. Adv Mater. 2014;26(1):85-124.

86. Rouillard A, Berglund C, Lee J, Polacheck W, Tsui Y, Bonassar L, et al. Methods for photocrosslinking alginate hydrogel scaffolds with high cell viability. Tissue Eng Part C Methods. 2011;17(2):173-79.

87. Schuurman W, Khristov V, Pot M, van Weeren P, Dhert W, Malda J. Bioprinting of hybrid tissue constructs with tailorable mechanical properties. Biofabrication. 2011;3(2):021001.

88. Visser J, Melchels F, Jeon J, van Bussel E, Kimpton L, Byrne H, et al. Reinforcement of hydrogels using three-dimensionally printed microfibres. Nat Commun. 2015;6.

89. Muschler G, Nakamoto C, Griffith L. Engineering Principles of Clinical Cell-Based Tissue Engineering. J Bone Joint Surg. 2004;86A(7):1541-58.

90. Santos M, Reis R. Vascularization in bone tissue engineering: physiology, current strategies, major hurdles and future challenges. Macromol Biosci. 2010;10(1):12-27.

91. Nguyen L, Annabi N, Nikkhah M, Bae H, Binan L, Park S, et al. Vascularized bone tissue engineering: approaches for potential improvement. Tissue Eng Part B Rev. 2012;18(5):363-82.

92. Mercado-Pagán Á, Stahl A, Shanjani Y, Yang Y. Vascularization in Bone Tissue Engineering Constructs. Ann Biomed Eng. 2015;43(3):718-29.

93. Costa P, Vaquette C, Baldwin J, Chhaya M, Gomes M, Reis R, et al. Biofabrication of customized bone grafts by combination of additive manufacturing and bioreactor knowhow. Biofabrication. 2014;6(3):035006.

94. Allori A, Sailon A, Clark E, Cretiu-Vasiliu C, Smay J, Ricci J, et al. Dynamic cell culture for vascularized bone engineering. J Am Coll Surg. 2008;207(3, Supplement):S51-S2.

95. Tandon N, Cimetta E, Bhumiratana S, Godier-Furnemont A, Maidhof R, Vunjak-Novakovic G. Chapter II.6.6 - Bioreactors for Tissue Engineering. In: Ratner B, Hoffman A, Schoen F, Lemons J, editors. Biomaterials Science. 3rd ed: Academic Press; 2013. p. 1178-94.

96. Miller J, Stevens K, Yang M, Baker B, Nguyen D, Cohen D, et al. Rapid casting of patterned vascular networks for perfusable engineered three-dimensional tissues. Nat Mater. 2012;11(9):768-74.

97. Moroni L, Schotel R, Sohier J, de Wijn J, van Blitterswijk C. Polymer hollow fiber three-dimensional matrices with controllable cavity and shell thickness. Biomaterials. 2006;27(35):5918-26.

98. Lee V, Kim D, Ngo H, Lee Y, Seo L, Yoo S-S, et al. Creating perfused functional vascular channels using 3D bio-printing technology. Biomaterials. 2014;35(28):8092-102.

99. Kolesky D, Truby R, Gladman A, Busbee T, Homan K, Lewis J. 3D Bioprinting of Vascularized, Heterogeneous Cell-Laden Tissue Constructs. Adv Mater. 2014;26(19):3124-30.

100. Kanczler J, Oreffo R. Osteogenesis and angiogenesis: the potential for engineering bone. Eur Cell Mater. 2008;15:100-14.

101. Chiu L, Radisic M. Scaffolds with covalently immobilized VEGF and Angiopoietin-1 for vascularization of engineered tissues. Biomaterials. 2010;31(2):226-41.

102. Shah N, Macdonald M, Beben Y, Padera R, Samuel R, Hammond P. Tunable dual growth factor delivery from polyelectrolyte multilayer films. Biomaterials. 2011;32(26):6183-93.

103. Karageorgiou V, Kaplan D. Porosity of 3D biomaterial scaffolds and osteogenesis. Biomaterials. 2005;26(27):5474-91.

104. Oh S, Park I, Kim J, Lee J. In vitro and in vivo characteristics of PCL scaffolds with pore size gradient fabricated by a centrifugation method. Biomaterials. 2007;28(9):1664-71.

105. Narayan D, Venkatraman S. Effect of pore size and interpore distance on endothelial cell growth on polymers. J Biomed Mater Res Part A. 2008;87A(3):710-18.

106. Bai F, Wang Z, Lu J, Liu J, Chen G, Lv R, et al. The Correlation Between the Internal Structure and Vascularization of Controllable Porous Bioceramic Materials In Vivo: A Quantitative Study. Tissue Eng Part A. 2010;16(12):3791-803.

107. Klenke F, Liu Y, Yuan H, Hunziker E, Siebenrock K, Hofstetter W. Impact of pore size on the vascularization and osseointegration of ceramic bone substitutes in vivo. J Biomed Mater Res Part A. 2008;85A(3):777-86.

108. Ghanaati S, Barbeck M, Orth C, Willershausen I, Thimm B, Hoffmann C, et al. Influence of β-tricalcium phosphate granule size and morphology on tissue reaction in vivo. Acta Biomater. 2010;6(12):4476-87.

109. Linnes M, Ratner B, Giachelli C. A fibrinogen based precision microporous scaffold for tissue engineering. Biomaterials. 2007;28:5298-306.

110. Osathanon T, Linnes M, Rajachar R, Ratner B, Somerman M, Giachelli C. Microporous nanofibrous fibrin-based scaffolds for bone tissue engineering. Biomaterials. 2008;29(30):4091-99.

111. Bryers J, Giachelli C, Ratner B. Engineering biomaterials to integrate and heal: the biocompatibility paradigm shifts. Biotechnol Bioeng. 2012;109(8):1898-911.

112. Oreffo R, Cooper C, Mason C, Clements M. Mesenchymal stem cells. Stem Cell Rev. 2005;1(2):169-78.

113. Tare R, Babister J, Kanczler J, Oreffo R. Skeletal stem cells: phenotype, biology and environmental niches informing tissue regeneration. Mol Cell Endocrinol. 2008;288(1-2):11-21.

114. Robey P. Cell sources for bone regeneration: the good, the bad, and the ugly (but promising). Tissue Eng Part B Rev. 2011;17(6):423-30.

115. Tare R, Mitchell P, Kanczler J, Oreffo R. Isolation, differentiation, and characterisation of skeletal stem cells from human bone marrow in vitro and in vivo. Methods Mol Biol. 2012;816:83-99.

116. Dawson J, Kanczler J, Tare R, Kassem M, Oreffo R. Concise review: bridging the gap: bone regeneration using skeletal stem cell-based strategies - where are we now? Stem Cells. 2014;32(1):35-44.

117. El Tamer M, Reis R. Progenitor and stem cells for bone and cartilage regeneration. J Tissue Eng Regen Med. 2009;3(5):327-37.

118. Szpalski C, Barbaro M, Sagebin F, Warren S. Bone Tissue Engineering: Current Strategies and Techniques - Part II: Cell types. Tissue Eng Part B Rev. 2012;18(4):258-69.

119. Wang F, Yu M, Yan X, Wen Y, Zeng Q, Yue W, et al. Gingiva-Derived Mesenchymal Stem Cell-Mediated Therapeutic Approach for Bone Tissue Regeneration. Stem Cells Dev. 2011;20(12):2093-102.

120. De Peppo G, Marcos-Campos I, Kahler D, Alsalman D, Shang L, Vunjak-Novakovic G, et al. Engineering bone tissue substitutes from human induced pluripotent stem cells. Proc Natl Acad Sci USA. 2013;110:8680-85.

121. Liu J, Chen W, Zhao Z, Xu H. Reprogramming of mesenchymal stem cells derived from iPSCs seeded on biofunctionalized calcium phosphate scaffold for bone engineering. Biomaterials. 2013;34(32):7862-72.

122. Phillips M, Kuznetsov S, Cherman N, Park K, Chen K, McClendon B, et al. Directed Differentiation of Human Induced Pluripotent Stem Cells Toward Bone and Cartilage: In Vitro Versus In Vivo Assays. Stem Cells Transl Med. 2014;3(7):867-78.

123. Csobonyeiova M, Polak S, Zamborsky R, Danisovic L. iPS cell technologies and their prospect for bone regeneration and disease modeling: A mini review. J Adv Res. 2017;8(4):321-27.

124. Liu Y, Chan J, Teoh S. Review of vascularised bone tissue-engineering strategies with a focus on co-culture systems. J Tissue Eng Regen Med. 2015;9(2):85-105.

125. Marolt D, Knezevic M, Vunjak-Novakovic G. Bone tissue engineering with human stem cells. Stem Cell Res Ther. 2010;1(10).

126. Seong J, Kim B, Park J, Kwon I, Mantalaris A, Hwang Y. Stem cells in bone tissue engineering. Biomed Mater. 2010;5(6):062001.

127. Caplan A. Chapter II.6.4 - Cell Sources for Tissue Engineering: Mesenchymal Stem Cells. In: Ratner B, Hoffman A, Schoen F, Lemons J, editors. Biomaterials Science. 3rd ed: Academic Press; 2012. p. 1159-64.

128. Wang D, Miura M, Demura H, Sato K. Anabolic Effects of 1,25-DihydroxyvitaminD3 on osteoblasts are enhanced by Vascular Endothelial Growth

Factor produced by osteoblasts and by growth factors produced by endothelial cells. Endocrinol. 1997;138(7):2953-62.

129. Unger R, Dohle E, Kirkpatrick C. Improving vascularization of engineered bone through the generation of pro-angiogenic effects in co-culture systems. Adv Drug Deliv Rev. 2015;94:116-25.

130. Liu Y, Teoh S, Chong M, Yeow C, Kamm R, Choolani M, et al. Contrasting effects of vasculogenic induction upon biaxial bioreactor stimulation of mesenchymal stem cells and endothelial progenitor cells cocultures in three-dimensional scaffolds under in vitro and in vivo paradigms for vascularized bone tissue engineering. Tissue Eng Part A. 2013;19(7-8):893-904.

131. Stevens B, Yang Y, Mohandas A, Stucker B, Nguyen K. A review of materials, fabrication methods, and strategies used to enhance bone regeneration in engineered bone tissues. J Biomed Mater Res B App Biomater. 2008;85(2):573-82.

132. O'Brien F. Biomaterials & scaffolds for tissue engineering. Mater Today. 2011;14(3):88-95.

133. Leijten J, Chai Y, Papantoniou I, Geris L, Schrooten J, Luyten F. Cell based advanced therapeutic medicinal products for bone repair: Keep it simple? Adv Drug Deliv Rev. 2015;84:30-44.

134. Amini A, Laurencin C, Nukavarapu S. Bone tissue engineering: recent advances and challenges. Crit Rev Biomed Eng. 2012;40(5):363-408.

135. Billiet T, Vandenhaute M, Schelfhout J, Van Vlierberghe S, Dubruel P. A review of trends and limitations in hydrogel-rapid prototyping for tissue engineering. Biomaterials. 2012;33(26):6020-41.

136. Kasper F, Singh M, Mikos A. Chapter II.6.3 - Tissue Engineering Scaffolds. In: Ratner B, Hoffman A, Schoen F, Lemons J, editors. Biomaterials Science. 3rd ed: Academic Press; 2013. p. 1138-59.

137. Garg T, Goyal A. Biomaterial-based scaffolds-current status and future directions. Exp Opin Drug Deliv. 2014;11(5):767-89.

138. Fernandez-Yague M, Abbah S, McNamara L, Zeugolis D, Pandit A, Biggs M. Biomimetic approaches in bone tissue engineering: Integrating biological and physicomechanical strategies. Adv Drug Deliv Rev. 2015;84:1-29.

139. Kim J, Ma T. Bioreactor strategy in bone tissue engineering: pre-culture and osteogenic differentiation under two flow configurations. Tissue Eng Part A. 2012;18(21-22):2354-64.

140. Das A, Botchwey E. Evaluation of angiogenesis and osteogenesis. Tissue Eng Part B Rev. 2011;17(6):403-14.

141. Hung B, Hutton D, Grayson W. Mechanical control of tissue-engineered bone. Stem Cell Res Ther. 2013;4(1):10.

142. Huang C, Chiang H, Lin H, Hosseinkhani H, Ou K-L, Peng P. Comparison of Cell Response and Surface Characteristics on Titanium Implant with SLA and SLAffinity Functionalization. J Electrochem Soc. 2014;161(3):G15-20.

143. Tsai M-H, Haung C-F, Shyu S-S, Chou Y-R, Lin M-H, Peng P-W, et al. Surface modification induced phase transformation and structure variation on the rapidly solidified recast layer of titanium. Mater Character. 2015;106:463-69.

144. Dalby M, Gadegaard N, Oreffo R. Harnessing nanotopography and integrin-matrix interactions to influence stem cell fate. Nat Mater. 2014;13(6):558-69.

145. Biggs M, Richards R, Gadegaard N, Wilkinson C, Oreffo R, Dalby M. The use of nanoscale topography to modulate the dynamics of adhesion formation in primary osteoblasts and ERK/MAPK signalling in STRO-1+ enriched skeletal stem cells. Biomaterials. 2009;30(28):5094-103.

146. Oh S, Brammer K, Li Y, Teng D, Engler A, Chien S, et al. Stem cell fate dictated solely by altered nanotube dimension. Proc Natl Acad Sci USA. 2009;106(7):2130-35.

147. Nadeem D, Sjostrom T, Wilkinson A, Smith C, Oreffo R, Dalby M, et al. Embossing of micropatterned ceramics and their cellular response. J Biomed Mater Res A. 2013;101(11):3247-55.

148. Cheng A, Humayun A, Cohen D, Boyan B, Schwartz Z. Additively manufactured 3D porous Ti-6Al-4V constructs mimic trabecular bone structure and regulate osteoblast proliferation, differentiation and local factor production in a porosity and surface roughness dependent manner. Biofabrication. 2014;6(4):045007.

149. Mills R, Frith J, Hudson J, Cooper-White J. Effect of geometric challenges on cell migration. Tissue Eng Part C Methods. 2011;17(10):999-1010.

150. Hong S, Song S-J, Lee J, Jang H, Choi J, Sun K, et al. Cellular behavior in micropatterned hydrogels by bioprinting system depended on the cell types and cellular interaction. J Biosci Bioeng. 2013;116(2):224-30.

151. Ho-Shui-Ling A, Bolander J, Rustom LE, Johnson AW, Luyten FP, Picart C. Bone regeneration strategies: Engineered scaffolds, bioactive molecules and stem cells current stage and future perspectives. Biomaterials. 2018;180:143-62.

152. Gothard D, Smith E, Kanczler J, Rashidi H, Qutachi O, Henstock J, et al. Tissue Engineered Bone Using Select Growth Factors: A Comprehensive Review of Animal Studies and Clinical Translation Studies in Man. Eur Cell Mater. 2014;28:166-208.

153. Santo V, Gomes M, Mano J, Reis R. Controlled release strategies for bone, cartilage, and osteochondral engineering - Part II: challenges on the evolution from single to multiple bioactive factor delivery. Tissue Eng Part B Rev. 2013;19(4):327-52.

154. Young S, Patel Z, Kretlow J, Murphy M, Mountziaris P, Baggett L, et al. Dose Effect of Dual Delivery of Vascular Endothelial Growth Factor and Bone Morphogenic Protein-2 on Bone Regeneration in a Rat Critical-Size Defect Model. Tissue Eng Part A. 2009;15(9):2347-62.

155. Kuhn L, Ou G, Charles L, Hurley M, Rodner C, Gronowicz G. Fibroblast Growth Factor-2 and Bone Morphogenetic Protein-2 Have a Synergistic Stimulatory Effect on Bone Formation in Cell Cultures From Elderly Mouse and Human Bone. J Gerontol A: Biol Sci Med Sci. 2013;68(10):1170-80.

156. Dang M, Saunders L, Niu X, Fan Y, Ma PX. Biomimetic delivery of signals for bone tissue engineering. Bone Res. 2018;6:25.

157. Suarez-Gonzalez D, Lee J, Diggs A, Lu Y, Nemke B, Markel M, et al. Controlled multiple growth factor delivery from bone tissue engineering scaffolds via designed affinity. Tissue Eng Part A. 2014;20(15-16):2077-87.

158. Leach J, Mooney D. Bone engineering by controlled delivery of osteoinductive molecules and cells. Exp Opin Biol Ther. 2004;4(7):1015-27.

159. Zhang H, Migneco F, Lin C, Hollister S. Chemically-conjugated bone morphogenetic protein-2 on three-dimensional polycaprolactone scaffolds stimulates osteogenic activity in bone marrow stromal cells. Tissue Eng Part A. 2010;16(11):3441-48.

160. Mouriño V, Cattalini J, Roether J, Dubey P, Roy I, Boccaccini A. Composite polymer-bioceramic scaffolds with drug delivery capability for bone tissue engineering. Exp Opin Drug Deliv. 2013;10(10):1353-65.

161. Sawkins M, Mistry P, Brown B, Shakesheff K, Bonassar L, Yang J. Cell and protein compatible 3D bioprinting of mechanically strong constructs for bone repair. Biofabrication. 2015;7(3):035004.

162. He X, Ma J, Jabbari E. Effect of grafting RGD and BMP-2 protein-derived peptides to a hydrogel substrate on osteogenic differentiation of marrow stromal cells. Langmuir. 2008;24(21):12508-16.

163. Simmons C, Alsberg E, Hsiong S, Kim W, Mooney D. Dual growth factor delivery and controlled scaffold degradation enhance in vivo bone formation by transplanted bone marrow stromal cells. Bone. 2004;35(2):562-69.

164. De Witte T, Fratila-Apachitei L, Zadpoor A, Peppas N. Bone tissue engineering via growth factor delivery: from scaffolds to complex matrices. Regen Biomater. 2018;5(4):197-211.

165. Lu S, Lam J, Trachtenberg J, Lee E, Seyednejad H, van den Beucken J, et al. Dual growth factor delivery from bilayered, biodegradable hydrogel composites for spatially-guided osteochondral tissue repair. Biomaterials. 2014;35(31):8829-39.

166. Radhakrishnan J, Manigandan A, Chinnaswamy P, Subramanian A, Sethuraman S. Gradient nano-engineered in situ forming composite hydrogel for osteochondral regeneration. Biomaterials. 2018;162:82-98.

167. Samorezov J, Alsberg E. Spatial regulation of controlled bioactive factor delivery for bone tissue engineering. Adv Drug Deliv Rev. 2015;84:45-67.

168. Phillippi J, Miller E, Weiss L, Huard J, Waggoner A, Campbell P. Microenvironments engineered by inkjet bioprinting spatially direct adult stem cells toward muscle- and bone-like subpopulations. Stem Cells. 2008;26(1):127-34.

169. Vorndran E, Klammert U, Ewald A, Barralet J, Gbureck U. Simultaneous Immobilization of Bioactives During 3D Powder Printing of Bioceramic Drug-Release Matrices. Adv Funct Mater. 2010;20(10):1585-91.

170. Martin I, Simmons P, Williams D. Manufacturing Challenges in Regenerative Medicine. Sci Transl Med. 2014;6(232):232fs16.

171. Melchels F, Wiggenhauser P, Warne D, Barry M, Ong F, Chong W, et al. CAD/CAM-assisted breast reconstruction. Biofabrication. 2011;3(3):034114.

172. Wang Z, Mondry A. Volume-based non-continuum modeling of bone functional adaptation. Theor Biol Med Model. 2005;2:6.

173. Smith E, Kanczler J, Gothard D, Roberts C, Wells J, White L, et al. Evaluation of skeletal tissue repair, Part 1: Assessment of novel growth-factor-releasing hydrogels in an ex vivo chick femur defect model. Acta Biomater. 2014;10(10):4186-96.

174. Moreno-Jimenez I, Hulsart-Billstrom G, Lanham S, Janeczek A, Kontouli N, Kanczler J, et al. The chorioallantoic membrane (CAM) assay for the study of human bone regeneration: a refinement animal model for tissue engineering. Sci Rep. 2016;6:32168.

175. Nowak-Sliwinska P, Segura T, Iruela-Arispe M. The chicken chorioallantoic membrane model in biology, medicine and bioengineering. Angiogenesis. 2014;17(4):779-804.

176. Smith E, Kanczler J, Oreffo R. A new take on an old story: chick limb organ culture for skeletal niche development and regenerative medicine evaluation. Eur Cell Mater. 2013;26:91-106.

177. Rezwan K, Chen Q, Blaker J, Boccaccini A. Biodegradable and bioactive porous polymer/inorganic composite scaffolds for bone tissue engineering. Biomaterials. 2006;27(18):3413-31.

178. Szpalski C, Wetterau M, Barr J, Warren S. Bone Tissue Engineering: Current Strategies and Techniques - Part I: Scaffolds. Tissue Eng Part B Rev. 2012;18(4):246-57.

179. Lin C-C, Anseth K. Chapter II.4.3 - The Biodegradation of Biodegradable Polymeric Biomaterials. In: Ratner B, Hoffman A, Schoen F, Lemons J, editors. Biomaterials Science. 3rd ed: Academic Press; 2013. p. 716-28.

180. Williams D. Chapter 9 - Biocompatibility. In: Blitterswijk C, Thomsen P, Lindahl A, Hubbell J, Williams D, Cancedda R, et al., editors. Tissue Engineering. Burlington: Academic Press; 2008. p. 255-78.

181. Appel A, Anastasio M, Larson J, Brey E. Imaging challenges in biomaterials and tissue engineering. Biomaterials. 2013;34(28):6615-30.

182. Ventura M, Boerman O, de Korte C, Rijpkema M, Heerschap A, Oosterwijk E, et al. Preclinical Imaging in Bone Tissue Engineering. Tissue Eng Part B Rev. 2014;20:578-95.

183. Leferink A, van Blitterswijk C, Moroni L. Methods of Monitoring Cell Fate and Tissue Growth in Three-Dimensional Scaffold-Based Strategies for In Vitro Tissue Engineering. Tissue Eng Part B Rev. 2016;22:265-83.

184. Vielreicher M, Schürmann S, Detsch R, Schmidt M, Buttgereit A, Boccaccini A, et al. Taking a deep look: modern microscopy technologies to optimize the design and functionality of biocompatible scaffolds for tissue engineering in regenerative medicine. J R Soc Interf. 2013;10(86).

185. Nam S, Ricles L, Suggs L, Emelianov S. Imaging strategies for tissue engineering applications. Tissue Eng Part B Rev. 2015;21(1):88-102.

186. Wang M, Vorwald C, Dreher M, Mott E, Cheng M-H, Cinar A, et al. Evaluating 3D-Printed Biomaterials as Scaffolds for Vascularized Bone Tissue Engineering. Adv Mater. 2015;27(1):138-44.

187. Schladitz K. Quantitative micro-CT. J Microsc. 2011;243(2):111-17.

188. Weber F, Bohme J, Scheidt H, Grunder W, Rammelt S, Hacker M, et al. 31P and 13C solid-state NMR spectroscopy to study collagen synthesis and biomineralization in polymer-based bone implants. NMR Biomed. 2012;25(3):464-75.

189. Lin C, Chang Y, Kao C, Lu C, Sung L, Yen T, et al. Augmented healing of critical-size calvarial defects by baculovirus-engineered MSCs that persistently express growth factors. Biomaterials. 2012;33(14):3682-92.

190. Zhou J, Lin H, Fang T, Li X, Dai W, Uemura T, et al. The repair of large segmental bone defects in the rabbit with vascularized tissue engineered bone. Biomaterials. 2010;31(6):1171-79.

191. El Backly R, Zaky S, Muraglia A, Tonachini L, Brun F, Canciani B, et al. A platelet-rich plasma-based membrane as a periosteal substitute with enhanced osteogenic and angiogenic properties: a new concept for bone repair. Tissue Eng Part A. 2013;19(1-2):152-65.

192. Demers J, Davis S, Pogue B, Morris M. Multichannel diffuse optical Raman tomography for bone characterization in vivo: a phantom study. Biomed Opt Express. 2012;3:2299-305.

193. Zhang Q, Mochalin V, Neitzel I, Knoke I, Han J, Klug C, et al. Fluorescent PLLA-nanodiamond composites for bone tissue engineering. Biomaterials. 2011;32(1):87-94.

194. Wartella K, Khalilzad-Sharghi V, Kelso M, Kovar J, Kaplan D, Xu H, et al. Multi-modal imaging for assessment of tissue-engineered bone in a critical-sized calvarial defect mouse model. J Tissue Eng Regen Med. 2017;11(6):1732-40.

195. Rodenberg E, Azhdarinia A, Lazard Z, Hall M, Kwon S, Wilganowski N, et al. Matrix metalloproteinase-9 is a diagnostic marker of heterotopic ossification in a murine model. Tissue Eng Part A. 2011;17(19-20):2487-96.

196. Santiesteban D, Kubelick K, Dhada K, Dumani D, Suggs L, Emelianov S. Monitoring/Imaging and Regenerative Agents for Enhancing Tissue Engineering Characterization and Therapies. Ann Biomed Eng. 2016;44(3):750-72.

197. Henning A, Jiang M, Yalcin H, Butcher J. Quantitative three-dimensional imaging of live avian embryonic morphogenesis via micro-computed tomography. Dev Dyn. 2011;240(8):1949-57.

198. Weissleder R, Nahrendorf M. Advancing biomedical imaging. Proc Natl Acad Sci USA. 2015;112(47):14424-28.

199. Bayraktar D, Tas A. Chemical preparation of carbonated calcium hydroxyapatite powders at 37C in urea-containing synthetic body fluids. J Euro Ceramic Soc. 1999;19:2573-79.

200. Kokubo T, Takadama H. How useful is SBF in predicting in vivo bone bioactivity? Biomaterials. 2006;27(15):2907-15.

201. Stewart K, Walsh S, Screen J, Jefferiss C, Chainey J, Jordan G, et al. Further characterization of cells expressing STRO-1 in cultures of adult human bone marrow stromal cells. J Bone Miner Res. 1999;14(8):1345-56.

202. Lee J, Tsang W, Chow K. Simple Modifications to Standard TRIzol® Protocol Allow High-Yield RNA Extraction from Cells on Resorbable Materials. J Biomater Nanobiotechnol. 2011;02(01):41-8.

203. Livak K, Schmittgen T. Analysis of Relative Gene Expression Data Using Real-Time Quantitative PCR and the 2−ΔΔCT Method. Methods. 2001;25(4):402-08.

204. Kuznetsov S, Krebsbach P, Satomura K, Kerr J, Riminucci M, Benayahu D, et al. Single-Colony Derived Strains of Human Marrow Stromal Fibroblasts Form Bone After Transplantation In Vivo. J Bone Miner Res. 1997;12:1335-47.

205. Pittenger M, Mackay A, Beck S, Jaiswal R, Douglas R, Mosca J, et al. Multilineage potential of adult human mesenchymal stem cells. Science. 1999;284:143-47.

206. Caplan A. Mesenchymal stem cells. J Orthop Res. 1991;9:641-50.

207. Chan CK, Seo EY, Chen JY, Lo D, McArdle A, Sinha R, et al. Identification and specification of the mouse skeletal stem cell. Cell. 2015;160(1-2):285-98.

208. Chan C, Gulati G, Sinha R, Tompkins J, Lopez M, Carter A, et al. Identification of the Human Skeletal Stem Cell. Cell. 2018;175(1):43-56.

209. Robey P, Kuznetsov S, Ren J, Klein H, Sabatino M, Stroncek D. Generation of clinical grade human bone marrow stromal cells for use in bone regeneration. Bone. 2015;70:87-92.

210. Agata H, Asahina I, Watanabe N, Ishii Y, Kubo N, Ohshima S, et al. Characteristic change and loss of in vivo osteogenic abilities of human bone marrow stromal cells during passage. Tissue Eng Part A. 2010;16:663-73.

211. Ma J, Both S, Yang F, Cui F, Pan J, Meijer G, et al. Concise review: cell-based strategies in bone tissue engineering and regenerative medicine. Stem Cells Transl Med. 2014;3(1):98-107.

212. Modder U, Roforth M, Nicks K, Peterson J, McCready L, Monroe D, et al. Characterization of mesenchymal progenitor cells isolated from human bone marrow by negative selection. Bone. 2012;50(3):804-10.

213. Granéli C, Thorfve A, Ruetschi U, Brisby H, Thomsen P, Lindahl A, et al. Novel markers of osteogenic and adipogenic differentiation of human bone marrow stromal cells identified using a quantitative proteomics approach. Stem Cell Res. 2014;12(1):153-65.

214. Gothard D, Greenhough J, Ralph E, Oreffo R. Prospective isolation of human bone marrow stromal cell subsets: A comparative study between Stro-1-, CD146- and CD105-enriched populations. J Tissue Eng. 2014;5.

215. Simmons P, Torok-Storb B. Identification of stromal cell precursors in human bone marrow by a novel monoclonal antibody, STRO-1. Blood. 1991;78:55-62.

216. Ning H, Lin G, Lue T, Lin C. Mesenchymal stem cell marker Stro-1 is a 75 kd endothelial antigen. Biochem Biophys Res Commun. 2011;413(2):353-57.

217. Fitter S, Gronthos S, Ooi S, Zannettino A. The Mesenchymal Precursor Cell Marker Antibody STRO-1 Binds to Cell Surface Heat Shock Cognate 70. Stem Cells. 2017;35(4):940-51.

218. Lv F, Tuan R, Cheung K, Leung V. Concise review: the surface markers and identity of human mesenchymal stem cells. Stem Cells. 2014;32(6):1408-19.

219. MacArthur B, Tare R, Please C, Prescott P, Oreffo R. A non-invasive method for in situ quantification of subpopulation behaviour in mixed cell culture. J R Soc Interface. 2006;3(6):63-9.

220. Gronthos S, Zannettino A, Hay S, Shi S, Graves S, Kortesidis A, et al. Molecular and cellular characterisation of highly purified stromal stem cells derived from human bone marrow. J Cell Sci. 2003;116:1827-35.

221. Gronthos S, Zannettino A, Graves S, Ohta S, Hay S, Simmons P. Differential cell surface expression of the STRO-1 and alkaline phosphatase antigens on discrete developmental stages in primary cultures of human bone cells. J Bone Miner Res. 1999;14(1):47-56.

222. Shi S, Gronthos S. Perivascular niche of postnatal mesenchymal stem cells in human bone marrow and dental pulp. J Bone Miner Res. 2003;18:696-704.

223. Gronthos S, Graves S, Ohta S, Simmons P. The STRO-1+ fraction of adult human bone marrow contains the osteogenic precursors. Blood. 1994;84:4164-73.

224. Mason S, Kohles S, Winn S, Zelick R. The Influence of Vitamin D Metabolism on Gene Expression, Matrix Production and Mineralization During Osteoprecursor Cell-Based Bone Development. J Endocrinol Metabol. 2014;4:1-12.

225. Beresford J, Gallagher J, Russell R. 1,25-Dihydroxyvitamin D3 and Human Bone-Derived Cells in vitro: Effects on Alkaline Phosphatase, Type I Collagen and Proliferation. Endocrinol. 1986;119(4):1776-85.

226. Franceschi R, Young J. Regulation of alkaline phosphatase by 1,25-dihydroxyvitamin D3 and ascorbic acid in bone-derived cells. J Bone Miner Res. 1990;5(11):1157-67.

227. van Driel M, van Leeuwen J. Vitamin D endocrine system and osteoblasts. Bonekey Rep. 2014;3:493.

228. Bellows C, Reimers S, Heersche J. Expression of mRNAs for type 1 collagen, bone sialoprotein, osteocalcin, and osteopontin at different stages of osteoblastic differentiation and their regulation by 1,25 dihydroxyvitamin D3. Cell Tissue Res. 1999;297:249-59.

229. Dalby M, Gadegaard N, Tare R, Andar A, Riehle M, Herzyk P, et al. The control of human mesenchymal cell differentiation using nanoscale symmetry and disorder. Nat Mater. 2007;6(12):997-1003.

230. Hong D, Chen H, Yu H, Liang Y, Wang C, Lian Q, et al. Morphological and proteomic analysis of early stage of osteoblast differentiation in osteoblastic progenitor cells. Exp Cell Res. 2010;316(14):2291-300.

231. Golub E, Boesze-Battaglia K. The role of alkaline phosphatase in mineralization. Curr Opin Orthop. 2007;18:444-48.

232. Siffert R. The role of alkaline phosphatase in osteogenesis. J Exp Med. 1950;93:415-26.

233. Lojda Z, Gossrau R, Schiebler T. Enzyme Histochemistry: A Laboratory Manual. 1st ed: Springer Science & Business Media; 2012.

234. Karsenty G, Kronenberg H, Settembre C. Genetic control of bone formation. Annu Rev Cell Dev Biol. 2009;25:629-48.

235. Bedalov A, Salvatori R, Dodig M, Kapural B, Pavlin D, Kream B, et al. 1,25-Dihydroxyvitamin D3 inhibition of Col1a1 promoter expression in calvariae from neonatal transsgenic mice. Biochimica et Biophysica Acta - Gene Structure and Expression. 1998;1398:285-93.

236. Aubin J, Liu F, Malaval L, Gupta A. Osteoblast and chondroblast differentiation. Bone. 1995;17:S77-S83.

237. Malloy P, Pike J, Feldman D. The Vitamin D receptor and the syndrome of hereditary 1,25-dihydroxyvitamin D-resistant rickets. Endocrine Rev. 1999;20:156-88.

238. Brusnahan S, McGuire T, Jackson J, Lane J, Garvin K, O'Kane B, et al. Human blood and marrow side population stem cell and Stro-1 positive bone marrow stromal cell numbers decline with age, with an increase in quality of surviving stem cells: correlation with cytokines. Mech Ageing Dev. 2010;131(11-12):718-22.

239. Long M, Rack H. Titanium alloys in total joint replacement—a materials science perspective. Biomaterials. 1998;19(18):1621-39.

240. Xue W, Krishna B, Bandyopadhyay A, Bose S. Processing and biocompatibility evaluation of laser processed porous titanium. Acta Biomater. 2007;3(6):1007-18.

241. Kirmanidou Y, Sidira M, Drosou M, Bennani V, Bakopoulou A, Tsouknidas A, et al. New Ti-Alloys and Surface Modifications to Improve the Mechanical Properties and the Biological Response to Orthopedic and Dental Implants: A Review. Biomed Res Int. 2016;2016:2908570.

242. Goriainov V, Cook R, Latham J, Dunlop D, Oreffo R. Bone and metal: an orthopaedic perspective on osseointegration of metals. Acta Biomater. 2014;10(10):4043-57.

243. Hutmacher D. Scaffold design and fabrication technologies for engineering tissues — state of the art and future perspectives. J Biomater Sci. 2001;12(1):107-24.

244. Ducheyne P, Healy K, Hutmacher D, Grainger D, Kirkpatrick C. Comprehensive Biomaterials II. 2nd ed: Elsevier Science; 2017.

245. Mota C, Puppi D, Chiellini F, Chiellini E. Additive manufacturing techniques for the production of tissue engineering constructs. J Tissue Eng Regen Med. 2015;9(3):174-90.

246. Pedde R, Mirani B, Navaei A, Styan T, Wong S, Mehrali M, et al. Emerging Biofabrication Strategies for Engineering Complex Tissue Constructs. Adv Mater. 2017;29(19).

247. Lewallen E, Riester S, Bonin C, Kremers H, Dudakovic A, Kakar S, et al. Biological strategies for improved osseointegration and osteoinduction of porous metal orthopedic implants. Tissue Eng Part B Rev. 2015;21(2):218-30.

248. Feller L, Jadwat Y, Khammissa R, Meyerov R, Schechter I, Lemmer J. Cellular responses evoked by different surface characteristics of intraosseous titanium implants. Biomed Res Int. 2015;2015:171945.

249. Hotchkiss K, Reddy G, Hyzy S, Schwartz Z, Boyan B, Olivares-Navarrete R. Titanium surface characteristics, including topography and wettability, alter macrophage activation. Acta Biomater. 2016;31:425-34.

250. Bosshardt D, Chappuis V, Buser D. Osseointegration of titanium, titanium alloy and zirconia dental implants: current knowledge and open questions. Periodontol 2000. 2017;73:22-40.

251. Lincks J, Boyan B, Blanchard C, Lohmann C, Liu Y, Cochran D, et al. Response of MG63 osteoblast-like cells to titanium and titanium alloy is dependent on surface roughness and composition. Biomaterials. 1998;19(23):2219-32.

252. Zinger O, Zhao G, Schwartz Z, Simpson J, Wieland M, Landolt D, et al. Differential regulation of osteoblasts by substrate microstructural features. Biomaterials. 2005;26(14):1837-47.

253. Zhao G, Raines A, Wieland M, Schwartz Z, Boyan B. Requirement for both micron- and submicron scale structure for synergistic responses of osteoblasts to substrate surface energy and topography. Biomaterials. 2007;28(18):2821-29.

254. Gittens R, McLachlan T, Olivares-Navarrete R, Cai Y, Berner S, Tannenbaum R, et al. The effects of combined micron-/submicron-scale surface roughness and nanoscale features on cell proliferation and differentiation. Biomaterials. 2011;32(13):3395-403.

255. Banik B, Riley T, Platt C, Brown J. Human Mesenchymal Stem Cell Morphology and Migration on Microtextured Titanium. Front Bioeng Biotechnol. 2016;4:41.

256. Gittens R, Scheideler L, Rupp F, Hyzy S, Geis-Gerstorfer J, Schwartz Z, et al. A review on the wettability of dental implant surfaces II: Biological and clinical aspects. Acta Biomater. 2014;10(7):2907-18.

257. Morra M, Cassinelli C, Cascardo G, Bollati D, Baena R. Gene expression of markers of osteogenic differentiation of human mesenchymal cells on collagen I-modified microrough titanium surfaces. J Biomed Mater Res A. 2011;96(2):449-55.

258. Pullisaar H, Tiainen H, Landin M, Lyngstadaas S, Haugen H, Reseland J, et al. Enhanced in vitro osteoblast differentiation on TiO2 scaffold coated with alginate hydrogel containing simvastatin. J Tissue Eng. 2013;4:2041731413515670.

259. Fleischmann L, Crismani A, Falkensammer F, Bantleon H, Rausch-Fan X, Andrukhov O. Behavior of osteoblasts on TI surface with two different coating designed for orthodontic devices. J Mater Sci Mater Med. 2015;26(1):5335.

260. Moura C, Souza M, Kohal R, Dechichi P, Zanetta-Barbosa D, Jimbo R, et al. Evaluation of osteogenic cell culture and osteogenic/peripheral blood mononuclear human cell co-culture on modified titanium surfaces. Biomed Mater. 2013;8(3):035002.

261. Zhao G, Zinger O, Schwartz Z, Wieland M, Landolt D, Boyan B. Osteoblast-like cells are sensitive to submicron-scale surface structure. Clin Oral Implants Res. 2006;17(3):258-64.

262. Otsuki B, Takemoto M, Fujibayashi S, Neo M, Kokubo T, Nakamura T. Pore throat size and connectivity determine bone and tissue ingrowth into porous implants: three-dimensional micro-CT based structural analyses of porous bioactive titanium implants. Biomaterials. 2006;27(35):5892-900.

263. Li J, Habibovic P, van den Doel M, Wilson C, de Wijn J, van Blitterswijk C, et al. Bone ingrowth in porous titanium implants produced by 3D fiber deposition. Biomaterials. 2007;28(18):2810-20.

264. Bandyopadhyay A, Shivaram A, Tarafder S, Sahasrabudhe H, Banerjee D, Bose S. In Vivo Response of Laser Processed Porous Titanium Implants for Load-Bearing Implants. Ann Biomed Eng. 2016:1-12.

265. Itala A, Ylanen H, Ekholm C, Karlsson K, Aro H. Pore diameter of more than 100 um is not requisite for bone ingrowth in rabbits. J Biomed Mater Res A. 2001;58(6):679-83.

266. Hollander D, von Walter M, Wirtz T, Sellei R, Schmidt-Rohlfing B, Paar O, et al. Structural, mechanical and in vitro characterization of individually structured Ti-6Al-4V produced by direct laser forming. Biomaterials. 2006;27(7):955-63.

267. Shen H, Li H, Brinson L. Effect of microstructural configurations on the mechanical responses of porous titanium: A numerical design of experiment analysis for orthopedic applications. Mech Mater. 2008;40(9):708-20.

268. Warnke P, Douglas T, Wollny P, Sherry E, Steiner M, Galonska S, et al. Rapid prototyping: porous titanium alloy scaffolds produced by selective laser melting for bone tissue engineering. Tissue Eng Part C Methods. 2009;15(2):115-24.

269. Van der Stok J, Wang H, Amin Yavari S, Siebelt M, Sandker M, Waarsing J, et al. Enhanced bone regeneration of cortical segmental bone defects using porous titanium scaffolds incorporated with colloidal gelatin gels for time- and dose-controlled delivery of dual growth factors. Tissue Eng Part A. 2013;19(23-24):2605-14.

270. Wang X, Xu S, Zhou S, Xu W, Leary M, Choong P, et al. Topological design and additive manufacturing of porous metals for bone scaffolds and orthopaedic implants: A review. Biomaterials. 2016;83:127-41.

271. Zhao C, Cao P, Ji W, Han P, Zhang J, Zhang F, et al. Hierarchical titanium surface textures affect osteoblastic functions. J Biomed Mater Res A. 2011;99(4):666-75.

272. Lai H, Zhuang L, Liu X, Wieland M, Zhang Z, Zhang Z. The influence of surface energy on early adherent events of osteoblast on titanium substrates. J Biomed Mater Res A. 2010;93(1):289-96.

273. Zisman W. Relation of the Equilibrium Contact Angle to Liquid and Solid Constitution. In: Fowkes F, editor. Contact angle, wettability, and adhesion. Advances in Chemistry. 43: American Chemical Society; 1964. p. 1-51.

274. Rauh J, Jacobi A, Stiehler M. Identification of Stable Reference Genes for Gene Expression Analysis of Three-Dimensional Cultivated Human Bone Marrow-Derived Mesenchymal Stromal Cells for Bone Tissue Engineering. Tissue Eng Part C Methods. 2015;21:192-206.

275. Olivares-Navarrete R, Raz P, Zhao G, Chen J, Wieland M, Cochran D, et al. Integrin alpha2beta1 plays a critical role in osteoblast response to micron-scale surface structure and surface energy of titanium substrates. Proc Natl Acad Sci USA. 2008;105(41):15767-72.

276. Olivares-Navarrete R, Hyzy S, Berg M, Schneider J, Hotchkiss K, Schwartz Z, et al. Osteoblast lineage cells can discriminate microscale topographic features on titanium-aluminum-vanadium surfaces. Ann Biomed Eng. 2014;42(12):2551-61.

277. Zhao G, Schwartz Z, Wieland M, Rupp F, Geis-Gerstorfer J, Cochran D, et al. High surface energy enhances cell response to titanium substrate microstructure. J Biomed Mater Res A. 2005;74(1):49-58.

278. Raines A, Olivares-Navarrete R, Wieland M, Cochran D, Schwartz Z, Boyan B. Regulation of angiogenesis during osseointegration by titanium surface microstructure and energy. Biomaterials. 2010;31(18):4909-17.

279. Boyan B, Batzer R, Kieswetter K, Liu Y, Cochran D, Szmuckler-Moncler S, et al. Titanium surface roughness alters responsiveness of MG63 osteoblast-like cells to 1 alpha,25-(OH)2D3. J Biomed Mater Res. 1998;39(1):77-85.

280. Sansone V, Pagani D, Melato M. The effects on bone cells of metal ions released from orthopaedic implants. A review. Clin Cases Miner Bone Metabol. 2013;10:34-40.

281. Ikarashi Y, Toyoda K, Kobayashi E, Doi H, Yoneyama T, Hamanaka H, et al. Improved biocompatibility of titanium-zirconium (Ti-Zr) alloy: tissue reaction and sensitisation to Ti-Zr alloy compared with pure Ti and Zr in rat implantation study. Mater Trans. 2005;46:2260-67.

282. Markhoff J, Krogull M, Schulze C, Rotsch C, Hunger S, Bader R. Biocompatibility and Inflammatory Potential of Titanium Alloys Cultivated with Human Osteoblasts, Fibroblasts and Macrophages. Materials (Basel). 2017;10(1).

283. Fernández-Rodríguez M, Sánchez-Treviño A, De Luna-Bertos E, Ramos-Torrecillas J, García-Martínez O, Ruiz C, et al. Wettability and osteoblastic cell adhesion on ultrapolished commercially pure titanium surfaces: the role of the oxidation and pollution states. J Adhes Sci Technol. 2014;28(12):1207-18.

284. Gail M, Boone C. The locomotion of mouse fibroblasts in tissue culture. Biophys J. 1970;10:980-93.

285. Di Luca A, Longoni A, Criscenti G, Lorenzo-Moldero I, Klein-Gunnewiek M, Vancso J, et al. Surface energy and stiffness discrete gradients in additive manufactured scaffolds for osteochondral regeneration. Biofabrication. 2016;8(1):015014.

286. Olivares-Navarrete R, Hyzy S, Hutton D, Erdman C, Wieland M, Boyan B, et al. Direct and indirect effects of microstructured titanium substrates on the induction of mesenchymal stem cell differentiation towards the osteoblast lineage. Biomaterials. 2010;31(10):2728-35.

287. Thiele J, Ma Y, Bruekers S, Ma S, Huck W. 25th Anniversary Article: Designer Hydrogels for Cell Cultures: A Materials Selection Guide. Adv Mater. 2014;26(1):125-48.

288. Chimene D, Lennox K, Kaunas R, Gaharwar A. Advanced Bioinks for 3D Printing: A Materials Science Perspective. Ann Biomed Eng. 2016;44(6):2090-102.

289. Wong D, Ranganath T, Kasko A. Low-Dose, Long-Wave UV Light Does Not Affect Gene Expression of Human Mesenchymal Stem Cells. PLoS One. 2015;10(9):e0139307.

290. Guarino V, Altobelli R, della Sala F, Borzacchiello A, Ambrosio L. Alginate Processing Routes to Fabricate Bioinspired Platforms for Tissue Engineering and Drug Delivery. In: Rehm B, Moradali M, editors. Alginates and Their Biomedical Applications. 11: Springer, Singapore; 2018. p. 101-20.

291. Lee K, Mooney D. Alginate: properties and biomedical applications. Prog Polym Sci. 2012;37(1):106-26.

292. Gomes M, Azevedo H, Malafaya P, Silva S, Oliveira J, Silva G, et al. Chapter 6 - Natural Polymers in tissue engineering applications. In: Blitterswijk C, Thomsen P, Lindahl A, Hubbell J, Williams D, Cancedda R, et al., editors. Tissue Engineering. Burlington: Academic Press; 2008. p. 145-92.

293. Drury J, Dennis R, Mooney D. The tensile properties of alginate hydrogels. Biomaterials. 2004;25(16):3187-99.

294. Lee K, Mooney D. Hydrogels for tissue engineering. Chem Rev. 2001;101:1869-77.

295. Andersen T, Auk-Emblem P, Dornish M. 3D Cell Culture in Alginate Hydrogels. Microarrays (Basel). 2015;4(2):133-61.

296. Camci-Unal G, Cuttica D, Annabi N, Demarchi D, Khademhosseini A. Synthesis and characterization of hybrid hyaluronic acid-gelatin hydrogels. Biomacromolecules. 2013;14(4):1085-92.

297. Wang X, Ao Q, Tian X, Fan J, Tong H, Hou W, et al. Gelatin-Based Hydrogels for Organ 3D Bioprinting. Polymers. 2017;9(12):401.

298. Short A, Koralla D, Deshmukh A, Wissel B, Stocker B, Calhoun M, et al. Hydrogels that allow and facilitate bone repair, remodeling, and regeneration. J Mater Chem B. 2015;3(40):7818-30.

299. Billiet T, Gevaert E, De Schryver T, Cornelissen M, Dubruel P. The 3D printing of gelatin methacrylamide cell-laden tissue-engineered constructs with high cell viability. Biomaterials. 2014;35(1):49-62.

300. Picard J, Giraudier S, Larreta-Garde V. Controlled remodeling of a protein-polysaccharide mixed gel: examples of gelatin-hyaluronic acid mixtures. Soft Matter. 2009;5(21):4198-205.

301. Cardoso D, van den Beucken J, Both L, Bender J, Jansen J, Leeuwenburgh S. Gelation and biocompatibility of injectable alginate-calcium phosphate gels for bone regeneration. J Biomed Mater Res A. 2014;102(3):808-17.

302. Douglas T, Krok-Borkowicz M, Macuda A, Pietryga K, Pamula E. Enrichment of thermosensitive chitosan hydrogels with glycerol and alkaline phosphatase for bone tissue engineering applications. Acta Bioeng Biomech. 2016;18:51-7.

303. Wang X, Paloheimo K-S, Xu H, Liu C. Cryopreservation of Cell/Hydrogel Constructs Based on a New Cell-assembling Technique. J Bioact Compat Polym. 2010;25(6):634-53.

304. Benning L, Gutzweiler L, Trondle K, Riba J, Zengerle R, Koltay P, et al. Cytocompatibility testing of hydrogels toward bioprinting of mesenchymal stem cells. J Biomed Mater Res A. 2017;105(12):3231-41.

305. Rowe S, Lee S, Stegemann J. Influence of thrombin concentration on the mechanical and morphological properties of cell-seeded fibrin hydrogels. Acta Biomater. 2007;3:59-67.

306. Catelas I, Sese N, Wu B, Dunn J, Helgerson S, Tawil B. Human mesenchymal stem cell proliferation and osteogenic differentiation in fibrin gels in vitro. Tissue Eng. 2006;12:2385-96.

307. Linsley C, Wu B, Tawil B. The effect of fibrinogen, collagen type I, and fibronectin on mesenchymal stem cell growth and differentiation into osteoblasts. Tissue Eng Part A. 2013;19(11-12):1416-23.

308. Janmey P, Winer J, Weisel J. Fibrin gels and their clinical and bioengineering applications. J R Soc Interface. 2009;6(30):1-10.

309. Brown A, Barker T. Fibrin-based biomaterials: modulation of macroscopic properties through rational design at the molecular level. Acta Biomater. 2014;10(4):1502-14.

310. Davis H, Miller S, Case E, Leach J. Supplementation of fibrin gels with sodium chloride enhances physical properties and ensuing osteogenic response. Acta Biomater. 2011;7(2):691-99.

311. Dikovsky D, Bianco-Peled H, Seliktar D. The effect of structural alterations of PEG-fibrinogen hydrogel scaffolds on 3-D cellular morphology and cellular migration. Biomaterials. 2006;27(8):1496-506.

312. Akpalo E, Bidault L, Boissiere M, Vancaeyzeele C, Fichet O, Larreta-Garde V. Fibrin-polyethylene oxide interpenetrating polymer networks: new self-supported biomaterials combining the properties of both protein gel and synthetic polymer. Acta Biomater. 2011;7(6):2418-27.

313. Oh J, Kim H, Kim T, Woo K. Comparative evaluation of the biological properties of fibrin for bone regeneration. BMB Rep. 2014;47(2):110-14.

314. Weisel J, Litvinov R. Mechanisms of fibrin polymerization and clinical implications. Blood. 2013;121(10):1712-19.

315. Badylak S, Freytes D, Gilbert T. Extracellular matrix as a biological scaffold material: Structure and function. Acta Biomater. 2009;5(1):1-13.

316. Badylak S, Gilbert T, Myers-Irvin J. The extracellular matrix as a biologic scaffold for tissue engineering. In: Blitterswijk C, Thomsen P, Lindahl A, Hubbell J, Williams D, Cancedda R, et al., editors. Tissue Engineering: Advanced Press; 2008. p. 121-43.

317. Drachuk I, Gupta M, Tsukruk V. Biomimetic Coatings to Control Cellular Function through Cell Surface Engineering. Adv Funct Mater. 2013;23(36):4437-53.

318. Pati F, Jang J, Ha D, Won Kim S, Rhie J, Shim J, et al. Printing three-dimensional tissue analogues with decellularized extracellular matrix bioink. Nat Commun. 2014;5:3935.

319. Mansour A, Mezour M, Badran Z, Tamimi F. Extracellular Matrices for Bone Regeneration: A Literature Review. Tissue Eng Part A. 2017;23:1436-51.

320. Wierzbicka-Patynowski I, Schwarzbauer J. The ins and outs of fibronectin matrix assembly. J Cell Sci. 2003;116:3269-76.

321. Faia-Torres A, Goren T, Ihalainen T, Guimond-Lischer S, Charnley M, Rottmar M, et al. Regulation of human mesenchymal stem cell osteogenesis by specific surface density of fibronectin: a gradient study. ACS Appl Mater Interfaces. 2015;7(4):2367-75.

322. Zhang W, Tsurushima H, Oyane A, Yazaki Y, Sogo Y, Ito A, et al. BMP-2 gene-fibronectin-apatite composite layer enhances bone formation. J Biomed Sci. 2011;18:62.

323. Volpi N, Schiller J, Stern R, Soltes L. Role, Metabolism, Chemical Modifications and Applications of Hyaluronan. Curr Med Chem. 2009;16:1718-45.

324. Knopf-Marques H, Pravda M, Wolfova L, Velebny V, Schaaf P, Vrana N, et al. Hyaluronic Acid and Its Derivatives in Coating and Delivery Systems: Applications in Tissue Engineering, Regenerative Medicine and Immunomodulation. Adv Healthc Mater. 2016;5(22):2841-55.

325. Turley E, Noble P, Bourguignon L. Signaling properties of hyaluronan receptors. J Biol Chem. 2002;277(7):4589-92.

326. Pre E, Conti G, Sbarbati A. Hyaluronic Acid (HA) Scaffolds and Multipotent Stromal Cells (MSCs) in Regenerative Medicine. Stem Cell Rev. 2016;12(6):664-81.

327. Wen J, Vincent L, Fuhrmann A, Choi Y, Hribar K, Taylor-Weiner H, et al. Interplay of matrix stiffness and protein tethering in stem cell differentiation. Nat Mater. 2014;13(10):979-87.

328. Wüst S, Godla M, Müller R, Hofmann S. Tunable hydrogel composite with two-step processing in combination with innovative hardware upgrade for cell-based three-dimensional bioprinting. Acta Biomater. 2014;10(2):630-40.

329. Rutz A, Hyland K, Jakus A, Burghardt W, Shah R. A multimaterial bioink method for 3D printing tunable, cell-compatible hydrogels. Adv Mater. 2015;27(9):1607-14.

330. Tabriz A, Hermida M, Leslie N, Shu W. Three-dimensional bioprinting of complex cell laden alginate hydrogel structures. Biofabrication. 2015;7(4):045012.

331. Huang G, Wang L, Wang S, Han Y, Wu J, Zhang Q, et al. Engineering three-dimensional cell mechanical microenvironment with hydrogels. Biofabrication. 2012;4(4):042001.

332. Lutolf M, Lauer-Fields J, Schmoekel H, Metters A, Weber F, Fields G, et al. Synthetic matrix metalloproteinase-sensitive hydrogels for the conduction of tissue

regeneration: engineering cell-invasion characteristics. Proc Natl Acad Sci USA. 2003;100(9):5413-18.

333. Xing Q, Yates K, Vogt C, Qian Z, Frost M, Zhao F. Increasing mechanical strength of gelatin hydrogels by divalent metal ion removal. Sci Rep. 2014;4:1-10.

334. van den Bosch E, Gielens C. Gelatin degradation at elevated temperature. Int J Biol Macromol. 2003;32(3-5):129-38.

335. Gilmore A. Anoikis. Cell Death Differ. 2005;12 Suppl 2:1473-77.

336. Dinsdale C, Mirza F, Wiebe J. Glycerol alters cytoskeleton and cell adhesion while inhibiting cell proliferation. Cell Biol Int Rep. 1992;16(7):591-602.

337. Gudapati H, Yan J, Huang Y, Chrisey D. Alginate gelation-induced cell death during laser-assisted cell printing. Biofabrication. 2014;6(3):035022.

338. Selimović Š, Oh J, Bae H, Dokmeci M, Khademhosseini A. Microscale Strategies for Generating Cell-Encapsulating Hydrogels. Polymers. 2012;4(3):1554-79.

339. Irvine S, Venkatraman S. Bioprinting and Differentiation of Stem Cells. Molecules. 2016;21(9).

340. Derby B. Bioprinting: inkjet printing proteins and hybrid cell-containing materials and structures. J Mater Chem. 2008;18(47):5717-21.

341. Shim J, Jang K, Hahn S, Park J, Jung H, Oh K, et al. Three-dimensional bioprinting of multilayered constructs containing human mesenchymal stromal cells for osteochondral tissue regeneration in the rabbit knee joint. Biofabrication. 2016;8(1):014102.

342. Park J, Choi J, Shim J, Lee J, Park H, Kim S, et al. A comparative study on collagen type I and hyaluronic acid dependent cell behavior for osteochondral tissue bioprinting. Biofabrication. 2014;6(3):035004.

343. Ferreira A, Gentile P, Chiono V, Ciardelli G. Collagen for bone tissue regeneration. Acta Biomater. 2012;8(9):3191-200.

344. Phipps M, Clem W, Catledge S, Xu Y, Hennessy K, Thomas V, et al. Mesenchymal stem cell responses to bone-mimetic electrospun matrices composed of polycaprolactone, collagen I and nanoparticulate hydroxyapatite. PLoS One. 2011;6(2):e16813.

345. Forster Y, Bernhardt R, Hintze V, Moller S, Schnabelrauch M, Scharnweber D, et al. Collagen/glycosaminoglycan coatings enhance new bone formation in a critical size bone defect - A pilot study in rats. Mater Sci Eng C Mater Biol Appl. 2017;71:84-92.

346. Curry A, Pensa N, Barlow A, Bellis S. Taking cues from the extracellular matrix to design bone-mimetic regenerative scaffolds. Matrix Biol. 2016;52-54:397-412.

347. Oliveira S, Ringshia R, Legeros R, Clark E, Yost M, Terracio L, et al. An improved collagen scaffold for skeletal regeneration. J Biomed Mater Res A. 2010;94(2):371-79.

348. Abou Neel E, Bozec L, Knowles J, Syed O, Mudera V, Day R, et al. Collagen - emerging collagen based therapies hit the patient. Adv Drug Deliv Rev. 2013;65(4):429-56.

349. Papy-Garcia D, Albanese P. Heparan sulfate proteoglycans as key regulators of the mesenchymal niche of hematopoietic stem cells. Glycoconj J. 2017;34(3):377-91.

350. Jackson R, McDonald M, Nurcombe V, Little D, Cool S. The use of heparan sulfate to augment fracture repair in a rat fracture model. J Orthop Res. 2006;24(4):636-44.

351. Sarrazin S, Lamanna W, Esko J. Heparan sulfate proteoglycans. Cold Spring Harb Perspect Biol. 2011;3(7).

352. Cool S, Nurcombe V. The osteoblast-heparan sulfate axis: control of the bone cell lineage. Int J Biochem Cell Biol. 2005;37(9):1739-45.

353. Luong-Van E, Grondahl L, Nurcombe V, Cool S. In vitro biocompatibility and bioactivity of microencapsulated heparan sulfate. Biomaterials. 2007;28(12):2127-36.

354. Mansouri R, Jouan Y, Hay E, Blin-Wakkach C, Frain M, Ostertag A, et al. Osteoblastic heparan sulfate glycosaminoglycans control bone remodeling by regulating Wnt signaling and the crosstalk between bone surface and marrow cells. Cell Death Dis. 2017;8(6):e2902.

355. Parish C. The role of heparan sulphate in inflammation. Nat Rev Immunol. 2006;6(9):633-43.

356. Ringeisen B, Othon C, Barron J, Young D, Spargo B. Jet-based methods to print living cells. Biotechnol J. 2006;1(9):930-48.

357. Huebsch N, Arany P, Mao A, Shvartsman D, Ali O, Bencherif S, et al. Harnessing traction-mediated manipulation of the cell/matrix interface to control stem-cell fate. Nat Mater. 2010;9(6):518-26.

358. Freeman F, Kelly D. Tuning Alginate Bioink Stiffness and Composition for Controlled Growth Factor Delivery and to Spatially Direct MSC Fate within Bioprinted Tissues. Sci Rep. 2017;7(1):17042.

359. Discher D, Mooney D, Zandstra P. Growth factors, matrices, and forces combine and control stem cells. Science. 2009;324(5935):1673-77.

360. Markusen J, Mason C, Hull D, Town M, Tabor A, Clements M, et al. Behavior of Adult Human Mesenchymal Stem Cells Entrapped in Alginate-GRGDY Beads. Tissue Eng. 2006;12:821-30.

361. Maia F, Lourenco A, Granja P, Goncalves R, Barrias C. Effect of cell density on mesenchymal stem cells aggregation in RGD-alginate 3D matrices under osteoinductive conditions. Macromol Biosci. 2014;14(6):759-71.

362. Duggal S, Fronsdal K, Szoke K, Shahdadfar A, Melvik J, Brinchmann J. Phenotype and gene expression of human mesenchymal stem cells in alginate scaffolds. Tissue Eng Part A. 2009;15(7):1763-73.

363. Wu Z, Su X, Xu Y, Kong B, Sun W, Mi S. Bioprinting three-dimensional cell-laden tissue constructs with controllable degradation. Sci Rep. 2016;6:24474.

364. Blaeser A, Duarte Campos D, Puster U, Richtering W, Stevens M, Fischer H. Controlling Shear Stress in 3D Bioprinting is a Key Factor to Balance Printing Resolution and Stem Cell Integrity. Adv Healthc Mater. 2016;5(3):326-33.

365. Babalola O, Bonassar L. Effects of Seeding Density on Proteoglycan Assembly of Passaged Mesenchymal Stem Cells. Cell Mol Bioeng. 2010;3(3):197-206.

366. Nicodemus G, Bryant S. Cell encapsulation in biodegradable hydrogels for tissue engineering applications. Tissue Eng Part B Rev. 2008;14(2):149-65.

367. Gleadall A, Visscher D, Yang J, Thomas D, Segal J. Review of additive manufactured tissue engineering scaffolds: relationship between geometry and performance. Burns Trauma. 2018;6:19.

368. Giannitelli S, Accoto D, Trombetta M, Rainer A. Current trends in the design of scaffolds for computer-aided tissue engineering. Acta Biomater. 2014;10(2):580-94.

369. Roseti L, Parisi V, Petretta M, Cavallo C, Desando G, Bartolotti I, et al. Scaffolds for Bone Tissue Engineering: State of the art and new perspectives. Mater Sci Eng C Mater Biol Appl. 2017;78:1246-62.

370. Hutmacher D, Woodfield T, Dalton P, Lewis J. Scaffold design and fabrication. In: Blitterswijk C, Thomsen P, Lindahl A, Hubbell J, Williams D, Cancedda R, et al., editors. Tissue Engineering. Burlington: Academic Press; 2008. p. 403-54.

371. Siddiqui N, Asawa S, Birru B, Baadhe R, Rao S. PCL-Based Composite Scaffold Matrices for Tissue Engineering Applications. Mol Biotechnol. 2018.

372. Woodruff M, Hutmacher D. The return of a forgotten polymer—Polycaprolactone in the 21st century. Prog Polym Sci. 2010;35(10):1217-56.

373. van Dijkhuizen-Radersma R, Moroni L, Apeldoorn A, Zhang Z, Grijpma D. Chapter 7 - Degradable polymers for tissue engineering. In: Blitterswijk C, Thomsen P, Lindahl A, Hubbell J, Williams D, Cancedda R, et al., editors. Tissue Engineering. Burlington: Academic Press; 2008. p. 193-221.

374. Lam C, Savalani M, Teoh S, Hutmacher D. Dynamics of in vitro polymer degradation of polycaprolactone-based scaffolds: accelerated versus simulated physiological conditions. Biomed Mater. 2008;3(3):034108.

375. Lam C, Hutmacher D, Schantz J, Woodruff M, Teoh S. Evaluation of polycaprolactone scaffold degradation for 6 months in vitro and in vivo. J Biomed Mater Res A. 2009;90(3):906-19.

376. Lam C, Teoh S, Hutmacher D. Comparison of the degradation of polycaprolactone and polycaprolactone–(β-tricalcium phosphate) scaffolds in alkaline medium. Polymer Int. 2007;56(6):718-28.

377. Armentano I, Dottori M, Fortunati E, Mattioli S, Kenny J. Biodegradable polymer matrix nanocomposites for tissue engineering: A review. Polym Degrad Stab. 2010;95(11):2126-46.

378. Thuaksuban N, Nuntanaranont T, Pattanachot W, Suttapreyasri S, Cheung L. Biodegradable polycaprolactone-chitosan three-dimensional scaffolds fabricated by melt stretching and multilayer deposition for bone tissue engineering:

assessment of the physical properties and cellular response. Biomed Mater. 2011;6(1):015009.

379. Kim Y, Kim G. PCL/Alginate Composite Scaffolds for Hard Tissue Engineering: Fabrication, Characterization, and Cellular Activities. ACS Comb Sci. 2015;17(2):87-99.

380. Zhang H, Lin C, Hollister S. The interaction between bone marrow stromal cells and RGD-modified three-dimensional porous polycaprolactone scaffolds. Biomaterials. 2009;30(25):4063-69.

381. Yildirim E, Besunder R, Pappas D, Allen F, Guceri S, Sun W. Accelerated differentiation of osteoblast cells on polycaprolactone scaffolds driven by a combined effect of protein coating and plasma modification. Biofabrication. 2010;2(1):014109.

382. Fu S, Ni P, Wang B, Chu B, Zheng L, Luo F, et al. Injectable and thermo-sensitive PEG-PCL-PEG copolymer/collagen/n-HA hydrogel composite for guided bone regeneration. Biomaterials. 2012;33(19):4801-09.

383. Holmes B, Zhu W, Li J, Lee J, Zhang L. Development of Novel Three-Dimensional Printed Scaffolds for Osteochondral Regeneration. Tissue Eng Part A. 2015;21:403-15.

384. Chen W-H, Liu Y-Y, Zhang F-H, Yu Y-Z, Chen H-P, Hu Q-X. Osteochondral integrated scaffolds with gradient structure by 3D printing forming. Int J Automation Computing. 2015;12(2):220-28.

385. Zhang X, Fang G, Zhou J. Additively Manufactured Scaffolds for Bone Tissue Engineering and the Prediction of their Mechanical Behavior: A Review. Materials (Basel). 2017;10(1).

386. Shor L, Guceri S, Chang R, Gordon J, Kang Q, Hartsock L, et al. Precision extruding deposition (PED) fabrication of polycaprolactone (PCL) scaffolds for bone tissue engineering. Biofabrication. 2009;1(1):015003.

387. Olivares A, Marsal E, Planell J, Lacroix D. Finite element study of scaffold architecture design and culture conditions for tissue engineering. Biomaterials. 2009;30(30):6142-49.

388. Chua C, Leong K, Cheah C, Chua S. Development of a Tissue Engineering Scaffold Structure Library for Rapid Prototyping. Part 2: Parametric Library and Assembly Program. Int J Adv Manuf Technol. 2003;21:302-12.

389. Melchels F, Barradas A, van Blitterswijk C, de Boer J, Feijen J, Grijpma D. Effects of the architecture of tissue engineering scaffolds on cell seeding and culturing. Acta Biomater. 2010;6(11):4208-17.

390. Sobral J, Caridade S, Sousa R, Mano J, Reis R. Three-dimensional plotted scaffolds with controlled pore size gradients: Effect of scaffold geometry on mechanical performance and cell seeding efficiency. Acta Biomater. 2011;7(3):1009-18.

391. Domingos M, Chiellini F, Gloria A, Ambrosio L, Bartolo P, Chiellini E. Effect of process parameters on the morphological and mechanical properties of 3D Bioextruded poly(ε-caprolactone) scaffolds. Rapid Prototyping J. 2012;18(1):56-67.

392. Trachtenberg J, Mountziaris P, Miller J, Wettergreen M, Kasper F, Mikos A. Open-Source Three-Dimensional Printing of Biodegradable Polymer Scaffolds for Tissue Engineering. J Biomed Mater Res A. 2014;102:4326-35.

393. Zadpoor A. Bone tissue regeneration: the role of scaffold geometry. Biomater Sci. 2015;3(2):231-45.

394. Somo S, Akar B, Bayrak E, Larson J, Appel A, Mehdizadeh H, et al. Pore Interconnectivity Influences Growth Factor-Mediated Vascularization in Sphere-Templated Hydrogels. Tissue Eng Part C Methods. 2015;21(8):773-85.

395. Loh Q, Choong C. Three-dimensional scaffolds for tissue engineering applications: role of porosity and pore size. Tissue Eng Part B Rev. 2013;19(6):485-502.

396. Coelho P, Hollister S, Flanagan C, Fernandes P. Bioresorbable scaffolds for bone tissue engineering: Optimal design, fabrication, mechanical testing and scale-size effects analysis. Med Eng Phys. 2015;37:287-96.

397. Uth N, Mueller J, Smucker B, Yousefi A. Validation of scaffold design optimization in bone tissue engineering: finite element modeling versus designed experiments. Biofabrication. 2017;9(1):015023.

398. Thibault R, Mikos A, Kasper F. Scaffold/Extracellular matrix hybrid constructs for bone-tissue engineering. Adv Healthc Mater. 2013;2(1):13-24.

399. Motamedian S, Hosseinpour S, Ahsaie M, Khojasteh A. Smart scaffolds in bone tissue engineering: A systematic review of literature. World J Stem Cells. 2015;7(3):657-68.

400. Kang S-W, Kim J-S, Park K-S, Cha B-H, Shim J-H, Kim J, et al. Surface modification with fibrin/hyaluronic acid hydrogel on solid-free form-based scaffolds followed by BMP-2 loading to enhance bone regeneration. Bone. 2011;48:298-306.

401. Pati F, Song T-H, Rijal G, Jang J, Kim S, Cho D-W. Ornamenting 3D printed scaffolds with cell-laid extracellular matrix for bone tissue regeneration. Biomaterials. 2015;37:230-41.

402. Kesireddy V, Kasper F. Approaches for building bioactive elements into synthetic scaffolds for bone tissue engineering. J Mater Chem B. 2016;4(42):6773-86.

403. Roberts A, Wyslouzil B, Bonassar L. Aerosol delivery of mammalian cells for tissue engineering. Biotechnol Bioeng. 2005;91(7):801-07.

404. Veazey W, Anusavice K, Moore K. Mammalian cell delivery via aerosol deposition. J Biomed Mater Res B Appl Biomater. 2005;72(2):334-38.

405. Graham A, Olof S, Burke M, Armstrong J, Mikhailova E, Nicholson J, et al. High-Resolution Patterned Cellular Constructs by Droplet-Based 3D Printing. Sci Rep. 2017;7(1):7004.

406. Ahn S, Lee H, Bonassar L, Kim G. Cells (MC3T3-E1)-laden alginate scaffolds fabricated by a modified solid-freeform fabrication process supplemented with an aerosol spraying. Biomacromolecules. 2012;13(9):2997-3003.

407. Raucci M, Guarino V, Ambrosio L. Biomimetic strategies for bone repair and regeneration. J Funct Biomater. 2012;3(3):688-705.

408. Paxton N, Smolan W, Bock T, Melchels F, Groll J, Jungst T. Proposal to assess printability of bioinks for extrusion-based bioprinting and evaluation of rheological properties governing bioprintability. Biofabrication. 2017;9(4):044107.

409. Ding H, Tourlomousis F, Chang R. Bioprinting multidimensional constructs: a quantitative approach to understanding printed cell density and redistribution phenomena. Biomed Phys Eng Express. 2017;3(3):035016.

410. Jaecques S, Van Oosterwyck H, Muraru L, Van Cleynenbreugel T, De Smet E, Wevers M, et al. Individualised, micro CT-based finite element modelling as a tool for biomechanical analysis related to tissue engineering of bone. Biomaterials. 2004;25(9):1683-96.

411. Shipley R, Jones G, Dyson R, Sengers B, Bailey C, Catt C, et al. Design criteria for a printed tissue engineering construct: a mathematical homogenization approach. J Theor Biol. 2009;259(3):489-502.

412. Ribeiro J, Oliveira S, Alves J, Pedro A, Reis R, Fernandes E, et al. Structural monitoring and modeling of the mechanical deformation of three-dimensional printed poly(epsilon-caprolactone) scaffolds. Biofabrication. 2017;9(2):025015.

413. Bartnikowski M, Klein T, Melchels F, Woodruff M. Effects of scaffold architecture on mechanical characteristics and osteoblast response to static and perfusion bioreactor cultures. Biotechnol Bioeng. 2014;111(7):1440-51.

414. Hendriks J, Willem Visser C, Henke S, Leijten J, Saris D, Sun C, et al. Optimizing cell viability in droplet-based cell deposition. Sci Rep. 2015;5:11304.

415. Nganga S, Moritz N, Kolakovic R, Jakobsson K, Nyman J, Borgogna M, et al. Inkjet printing of Chitlac-nanosilver - a method to create functional coatings for non-metallic bone implants. Biofabrication. 2014;6(4):041001.

416. Holzl K, Lin S, Tytgat L, Van Vlierberghe S, Gu L, Ovsianikov A. Bioink properties before, during and after 3D bioprinting. Biofabrication. 2016;8(3):032002.

417. Xu T, Jin J, Gregory C, Hickman J, Boland T. Inkjet printing of viable mammalian cells. Biomaterials. 2005;26(1):93-9.

418. Chang R, Nam J, Sun W. Effects of dispensing pressure and nozzle diameter on cell survival from solid freeform fabrication-based direct cell writing. Tissue Eng Part A. 2008;14(1):41-8.

419. Hulsart-Billström G, Dawson J, Hofmann S, Müller R, Stoddart M, Alini M, et al. A surprisingly poor correlation between in vitro and in vivo testing of biomaterials for bone regeneration: results of a multicentre analysis. Eur Cell Mater. 2016;31:312-22.

420. Hajiali F, Tajbakhsh S, Shojaei A. Fabrication and Properties of Polycaprolactone Composites Containing Calcium Phosphate-Based Ceramics and Bioactive Glasses in Bone Tissue Engineering: A Review. Polym Rev. 2017;58(1):164-207.

421. D'Haese J, Ackhurst J, Wismeijer D, De Bruyn H, Tahmaseb A. Current state of the art of computer-guided implant surgery. Peridontol 2000. 2017;73:121-33.

422. Tetsworth K, Block S, Glatt V. Putting 3D modelling and 3D printing into practice: virtual surgery and preoperative planning to reconstruct complex post-traumatic skeletal deformities and defects. SICOT J. 2017;3:16.

423. Brindley D, Moorthy K, Lee J, Mason C, Kim H, Wall I. Bioprocess forces and their impact on cell behavior: implications for bone regeneration therapy. J Tissue Eng. 2011;2011:620247.

424. Wendt D, Timmins N, Malda J, Janssen F, Ratcliffe A, Vunjak-Novakovic G, et al. Chapter 16 - Bioreactors for tissue engineering. In: Blitterswijk C, Thomsen P, Lindahl A, Hubbell J, Williams D, Cancedda R, et al., editors. Tissue Engineering. Burlington: Academic Press; 2008. p. 483-506.

425. Lopa S, Madry H. Bioinspired scaffolds for osteochondral regeneration. Tissue Eng Part A. 2014;20(15-16):2052-76.